



From Astronomy to Chemistry: Origins of the Building Blocks of Life

Citation

Todd, Zoe R. 2020. From Astronomy to Chemistry: Origins of the Building Blocks of Life. Doctoral dissertation, Harvard University, Graduate School of Arts & Sciences.

Permanent link

<https://nrs.harvard.edu/URN-3:HUL.INSTREPOS:37365547>

Terms of Use

This article was downloaded from Harvard University's DASH repository, and is made available under the terms and conditions applicable to Other Posted Material, as set forth at <http://nrs.harvard.edu/urn-3:HUL.InstRepos:dash.current.terms-of-use#LAA>

Share Your Story

The Harvard community has made this article openly available.
Please share how this access benefits you. [Submit a story](#).

[Accessibility](#)

© 2020 - ZOE R. TODD
ALL RIGHTS RESERVED.

From Astronomy to Chemistry: Origins of the Building Blocks of Life

ABSTRACT

The circumstances surrounding the origins of life on Earth are still unknown, though substantial progress has been made recently. In general, the origins of life might have followed the path where first, simple feedstock molecules available in the planetary environment react to form the molecular building blocks of life, which then come together to make chemical polymers and eventually self-replicating systems that could constitute life. This thesis addresses the first part of this postulated process, attempting to answer the questions: 1) what planetary sources exist for various feedstock molecules and under what conditions do they provide relevant quantities for prebiotic chemistry, and 2) how can such molecules be used to make the building blocks of life, and in particular, what is the potential role of UV light in this process?

We examine both impacts and the atmosphere as potential sources of feedstock molecules on a planet. Specifically, we look at the possibility of delivery of HCN from impacts of comets on the early Earth and assess which conditions and circumstances might allow for sufficient levels of this molecule to drive prebiotic chemistry. We find that on a global scale, HCN delivered from cometary impacts is not likely to be relevant for prebiotic chemistry; however, on a local scale, cometary delivered HCN could exist in relevant concentrations for up to millions of years. We then examine the atmosphere as a source of sulfur-

and nitrogen-containing compounds in the form of sulfidic anions (HS^- , HSO_3^- , and SO_3^{2-}) and NO_x^- ions in order to constrain their possible concentrations in the planetary environment for origins of life chemistry. We find that SO_2 derived anions (HSO_3^- , and SO_3^{2-}) are more globally available at prebiotically-relevant concentrations than H_2S derived anions (HS^-), which suggests that SO_2 derived ions are more relevant feedstock molecules for prebiotic chemistry experiments. We also find that NO_x^- levels may have been lower than previously reported on the early Earth due to various degradation pathways that had not been considered.

We then transition to asking how UV light can influence the prebiotic chemistry invoking these feedstock molecules, continuing to consider the overall planetary environment. UV light would have been more ubiquitous on the early Earth, given the lack of oxygen species in the atmosphere. Furthermore, UV photons provide enough energy to potentially make or break chemical bonds. In particular, we examine how prebiotic photochemical reactions proposed in the past under narrowband UV emission would behave under the UV-environment present on the early Earth to assess the plausibility of such reactions. We find that two specific photochemical reactions of potential prebiotic relevance - the generation of simple sugars from photoreduction of cyanocuprates and hydrogen cyanide and the photochemically-driven conversion of ribocytidine into ribouridine - should function under the UV-environment available on the early Earth. While UV light could potentially drive various prebiotic chemical reactions, certain molecules are also damaged by UV light. We assess the

consistency of proposed prebiotic pathways by examining the UV-driven photodegradation of three key molecules in the 2-aminoazole family to place constraints on the environment under which such chemistry could function consistently. We find that the lifetimes of these molecules under the UV light expected on the early Earth range from 7-100 hours, setting limits on how fast these molecules must be used or produced. Finally, we look at the potential protection mechanisms for molecules that may be unstable to UV light, with the hope of constraining the environments and circumstances for a consistent prebiotic chemistry to develop and function. We find that the least stable 2-aminoazole from the previous set of experiments can have its lifetime extended by being present at higher concentrations (self-shielding) or being co-irradiated in the presence of other UV-absorbing molecules, specifically, nucleosides.

In this work, we invoke an interdisciplinary approach integrating various aspects of astronomy and chemistry. The ultimate goal is to use the planetary environment to better inform both the astronomical and chemical conditions and circumstances surrounding the origins of life.

Contents

1	INTRODUCTION	1
1.1	Life and its origins	1
1.2	Early Earth Environments	7
1.3	Past prebiotic experiments of note	13
1.4	Overview of this thesis	18
2	COMETARY DELIVERY OF HCN TO THE EARLY EARTH	23
2.1	Introduction	24
2.2	Model	26
2.3	Results	30
2.4	Discussion	43
2.5	Conclusions	47
2.6	Appendix A: Chemical Network	48
3	SULFIDIC ANION CONCENTRATIONS ON THE EARLY EARTH FOR SUR- FICIAL ORIGINS-OF-LIFE CHEMISTRY	55
3.1	Background	59
3.2	Methods	61
3.3	Results	66
3.4	Discussion	75
3.5	Conclusion & Next Steps	84
3.6	Appendix A: Atmospheric Sulfur Speciation	86

3.7	Appendix B: Activity Coefficient Calculation	87
3.8	Appendix C: Sensitivity of Henry's Law Constants to Salinity . .	87
3.9	Appendix D: Sensitivity of Analysis to Temperature	89
4	NITROGEN OXIDES CONCENTRATIONS IN NATURAL WATERS ON EARLY EARTH	96
4.1	Introduction	97
4.2	Kinetic Steady-State	100
4.3	Thermochemical Equilibrium	114
4.4	Discussion	121
4.5	Conclusions	127
4.6	Appendix A: Activity Coefficient Calculation	129
4.7	Appendix B: Redox Calculation	130
4.8	Appendix C: Redox Calculation Sensitivity Analysis	132
4.9	Appendix D: Lightning Production Calculation	140
4.10	Appendix E: NO _x Loss Processes	141
5	SOLVATED-ELECTRON PRODUCTION BY CYANOCUPRATES IS COMPATIBLE WITH THE UV-ENVIRONMENT ON A HADEAN-ARCHAEAN EARTH	151
5.1	Introduction	152
5.2	Results and Discussion	154
5.3	Conclusions	158
5.4	Experimental	160
5.5	Appendix A: General Methods	161
5.6	Appendix B: Cyanocuprate Mechanism	162
5.7	Appendix C: UV/Vis Spectroscopy	166
5.8	Appendix D: Cyanide Electrode Monitoring	173
5.9	Appendix E: LC-MS	175
5.10	Appendix F: Atmospheric Modeling	177
6	UV-DRIVEN DEAMINATION OF CYTIDINE RIBONUCLEOTIDES UNDER PLANETARY CONDITIONS	182

6.1	Introduction	183
6.2	Results	189
6.3	Discussion	201
6.4	Conclusions/Implications	204
6.5	Appendix A: Determination of extinction coefficients	205
6.6	Appendix B: Irradiation of U>p	206
7	UV PHOTOSTABILITY OF THREE 2-AMINOAZOLES WITH KEY ROLES IN PREBIOTIC CHEMISTRY ON THE EARLY EARTH	209
7.1	Introduction	210
7.2	Results and Discussion	212
7.3	Conclusions	220
7.4	Appendix A: General Methods	221
7.5	Appendix B: Standard Curves	222
7.6	Appendix C: Irradiation experiments analysis	222
7.7	Appendix D: Irradiation experiments concentration dependence	225
7.8	Appendix E: Reaction of AO and glyceraldehyde	226
7.9	Appendix F: Stability of AI vs. other imidazoles	231
7.10	Appendix G: Co-irradiation of AI and AO	233
7.11	Appendix H: Atmospheric Modeling	235
8	SHIELDING FROM UV PHOTODAMAGE: IMPLICATIONS FOR SURFICIAL ORIGINS OF LIFE CHEMISTRY ON THE EARLY EARTH	237
8.1	Introduction	238
8.2	Experimental	240
8.3	Results and Discussion	241
8.4	Conclusions	251
9	CONCLUSIONS AND FUTURE DIRECTIONS	253
9.1	Conclusions	253
9.2	Future Directions	257

Listing of figures

1.1.1	Origins of Life Scheme.	7
1.2.1	UV irradiation.	12
1.2.2	Impact-induced chemistry.	14
1.3.1	Powner+ 2009 ribonucleotide synthesis.	17
1.3.2	Cyanosulfidic network.	19
1.4.1	Thesis overview.	21
2.2.1	Temperature, pressure, density profiles.	28
2.2.2	Chemical Network Overview.	29
2.3.1	Abundance profiles with time.	31
2.3.2	Molecular abundances after impact with angle.	32
2.3.3	Weighted HCN survival.	33
2.3.4	HCN survival with radius and velocity.	35
2.3.5	Global delivery of HCN.	38
2.3.6	HCN aqueous hydrolysis.	40
2.3.7	HCN local delivery.	41
3.3.1	H ₂ S speciation.	67
3.3.2	SO ₂ speciation.	69
3.3.3	Speciation in pH=7 buffered solution.	71
3.3.4	UV radiance on early Earth.	74
3.4.1	Speciation in dynamic system.	82

3.8.1	Dependence on NaCl.	90
3.9.1	Temperature Dependence.	92
4.2.1	Kinetic losses in oceans.	110
4.2.2	Kinetic losses in Ponds.	111
4.2.3	Steady state concentrations.	113
4.3.1	Thermochemical Equilibrium.	120
4.6.1	Activity coefficients	131
4.8.1	T=2°C speciation.	134
4.8.2	T=45°C speciation.	135
4.8.3	Salinity dependence.	137
4.8.4	Henry's law constant temperature dependence.	138
4.9.1	NO _x production.	142
5.1.1	Cyanocuprate scheme.	154
5.2.1	Cyanocuprate irradiations.	155
5.2.2	Cyanocuprate Quantum Yields.	157
5.2.3	Cyanocuprate photocycle on the early Earth.	159
5.5.1	Tunable Lamp.	163
5.5.2	Rayonet photochemical reactor.	164
5.7.1	Photon Flux dependence.	167
5.7.2	Dicyano- and tricyano-cuprate absorption spectra	169
5.7.3	Dicyano- and tricyano-cuprates	170
5.7.4	CN photolysis.	172
5.8.1	Cyanide electrode vs. UV-absorbance monitoring.	176
5.9.1	HCN homologation mechanism.	178
5.9.2	LC-MS detection method.	179
5.9.3	LC-MS chromatogram for standard.	180
5.9.4	LC-MS chromatogram for 255 nm irradiation.	181
6.1.1	Potential mechanisms for UV-driven deamination.	186
6.2.1	Absorption spectrum with irradiation.	190

6.2.2	Wavelength-dependent rate constants.	191
6.2.3	Relative rate on the surface of early Earth.	192
6.2.4	Thermal recovery of photo-generated intermediate.	194
6.2.5	Heating recovers U>p.	196
6.2.6	C>p and U>p recovery and partitioning.	197
6.2.7	Cycles of irradiation.	198
6.2.8	Day/Night cycle.	200
6.5.1	NMR determination of extinction coefficients.	207
6.6.1	Irradiation of U>p.	208
7.1.1	2-aminoazoles scheme.	211
7.1.2	2-aminoazoles absorption spectra.	213
7.1.3	2-aminoazole degradation under UV irradiation.	214
7.1.4	Wavelength-dependent degradation rates.	215
7.2.1	Relative rates of degradation on the early Earth.	218
7.2.2	Lifetimes of 2-aminoazoles under solar-like UV.	219
7.5.1	Absorption spectra.	223
7.5.2	Standard Curves.	224
7.7.1	Concentration dependence.	226
7.8.1	AO and glyceraldehyde NMR experiments.	228
7.9.1	Photostability of other imidazoles.	232
7.10.1	Co-irradiation of AO and AI.	234
8.3.1	AO self-shielding	242
8.3.2	AO self-shielding rate constants	243
8.3.3	Shielding by Adenosine.	246
8.3.4	Shielding by Cytidine.	247
8.3.5	Shielding by Nucleosides	248
8.3.6	AO shielding lifetimes.	250

FOR NEE AND P.

Acknowledgments

THERE ARE NUMEROUS PEOPLE whom I must give my sincerest thanks to; for without them, this thesis would not have been possible. I would like to firstly thank my advisor, Dimitar Sasselov, for his continued support and guidance, and for the freedom to explore a non-traditional set of projects. I truly cannot thank him enough for all the unique opportunities and freedoms I have enjoyed throughout my time at Harvard. I would also like to give my most profound gratitude to Jack Szostak, who has given me a place and a home in his lab for the last five years. What was originally supposed to be a few months in his lab while Dimitar's lab was being built turned into five years of numerous projects, countless important collaborations, and even more friendships. I am most thankful for Jack's continued guidance and support. I would also like to thank Karin Öberg for her willingness to take on projects with me and include me in the astrochemistry group. Her advice, mentorship, and guidance has been invaluable for me, not only as a scientist, but also as a person. I feel incredibly fortunate and lucky to have been able to work with not just one, but three, incredibly talented and kind professors during my time at Harvard. I would also like to thank the chair of my thesis committee, Dave Charbonneau, for his encouragement and support. Without his advice, I would not have had the career opportunities I have been fortunate enough to come by. My sincerest thanks to Prof. Jim Kasting, not only for agreeing to be an external reader of this thesis, but also for having taught

a wonderful astrobiology course I had the privilege of taking during my time as an undergraduate. To all of you, I can't possibly thank you enough.

I would like to offer my sincerest thanks to the people without whom nothing would be possible: Fanny Ng and Christine Benoit. Their abilities to solve any problems and keep the labs running smoothly are nothing short of heroic. I especially thank Fanny for not only her support as a lab manager, but for her friendship. Having a friendly face watching out for me means more than I can adequately express.

Over the years, I've had numerous collaborations and friendships whom I also would like to thank. To the UV lab group, in particular, Sukrit Ranjan and Corinna Kufner, I thank you for the valuable collaborations and help with experiments. I thank the MGH Szostak group, including Anna Wang, Lijun Zhou, Li Li, James Tam, Derek O'Flaherty, Tom Wright, Constantin Giurgiu, Aleks Radokavic, Ayan Pal, Victor Lelyveld, Daniel Duzdevich, Kyle Strom, Saurja Das Gupta, and Tanush Jagdish for always being available to answer any chemistry questions I have, for the experimental help, and most of all for the friendship and good memories. Life in the lab would not have meant as much without having such a great group of people to work with. I would especially like to thank my baymate, Lydia Pazienza, who is not only a great scientist, but an even better friend. A very special thanks goes to Claudia Bonfio, for her irreplaceable friendship and for her support through good and bad times. I would like to thank my other collaborators and coauthors: Rafal Szabla, Albert Fahrenbach, Chris Magnani, Paul Rimmer, Andrew Babbin, and John Sutherland. I would also like to thank the astrochemistry group for all the fun times and new knowledge. They opened my eyes to a wide range of research and always were kind in providing explanations. Friday afternoon group meetings have never been so fun.

I would also like to thank the Harvard Origins of Life Initiative family, including all of the graduate students and especially Kelly Colbourn. I have many great memories from our various field trips and events. There's no other group of people I would rather get stuck driving in circles in Norway with than you! My

sincerest thanks to Kelly Colbourn for being the best associate director (and friend!) in the Origins community. Without her, nothing would be possible. My sincerest thanks also to Yaray Ku for her friendship and many fun brunches over the years.

I thank the CfA community, especially my many graduate student friends. I would especially like to thank Jane Huang and Catherine Zucker for being great officemates, Munazza Alam for being a wonderful mentoring co-coordinator and friend, and the class of 2015 for many fun problem-set solving sessions back in our first few years.

I have had the honor of teaching numerous incredible students throughout my time at Harvard. I thank them for their efforts in class and most of all their enthusiasm. It is this enthusiasm that often reminds me of just how fortunate I am to be able to do what I do. To all of my students over the years, and those in particular who made these experiences especially rewarding, you have my sincerest thanks.

I would also like to thank my family for their support. I appreciate it more than words can say. I must also thank my neurosurgeon, Dr. James Fick, without whom I would not still be here, and without whose conversations regarding brain tumors and black holes, I would be a lesser person for.

Finally, I must also thank my horse and pony, Stan and Peter, without whom I certainly would have gone crazy over the years. They have challenged me, to work as a team, to communicate better, and overall to have fun and enjoy every moment. There's absolutely no feeling in the world like galloping through the hills or ambling along on horseback.

1

Introduction

1.1 LIFE AND ITS ORIGINS

"THE COSMOS is within us. We are made of star-stuff. We are a way for the universe to know itself." This famous quote, uttered by Carl Sagan, is indeed true. Fundamentally, all of the elements inside our bodies, all the atoms comprising the materials surrounding us and our planet (except hydrogen), were made in stars. While amazing in and of itself, this quote by Sagan hints at an even more fundamental question. It is true that we are made of star stuff, but where did we come from and how did we get here? What conditions allowed for life to originate, evolve, and become so pervasive on our planet? Is the Earth special in this regard, or is life abundant throughout our galaxy and our universe? Are we, as humans, special? Is our planet special? These questions, similar to the likes of

”where did our universe come from,” and ”what is our ultimate fate,” are perhaps among the most fundamental we can ask. Of course, this means they are not easy to answer.

In the past few decades, the discovery of exoplanets has reinvigorated the quest for finding life outside of our planet. Exoplanet discoveries are continuously increasing; new missions, such as TESS, JWST, GMT, etc., will continue to yield new exoplanet discoveries and better characterizations. Perhaps the holy grail of exoplanet discoveries is to find another planet aside from our own that contains life. If we are to have any hope of searching for and detecting life on another planet, we must better understand our own origins on Earth. Despite having unprecedented access to the one planet where we know life originated, we do not yet understand the circumstances and environments on Earth that lead to our own beginnings. By studying origins of life on Earth, we become better equipped to understand what environments and conditions may be favorable on other planets to allow them to potentially host life. With an improved understanding of the origins of life on Earth, we are better prepared to search the most promising exoplanet targets for signs of life, and more capable of interpreting this data in order to truly assess if we, on Earth, are not alone.

In order to first address the question of the origins of life, one might look to define life. NASA’s definition of life: “A self-sustaining chemical system capable of Darwinian evolution,” with its open-ended nature, makes it difficult to provide a simple test for what is alive. Nevertheless, study of the origins of life proceeds despite the lack of a simple test, or even a well-accepted and specific definition of life. Jack Szostak argues in a 2012 article that the quest to study the origin of life does not require a definition of life itself [343].

Scientists have questioned where life came from since the 17th and 18th centuries (e.g. Darwin [67]) and philosophers discussed the subject long before this. Experiments by Francesco Redi and Lazzaro Spallanzani challenged the previously held belief originally stated by Aristotle [9] of spontaneous generation - the idea that life was created from non-living matter[330]. Redi showed that maggots do not spontaneously generate upon leaving meat out in open air, while

Spallanzani showed that microbial life does not spontaneously appear from heated broth, indicating that microbes are introduced into flasks from the air [330]. Definitive evidence from Louis Pasteur disproved spontaneous generation. In these experiments, Pasteur used flasks with long, twisted necks to achieve conditions where microbes from outside the flask could not be transported inward, though air from outside could exchange [330]. Inside the flask, he placed sterilized broth. If microbes from the air were responsible, they would not be able to seed life in the broth; however, if a spontaneous “life force” were capable of creating life, one could expect that microbes would still appear in the flasks. Pasteur also predicted that if the necks to the flasks were broken, the broth would further be able to grow life. Spontaneous generation was disproven definitively with Pasteur’s experiments, but this still doesn’t answer the question of where the original form of life came from.

Another relevant hypothesis addressing the origins of life is the idea of panspermia - that life was seeded on Earth, but originated elsewhere in the universe. According to this hypothesis, life could travel through space by means of dust, meteoroids, asteroids, spacecraft, or other bodies in space. Collisions of objects could disperse pieces of life in ejecta that ultimately make it to another planet, to seed the new object with life. Panspermia was first mentioned by Anaxagoras, a Greek philosopher living in the 5th century BC [367]. Arrhenius, a Swedish chemist, was the one to propel panspermia into a fully detailed scientific hypothesis [367]. Though this hypothesis could explain how life came to be on Earth, it still doesn’t address the question of how the first life formed. Instead of asking this question on the environment of the Earth, panspermia pushes the origin of life question to any number of almost infinite possibilities and environments.

This being said, many scientists have approached the question as to the origins of life from perhaps the simplest perspective: life arose on earth, from spontaneous conditions available in the environments provided on the early planet. Even with constraining origins of life to Earth, there are numerous various environments that could be favorable for the first life to form. Many hypotheses

regarding the environments and sequence of events regarding the origins of life exist, and many of these are in contention with one another. Potential environments for the origins of life, their properties and characteristics will be discussed in more detail in the following section. Though almost an infinite number of environments and circumstances can be imagined even if one constrains themselves to the early Earth, various hypotheses regarding the origins of life tend to fall into two sets of broad categories.

These categories - genetics-first and metabolism-first - are motivated by which trait of life is considered to be most important. In other words, what trait of life makes it alive? The genetics-first hypothesis believes that the most defining attribute of life is the ability to undergo Darwinian evolution, driven by selective pressures on genetic information, while metabolism-first contends that life most essentially uses chemical reactions to harvest energy. There exist many variations and even completely different theories (e.g. peptide-first, lipid-first) for the origins of life, but these are perhaps not as deeply rooted in the community.

The genetics-first hypothesis postulates that life first originated as a sequence of genetic material, capable of carrying simple information and replicating itself. Various types of genetic material have been invoked in different forms of the theory. While life today uses DNA to store and carry genetic information, RNA has been the focus of much work as potentially a precursor to DNA as genetic material. Indeed, the “RNA World,” first postulated by Alexander Rich in 1962, and first coined by Walter Gilbert in 1986, is one of the leading hypotheses for the origins of life in the genetics-first mentality. The RNA world postulates that self-replicating RNA molecules preceded the development of DNA and proteins that are associated with life today [107]. The key advantage of the RNA world is the ability for RNA to both carry genetic information and act as an enzyme to catalyze key chemical reactions. This solves the so-called “chicken-and-egg” problem of molecular biology: DNA, which stores genetic information, requires proteins to replicate; however, proteins must be coded by DNA in order to exist. RNA, on the other hand, could act to do both functions: carry genetic information and catalyze reactions, including possibly its own self-replication. In

this way, the RNA world postulates that RNA preceded DNA and proteins in the origin and evolution of life, but the RNA world still stipulates that some form of hereditary genetic information was crucial to the first forms of life.

Difficulties still persist with the RNA world theory though. RNA, a fairly complex molecule, has historically been difficult to synthesize under conditions mimicking the early Earth environment. For this reason, some advocate for a “pre-RNA world,” where a different type of genetic polymer, perhaps easier to synthesize on the early Earth, became the first self-replicating molecule (e.g. Eschenmoser [85], Lazcano and Miller [169]). This theory postulates that eventually, RNA replaced the original molecule, leading to the conventional RNA world. There is no strong consensus on which type of molecule would have made the best “pre-RNA”; indeed, molecules ranging from peptide nucleic acid (PNA, e.g. Nelson et al. [223]), threose nucleic acid (TNA, e.g. Orgel [231]), glycol nucleic acid (GNA, e.g. Zhang and Eriksson [403]), and others, have been suggested. In addition to the possibility of an earlier genetic polymer using a different backbone than RNA, it is possible that non-canonical bases were used (e.g. Cafferty and Hud [38], Kaur and Sharma [156]). It is still an open question as to the necessity of a pre-RNA world, and if it did occur, which molecule(s) could have been the first self-replicator(s).

Another piece of evidence supporting the RNA world hypothesis is the existence of RNA enzymes (also called ribozymes) in life today (e.g. Wilson and Lilley [377]). Some RNAs in life today have catalytic functions, including the formation of peptide bonds for protein synthesis, self-cleavage, or RNA splicing. These are critical functions still carried out by RNA catalysis in life today, suggesting the possibility that these are living fossils of earlier times in the history of life where RNA played a more important role in catalysis [377]. There is continual effort, spearheaded by the Joyce and Holliger labs, to create small, short ribozymes that can catalyze their own self-replication. While this feat has not yet been achieved, recent results show an RNA polymerase can synthesize the ancestor from which it evolved [349]. The polymerase can synthesize three fragments (and their complements), which assemble to form a functional

polymerase [349], suggesting that such an RNA world where a single type of molecule can both carry genetic information and catalyze critical reactions could be plausible.

Despite the advantage the RNA world yields, it is by no means universally accepted amongst the origins of life community. Indeed, there is often considerable tension and disagreement between the RNA world (or genetics-first) community and the proponents of metabolism-first. Alexander Oparin first formulated the metabolism-first hypothesis, which states that spontaneous, energetically-favorable reactions of simple molecules occur to yield simple precursors of life while energy from these reactions is coupled to productive origins-of-life chemistry [288]. This begins a metabolic cycle, where the simple organics first generated can catalyze and react to form additional and more complex organic molecules (e.g. Martin and Russell [186]). The process would eventually yield peptides and ultimately nucleic acids. In particular, this theory can advocate for the reductive citric acid cycle - where acetate is made from CO₂ and water - as potentially the first metabolic cycle [366]. Acetate and the citric acid cycle can be used to synthesize many of the molecules common to life today; in fact, the citric acid cycle plays an essential role in biochemistry today. One potential drawback to the metabolism-first hypothesis is the consideration of information storage and transfer. How would such a system store information, as genetic materials like RNA and DNA do, and how would this information be passed on to subsequent replicated life? To date, there is not a well-accepted answer to this question.

Neither the metabolism-first or genetics-first hypotheses are completely elucidated and accepted among the origins of life community; both still contain significant issues that need to be overcome for them to be considered scientifically robust. It should also be mentioned that these two theories are not the only ones in existence for the origins of life. Alternative theories postulate alternative “firsts”, e.g. the peptide-first theory says amino acids and peptides were the first to come about in life’s origins; the lipid-first theory indicates lipids were the most important. Ultimately, all of these theories have the same goal: to

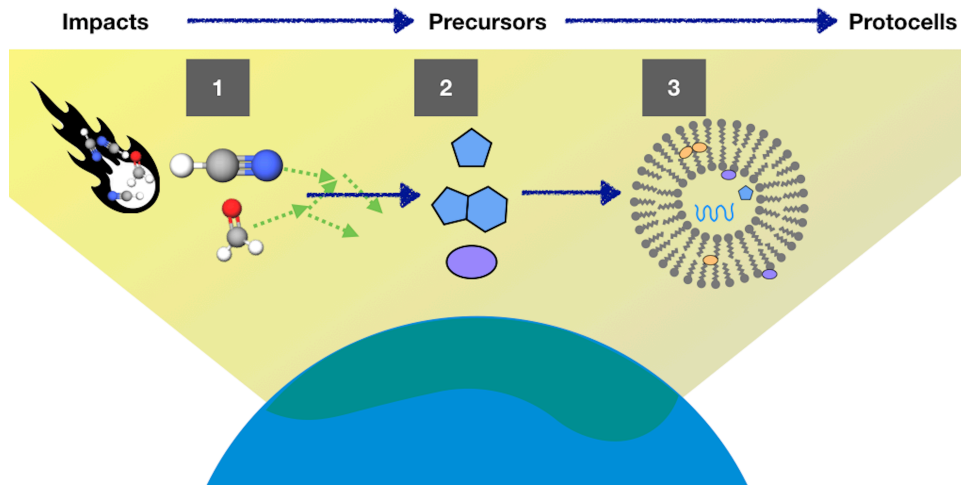


Figure 1.1.1: Scheme showing a possible pathway from initial molecules available from the planetary environment, to the prebiotic chemistry yielding precursors, to a self-replicating protocell that could be considered the first life.

reach a system that could be considered the first life. In such a theory, we would hope for simple, chemically robust and geochemically plausible routes towards obtaining a simple, self-replicating system capable of retaining and transmitting genetic information, converting this information into functional elements like peptides, and dividing itself in two, perhaps through division of protocells (e.g. Figure 1.1.1). The path towards such a system remain elusive, but substantial progress towards answering pieces of the puzzle have been made in the past and recently.

1.2 EARLY EARTH ENVIRONMENTS

When considering the hypotheses described above for origins of life, we are left with a nearly infinite set of possibilities and permutations to consider. For example, if considering the pre-RNA world, one would have to consider any number of unknown types of molecules, in order to attempt to find "the" genetic

material used in the origins of life. Alternatively, in the metabolism-first theory, one could imagine almost an infinite combination of reaction cycles and chains that could in principle lead to the origins of life. In both of these scenarios, the nearly impossibly large set of options to screen would seem to make systematic progress difficult. An alternative approach is to consider the environments available on the early Earth and instead ask which types of molecules and/or reactions would be possible in these conditions. By using the conditions and environments available on the planet at the time when life is thought to have originated, we can narrow down the possible set of options from nearly infinite to a more constrained and reasonable set. With this in mind, we will now discuss some of the environments thought to be available and interesting from the point of view of origins of life chemistry on the early Earth.

1.2.1 DEEP SEA HYDROTHERMAL VENTS

Deep sea hydrothermal vents, first discovered in 1977 [13], are environments where magma rises from under seafloor mountain ranges, also called mid-ocean ridges. Seawater can be heated to 400°C from heat coming from subsurface magma. At these elevated temperatures, chemical reactions can occur between various minerals and chemicals in the rocks, allowing the fluids to return to the vent surface containing a variety of chemicals and nutrients. The 1977 discovery showed a diverse ecosystem of life thriving at the deep sea hydrothermal vent - a shocking discovery because of the absolute lack of sunlight, which ultimately acts as the source of energy for essentially all life on the surface. This life used chemosynthesis, the process of converting chemical energy from inorganic reactions into synthesis of organic compounds. In some hydrothermal vent systems, called black smokers, geysers of hot and dark water flows from chimney-like rock structures coming from the seafloor. The fluid erupting from black smokers contain numerous minerals and chemicals, including dissolved transition metals like Fe(II) and Mn(II), CO₂, H₂S, H₂, and CH₄ [188]. Hydrothermal vents, in addition to having a rich mineral environment, are

interesting environments to consider prebiotic synthesis in due to the abundance of gradients that could be used to harness energy from. These environments see very hot water (e.g. 400°C) gushing out into cold seawater, providing a strong thermal gradient. Additionally, the strong chemical richness of the interior fluids moving into a considerable less-rich environment can lead to chemical and redox potential gradients [188]. Differences in the pH of interior and exterior fluids are also documented [188]. These environments could provide circumstances for sources of free energy and chemically diverse settings in which interesting prebiotic chemistry could occur. There is particular interest in the interaction of H₂ and CO₂ in hydrothermal vents. Since H₂ may be present in the hot fluids at fairly high concentrations, it may be able to react with CO to form reduced-carbon species in Fischer-Tropsch reactions. CO₂ has been suggested to be able to be reduced to form formate, carbon monoxide, formaldehyde, and methanol (e.g. Damer and Deamer [65]). Other chemicals present, including transition metals and metal sulfides, could allow for the synthesis of various sulfides and thioesters, among others (e.g. Cody [59], Heinen and Lauwers [127], Martin and Russell [187]), which could be useful in the beginnings of a metabolic network. Hydrothermal vents are thus one of the favored environments for the metabolism-first hypothesis of the origins of life [188].

1.2.2 SURFACE ENVIRONMENTS

An alternative to deep-sea hydrothermal vents, surface environments could also provide favorable scenarios for origins of life. Perhaps first postulated by Darwin [67] with his “warm little pond,” surface environments, including lakes, ponds, tidal pools, lagoons, etc. could be interesting environments. Here, there would be access to the atmosphere and potential energetic sources such as lightning and photochemistry. These will be discussed in more detail below, but they could provide a source of relevant feedstock molecules necessary for chemical reactions to make the building blocks of life. Surface environments would also have access to various types of cycles and gradients, including wet-dry cycles, which have

been postulated to drive interesting prebiotic chemical reactions, including the synthesis of nucleosides [18, 257], polymerization of nucleic acids into RNA [94, 242], etc.

LIGHTNING GENERATION

In one of perhaps the most famous prebiotic experiments in recent history, Stanley Miller and Harold Urey showed that passing an electrical discharge through a mixture of gases, simulating lightning in the atmosphere, lead to the synthesis of biomolecules like amino acids [205]. In the initial 1953 experiment and analysis, they identified five amino acids (glycine, α -alanine, β -alanine, aspartic acid, and α -aminobutyric acid) synthesized from passing electricity through a $\text{H}_2\text{O}/\text{H}_2/\text{CH}_4/\text{NH}_3$ atmosphere. When a similar experiment mimicking a volcanic eruption was revisited with more modern analytical techniques, a wider range of organics were detected [142]. While very interesting and exciting, it now appears as if the atmosphere of the early Earth was less reducing than that assumed in the Miller-Urey experiments (see e.g. Rugheimer et al. [285] and references therein). Under less reducing conditions, the synthesis of organic compounds from lightning discharge is less efficient (e.g. Chyba and Sagan [46]). However, lightning in the atmosphere has been invoked not only in the synthesis of relatively complex molecules such as amino acids, but also simpler feedstocks, including HCN [8, 24, 44] and NO_x [151, 183, 222], among others. Such molecules may ultimately make it to the surface and be deposited in environments, including lakes and ponds, where they could be useful for prebiotic chemistry.

PHOTOCHEMICAL GENERATION

UV light is one of the most abundant sources of energy available on the early Earth, due in part to the lack of oxygen and ozone in the atmosphere that today screen out most of these high energy photons. Instead, the early Earth would have been subjected to broadband UV light from 200-350 nm (Figure 1.2.1A

[259, 260]. These high energy photons can both make and break chemical bonds, leading to potentially UV-driven or UV-sensitive prebiotic chemistry. UV light has been invoked in the past in various prebiotic experiments, including synthesis of amino acids [300], ribonucleotides [256], and a cyanosulfidic network capable of synthesizing all four major types biomolecules [240]. Many of these past photochemical experiments were examined at a single (or a few) wavelengths; one typical example is 254 nm primary emission from mercury lamps (Figure 1.2.1B and C). Such irradiation is not representative of the UV-environment present on the surface of the early Earth. The possibility for wavelength-dependent photochemistry begs the question of if prebiotic photochemistry demonstrated in the laboratory at a single wavelength can actually function under the UV environment present on the early Earth.

UV light not only can do productive chemistry, but is also known to destroy chemical bonds and degrade organic material (e.g. Cockell [55], Sagan [290]). We must also consider then, whether the UV environment necessary to drive certain prebiotic chemical reactions is consistent with the stability, accumulation, and use of the intermediates and biomolecules it may promote. If the two are incompatible, alternative considerations or circumstances must be invoked. These circumstances could include separation of light- and dark-reactions, protection, and/or shielding of light-sensitive materials.

In addition to photochemistry on the surface of a planet, photons can also interact with the upper atmosphere to drive atmospheric synthesis of simple molecules. For example, atmospheric photochemistry has been invoked as a source of HCN [348, 397]. The efficiency of organic synthesis depends on the reducing state of the atmosphere. In particular, more reducing atmospheres with significant amounts of methane could allow for efficient organic formation via atmospheric photochemistry. Tian et al. (2011) find that modest amounts of HCN (≈ 30 Tg/yr) could be produced in a 1000 ppmv CH₄ atmosphere through photochemistry. Access to methane in the atmosphere requires a continuous source; without new production, methane is expected to either be lost to oxidation or polymerization in $< 10^4$ years [152]. If CH₄ is present in significant

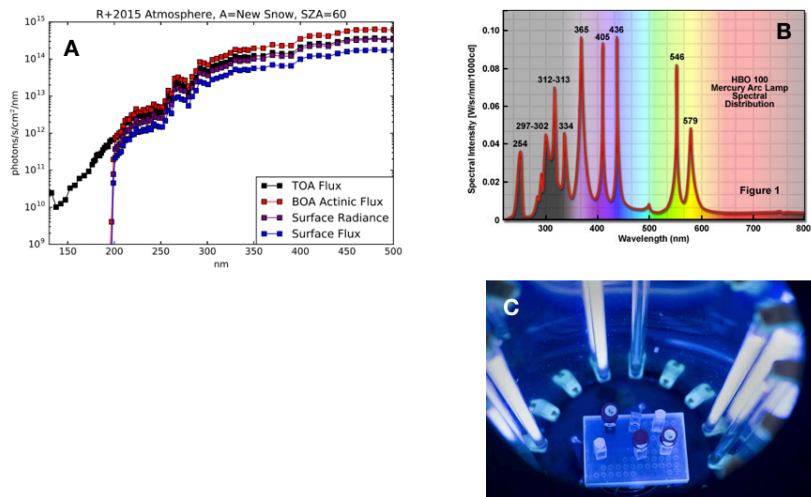


Figure 1.2.1: A. Spectrum of light expected on the surface of a planet, from Ranjan and Sasselov [259]. B. Spectrum from mercury lamps, with primary emission at 254 nm. C. Mercury lamps in a Rayonet RPR-200 reactor.

amounts, the atmosphere could form an organic haze layer similar to that of Titan. Aerosols in the atmosphere can trap or produce organic matter (e.g. Duce et al. [80], Yttri et al. [388]). Chyba and Sagan [46] estimate that organic production in a reducing atmosphere is among the most productive source of organics; however, in neutral or more oxidizing atmospheres, the organic yield from photochemical generation decreases.

IMPACT DELIVERY AND GENERATION

The early Earth likely underwent a period of more intense bombardment by asteroids and comets. Recently, it has come into question if this period was indeed a cataclysmic increase in impacts (termed the Late Heavy Bombardment)

or rather an exponential tail of the accretion process (e.g. Brassier et al. [27]). Comet or asteroid impacts have also been invoked as a source for organic molecule generation or delivery (e.g. Chyba and Sagan [46], Pierazzo and Chyba [248]). The high energy shock produced in the atmosphere during an impact has been shown to be capable of synthesizing various prebiotically interesting molecules, including HCN (e.g. Ferus et al. [96], Parkos et al. [238]), or even the nucleobases themselves (e.g. Ferus et al. [95, 97]). In addition to synthesis in the atmosphere during an impact, intact delivery of organics from exogenous material has been proposed. Exogenous material could be in the form of comet and asteroid impacts (e.g. Delsemme [77], Oro and Kimball [234]), meteorites (e.g. Anders [7]), or interplanetary dust particles (e.g. Anders [7], Maurette et al. [194]). Overall, impacts could provide organics and environments interesting from the point of view of prebiotic chemistry (see Figure 1.2.2).

1.3 PAST PREBIOTIC EXPERIMENTS OF NOTE

Previous work in prebiotic chemistry has at times focused more on exploring specific chemical reactions of potential interest. A few of these experiments are of particular note either for historical context or for relevance to work presented in this thesis, so they will be mentioned here.

1.3.1 FORMOSE REACTION

One of the most commonly invoked reactions to obtain sugars is the formose reaction [37]. In this reaction, formaldehyde polymerizes to give various sugars, including glycolaldehyde, glyceraldehyde, dihydroxyacetone, and larger sugars including tetroses and pentoses. The reaction is autocatalytic; that is, once two formaldehydes react to make glycolaldehyde, the reaction proceeds faster. The formose reaction, while appealing due to its simplicity and need for only one feedstock (formaldehyde), has some disadvantages when considering the prebiotic relevance. A significant concentration ($>0.01\text{ M}$) of formaldehyde is

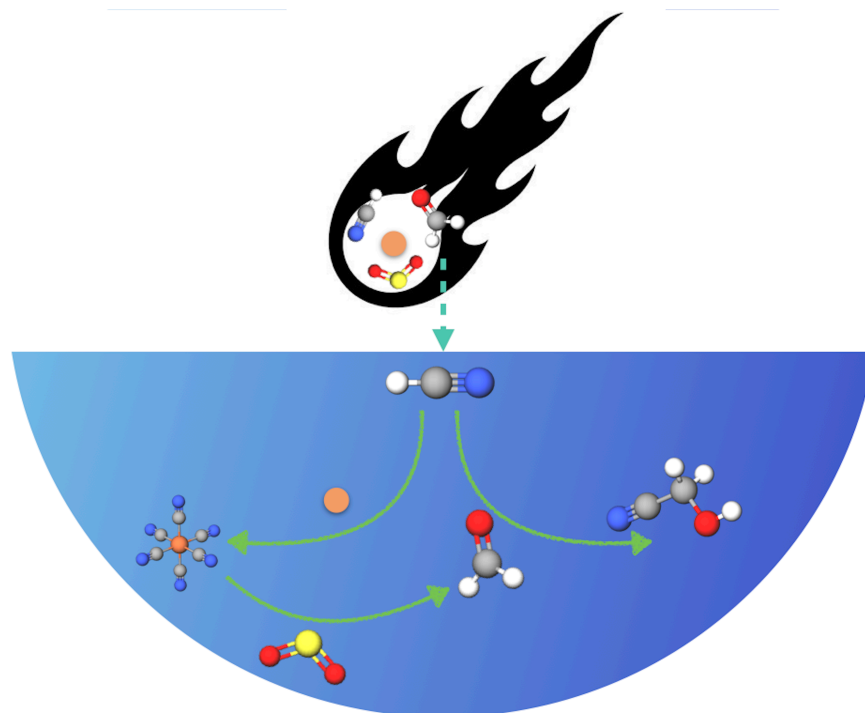


Figure 1.2.2: Certain cometary impacts may deliver and/or generate a chemical inventory available for prebiotic chemistry on the early Earth.

thought to be required to initiate the reaction [267, 303]; these levels may or may not be plausible in a robust manner on the early Earth. The reaction also typically uses alkaline conditions and the presence of divalent metal ions [52]. Perhaps an even greater hurdle to overcome with the formose reaction is the unspecificity of the reaction. In an RNA world scenario, the synthesis of ribose is desired. While the formose reaction does yield ribose (< 1%), it also gives a wide array of other products [308]. If the formose reaction is to be invoked as a source of sugars of interest, prebiotic chemists must contend with the corresponding challenges. This may not be untenable, but other solutions may need to be invoked. The presence of borate, for example, can stabilize certain sugars and lead to the favoring of ribose over other products, in particular [21]. However, this implies the environmental constraint that borate must be present. While there are geochemical scenarios in which this is the case, it remains an open question as to the robustness and plausibility of this reaction as a source of sugars for prebiotic chemistry.

1.3.2 ADENINE FROM POLYMERIZATION OF HCN

In the traditional view of the RNA World, RNA nucleotides would be synthesized by separately making the three main components (ribose sugar, nitrogenous base, and phosphate). The formose reaction has been invoked as the source of ribose, as described above. Adenine, one of the nitrogenous bases, can be synthesized under potentially prebiotic conditions by Oro [233, 234]. In these experiments, adenine was made by heating solutions of concentrated (1-15 M) hydrogen cyanide in aqueous ammonia. Temperatures ranged from 27-100° Celsius. This reaction, while perhaps unsurprising once realizing that adenine is a pentamer of HCN, was among the first syntheses of nucleobases under potentially plausible conditions. While HCN indeed is abundant in the cosmos and in our solar system, it may not have been robustly available in planetary environments in the concentrations used in these initial reactions. Once again, the planetary environment for such prebiotic reactions needs to be considered.

1.3.3 SYNTHESIS OF RIBONUCLEOTIDES

Historically, the prebiotic synthesis of ribonucleotides was expected to proceed by synthesizing the individual components (sugar, nitrogenous base, and phosphate) and then fusing them together. The formation of the glycosidic bond to fuse the nitrogenous base to the sugar had proven to be difficult - the yield was extremely low for purines [104] and the reaction did not proceed at all for pyrimidines [232]. So, in addition to the difficulties with synthesizing ribose and the nitrogenous bases (as described above), even if substituent components were available, their reaction together to form ribonucleosides was not robust. An alternative synthesis, proposed by Powner et al. [256], builds up the ribonucleotide from smaller feedstock pieces (Figure 1.3.1). Instead of building a sugar using oxygen-based chemistry and a nucleobase using nitrogenous chemistry, the Powner synthesis uses mixed oxygen-nitrogen chemistry to go from simple molecules like glycolaldehyde, glyceraldehyde, and cyanamide to 2-aminooxazole, ribose aminooxazoline, and the anhydronucleoside before β -ribocytidine-2',3'-cyclic phosphate is formed. Furthermore, upon UV irradiation, Powner et al. [256] observe partial conversion of β -ribocytidine-2',3'-cyclic phosphate to the corresponding uridine nucleotide, β -ribouridine-2',3'-cyclic phosphate. UV radiation not only gives two nucleotides effectively from only one synthesis, but it also selectively degrades non-canonical synthetic byproducts that are not used by life. Other work has used similar approaches to obtain ribonucleosides (e.g. Becker et al. [18]) and ribonucleotides (e.g. Becker et al. [19], Kim and Benner [158], Stairs et al. [325], Xu et al. [384]) from simple feedstock molecules. Given this recent progress, it seems more tractable than once before to be able to synthesize ribonucleotides under conditions present on the early Earth.

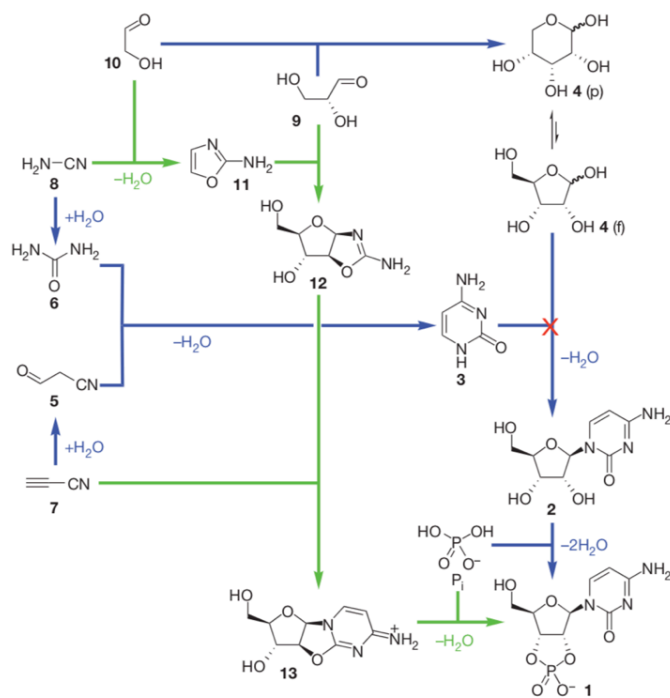


Figure 1.3.1: Synthesis of pyrimidine ribonucleotides from Powner et al. [256]. The problematic glycosidic bond formation is bypassed by using simple feedstock molecules (such as glycolaldehyde, glyceraldehyde, cyanamide, etc.) build up the nitrogen- and oxygen-containing parts of nucleotide concomitantly.

1.3.4 CYANOSULFIDIC CHEMISTRY NETWORK

Life uses four main types of biomolecules: sugars, lipids, amino acids, and ribonucleotides. Various prebiotic experiments had shown the synthesis of some of these molecules, but a unified set of conditions allowing the synthesis of all four had been a longstanding goal towards understanding the potential origins of life. Recent work from the Sutherland group showed that all four biomolecules could plausibly be synthesized from a cyanosulfidic photochemical network (see Figure 1.3.2) [240, 384]. In this work, reductive homologation of HCN driven by UV irradiation in the presence of a metal was used to build up simple two- and three-carbon sugars. These sugars could then go on to be used in the synthesis of ribonucleotides outlined by Powner et al. [256] to give this crucial set of biomolecules (though it should be noted only the pyrimidine ribonucleotides are demonstrated). Various amino acids can be synthesized throughout the pathway, in addition to lipid precursors. All of this chemistry is driven by the production of solvated electrons from UV light and the subsequent reaction of these electrons with HCN and the intermediates. Patel et al. [240] used H₂S as a source of sulfur and key ingredient to drive certain reactions. Furthermore, copper was the metal used to aid in the production of solvated electrons from UV light in Patel et al. [240], originally elucidated in Ritson and Sutherland [276] and [277]. Later work demonstrated the chemical network could function using iron instead of copper (e.g. ferrocyanide instead of cyanocuprate) and sulfite instead of hydrogen sulfide [385]. Both iron and sulfite are more robustly geochemically available than copper and hydrogen sulfide; therefore, the new system is more prebiotically plausible.

1.4 OVERVIEW OF THIS THESIS

In this thesis, we will show how considering the planetary environment and context can help constrain prebiotic chemistry. This work spans from astronomy to chemistry, all while using the backdrop of the planetary environment as

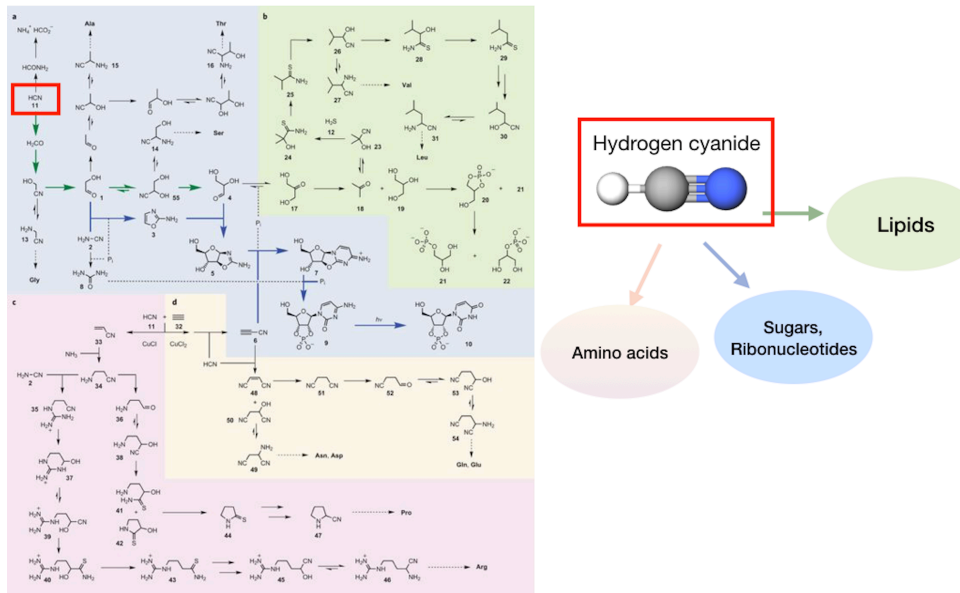


Figure 1.3.2: Prebiotically plausible cyanosulfidic chemical network leading to all four types of biomolecules [240].

context to hopefully merge various fields into a more coherent picture towards the origins of life on Earth. This thesis has two main thrusts: 1) where do the simple feedstock molecules necessary for prebiotic chemistry come from, and how can these considerations constrain the chemistry, and 2) how do such feedstock molecules come together to make the building blocks of life, and in particular, what role does UV light play? Figure 1.4.1 shows an overview of the various chapters and projects comprising this thesis. In Chapter 2, we assess how much HCN could be delivered from cometary impacts and under what scenarios it would be relevant for prebiotic chemistry. In chapters 3 and 4, we assess the implications for atmospheric sources of sulfur- and nitrogen-containing compounds, respectively (in particular, SO_2 , H_2S , and NO_x). In chapter 5 we address the UV-driven synthesis of sugars from simple precursors, including HCN. Chapter 6 discusses the photochemistry of ribonucleotides, including implications for their presence under planetary conditions. Chapter 7 examines the UV photostability of three key molecules in the cyanosulfidic network, in order to understand if their stability to UV light is compatible with the UV light invoked in other parts of the pathway. Finally, in chapter 8, we investigate the ability of molecules to be protected from damage caused by UV light, either from self-protection or protection by other UV-absorbing molecules. In this way, this work begins to present a picture of which simple chemicals are present on a planet for prebiotic chemistry, and how such a prebiotic chemistry could be used to make the building blocks of life.

This thesis aims to help address this cross-section of astronomy, planetary science, and chemistry. We attempt to understand how environments available on a planet could provide the building blocks of life, and assess possible constraints and implications toward understanding the origins of life. This work is not purely chemical or astronomical in nature; indeed, we blur the lines between these interdisciplinary fields. The planetary and astronomical environment is used to inform the chemistry, while the chemistry is taken as context for which planetary scenarios are relevant for origins of life. Throughout

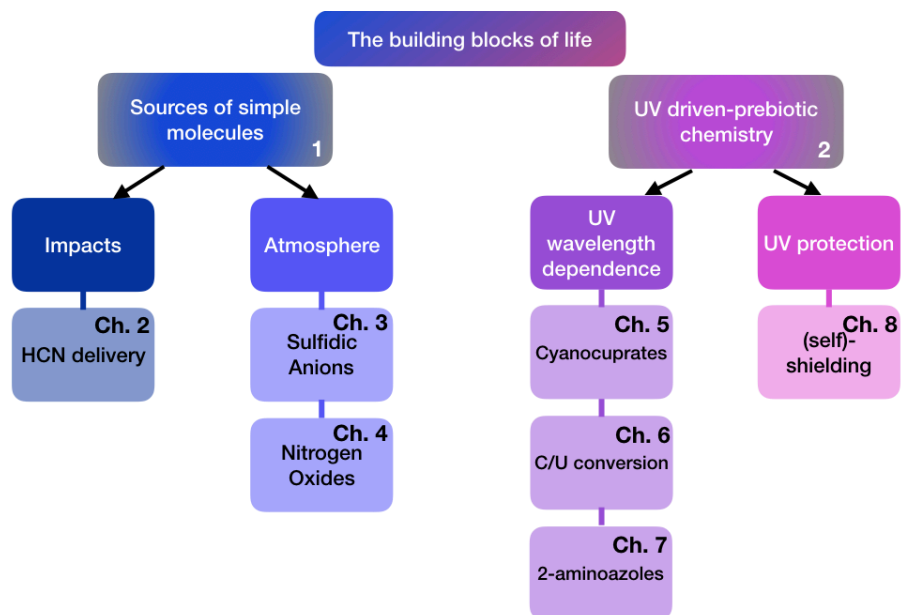


Figure 1.4.1: Breakdown of this thesis into its component project and chapters. There are two main thrusts to this work: 1) What sources of simple molecules are available on a planet, and 2) how does UV light effect prebiotic chemistry?

this work, I have come to realize that, when taken in combination, chemistry and astronomy, in the context of the planetary environment, have the potential to vastly increase our understanding, beyond what either can achieve on their own. By using astronomy and chemistry synergistically, we may be able to make key leaps in understanding that could allow for new and innovative breakthroughs in determining our own origins on this planet. If we are to be able to adequately address the question of if life exists on other planets, we must first gain a deeper understanding of how we, life on Earth, came to be. With this interdisciplinary approach, hopefully one day soon we will not only understand the origins of life on Earth, but also understand what this means for the possibility of other life existing in the universe.

2

Cometary Delivery of HCN to the Early Earth

Abstract

Delivery of water and organics by asteroid and comet impacts may have influenced prebiotic chemistry on the early Earth. Some recent prebiotic chemistry experiments emphasize hydrogen cyanide (HCN) as a feedstock molecule for the formation of sugars, ribonucleotides, amino acids, and lipid precursors. Here, we assess how much HCN originally contained in a comet would survive impact, using parametric temperature and pressure profiles together with a time-dependent chemistry model. We find that HCN survival mainly depends on whether the impact is hot enough to thermally decompose H_2O into reactive radicals, and is therefore rather insensitive to the details of the chemistry. In the most favorable impacts (low impact angle, low velocity, small

radius), this temperature threshold is not reached and intact delivery of HCN is possible. We estimate the global delivery of HCN during a period of early and late heavy bombardment of the early Earth, as well as local HCN concentrations achieved by individual impacts. In the latter case, comet impacts can provide prebiotically interesting HCN levels for thousands to millions of years, depending on properties of the impactor and of the local environment.¹

2.1 INTRODUCTION

THE ORIGIN OF LIFE on Earth presumably requires an inventory of molecules (e.g. ribonucleotides, amino acids, etc.), which would either need to be synthesized on or delivered to the early Earth. HCN has been implicated in many theories of prebiotic synthesis due to its high energy nitrile bond and its valuable nature as a simple source of carbon and nitrogen for building up more complex molecules. HCN can polymerize to form molecules such as its pentamer adenine, a nucleobase used in RNA and DNA, first shown more than 50 years ago by Oro [233]. Subsequent studies have shown that HCN can participate in the prebiotically plausible synthesis of nucleobases and nucleotides, sugars, amino acids, and lipids [49, 95, 97, 293, 294, 323, 336]. More recently, Patel et al. [240], Xu et al. [384, 385] developed a cyanosulfidic protometabolism that uses HCN as the basic source of carbon and nitrogen toward making all four major groups of prebiotic building blocks of life (sugars, nucleotides, amino acids, and lipids).

Sources of HCN on the early Earth are still discussed in the scientific community. HCN can, for example, be generated by photochemical reactions [348, 397], synthesized by lightning discharges [44, 329], and also produced upon impacts [96, 238, 332]. However, the plausibility and effectivity of these sources is not precisely constrained and would depend on atmospheric composition of the young Earth (e.g. Rimmer and Rugheimer [273]).

¹This thesis chapter is submitted as: Z. R. Todd and K. I. Oberg, *Astrobiology*, in revision.

Alongside processes of endogenous synthesis mentioned above, an alternative source of HCN could be impact delivery. Exogenous delivery of extraterrestrial material to the inner solar system has previously been considered as a potentially important source of the chemical building blocks of life [42, 48, 101, 234, 249] and recently re-emerged. The discovery of intact amino acids in meteorites on Earth (e.g. Cronin and Moore [63], Kvenvolden et al. [165] and the extraction of potentially membrane-forming lipids (e.g. Naraoka et al. [221], Shimoyama et al. [312, 313]) from meteorites show the possibility of transfer of quite complex chemical substances provided by atmospheric entry as well as impacts of interplanetary matter. Most work has focused on impacts of asteroid-type material, but comet impacts have also been proposed as plausible sources of prebiotic delivery, including amino acids [248]. More recently, the discovery of rich chemical variety and complexity on Comet 67P, including hydrocarbons, oxygenated carbon species, and nitrogen-bearing compounds (e.g. Altwegg et al. [3]), indicates comets are potentially capable of delivering part of Earth's organic inventory, including HCN.

Comet impacts may provide a robust and atmosphere-independent source of HCN, if substantial amounts of HCN survive the impact itself. Comets are known to contain fairly large amounts of HCN (e.g. Mumma and Charnley [218]). We use a chemical kinetic network and existing impact temperature and pressure models (section 2.2) to estimate HCN survival during comet impact. In section 2.3 we present the HCN survival fractions for different types of impacts (2.3.1) and use these calculations to estimate the total HCN delivery during a period of increased bombardment by impactors (2.3.2). In section 2.3.3, we assess under which circumstances impact-delivered HCN could persist locally at prebiotically interesting levels. Finally we compare our estimated HCN levels with those used in laboratory experiments (2.4.1), discuss our findings in light of other proposed sources of HCN (2.4.2), and outline current limitations and future improvements to the model (2.4.3).

2.2 MODEL

2.2.1 PRESSURE AND TEMPERATURE PROFILES DURING COMET IMPACTS

We use the results from the hydrocode models of Pierazzo Chyba (1999), hereafter referred to as PC99, to estimate temperature and pressure profiles during impact. PC99 calculate the temperatures and pressures experienced by 100 test particles in a 1 km comet impacting the Earth at a 90 degree angle and show these profiles for four such particles at various radii between the comet surface and center. Particles closer to the surface tend to experience hotter overall temperature profiles. To construct our comet impact models we interpolate between the coolest and hottest temperature profiles in PC99, which have $T_{peak} = 5500 - 12000$ K and $P_{peak} = 85 - 160$ GPa using the following parametric equations:

$$T = \left(A \left(\frac{(e^b - 1)/t^5}{e^{c/t} - 1} \right) \right) + T_o K$$

where A, b, and c are chosen to fit the PC99 tracks, and t is time in seconds. The PC99 tracks are well fit with $A = 3.05 \times 10^{-6}$ K s⁵ and $c = 1.4$ s at all radii, while b (unitless), depends on the specific radius and varies between 19.9-20.7.

The pressure profiles are fit with a similar parametric equation:

$$P = \left(D \left(\frac{(e^f - 1)/t^5}{e^{g/t} - 1} \right) \right) + P_o GPa$$

where D, f, and g are constants and t is time in seconds. We use the constants: $D = 3.05 \times 10^{-6}$ Gpa s⁵, $g = 0.5$ s, and f (unitless) increases linearly from 10.6-11.3 with radius.

From the temperature and pressure profiles, we approximate the total concentration of molecules (n_{tot}) as a function of time during the impact. Densities are calculated using the Van der Waals correction for finite volume of the gas:

$$(P)(V/n - b) = RT$$

,
where $b = 30.52 \times 10^{-6} \text{ m}^3/\text{mol}$ for water vapor [99]; this yields an initial density of $2.0 \times 10^{22} \text{ molecules/cm}^3$. At later times during the impact, we allow ideal gas law expansion to take over. Figure 2.2.1 shows the temperature, pressure, and N_{tot} profiles at six radii for our fiducial comet impact model ($r=1 \text{ km}$, $v=20 \text{ km/s}$). These radii-dependent tracks will later be used to determine the volume-integrated survival of HCN, as described in section 2.3.1. We note that since volume scales with the cube of the radius, most of the comet volume is found in the outer comet shells, which experience the highest temperatures.

2.2.2 IMPACT CHEMISTRY MODEL

We simulate the chemical evolution of the volatile component of impactors at six radii within the impacting comets, ranging from the comet core to the surface. Impactors initially contain volatile (e.g. icy/organic) molecules in a 100:20:20:0.15 $\text{H}_2\text{O}:\text{CO}_2:\text{CO}:\text{HCN}$ mixture, following typical comet observations (e.g. Mumma and Charnley [218]). HCN is the only nitrogen carrier included in our model, meaning we neglect any impact-generation of HCN and only assess how much HCN originally present survives the impact. We model the chemistry time-dependently with 31 species and 112 reactions (section 2.6), emphasizing HCN chemistry. The molecules initially present undergo thermal decomposition into reactive radicals (Figure 2.2.2a), which can then react with HCN to destroy it (Figure 2.2.2b). Additional chemistry can occur with various species produced from such reactions, typically either resulting in destruction of the nitrile bond present in the initial HCN, or regeneration of HCN (Figure 2.2.2c). Reactions were compiled from the online database KIDA [368] and the literature (see 2.6 for references).

Temperature-dependent reaction rate constants (k_n) are determined for each time step and used to calculate the concentrations of each species (C_i) during each temperature-pressure track. Concentrations are updated at each timestep to

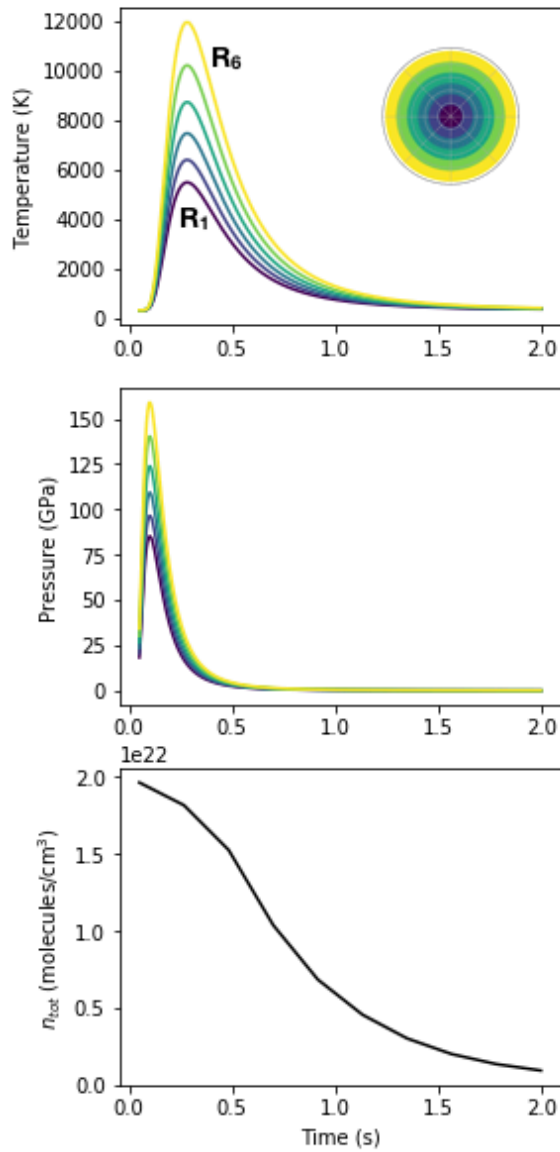
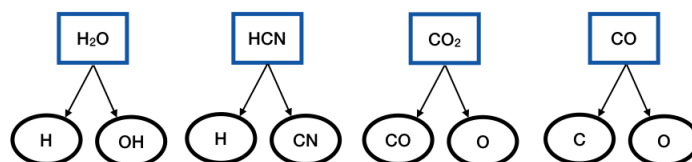
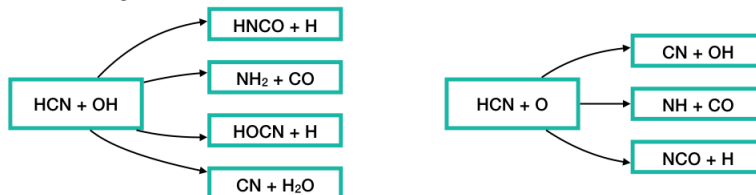


Figure 2.2.1: (A) Temperature, (B) pressure, and (C) profiles for various radius shells for a $r=1$ km, $v=20$ km/s, vertical impactor, as indicated by the comet diagram in the top right of panel A.

A - Thermal decomposition



B - HCN degradation reactions



C - Nitrile chemistry



Figure 2.2.2: Summary of the architecture of the chemical network. (A) The initial molecules contained in the comet are thermally decomposed into radicals under high temperatures. (B) Reactions of radicals and HCN lead to destruction of HCN to form a variety of other products. (C) Molecules still containing a nitrile bond can undergo further reactions, either to degrade the nitrile bond or to regenerate HCN.

account for the expanding volume during impact, following Figure 2.2.1c.

In addition to our fiducial chemical network we also constructed a smaller one, which only considers water decomposition and the OH-driven destruction of HCN, which we use to evaluate the importance of the detailed chemistry in Figure 2.2.2b and 2.2.2c for nitrile survival.

2.3 RESULTS

2.3.1 HCN SURVIVAL IN FIDUCIAL COMET IMPACT

We simulate the impact chemistry of a fiducial $r=1$ km, $v=20$ km/s spherical impactor, at six equally spaced radius shells, with impact angles between 0.5 and 90 degrees, in 5 degree intervals. Impacts occur at all angles; the impact angle affects the overall temperature and pressure profiles in the impactor. More oblique impactors pass through more of the atmosphere and experience a larger drag force, leading to lower temperatures during impact and ultimately more chemical survival. The temperature during an oblique impact can be scaled as shown by Pierazzo and Melosh [250]:

$$T_{eff} = T_o(\sin(\theta))^{0.8}$$

, where T_o is the temperature of a vertical (i.e. $\theta = 90^\circ$) impactor that is parameterized in section 2.2.1.

For vertical impactors, we use the temperature and pressure profiles from Figure 2.2.1 and evolve the chemical kinetic network to assess HCN survival. For non-vertical impactors, we scale the temperature profiles accordingly and allow the chemical kinetic network to run and determine total HCN survival. Figure 2.3.1 shows an example of the time-dependent chemistry for the case of the innermost (R_1) radius shell for 5° and 10° impactors using both the simplified and full models. At lower impact angles, the maximum temperatures are too low for substantial H_2O thermal decomposition, leading to negligible amounts of HCN loss. At 10° , temperatures experienced are sufficient to degrade some H_2O

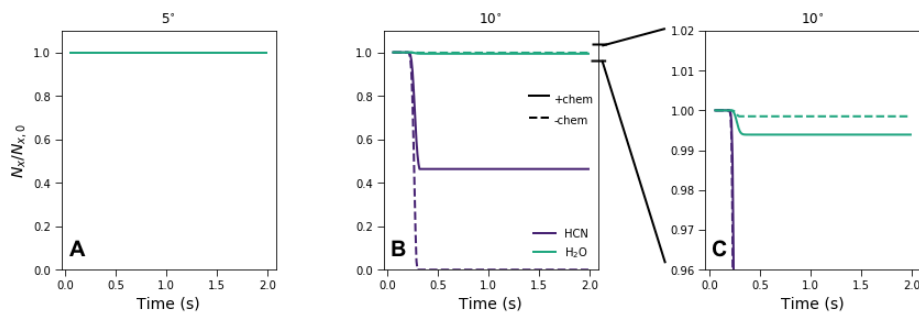


Figure 2.3.1: Abundance of selected species during the temperature evolution for 5° and 10° impactors in the innermost shell in the simplified (dashed) and full (solid) models. The species are scaled to their initial abundance and are presented on a linear scale. (A) At 5° , there is essentially no HCN or H_2O degradation. (B) At 10° , HCN is either partially (full model) or completely (simplified model) lost. (C) At 10° , H_2O experiences slight degradation in both the full and simplified models.

into OH and H radicals, initiating the HCN destruction chemistry and leading to negligible HCN survival in the simplified model and partial HCN survival in the full model.

Figure 2.3.2 shows the abundances of the initial molecules contained in the comet as a function of impact angle at three different comet radii for simulations at the lower impact angles, where some HCN survival is possible. We find that HCN survives with virtually no destruction at all radii for $\theta < 10^\circ$, in the inner three shells for $\theta < 20^\circ$, and in the inner shell for $\theta < 30^\circ$. At $\theta > 30^\circ$, HCN survival is minimal throughout the comet, i.e. $\ll 0.1\%$.

After running the full chemical models to obtain the abundances of all species for each impact angle and radius shell, we determine a total survival percentage of HCN by considering the probability distribution function of impact angles.

Pierazzo and Melosh [251] derive the probability, dP , of an impact occurring in the angle range for both gravitating and non-gravitating bodies as:

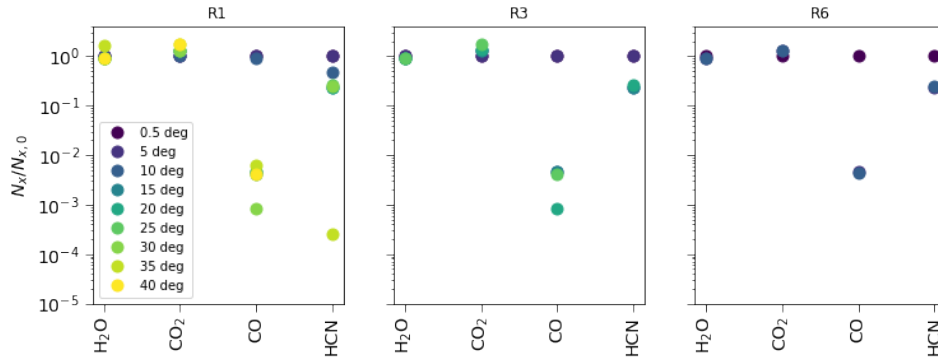


Figure 2.3.2: Abundances of H₂O, CO₂, CO, and HCN after thermal evolution for various impact angles in three radius shells. At lower impact angles, the initial molecular abundances remain fairly unchanged, but as the temperature profiles experienced increase (either from increased impact angles or more exterior radii), significant destruction of HCN is observed.

$$dP = 2\sin\theta\cos\theta d\theta$$

Approximately 18% of impacts will occur with $\theta < 25^\circ$, the approximate threshold for any HCN survival for our fiducial comet.

We calculate the HCN survival fraction as a function of impact angle and comet radius (Figure 2.3.3A), then integrate over all angles to obtain the population-averaged survival percentage at six comet radii. We then integrate again over the volume of the comet to obtain the total survival fraction of HCN for a fiducial impactor, averaged over impact angle and volume. This gives 2.3% HCN survival over the entire volume of the impactor (Figure 2.3.3B). The largest contributions to HCN delivery come from impacts at fairly oblique angles.

We assess the sensitivity of our model to the initial ratios of molecules by allowing the HCN fraction to vary from 0.007% to 0.7%, the typically observed range of HCN in comets. We find that the HCN survival fraction is rather insensitive to the initial composition.

For validation purposes, we test our simplified model (only including thermal destruction and OH-driven HCN destruction) and find that the impact angle

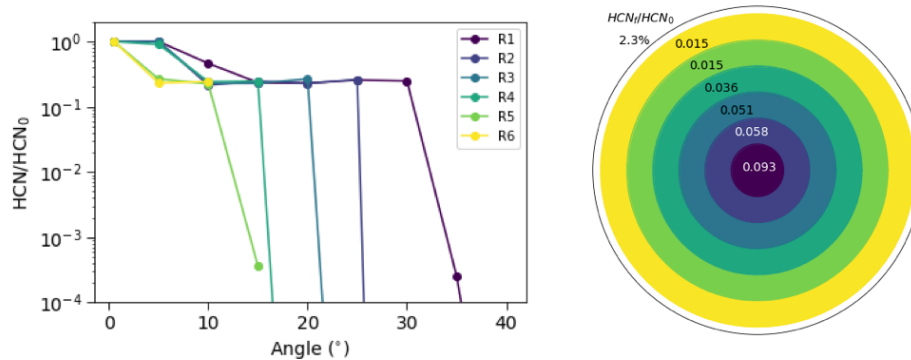


Figure 2.3.3: (A) HCN survival as a function of impact angle for the six radius shells considered. The inner radii are more shielded and therefore allow for HCN survival up to greater impact angles. (B) HCN survival for different radii shells when weighted over the probability distribution of impact angles. Integrating these survival fractions over the entire volume of the impactor gives 2.3% HCN survival (weighted over impact angle).

threshold for HCN survival is within a factor of a few compared to the model that incorporates more chemistry. The total volume-integrated and impact-angle averaged HCN survival is 0.7% for the simplified model (compared to 2.3% for the full network, i.e. roughly a factor of 3 lower). These similar results demonstrate that the order of magnitude of HCN survival during impact is not sensitive to the details of the chemical network, but that chemistry during impact results in some increased survival. We also note that HCN production during impact is likely, but this is beyond the scope of this study, which has no other source of N than HCN, whereas comets do contain other nitrogen-bearing species, e.g. NH_3 , N_2 .

2.3.2 CUMULATIVE HCN DELIVERY

In the previous section we calculated the fractional HCN survival during comet impact integrating over the comet volume and the distribution of impact angles, for our fiducial model. The HCN survival also depends on radius and velocity, and the net amount of HCN delivered also depends on the initial cometary

abundance of HCN. We address these parameters, how they affect HCN survival and content, and their distributions among comets to determine the global delivery of HCN expected over a period of increased bombardment.

HCN SURVIVAL

PC99 showed that molecular survival also depends on the radius and velocity of the impactor. At higher velocities, the impactor has more energy and reaches higher temperatures. Larger impactors require more time for a shock wave to propagate through, so material will stay in a shocked (and thus hotter) state for longer. So, we expect organic survival to decrease with both increased impactor velocity and radius. We adopt the findings of PC99, who found a roughly linear behavior on a semilog plot between amino acid survival and comet radius and between survival and impact velocity. We expect that HCN survival will behave similarly, since in both cases survival depends on thermal decomposition activated at similar temperatures; in their model they only consider the direct thermal decomposition of amino acids, while in our case the relationship is indirect since HCN loss depends on thermal decomposition of H₂O. We therefore use the average slope of log(survival) vs. radius and vs. velocity from PC99 to determine a parameterized survival function for HCN, where γ is the fractional HCN survival (in decimal form), given by:

$$\log(\gamma) = A - 0.2066 r(\text{km}) - 0.05636 v(\text{km/s})$$

, where A is a constant calculated from the HCN survival during $r=1$ km, $v=20$ km/s impacts. The survival fraction from the full chemical network gives $A=-0.299$, and from the simplified chemical network $A=-0.801$. We show the HCN survival with varying r and v in Figure 2.3.4 for both the full chemistry (solid) and simplified (dashed) models.

In order to estimate the total amount of HCN that could have been delivered

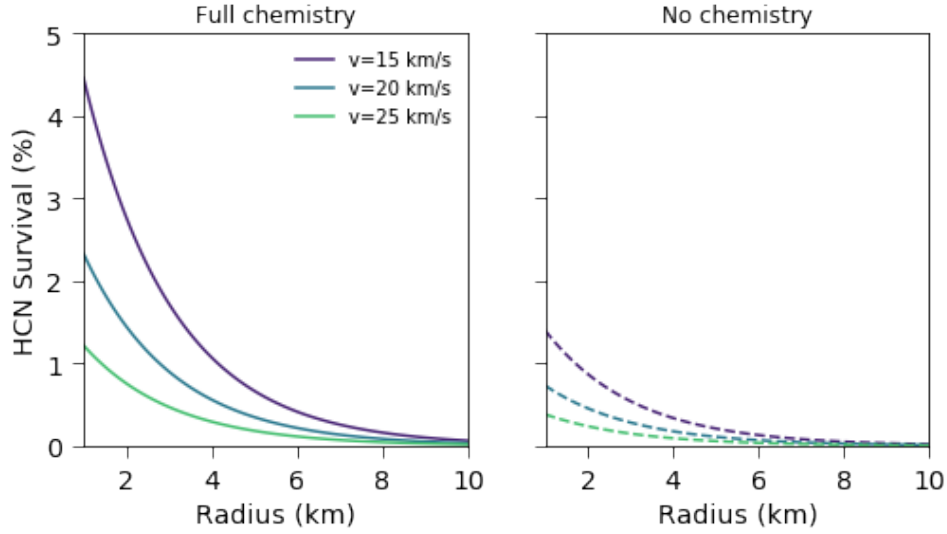


Figure 2.3.4: HCN survival for impactors of varying radii and velocities for the full chemical model (solid lines) and simplified model (dashed lines). Lower impact velocities and smaller radii are more favorable for HCN survival during impact.

to the Earth, we consider probability distributions of impactor radii and velocities suggested by the literature. The cumulative size distribution of impactor radii follows a power law, with a slope of 1.92 ± 0.2 for Jupiter family comets with $r > 1.25$ km [318]. We adopt this distribution for impactors with $1 < r(\text{km}) < R_{\text{max}}$. The maximum radius of impactors is contested; estimates based on the crater records of various moons suggest a range of roughly 6-40 km [45, 171, 214, 310]. Similar to PC99, we use a maximum radius of 5 km as a fiducial model, but also calculate the cumulative survival when R_{max} is 10 km to assess the sensitivity of the results.

The distribution of impact velocities in the young Solar System is unknown, and we instead rely on data from contemporary impacts; Hughes and Williams [137] report a mean Earth impact velocity of 24.3 ± 2.5 km/s, which is consistent with the distribution of velocities used in PC99. We therefore follow PC99 and assume that 30% of impacts occur with $15 < v(\text{km/s}) < 20$, 30% with $20 < v(\text{km/s}) < 25$, 20% with $25 < v(\text{km/s}) < 30$ and 20% with

$30 < v(\text{km/s}) < 35$. Within these velocity bins, we assume flat probability distributions. If the velocity is > 25 km/s, no organic survival is allowed, since these velocities are capable of causing impact blowoff of the atmosphere.

HCN CONCENTRATION

The final parameter to consider is the initial HCN concentration in comets. Spectroscopic observations of comets (e.g. Mumma and Charnley [218]) find that a majority of comets lie in the 0.1-0.3% HCN/H₂O range. These observations are consistent with results from ROSINA [284], which find an HCN abundance of 0.09 and 0.62 (in percent water content) in the summer and winter hemispheres, respectively. We allow the HCN/H₂O ratio to follow a Gaussian centered at 0.15%, with a width of 0.1%, which is consistent with observations from comets.

GLOBAL DELIVERY

We would like to determine the total amount and flux of HCN that could reasonably be delivered to the early Earth during a period of increased bombardment. We populate 10000 impactors with initial HCN/H₂O ratio, radius, and velocity according to the appropriate probability distributions, as described in the previous sections. The HCN survival for each body is determined using the scaling relation and the initial HCN abundance and a water content randomly chosen between 30-50% (e.g. Fayolle et al. [92]) are used to determine the total amount of surviving HCN for each impactor. We sum the HCN and H₂O over the population to get the total amounts of these molecules delivered per 10000 impacts.

The precise amount of cometary material delivered to the Earth during such a period is not known, but geochemical and isotopic constraints exist. Morbidelli et al. [213] use D/H ratios to suggest that of Earth's ocean water was delivered by comets, while other suggested constraints are far more stringent, e.g. Dauphas et al. [68] suggest 0.1% water delivered by comets. Marty et al. [190] determine

that if comet 67P is a typical comet, $<1\%$ of Earth's water was contributed by comets. Due to the continued uncertainties in the amount of water delivered by comets, we consider three cases: 0.1, 1, and 10% of Earth's ocean water delivered by comets and we scale the surviving HCN amounts to correspond to these three cases. Figure 2.3.5 shows the cumulative delivery of HCN corresponding to these three cases of water delivery by comets over a fiducial timescale of 100 Myr. The solid lines represent the model with $R_{max} = 5$ km, while the dashed lines show the case of $R_{max} = 10$ km. We find a total of 1.3×10^{14} kg HCN for the case of 1% water delivered by comets if $R_{max} = 5$ km, which corresponds to a partial pressure of 2.7×10^{-5} bar HCN, assuming a 90% N_2 , 10% CO_2 atmosphere (e.g. Rugheimer et al. [285]). If this net amount of HCN were dissolved instantaneously and homogeneously in the ocean (volume of 1.4×10^{21} L, PC99), the concentration of HCN would be $3.4 \mu\text{M}$. The 10% and 0.1% water delivery cases would give 34 and $0.34 \mu\text{M}$, respectively. However, these impacts would occur over an extended period of time, the duration of which is not precisely constrained. Estimates of the duration of increased bombardment range from >400 Myr (e.g. Barlow [16], Bottke et al. [25], Fassett and Minton [91]) to 50-200 Myr (Ryder [289], Tera et al. [346]). When adding the consideration that HCN delivery occurs on the order of hundreds of millions of years (and therefore HCN has ample time to degrade), the amount of HCN delivered intact by comets is likely to be insignificant on a global scale.

2.3.3 LOCAL HCN DELIVERY AND LIFETIMES

The above results show that HCN delivery from impacts is likely not important on a global scale, but it is possible that individual impactors could deliver significant levels of HCN on a local scale. We consider the local scenario, where impact-delivered HCN is only dissolved in water brought by the comet, as an extreme end member to determine the maximum HCN concentrations delivered from single, favorable (i.e. low impact angle, low velocity, and small radius) impacts. This is an end-member case providing an upper limit on possible HCN

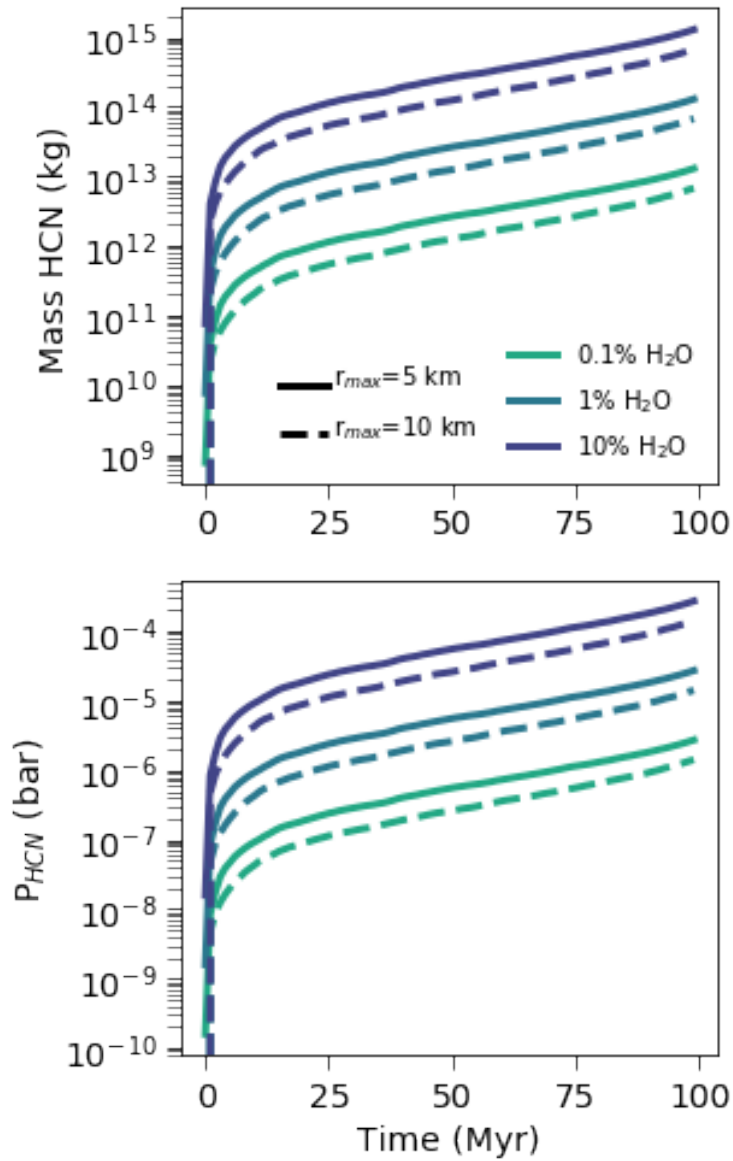
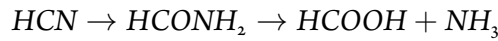


Figure 2.3.5: Total mass and partial pressure of HCN delivered for the three cases of various water delivery, assuming a 100 Myr delivery period. The total amount of HCN delivered in the case of 1% water delivery, $R_{\text{max}} = 5$ km case is 1.3×10^{14} kg, which corresponds to 2.7×10^{-5} bar HCN in a 90% N₂, 10% CO₂ atmosphere.

concentrations; in reality, depending on the amount of water in the environment near the impact, HCN concentrations could be lower. HCN will ultimately degrade with time, but it may persist in relevant quantities for prebiotic chemistry for extended periods of time.

In an aqueous environment, the main HCN loss term is HCN hydrolysis into formamide (HCONH_2) and then to formic acid (HCOOH):



The hydrolysis of HCN can be catalyzed by either acid or base [209], to give a modified rate of HCN loss of:

$$\frac{-d[\text{HCN}]}{dt} = \left(k_{1,\text{H}^+} + \frac{k_{1,\text{OH}^-}K_w}{[\text{H}^+] + K_{\text{HCN}}} \right) [\Sigma\text{HCN}]$$

, where $[\Sigma\text{HCN}] = [\text{HCN}] + [\text{CN}^-]$, $K_w = [\text{H}^+][\text{OH}^-]$, and $K_{\text{HCN}} = [\text{H}^+][\text{CN}^-]/[\text{HCN}]$.

The acid- and base-catalyzed hydrolysis rates, from Miyakawa et al. [209] are:

$$\log(k_{1,\text{H}^+}) = \frac{-4950}{T} + 8.43$$

$$\log(k_{1,\text{OH}^-}) = \frac{-4240}{T} + 11.1$$

where $k_{1,\text{H}^+/\text{OH}^-}$ is given in $\text{M}^{-1}\text{s}^{-1}$ and T is in K.

Figure 2.3.6 shows the degradation of HCN for a pH=6 and $T=10^\circ\text{C}$ following impact angles of 5° , 15° , and 25° and assuming that any HCN that survives the impact is dissolved locally in the comet-delivered water. Under these hydrolysis conditions, 5° , 15° , and 25° impactors with $r=1$ km, $v=20$ km/s would result in $[\text{HCN}] > 1\text{mM}$ for ≈ 310 kyr, 150 kyr, and 0 kyr, respectively. We find $[\text{HCN}] > 1\mu\text{M}$ for 500-1000 kyr for impact angles between $5-25^\circ$.

Using the same method as above, we determined the post-impact

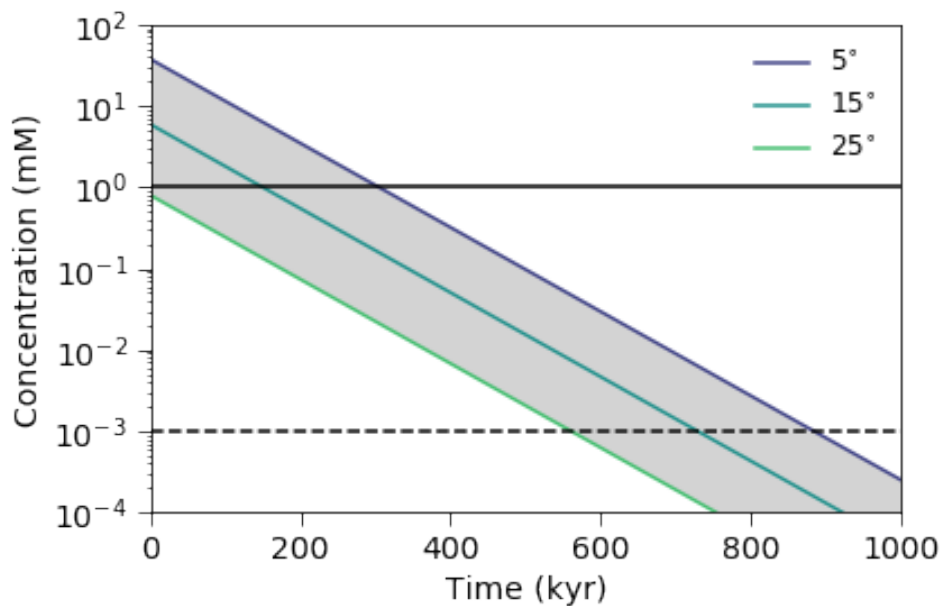


Figure 2.3.6: Concentration of HCN as a function of time in an aqueous environment with pH 6 and $T=10\text{C}$ for a $r=1$ km, $v=20$ km/s impactor at three different impact angles. The solid line shows millimolar concentrations, which have been demonstrated to work in the laboratory. The dotted line shows micromolar concentrations, which is a rough hypothetical limit to potentially relevant concentrations. 18% of impacts should occur with $\theta < 25^\circ$, the approximate threshold for HCN survival.

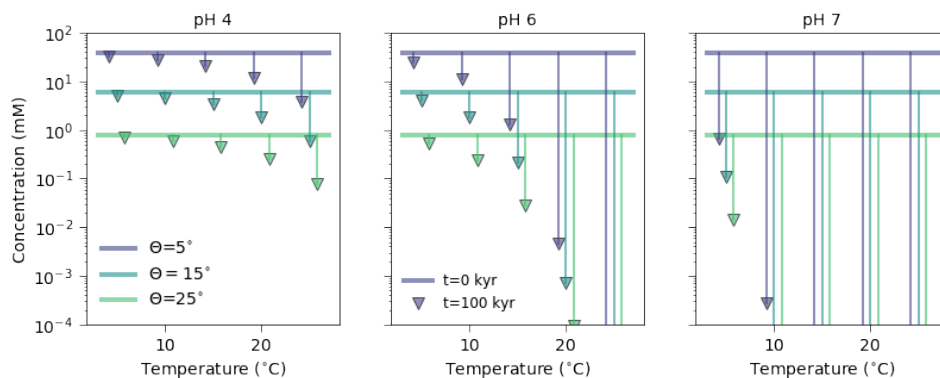


Figure 2.3.7: Concentrations of HCN from local impacts with various parameters initially (lines) and after 100 kyr (triangles). The initial concentration is set by the HCN survival for a given impact angle (color), radius (held at $r=1$ km here) and impact velocity (held constant at 20 km/s here). The concentration with time is determined by the aqueous hydrolysis of HCN, which depends on the pH (columns) and temperature (x-axis) of the environment. Lower impact angles can initially have $[\text{HCN}] > \text{mM}$ levels, which can persist above micromolar levels for longer than 100 kyr in moderately acidic (pH 4 and 6) environments for a range of temperatures, impact angles, and radii. More basic aqueous environments (e.g. pH 8) result in rapid hydrolysis of HCN, leaving none still present at 100 kyr.

concentrations of HCN for a range of impact parameters and aqueous environments. Figure 2.3.7 shows the initial HCN concentrations from local delivery for $r=1$ km impactors with angles of $5-25^\circ$ (represented by lines), along with the concentration of HCN after 100 kyr has elapsed (triangles). We find that moderately acidic (pH 4 and 6) and lower temperature conditions experience relatively slow HCN degradation over time, while basic and warmer environments lead to rapid loss of HCN. The most favorable impacts (i.e. lower impact angle and smaller radius) can have HCN concentrations in excess of millimolar levels for >100 kyr. In fact, under the most favorable conditions (pH 4, 5°C , low angle, low velocity, small radius), HCN can last for ≈ 3 Myr at $>\text{mM}$ levels, and ≈ 8 Myr at $>\mu\text{M}$ levels. At pH 6, 15°C , HCN can exist above micromolar levels for about 200-500 kyr, for an $r=1$ km, $v=20$ km/s impactor, depending on the impact angle. For larger impacts, the survival decreases by up to 60%, i.e. for 5 and 10 km impactors the survival is 50-80% and 40-60%, respectively, compared to 1 km impactors. At a velocity of 15 km/s, HCN survival is enhanced by a factor of 1.1-1.4 over the $v=20$ km/s impacts; at $v=25$ km/s, survival is 60-90% that of $v=20$ km/s.

We can then ask how the time interval between impacts with favorable HCN survival outcomes compares to the lifetime of HCN as a result of such impact. If 1% of Earth's ocean water is delivered by comets over the course of 100 Myr, impactors with $\theta < 5^\circ$ occur on average every 9 kyr, which is much smaller than the lifetime of HCN after such an impact, provided that the aqueous environment is also favorable, i.e. not too warm or basic). This implies that during a period of increased cometary bombardment, there could be multiple local impact environments with prebiotically relevant HCN levels at the same time.

2.4 DISCUSSION

2.4.1 ESTIMATED HCN LEVELS VS. LABORATORY EXPERIMENTS

In the previous section, we have shown that HCN can be delivered from comet impacts in significant levels and can persist in the local environment for prolonged periods of time under certain conditions. Under the most favorable circumstances, HCN survives at concentrations above millimolar levels for several Myr. Laboratory experiments that use HCN as a building block for prebiotic chemistry generally use from tens to hundreds of millimolar (e.g. Ritson and Sutherland [276]), to sub-millimolar (e.g. Todd et al. [350]). The reactions in Ritson and Sutherland [276] lasted roughly eight hours; those in Todd et al. [350] proceeded in four hours. Comparing these laboratory conditions to the timescales and concentrations we find possible in this study are encouraging: HCN can last for many times longer than such laboratory experiments take. Of course, laboratory experiments occur in the most favorable conditions and are often optimized to increase the efficiency or speed of the reaction. Nevertheless, having access to these prebiotically-relevant concentrations of HCN for thousands to millions of years on the early Earth could provide the circumstances for prebiotic chemistry using HCN to be successful.

We present two extreme cases for HCN delivery: global and local. In the global case, when all delivered HCN is dissolved in the entire volume of the ocean, HCN concentrations become negligibly small. In the local case of HCN delivered purely in cometary-delivered water, favorable impacts can provide significant levels of HCN for extended periods of time. In reality, most cases probably fall somewhere between the two end cases: delivered HCN will be dissolved in some combination of cometary-delivered water and water from the nearby environment. This will act to decrease the overall HCN concentration and lifetime from what we calculate in the local scenario, but depending on the amount of dilution, HCN may still be available in reasonable concentrations and timescales for prebiotic chemistry.

2.4.2 COMPARISON TO DIFFERENT SOURCES OF HCN

In our model for global delivery, 1% ocean water delivered by comets over 100 Myr gives roughly 1.3×10^6 kg/yr delivery flux. This value scales linearly with amount of water assumed to be delivered and inversely linearly with bombardment duration. However, the intact delivery that we consider here is not the only potential source of HCN on the early Earth. HCN could have been generated through atmospheric photochemical production, synthesis by lightning, and atmospheric production during impacts.

Atmospheric photochemistry can split molecular nitrogen into nitrogen atoms, which can then react with carbon-containing molecules in the atmosphere to make HCN [397]. The efficiency of this process is largely dependent on the composition of the atmosphere, with more reducing atmospheres yielding higher production rates of HCN. The Zahnle [397] results give $> 7 \times 10^{10}$ kg/yr depending on the amount of CH_4 ; Tian et al. [348] find 3×10^{10} kg/yr in a CH_4 -rich atmosphere (1000 ppmv). Oxidizing atmospheres only convert 0.1-1% of the carbon in methane to HCN if CH_4 is below a threshold of 10^{11} molecules/cm²/s, corresponding to $< 10^{8-9}$ kg/yr of HCN [397]. In particularly CH_4 -poor atmospheres, this value could drop significantly lower. Energy from lightning discharges can also break apart molecules like N_2 and other carbon compounds to allow for generation of HCN. Stribling and Miller [329] estimated 1.4×10^{10} kg/yr from lightning synthesis in a methane rich atmosphere. Chameides and Walker [44] find 4.5×10^9 kg/yr of HCN produced by lightning in a methane-rich atmosphere, but three orders of magnitude lower for a CO -dominated atmosphere, and only 4.5×10^2 kg/yr for a CO_2 -dominated atmosphere.

Overall, in reducing atmospheres, photochemical and lightning generation exceeds delivery in impacts, but the case may be different for more oxidizing atmospheres. Recent lines of evidence (e.g. igneous detrital zircons, Trail et al. [353]) point toward a less reducing atmosphere on the early Earth than previously thought, though the oxidation state of Earth's early atmosphere is still

quite unconstrained (Zahnle et al. [396] and references therein, Kasting [150], and references therein).

Another potential source of HCN on the early Earth is synthesis in the atmosphere after impact (e.g. Ferus et al. [96], Parkos et al. [238], Sugita and Schultz [332]). Parkos et al. [238] estimate 7.0×10^4 and 1.2×10^6 mol HCN produced per impact respectively, using equilibrium chemistry and non-equilibrium chemistry, corresponding to a total delivery of 1×10^{11} and 1.8×10^{12} mol HCN if comets deliver 1% of the Earth's water. Over a 100 Myr period, this corresponds to 28 and 490 kg/yr, respectively; this is several orders of magnitude below our estimates of how much can be delivered through survival of cometary HCN. The efficiency of HCN production via these various methods (photochemistry, lightning, impact generation) depends on the local C/O ratio, with $C/O > 1$ favoring HCN production [273]. In summary, in oxidizing atmospheres, survival of cometary HCN may be the major global source of HCN on the young Earth, and regardless of the atmospheric composition, local delivery of HCN through comet impacts may be sufficient to feed a Sutherland-type prebiotic chemistry (e.g. Patel et al. [240]).

2.4.3 MODEL UNCERTAINTIES AND FUTURE DIRECTIONS

There are a number of uncertainties and assumptions incorporated into our model that may affect the overall results. Perhaps the largest uncertainty when calculating the total amount of HCN delivered by comets is the amount of cometary material actually impacting the early Earth during the era of abiogenesis. The postulated Late Heavy Bombardment is currently contested, and the precise amounts and fractions of cometary and asteroidal material delivered during the early history of the solar system is contested as well. We attempt to address this uncertainty by allowing for three different cases of total cometary delivery, corresponding to delivering 0.1, 1, and 10% of Earth's ocean water. An improved understanding of the impact history of comets in the early solar system would help constrain this parameter.

Another major source of uncertainty is the lack of modern simulations of comet impacts, and the temperature and pressure environments immediately following different kinds of impacts. Our current assumptions are based on simulations from 1999 (PC99), and may actually result in underestimates of how much material can survive comet impacts; Blank et al. [22] use a 3d model and find significantly lower temperatures reached during impact than PC99, but a detailed publication is not available. New thermal models of impacts and specifically addressing how organic survival is affected would allow our model to no longer rely on such assumptions.

Furthermore, the model does not include various solid state interactions occurring during the initial vaporization of the solid material. At the very high pressures experienced soon after impact, dissociation of molecules like water and HCN into radicals could be inhibited somewhat due to Le Chatelier's principle. In this case, our results would be lower limits, since it is the initial dissociation of molecules that drives the destruction of HCN.

In addition to these uncertainties, we also made several simplified assumptions to what happens during and after impact. For example, we neglect impact generation of HCN, which has been suggested previously to be of importance (e.g. Ferus et al. [96], Sugita and Schultz [332]). We also only consider hydrolysis as the dominant sink of HCN once it reaches an aqueous environment. Undoubtedly, other processes, including degassing, further chemical reactions, etc., can act to change the HCN concentrations from our calculated values here. However, we also neglect potential storage mechanisms for HCN, including formation of metalocyanide complexes (e.g. ferrocyanides). As proposed by Xu et al. [385] and Sutherland [336], HCN can form these feedstock molecules and subsequently be released from them under certain circumstances. In such a case, the lifetime of HCN could be extended to arbitrarily longer timescales.

Despite these uncertainties and limitations to our model, we expect that the overall conclusions of this work will remain true: delivery of HCN from impacts on a global scale is not likely to be extremely relevant, but the occasional favorable impact could provide elevated and prebiotically relevant levels of HCN

on local scales for significant periods of time. In future work, we hope to incorporate additional details, including impact generation and a wider range of volatiles contained in comets, in order to obtain a more complete picture of the chemical environment available after an impact.

2.5 CONCLUSIONS

Here, we have considered intact delivery of HCN from impacts of comets as a source of HCN on the early Earth. We used a stochastic Monte-Carlo-like framework along with a chemical kinetic network to determine the amounts of HCN delivered by comets, using available literature models of comet impact physics and comet population characteristics. We find that comet delivery is unlikely to be relevant on a global scale (dissolution into the ocean brings the concentration of HCN to micromolar levels, assuming 1% water delivered by comets, and the steady-state concentration would be smaller due to HCN hydrolysis). However, individual impactors can provide elevated levels of HCN in the local environment, where surviving HCN is dissolved in only water brought by the comet. HCN survival is most favorable for low impact angle, low velocity, small radius impacts. The aqueous environmental conditions after the impact dictate how long HCN would be available above prebiotically-relevant concentrations. Lower temperatures and moderately acidic pHs (pH 4) are most favorable, and could give $[\text{HCN}] > \text{mM}$ levels for up to 3 Myr, and $[\text{HCN}] > \mu\text{M}$ for up to 8 Myr. While this scenario only includes HCN hydrolysis as a sink, we also neglect entrapment of HCN in relatively stable metalocyanides that could act as a storage mechanism and occasionally release relevant amounts of HCN to an aqueous environment. We thus suggest that impacts with favorable characteristics could potentially provide enough HCN for long enough time periods to be relevant for origins-of-life chemistry and could provide an atmosphere-independent source of HCN.

Acknowledgements

We would like to thank E. C. Fayolle for insights regarding thermal models

used and C. Giurgiu for discussions on the aqueous HCN chemistry. We would also like to thank D. D. Sasselov and S. Ranjan for helpful comments and insights. We are especially grateful to H. J. Melosh for helpful comments and suggestions during the review process. This work was supported by an award from the Simons Foundation (SCOL 321183, KO). We would also like to acknowledge funding from the Harvard Origins of Life Initiative.

2.6 APPENDIX A: CHEMICAL NETWORK

The full reaction network is listed in Table 2.6.1 and 2.6.2. The two body reactions follow the equation $k_n = AT^\beta e^{-\gamma/T}$, except KIDA reactions, which have the form: $k_n = A(T/300)^\beta e^{-\gamma/T}$. Three body reaction rates are calculated via:

$$k_{o,n} = A(T/300)^\beta e^{-\gamma/T}$$

$$P_r = \frac{k_o[M]}{k_\infty}$$

$$F = F_c^{1/\left(1 + \left(\frac{\log P_r + c}{N - d \log P_r + c}\right)^2\right)}$$

The constants have the following values, unless otherwise noted: $c = -0.4$, $N = 0.75$, $d = 0.14$, $F_c = 1.0$.

	Reaction	A	β	γ	Ref
1	$\text{H}_2\text{O} + \text{M} \rightarrow \text{H} + \text{OH} + \text{M}$	2.14×10^{-9}	0	5.29×10^4	[17]
2	$\text{CO}_2 + \text{M} \rightarrow \text{CO} + \text{O} + \text{M}$	5.22×10^{-10}	0	5.13×10^4	[229]
3	$\text{CO} + \text{M} \rightarrow \text{C} + \text{O} + \text{M}$	1.33×10^{15}	-5.5	1.29×10^5	[122]
4	$\text{CO} + \text{OH} \rightarrow \text{CO}_2 + \text{H}$	3.52×10^{-12}	0	2.63×10^3	[380]
5	$\text{HCN} + \text{M} \rightarrow \text{H} + \text{CN} + \text{M}$	1.66×10^{-8}	0	5.47×10^4	[340]

6	$\text{CN} + \text{M} \rightarrow \text{C} + \text{N} + \text{M}$	1.99×10^{-10}	0	7.10×10^4	[317]
7	$\text{HCN} + \text{OH} \rightarrow \text{NH}_2 + \text{CO}$	1.30×10^{-27}	4	2.01×10^3	[203]
8	$\text{HCN} + \text{OH} \rightarrow \text{HOCN} + \text{H}$	9.72×10^{-20}	2.4	6.29×10^3	[203]
9	$\text{HCN} + \text{OH} \rightarrow \text{CN} + \text{H}_2\text{O}$	6.48×10^{-18}	1.83	5.18×10^3	[382]
10	$\text{HCN} + \text{OH} \rightarrow \text{HNCO} + \text{H}$	3.29×10^{-27}	4	5.03×10^2	[203]
11	$\text{HCN} + \text{O} \rightarrow \text{CN} + \text{OH}$	4.49×10^{-15}	1.58	1.34×10^4	[202]
12	$\text{HCN} + \text{O} \rightarrow \text{NH} + \text{CO}$	5.73×10^{-21}	2.64	2.51×10^3	[202]
13	$\text{HCN} + \text{O} \rightarrow \text{NCO} + \text{H}$	2.29×10^{-20}	2.64	2.51×10^3	[202]
14	$\text{CN} + \text{C} \rightarrow \text{C}_2 + \text{N}$	4.98×10^{-10}	0	1.81×10^4	[317]
15	$\text{CN} + \text{H}_2\text{O} \rightarrow \text{HCN} + \text{OH}$	3.80×10^{-11}	0	6.70×10^3	[342]
16	$\text{CN} + \text{N} \rightarrow \text{N}_2 + \text{C}$	7.31×10^{-10}	0	4.53×10^3	[317]
17	$\text{CN} + \text{HCN} \rightarrow \text{C}_2\text{N}_2 + \text{H}$	2.51×10^{-17}	1.71	7.70×10^2	[381]
18	$\text{CN} + \text{O} \rightarrow \text{CO} + \text{N}$	1.50×10^{-10}	0	6.56×10^2	[70]
19	$\text{CN} + \text{OH} \rightarrow \text{NCO} + \text{H}$	6.64×10^{-11}	0	0	[381]
20	$\text{CN} + \text{H}_2 \rightarrow \text{HCN} + \text{H}$	4.90×10^{-19}	2.45	1.13×10^3	[381]
21	$\text{CN} + \text{HNCO} \rightarrow \text{HCN} + \text{H}$	2.49×10^{-11}	0	0	[357]
22	$\text{C}_2\text{N}_2 + \text{M} \rightarrow 2\text{CN} + \text{M}$	1.05×10^{-7}	0	4.72×10^4	[341]
23	$\text{C}_2\text{N}_2 + \text{O} \rightarrow \text{CN} + \text{NCO}$	8.31×10^{-13}	0	0	[180]

24	$C_2N_2 + OH \rightarrow CN +$ HNCO	3.09×10^{-13}	o	1.45×10^3	[246]
25	$NCO + M \rightarrow N + CO$ + M	5.25×10^{-8}	-0.5	2.40×10^4	[181]
26	$NCO + O \rightarrow CO +$ NO	9.35×10^{-11}	o	o	[181]
27	$NCO + H \rightarrow NH +$ CO	1.74×10^{-10}	o	1.00×10^3	[181]
28	$HNCO + O \rightarrow NH +$ CO ₂	3.16×10^{-11}	o	7.15×10^3	[200]
29	$HNCO + O \rightarrow OH +$ NCO	2.33×10^{-10}	o	1.03×10^4	[200]
30	$HNCO + H \rightarrow NH_2 +$ CO	3.49×10^{-10}	o	8.50×10^3	[199]
31	$HNCO + M \rightarrow NH +$ CO	1.63×10^{-8}	o	4.30×10^4	[198]
32	$H_2CN + O \rightarrow OH +$ HCN	4.00×10^{-11}	o	o	[368]
33	$H_2CN + H \rightarrow H_2 +$ HCN	6.00×10^{-11}	o	o	[368]
34	$H_2CN + N \rightarrow NH +$ HCN	5.00×10^{-12}	o	o	[368]
35	$H_2CN + C \rightarrow CH +$ HCN	3.00×10^{-11}	o	o	[368]
36	$H_2CN + N \rightarrow N_2 +$ CH ₂	4.00×10^{-11}	o	o	[368]
37	$HCO + O \rightarrow H + CO_2$	5.00×10^{-11}	o	o	[368]
38	$HCO + O \rightarrow CO +$ OH	5.00×10^{-11}	o	o	[368]

39	HCO + CN → HCN + CO	1.00×10^{-10}	o	o	[368]
40	HCO + OH → CO + H ₂ O	1.80×10^{-10}	o	o	[368]
41	HCO + H → CO + H ₂	1.83×10^{-10}	o	o	[103]
42	HCO + N → H + NCO	1.00×10^{-10}	o	o	[368]
43	HCO + N → CO + NH	5.71×10^{-12}	0.5	1.00×10^3	[368]
44	HCO + C → CH + CO	1.80×10^{-10}	o	o	[368]
45	HCO + CH ₂ → CO + CH ₃	3.00×10^{-11}	o	o	[368]
46	CH ₂ + O → 2H + CO	1.00×10^{-10}	o	o	[368]
47	CH ₂ + O → CO + H ₂	4.00×10^{-11}	o	o	[368]
48	CH ₂ + O → H + HCO	2.00×10^{-12}	o	o	[368]
49	CH ₂ + OH → H + H ₂ CO	3.00×10^{-10}	o	o	[368]
50	CH ₂ + OH → CH + H ₂ O	1.44×10^{-11}	0.5	3.00×10^3	[368]
51	CH ₂ + OH → O + CH ₃ 52	CH ₂ + C → 2.69×10^{-12}	o	2.36×10^4	[368]
53	CH ₂ + C → H + CCH	1.00×10^{-10}	o	o	[368]
54	CH ₂ + H → $2.20 \times$ 10^{-10}	o	o	[368]	
55	CH ₂ + H ₂ → $5.00 \times$ 10^{-11}	o	4.87×10^3	[368]	
56	CH ₂ + N → H + HCN	5.00×10^{-11}	0.17	o	[368]
57	C ₂ + N → C + CN	2.00×10^{-11}	0.17	o	[368]
58	C ₂ + O → C + CO	2.00×10^{-10}	-0.12	o	[368]
59	C ₂ + H → C + CH	4.67×10^{-10}	0.5	3.04×10^4	[368]

60	$O + H_2 \rightarrow H + OH$	6.34×10^{-12}	o	4.00×10^3	[368]
61	$N_2 + O \rightarrow N + NO$	2.51×10^{-10}	o	3.86×10^4	[368]
62	$HOCN + C \rightarrow CO + HCN$	3.33×10^{-11}	o	o	[368]
63	$HOCN + O \rightarrow OH + NCO$	3.33×10^{-11}	o	2.47×10^3	[368]
64	$C + N_2 \rightarrow CN + N$	8.70×10^{-11}	o	2.26×10^4	[368]
65	$O + H_2O \rightarrow OH + OH$	7.59×10^{-15}	1.3	8.61×10^3	[60]
66	$OH + H_2 \rightarrow H + H_2O$	1.94×10^{-15}	1.3	1.83×10^3	[79]
67	$H_2 + O \rightarrow OH + H$	3.02×10^{-14}	1.0	4.48×10^3	[60]
68	$H_2O + H \rightarrow OH + H_2$	3.99×10^{-10}	o	1.08×10^4	[69]
69	$H_2 + M \rightarrow H + H + M$	3.64×10^{-10}	o	4.83×10^4	[17]
70	$NH + H \rightarrow N + H_2$	1.66×10^{-10}	o	o	[202]
71	$CH_3 + O \rightarrow H + H_2CO$	1.08×10^{-10}	o	o	[368]
72	$CH_3 + O \rightarrow H + CO + H_2$	2.2×10^{-11}	o	o	[368]
73	$CH_3 + OH \rightarrow H_2 + H_2CO$	5.3×10^{-15}	o	2.53×10^3	[368]
74	$CH_3 + OH \rightarrow O + CH_4$	3.27×10^{-14}	2.2	2.24×10^3	[368]
75	$CH_3 + OH \rightarrow CH_2 + H_2O$	1.2×10^{-10}	o	1.4×10^3	[368]
76	$CH_3 + H \rightarrow H_2 + CH_2$	1.0×10^{-10}	o	7.6×10^3	[368]
77	$CH_3 + N \rightarrow H + H + HCN$	6.0×10^{-12}	0.17	o	[368]
78	$CH_3 + N \rightarrow H + H_2CN$	5.6×10^{-11}	0.17	o	[368]
79	$NH_3 + O \rightarrow OH + NH_2$	1.03×10^{-12}	1.85	2.0×10^2	[368]

80	$\text{NH}_3 + \text{OH} \rightarrow \text{H}_2\text{O} + \text{NH}_2$	3.5×10^{-12}	0	9.25×10^2	[368]
81	$\text{NH}_3 + \text{H} \rightarrow \text{H}_2 + \text{NH}_2$	6.54×10^{-13}	2.76	5.17×10^3	[368]
82	$\text{NH}_3 + \text{C} \rightarrow \text{H}_2\text{CN} + \text{H}$	6.70×10^{-11}	-0.51	0	[368]
83	$\text{H}_2\text{CO} + \text{O} \rightarrow \text{OH} + \text{HCO}$	1.78×10^{-11}	0.57	1.39×10^3	[368]
84	$\text{H}_2\text{CO} + \text{OH} \rightarrow \text{H}_2\text{O} + \text{HCO}$	2.31×10^{-11}	0	3.04×10^2	[368]
85	$\text{H}_2\text{CO} + \text{H} \rightarrow \text{H}_2 + \text{HCO}$	1.22×10^{-32}	-3.81	2.02×10^2	[368]
86	$\text{H}_2\text{CO} + \text{C} \rightarrow \text{CO} + \text{CH}_2$	3.0×10^{-10}	0	0	[368]
87	$\text{N}_2 + \text{O} \rightarrow \text{NO} + \text{N}$	2.51×10^{-10}	0	3.86×10^4	[368]
88	$\text{H}_2 + \text{O} \rightarrow \text{H} + \text{OH}$	6.34×10^{-12}	0	4.0×10^3	[368]
89	$\text{H}_2 + \text{OH} \rightarrow \text{H} + \text{H}_2\text{O}$	7.7×10^{-12}	0	2.1×10^3	[368]
90	$\text{CH} + \text{O} \rightarrow \text{H} + \text{CO}$	9.4×10^{-11}	0	0	[368]
91	$\text{CH} + \text{OH} \rightarrow \text{H} + \text{HCO}$	1.44×10^{-11}	0.5	5.0×10^3	[368]
92	$\text{CH} + \text{H} \rightarrow \text{C} + \text{H}_2$	1.24×10^{-10}	0.26	0	[368]
93	$\text{CH} + \text{N} \rightarrow \text{H} + \text{CN}$	1.4×10^{-10}	0.41	0	[368]
94	$\text{CH} + \text{N} \rightarrow \text{C} + \text{NH}$	3.03×10^{-11}	0.65	1.21×10^3	[368]
95	$\text{NO} + \text{H} \rightarrow \text{O} + \text{NH}$	9.3×10^{-10}	-0.1	3.52×10^4	[368]
96	$\text{NO} + \text{H} \rightarrow \text{N} + \text{OH}$	3.6×10^{-10}	0	2.49×10^4	[368]
97	$\text{NO} + \text{O} \rightarrow \text{N} + \text{O}_2$	8.93×10^{-13}	1.0	1.95×10^4	[368]

Table 2.6.1: Two body reactions and associated values for determining rate constants. Rates are calculated via $k_n = AT^\beta e^{-\gamma/T}$, except those from KIDA*, which are calculated via $k_n = A(T/300)^\beta e^{-\gamma/T}$, where A is in $\text{cm}^3/\text{molecule/s}$.

Reaction	A	β	γ	k_∞
----------	---	---------	----------	------------

98	$O + H + M \rightarrow OH + M$	4.33×10^{-32}	-1.0	0	1.0×10^{-10}
99	$OH + H + M \rightarrow H_2O + M$	6.78×10^{-31}	-2.0	0	1.0×10^{-10}
100	$CN + CN + M \rightarrow C_2N_2 + M$	7.77×10^{-31}	-2.61	0	5.50×10^{-11}
101	$C + C + M \rightarrow C_2 + M$	5.30×10^{-31}	-1.6	0	2.16×10^{-11}
102	$CO + O + M \rightarrow CO_2 + M$	1.70×10^{-33}	0	1.51×10^3	1.0×10^{-10}
103	$N + N + M \rightarrow N_2 + M$	4.10×10^{-34}	0	0	1.0×10^{-10}
104	$NH + NH + M \rightarrow N_2 + H_2 + M$	3.22×10^{-29}	0	0	9.4×10^{-12}
105	$H + H + M \rightarrow H_2 + M$	9.14×10^{-33}	-0.6	0	1.0×10^{-10}
106	$H + NH_2 + M \rightarrow NH_3 + M$	6.90×10^{-34}	0.387	-7.84×10^3	7.6×10^{-10}
107	$H + CN + M \rightarrow HCN + M$	7.77×10^{-31}	-2.2	5.67×10^2	$5.5 \times 10^{-11} (T/300)^{-0.5}$
108	$H + HCN + M \rightarrow H_2CN + M$	3.30×10^{-30}	-2.73	3.86×10^3	$1.50 \times 10^{-15} \exp(-2.44 \times 10^3/T)$
109	$CO + H + M \rightarrow HCO + M$	5.29×10^{-34}	0	3.73×10^2	1.0×10^{-10}
110	$C + H_2 + M \rightarrow CH_2 + M$	7.0×10^{-32}	0	0	$2.06 \times 10^{-11} \exp(-5.54 \times 10^1/T)$
111	$N + H + M \rightarrow NH + M$	²			

Table 2.6.2: Three body reactions and associated values.

²Reaction not found in KIDA; assumed to have same rate constant as reaction 98

3

Sulfidic Anion Concentrations on the Early Earth for Surficial Origins-of-Life Chemistry

Abstract

A key challenge in origin-of-life studies is understanding the environmental conditions on early Earth under which abiogenesis occurred. While some constraints do exist (e.g., zircon evidence for surface liquid water), relatively few constraints exist on the abundances of trace chemical species, which are relevant to assessing the plausibility and guiding the development of postulated prebiotic chemical pathways which depend on these species. In this work, we combine literature photochemistry models with simple equilibrium chemistry calculations to place constraints on the plausible range of concentrations of

sulfidic anions (HS , HSO_3^- , SO_3^{2-}) available in surficial aquatic reservoirs on early Earth due to outgassing of SO_2 and H_2S and their dissolution into small shallow surface water reservoirs like lakes. We find that this mechanism could have supplied prebiotically relevant levels of SO_2 -derived anions, but not H_2S -derived anions. Radiative transfer modeling suggests UV light would have remained abundant on the planet surface for all but the largest volcanic explosions. We apply our results to the case study of the proposed prebiotic reaction network of Patel et al. [240] and discuss the implications for improving its prebiotic plausibility. In general, epochs of moderately high volcanism could have been especially conducive to cyanosulfidic prebiotic chemistry. Our work can be similarly applied to assess and improve the prebiotic plausibility of other postulated surficial prebiotic chemistries that are sensitive to sulfidic anions, and our methods adapted to study other atmospherically derived trace species.¹

A KEY CHALLENGE FOR origins-of-life studies is determining the environmental conditions on early Earth. Environmental conditions (e.g., pH, temperature, pressure, chemical feedstock abundance, etc) play a major role in determining the kinds of prebiotic chemistry that are possible or probable, and hence can help constrain the plausibility of proposed origin-of-life scenarios (e.g, Urey [360], Corliss et al. [61], McCollom [195], Ruiz-Mirazo et al. [286]). Consequently, it is critical to understand the range of environmental conditions available on the early Earth for abiogenesis to proceed. Work over the past few decades has begun to constrain the environmental conditions that may have been available for abiogenesis, including but not limited to the past presence of liquid water, the availability of UV light at the surface, the mix of gases being outgassed to the atmosphere, the bulk pH of the ocean, and the conditions available at deep-sea hydrothermal vents [12, 20, 76, 89, 115, 132, 196, 211, 217, 228, 260, 320, 353].

One challenging environmental factor to constrain is the abundance of trace chemical species on early Earth. These species can be important to proposed

¹This thesis chapter was published as: S. Ranjan, Z. R. Todd, J. D. Sutherland, and D. D. Sasselov (2018) *Astrobiology*, 18(8), 1023-1040.

prebiotic chemical pathways as feedstocks or catalysts, but their abundances on the early Earth can be difficult to determine due to their rarity and hence limited impact on an already scarce rock record. In this paper, we explore the plausible abundances of one such family of molecules: sulfidic anions, i.e. sulfur-bearing aqueous anions (e.g., hydrosulfide, HS^- ; bisulfite, HSO_3^- ; sulfite, SO_3^{2-}). Our initial interest in these molecules was stimulated by the role they play in the prebiotic chemistry proposed by Patel et al. [240], but our calculations are applicable to studies of surficial prebiotic chemistry in general. For discussion of the relevance of the surface environment and its attendant processes to prebiotic chemistry, see, e.g., Forsythe et al. [102], He et al. [125], Mulkidjanian et al. [217], Mutschler et al. [219], Rapf and Vaida [265], Walker et al. [370]. Our results are not relevant to deep-sea origin-of-life scenarios, such as Larowe and Regnier [167], Martin et al. [188], McCollom and Seewald [196], Sojo et al. [320].

We specifically explore the atmosphere as a planetary source for sulfidic anions through dissolution of volcanically outgassed SO_2 and H_2S in small, shallow aqueous reservoirs like lakes. The prebiotic Earth's atmosphere is thought to have been anoxic and more reducing than modern Earth [155], and volcanism levels have been hypothesized to have been higher [271]. Then the abundance of atmospheric H_2S and especially SO_2 should have been higher compared to modern day levels, and aqueous reservoirs in equilibrium with the atmosphere would have dissolved some of these gases in accordance with Henry's Law, forming sulfidic anions through subsequent dissociation reactions. We use simple equilibrium chemistry combined with literature photochemical modelling to estimate the concentrations of these sulfidic anions as a function of pSO_2 and pH_2S , and as a function of total sulfur outgassing flux. Elevated levels of atmospheric sulfur can lead to the formation of UV shielding gases and aerosols; consequently, we use radiative transfer calculations to constrain the surface UV radiation environment as a function of total sulfur outgassing flux. UV light is of interest to prebiotic chemists both as a potential stressor for abiogenesis [56, 290], as a potential eustressor for abiogenesis

[216, 239, 265, 291, 384], and because of evidence that the nucleobases evolved in a UV-rich environment [20, 275].

We apply our calculations to the case study of the cyanosulfidic prebiotic systems chemistry of Patel et al. [240]. Building on the work of Powner et al. [256] and Ritson and Sutherland [276], Patel et al. [240] proposed a prebiotic reaction network for the synthesis of activated ribonucleotides, short sugars, amino acids and lipid precursors from a limited set of feedstock molecules in aqueous solution under UV irradiation (at 254 nm). This reaction network is of interest because of the progress it makes towards the longstanding problem of nucleotide synthesis, because it offers the promise of a common origin for many biomolecules, and because it imposes specific geochemical requirements on its environment, which can be compared against what was available on early Earth to constrain and improve the chemistry's prebiotic plausibility [129, 323, 324]. Relevant to our work, the Patel et al. [240] chemistry requires sulfidic anions to proceed, as both a photoreductant and as a feedstock for a subset of the network's reactions. Patel et al. [240] proposed impactors as a source for the sulfidic anions; while possible, this scenario imposes an additional, local requirement for this chemistry to function. On the other hand, if the atmosphere could supply adequate sulfidic reductant (and feedstock) on a global basis, it would reduce the requirements for parts (or all) of this reaction network to function, and would make it more compelling as an origins-of-life scenario. We evaluate this scenario. While our paper focuses on the chemistry of Patel et al. [240] as a case study, our work can be used to evaluate and improve the plausibility of any proposed sulfidic anion-sensitive surficial prebiotic chemistry. Our methods can be adapted to study the prebiotic surficial concentrations of other atmospherically-sourced aqueous species.

3.1 BACKGROUND

3.1.1 PLAUSIBLE PREBIOTIC LEVELS OF H₂S AND SO₂

The abundances of H₂S and SO₂ in the Earth's atmosphere are set by photochemistry, and are sensitive to a variety of factors. One of the most important of these factors is the outgassing rate of these compounds from volcanoes into the atmosphere. Absent biogenic sources, atmospheric photochemistry models typically assume abiotic SO₂ outgassing rates of $1 - 3 \times 10^9 \text{ cm}^{-2} \text{ s}^{-1}$ [51, 136, 153, 395], consistent with the measured modern mean volcanogenic SO₂ outgassing rate of $1.7 - 2.4 \times 10^9 \text{ cm}^{-2} \text{ s}^{-1}$ [119]. H₂S emission rates are indirectly estimated and much less certain; they range from $3.1 \times 10^8 - 7.7 \times 10^9 \text{ cm}^{-2} \text{ s}^{-1}$. A common assumption in atmospheric modelling is that SO₂ and H₂S are outgassed in a 10:1 ratio (e.g., Claire et al. 51, Zahnle et al. 395).

The early Earth is often hypothesized to have been characterized by higher levels of volcanic outgassing compared to the modern Earth due to presumed higher levels of internal heat and tectonic activity. Models often assume that Archaean SO₂ outgassing rates were $\sim 3 \times$ modern [153, 271, 395]. However, Halevy and Head [116] point out that during the emplacement of major volcanogenic features such as the terrestrial basaltic plains, sulfur outgassing rates as high as $10^{10} - 10^{11.5} \text{ cm}^{-2} \text{ s}^{-1}$ are possible, with the upper limit on outgassing rate coming from estimates of sulfur flux during emplacement of the Deccan Traps on Earth [306].

No firm constraints exist for SO₂ and H₂S levels on the prebiotic Earth. Kasting et al. [153] modeled a plausible prebiotic atmosphere of 2 bars CO₂, 0.8 bar N₂ atmosphere under $0.75 \times$ present-day solar irradiation to account for the effects of the faint young Sun at 3.9 Ga. Kasting et al. [153] assumed that sulfur was outgassed entirely as SO₂ at a total sulfur outgassing flux of $\phi_s = 3 \times 10^9 \text{ cm}^{-2} \text{ s}^{-1}$ into an atmosphere overlying an ocean saturated in SO₂; this last condition favors accumulation of SO₂ in the atmosphere. Claire et al. [51]

modeled an atmosphere of 0.99 bar N₂ and 0.01 bar CO₂, under irradiation by the 2.5 Ga Sun, with an SO₂:H₂S outgassing ratio of 10:1, for $\varphi_S = 1 \times 10^8 - 1 \times 10^{10} \text{ cm}^{-2} \text{ s}^{-1}$. Hu et al. [136] modeled an atmosphere consisting of 0.9 bar CO₂ and 0.1 bar N₂ under irradiation by the modern Sun, with an SO₂:H₂S emission ratio of 2, for $\varphi_S = 3 \times 10^9 - 1 \times 10^{13} \text{ cm}^{-2} \text{ s}^{-1}$. The SO₂ and H₂S mixing ratios calculated by these models are shown in Table 3.1.1; these mixing ratios may be trivially converted to partial pressures by multiplying against the bulk atmospheric pressure. Note that the Claire et al. [51] and Kasting et al. [153] values are surface mixing ratios, while the Hu et al. [136] values are column-integrated mixing ratios. Since H₂S and SO₂ abundances tend to decrease with altitude due to losses from photochemistry, column-integrated mixing ratios should be somewhat less than the surface mixing ratio. However, since density also decreases with altitude, mixing ratios at lower altitudes are more strongly weighted in the calculation of column-integrated mixing ratios, so the column-integrated mixing ratio tends to be close to the surface mixing ratio.

Table 3.1.1: Mixing ratios of H₂S and SO₂ for different early Earth models in the literature and different φ_S .

Model	r_{H_2S}	r_{SO_2}
Kasting et al. [153] ^a , $\varphi_S = 3 \times 10^9 \text{ cm}^{-2} \text{ s}^{-1}$	2×10^{-10}	2×10^{-9}
Claire et al. [51] ^a , $\varphi_S = 3 \times 10^9 \text{ cm}^{-2} \text{ s}^{-1}$	1×10^{-11}	5×10^{-11}
Hu et al. [136] ^b , $\varphi_S = 3 \times 10^9 \text{ cm}^{-2} \text{ s}^{-1}$	4×10^{-10}	3×10^{-10}
Claire et al. [51] ^a , $\varphi_S = 1 \times 10^{10} \text{ cm}^{-2} \text{ s}^{-1}$	3×10^{-11}	1×10^{-10}
Hu et al. [136] ^b , $\varphi_S = 1 \times 10^{10} \text{ cm}^{-2} \text{ s}^{-1}$	1×10^{-9}	9×10^{-10}

a: Surface mixing ratio

b: Column-integrated mixing ratio

These models broadly agree that SO₂ and H₂S levels were low and increase with sulfur emission rate, but their estimates for r_{SO_2} and r_{H_2S} disagree with each other by up to a factor of 400. The Hu et al. [136] estimates are typically higher than the other estimates considered. The variation in these abundances demonstrates the sensitivity of SO₂ and H₂S levels to atmospheric parameters such as composition and deposition velocities. Of these models, we find Hu et al.

[136] best matches the current fiducial understanding of conditions on early Earth: an atmosphere dominated by CO₂ and N₂, with volcanic outgassing of both SO₂ and H₂S, with oceans not saturated in SO₂ (as compared to possibilities for early Mars; see Halevy et al. 117). Hu et al. [136] also has the advantage of calculating atmospheric composition at higher values of sulfur outgassing flux than Kasting et al. [153] and Claire et al. [51], encompassing the $1 \times 10^{11.5}$ cm⁻² s⁻¹ flux which is the upper limit of what Halevy and Head [116] suggest possible for the emplacement of terrestrial basaltic plains. Hu et al. [136] model processes including wet and dry deposition, formation of H₂SO₄ and S₈ aerosol, and photochemistry and thermochemistry, with > 1000 reactions included in their reaction network. We therefore use Hu et al. [136] as a guide when estimating H₂S and SO₂ levels as a function of sulfur outgassing flux (see Appendix 3.6), with the understanding that further, prebiotic-Earth specific modelling is required to constrain this relation with certainty.

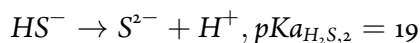
3.2 METHODS

We consider a gas Z dissolving into a surficial aqueous reservoir ($\lesssim 1$ m deep), through which the UV light required for prebiotic biomolecules synthesis can penetrate [259]; our archetypal such environment is a lake. To isolate the effects of atmospheric supply of Z, we assume no other source of Z to be present (e.g., no geothermal source at the lake bottom). Henry's Law states that the concentration of Z, [Z], in aqueous solution at the air/water interface is proportional to the partial pressure of the gas at that interface. We assume the aqueous reservoir to be well-mixed and equilibrated throughout, so that the concentration of [Z] is uniform throughout the reservoir at the surficial value. If the reservoir is not well-mixed, then the dissolved gas concentration will vary deeper into the reservoir. Under our assumption of no non-atmospheric source of Z, [Z] would decrease with depth for a poorly-mixed aqueous reservoir.

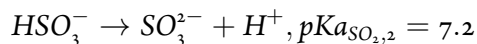
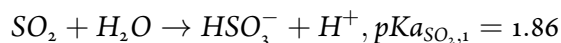
This method of calculating [Z] is predicated on the assumption that the aqueous body is in equilibrium with the atmosphere, that is, that the solution is

saturated in Z and the sink and source of Z is outgassing and deposition from the atmosphere. This assumption is valid when there are no other sinks to drive the system away from equilibrium. We discuss the veracity of this assumption in Section 3.4.2. In brief, this assumption is valid for shallow, well-mixed lakes that are not very acidic or hot, but not valid for deep, acidic, or hot waters. For these scenarios, our calculations provide upper bounds on $[Z]$.

In aqueous solution, H_2S undergoes the dissociation reactions



Where the pKa values are taken from [?], and can be related to the corresponding equilibrium constants by $Ka_X = 10^{-pKa_X}$. Similarly, SO_2 undergoes the reactions



Where the pKa values are from Neta and Huie [224].

To compute the abundances of these different sulfur-bearing compounds as a function of $[Z]$, we must make assumptions as to the background chemistry of the aqueous reservoir they are dissolved in, especially its pH. If the reservoir is completely unbuffered (e.g., pure water), its pH (and hence the speciation of S-bearing compounds) will be completely determined by $[Z]$. At the other extreme, if the reservoir is completely buffered, its pH will be independent of $[Z]$. Natural waters typically lie in between these two extremes; they are often buffered by mineral or atmospheric interactions towards a certain pH^2 , but with

²For example, the oceans on modern Earth are buffered to a pH of 8.1 – 8.2 due primarily to carbonate buffering [118, 399]; estimates of ancient ocean pH vary, but often invoke slightly lower pH due to posited higher CO_2 levels early in Earth's history (see, e.g., Morse and Mackenzie [215],

enough atmospheric supply their buffers can be overwhelmed. We explore these bracketing cases below, with the understanding that the true speciation behavior in nature was most likely somewhere in between.

3.2.1 CALCULATING DISSOLVED GAS CONCENTRATION

We use Henry's law, coupled with the well-mixed reservoir assumption, to calculate the concentration of molecules dissolved from the atmosphere. Henry's Law states that for a species Z ,

$$[Z] = H_Z f_Z,$$

where H_Z is the gas-specific Henry's Law constant and f_Z is the fugacity of the gas. Over the range of temperatures and pressures relevant to surficial prebiotic chemistry, the gases in our study are ideal, and consequently $f_Z = p_Z$, the partial pressure of Z . We make this simplifying assumption throughout our study.

At $T_o = 298.15$ K, the Henry's Law constants for H_2S and SO_2 dissolving in pure water are $H_{H_2S} = 0.101$ M/bar and $H_{SO_2} = 1.34$ M/bar, respectively. Increasing salinity tends to decrease H_G , a process known as salting out. Similarly, increasing temperature also tends to decrease H_G . Our overall results are insensitive to variations in temperature of ± 25 K from T_o and $0 \leq [NaCl] \leq 1$ M; see Appendix 3.8 and Appendix 3.9.1. For simplicity, we therefore neglect the temperature- and salinity-dependence of Henry's Law.

3.2.2 UNBUFFERED SOLUTION

Consider an unbuffered solution with dissolved Z , whose properties are determined entirely by the reactions Z and its products undergo. From the definition of equilibrium constant, we can use the H_2S and SO_2 speciation reactions to write:

Amend and McCollom [4]; Halevy and Bachan [115] and sources therein). Smaller bodies, like lakes, can have an even wider range of pHs due to local conditions; lakes on modern Earth can have $pH < 1$ (e.g., Kawah Ijen crater lake; Löhr et al. 177), and $pH > 11$ (e.g., Lake Natron; Grant and Jones 111).

$$\frac{a_{\text{HS}^-} a_{\text{H}^+}}{a_{\text{H}_2\text{S}}} = K a_{\text{H}_2\text{S},1}$$

$$\frac{a_{\text{S}^{2-}} a_{\text{H}^+}}{a_{\text{HS}^-}} = K a_{\text{H}_2\text{S},2}$$

and

$$\frac{a_{\text{HSO}_3^-} a_{\text{H}^+}}{a_{\text{SO}_2}} = K a_{\text{SO}_2,1}$$

$$\frac{a_{\text{SO}_3^{2-}} a_{\text{H}^+}}{a_{\text{HSO}_3^-}} = K a_{\text{SO}_2,2}$$

$$\frac{a_{\text{HS}_2\text{O}_5^-}}{a_{\text{SO}_2} a_{\text{HSO}_3^-}} = K a_{\text{SO}_2,3}$$

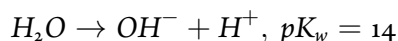
Where a_C is the activity of species C . a_C is related to the concentration of C , $[C]$, by $a_C = \gamma_C [C]$, where γ_C is the activity coefficient [208]. The use of activities instead of concentrations accounts for ion-ion and ion-H₂O interactions. $\gamma = 1$ for a solution with an ionic strength of $I = 0$. For ionic strengths of 0-0.1 M, we calculate the activity coefficients for each species as a function of solution ionic strength using Extended Debye-Huckel theory [75]. The activity coefficients in this formalism are calculated by:

$$\log(\gamma_C) = -Az_C^2 \frac{I^{0.5}}{1 + Ba_C I^{0.5}}$$

Here, A and B are constants that depend on the temperature, density, and dielectric constant of the solvent; we use $A = 0.5085 \text{ M}^{-1/2}$ and $B = 0.3281 \text{ M}^{-1/2-1}$, corresponding to 25°C water [208] (our results are robust to this assumption; see Appendix 3.9). z_C is the charge of species C . a_C is an ion-specific parameter with values related to the hydration radius of the aqueous species; we took our a_C values from Misra [208]. We were unable to locate a value of a_C for HS_2O_5^- , and consequently take $\gamma_{\text{HS}_2\text{O}_5^-} = 1$ throughout. I is the ionic strength of the solution, defined as:

$$I = 0.5(\sum_C [C] z_C^2)$$

We can combine these equations with the equation for water dissociation:



$$(a_{H^+})(a_{OH^-}) = K_w$$

and the requirement for charge conservation:

$$\sum_C z_C [C] = 0$$

With $[Z]$ specified by Henry's Law and our assumption of a well-mixed reservoir, this system is fully determined, and we can numerically solve it to determine the concentration of each of the species above as a function of pZ and I . A wide range of ionic strengths are possible for natural waters; modern freshwater systems like rivers have typical ionic strengths of order $1 \times 10^{-3} M$ [?], whereas modern terrestrial oceans have an ionic strength of $0.7 M$ ³. The concentrations of divalent cations, especially Mg^{2+} and Ca^{2+} , in early oceans has been suggested to be near $10 mM$ [72]. A more fundamental constraint comes from vesicle formation, which is known to be inhibited at high salt concentrations and hence ionic strengths: Maurer and Nguyen [193] report that lipid vesicle formation is impeded in solutions with $I > 0.1 M$. These considerations motivate our focus on low ionic strength waters, with $I \leq 0.1 M$ ⁴.

We calculate the speciation of sulfur-bearing species from dissolved H_2S and SO_2 for $I = 0$ and $I = 0.1 M$; the results are shown in Figs. 3.3.1 and 3.3.2. $I = 0$ is the lowest possible ionic strength, and $I = 0.1 M$ corresponds to the limit from lipid vesicle formation.

³<http://www.aqion.de/site/69>, accessed 29 November 2016

⁴A further practical challenge with extending our calculations to higher ionic strengths is that the parameters required to compute the activity coefficients at high ionic strengths (e.g., via the Truesdell and Jones 356 formalism) are not available for many of the species we consider.

3.2.3 BUFFERED SOLUTION

Consider now an aqueous reservoir that is buffered to a given pH. For example, the pH of the modern oceans is buffered by calcium carbonate to a global mean value of 8.1 – 8.2 [118]. Then, we know $[H^+]$, and can hence calculate the speciation of dissolved H_2S and SO_2 from the equilibrium constant equations 3.2.2-3.2.2 and 3.2.2-?? individually. Our results are insensitive to ionic strength for $I \leq 0.1M$ (see Figs. 3.3.1 and 3.3.2, and Appendix 3.7), and $I \leq 0.1M$ is required for vesicle formation and other prebiotic chemistry [193?], motivating us to take $I = 0$ for simplicity.

With Henry's Law and our assumption of a well-mixed reservoir, we can readily calculate the concentration of the above species as a function of pH_2S or pSO_2 and pH. The results of this calculation are presented in Figs. 3.3.1 and 3.3.2 for three representative pHs. We selected $pH=8.2$, corresponding to modern ocean; $pH=7$, corresponding to the near-neutral phosphate-buffered conditions in which Patel et al. [240] conducted their experiments; and $pH=4.25$, corresponding to raindrops in a $pCO_2 \sim 0.1$ bar atmosphere [117]. Such high CO_2 levels are hypothesized for the young Earth in order to power a greenhouse effect large enough to maintain clement surface conditions [150].

The code used to implement these calculations is available for validation and extension at <https://github.com/sukritranjan/RanjanToddSutherlandSasselov2017.git>.

3.3 RESULTS

3.3.1 H_2S vs SO_2

Fig. 3.3.1 shows the speciation of sulfur-bearing compounds from dissolved H_2S for an unbuffered reservoir, and reservoirs buffered to various pHs. Over the range of ionic strengths considered, HS^- is the dominant anion, and S^{2-} is present at negligible concentrations. As pH_2S increases, the pH of the unbuffered

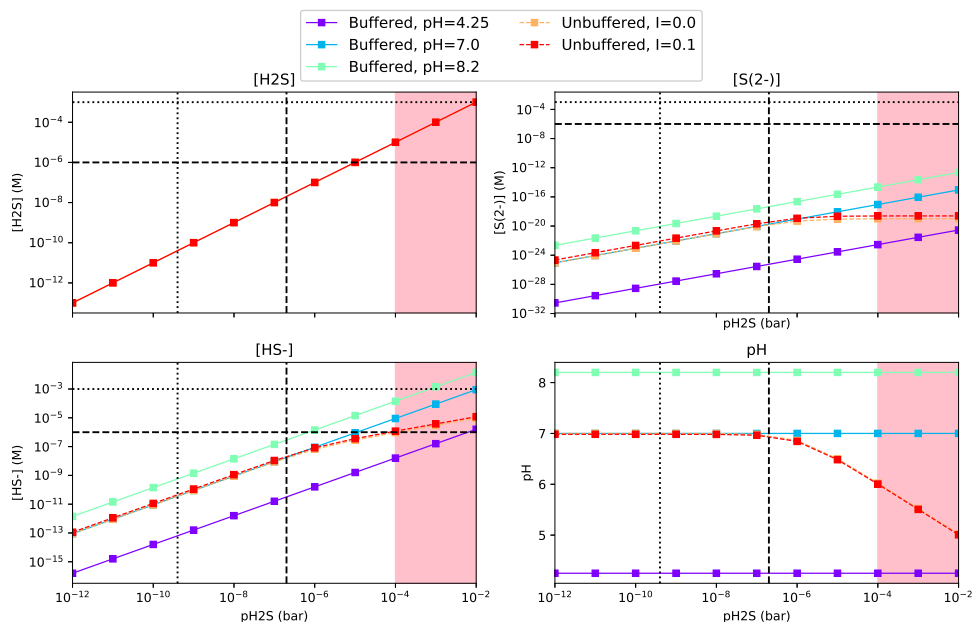


Figure 3.3.1: Concentrations of sulfur bearing compounds and pH as a function of $p_{\text{H}_2\text{S}}$ for a well-mixed aqueous reservoir. $[\text{H}_2\text{S}]$ is calculated from Henry's Law; the concentrations of HS^- and S^{2-} are calculated from equilibrium chemistry for 1) solutions buffered to various pHs, and 2) unbuffered solutions with varying ionic strengths. The vertical dotted line demarcates the expected $p_{\text{H}_2\text{S}}$ for an abiotic Earth with a weakly reducing $\text{CO}_2\text{-N}_2$ atmosphere with modern levels of sulfur outgassing, from Hu et al. [136]. The vertical dashed line demarcates the expected $p_{\text{H}_2\text{S}}$ for the same model, but with outgassing levels of sulfur corresponding to the upper limit of the estimate for the emplacement of the terrestrial flood basalts. In the red shaded area, $p_{\text{H}_2\text{S}}$ is so high it blocks UV light from the planet surface, meaning UV-dependent prebiotic pathways, e.g., those of Patel et al. [240], cannot function [?]. The red curve largely overplots the orange, demonstrating the minimal impact of ionic strength on the calculation for $I \leq 0.1$. The horizontal dashed and dotted lines demarcate micromolar and millimolar concentrations, respectively. The cyanosulfidic chemistry of Patel et al. [240] has been demonstrated at millimolar S-bearing photoreductant concentrations, and at least high micromolar levels of these compounds are thought to be required for high-yield prebiotic chemistry.

reservoir drops, but slowly. This is expected, since H_2S is a weak acid.

Fig. 3.3.2 shows the speciation of sulfur-bearing compounds from dissolved SO_2 for an unbuffered reservoir, and reservoirs buffered to various pHs. Because of the lack of O_2 in this anoxic era, the first dissociation of SO_2 forms sulfite, rather than sulfate. HSO_3^- and SO_3^{2-} are present at comparable levels; HS_2O_5^- is negligible. As $p\text{SO}_2$ increases, the pH of the unbuffered reservoir falls off rapidly; this is expected since hydrated SO_2 is a strong acid.

SO_2 is an order of magnitude more soluble than H_2S , and its first dissociation is much more strongly favored ($pK_{a_{\text{SO}_2,1}} = 1.86$ vs $pK_{a_{\text{H}_2\text{S},1}} = 7.05$). Consequently, far higher concentrations of sulfidic anions can be sustained for a given $p\text{SO}_2$ than for the same $p\text{H}_2\text{S}$ (see Figs. 3.3.1 and 3.3.2). Maintaining micromolar concentrations of HS^- requires $p\text{H}_2\text{S} \geq 1 \times 10^{-6}$ bar at $\text{pH}=8.2$ (modern ocean), and $p\text{H}_2\text{S} \geq 1 \times 10^{-5}$ bar for more neutral pHs. Maintaining micromolar concentrations of S^{2-} is impossible over plausible ranges of pH and sulfur outgassing flux ($pK_{a_{\text{H}_2\text{S},2}} = 19$). The concentration of sulfidic anions could be increased by going to higher pH and salinity. However, the reactions of, e.g., Patel et al. [240] have not been demonstrated to proceed under such conditions.

By contrast, dissolved SO_2 gives rise to comparatively high concentrations of sulfidic anions due to higher solubility and a more favorable first ionization. Micromolar concentrations of HSO_3^- are possible for $p\text{SO}_2 > 1 \times 10^{-11}$ bar for all but very acidic solutions; micromolar concentrations of SO_3^{2-} are possible for solutions buffered to $\text{pH} \geq 7$ over the same range. Millimolar levels of HSO_3^- and SO_3^{2-} are possible for solutions buffered to $\text{pH} \geq 8.2$ for $p\text{SO}_2 \gtrsim 10^{-10}$ bar, and for $\text{pH} \geq 7$ solutions for $p\text{SO}_2 \gtrsim 10^{-8}$ bar. $p\text{SO}_2 \geq 3 \times 10^{-10}$ bar is expected for outgassing rates corresponding to the steady-state on early Earth according to the model of Hu et al. [136] ($\varphi_{\text{S}} = 3 \times 10^9 \text{ cm}^{-2} \text{ s}^{-1}$). During transient epochs of intense volcanism such as the emplacement of basaltic plains, emission rates might have risen as high as $\varphi_{\text{S}} = 10^{11.5} \text{ cm}^{-2} \text{ s}^{-1}$ [116, 306], corresponding to $p\text{SO}_2 = 1 \times 10^{-8}$ bar. We note that estimates based on Hu et al. [136] are for column-integrated abundances, and the surface abundances were likely modestly

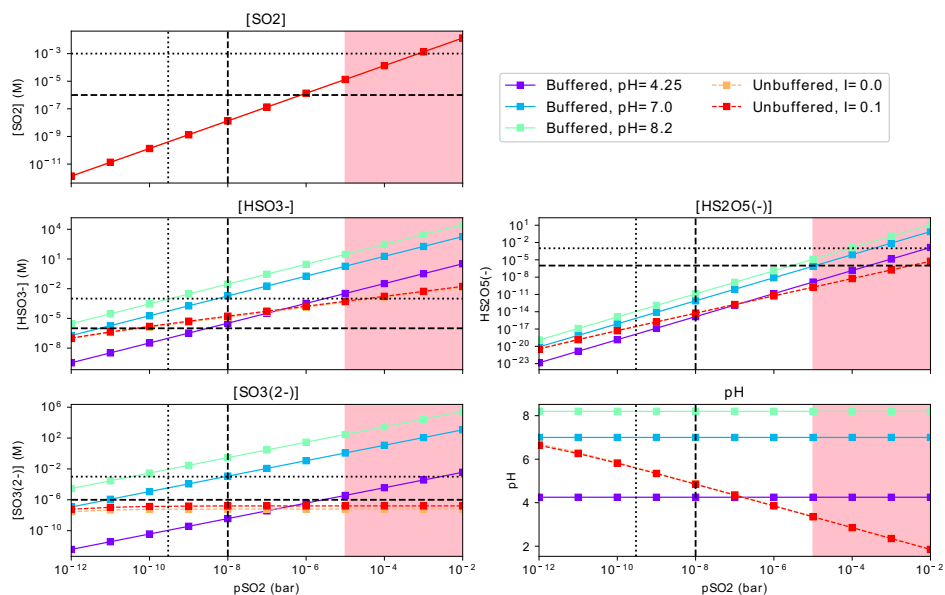


Figure 3.3.2: Concentrations of sulfur bearing compounds and pH as a function of $p\text{SO}_2$ for a well-mixed aqueous reservoir. $[\text{SO}_2]$ is calculated from Henry's Law; the concentrations of HSO_3^- , SO_3^{2-} , and HS_2O_5^- are calculated from equilibrium chemistry for 1) solutions buffered to various pHs, and 2) unbuffered solutions with varying ionic strengths. The vertical dotted line demarcates the expected $p\text{SO}_2$ for an abiotic Earth with a weakly reducing $\text{CO}_2\text{-N}_2$ atmosphere with modern levels of sulfur outgassing, from Hu et al. [136]. The vertical dashed line demarcates the expected $p\text{SO}_2$ for the same model, but with outgassing levels of sulfur corresponding to the upper limit of the estimate for the emplacement of the terrestrial flood basalts. In the red shaded area, $p\text{SO}_2$ is so high it blocks UV light from the planet surface, meaning UV-dependent prebiotic pathways, e.g., those of Patel et al. [240], cannot function [?]. The red curve largely overplots the orange, demonstrating the minimal impact of ionic strength on the calculation for $I \leq 0.1$. The horizontal dashed and dotted lines demarcate micromolar and millimolar concentrations, respectively. The cyanosulfidic chemistry of Patel et al. [240] has been demonstrated at millimolar S-bearing photoreductant concentrations, and at least high micromolar levels of these compounds are thought to be required for high-yield prebiotic chemistry.

larger. Hence, it seems likely that the atmosphere could have supplied micromolar-levels of SO_2 -derived anions for prebiotic chemistry, and perhaps even millimolar concentrations if the solution were buffered to slightly alkaline pH (e.g., pH comparable to the modern ocean).

3.3.2 H_2S AND SO_2

In Section 3.3.1 we evaluated the prospects for buildup of sulfur-bearing anions from dissolved atmospheric H_2S and SO_2 in isolation. However, H_2S and SO_2 are injected simultaneously into the atmosphere by volcanism, and would have been present at the same time. Fig. 3.3.3 presents the speciation of sulfur-bearing molecules from dissolved atmospheric H_2S and SO_2 in a solution buffered to pH= 7 as a function of total sulfur outgassing rate, φ_S . This pH corresponds approximately to the phosphate-buffered conditions in which the chemistry of Patel et al. [240] proceeded⁵. If the solution were buffered to higher pH sulfidic anion concentrations would be higher due to a more favorable first dissociation, and vice versa.

As before, we connected the H_2S and SO_2 abundances connected to φ_S by the high- CO_2 model calculations of Hu et al. [136]. We took the surface mixing ratio of these gases to equal the column-integrated mixing ratio, which may slightly underestimate the surface mixing ratio of these gases. $\varphi_S = 1 - 3 \times 10^9 \text{ cm}^{-2} \text{ s}^{-1}$ for modern Earth, and $\varphi_S = 10^{10} - 10^{11.5} \text{ cm}^{-2} \text{ s}^{-1}$ have been suggested on a transient (1-10 year) basis for major volcanic episodes like the emplacement of basaltic plains on Earth [116, 306]. As discussed in Section 3.3.1, SO_2 -derived anions can build to micromolar levels at modern outgassing rates, and can build to millimolar levels during volcanic episodes like the emplacement of basaltic plains, while H_2S -derived anions cannot, absent highly alkaline conditions.

⁵It is thought that these chemistries should proceed over a broad range of pH. However, they will proceed best for $\text{pH} \lesssim 9.2$ (so that HCN tends to remain protonated) and $\text{pH} \gtrsim 7$ (so that the sulfidic anions tend to remain deprotonated)

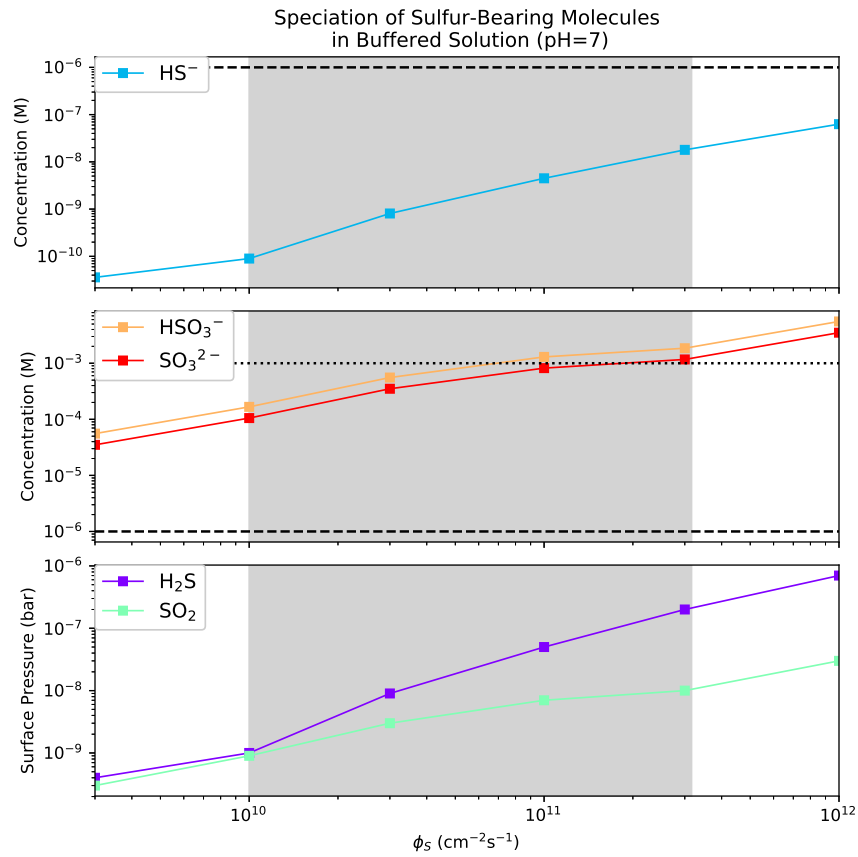


Figure 3.3.3: Speciation of sulfur-bearing molecules in an aqueous reservoir buffered to pH=7 as a function of total sulfur emission flux ϕ_S . The range of ϕ_S highlighted by Halevy and Head [116] for emplacement of basaltic plains on Earth is shaded in grey. Horizontal dashed and dotted lines demarcate micromolar and millimolar concentrations, respectively.

3.3.3 COUPLING TO THE UV SURFACE ENVIRONMENT

H₂S, SO₂, and their photochemical aerosol by-products (S₈, H₂SO₄) are robust UV shields, and at elevated levels their presence can dramatically reduce surface UV radiation [136]. This effect could be good for origin-of-life scenarios which do not require UV light, since UV light can photolytically destroy newly formed biomolecules (e.g., Sagan 290). On the other hand, it could be bad for UV-dependent prebiotic chemistry, which depend on UV light to power their syntheses (e.g., Ritson and Sutherland 276, Patel et al. 240, Xu et al. 384). In the latter case, it begs the question whether the elevated levels of SO₂ and H₂S that could supply the sulfidic anions required for cyanosulfidic chemistry might also quench the UV radiation also required by these pathways.

To explore this question, we calculated the attenuation of incoming 3.9 Ga solar radiation (calculated from the models of Claire et al. 50) by an CO₂-N₂-SO₂-H₂S atmosphere, using a two-stream radiative transfer model [261]. We set the solar zenith angle to 48.2°, corresponding to the insolation-weighted mean value [64], and the albedo to 0.2, a representative value for rocky planets consistent with past modelling⁶ [285, 305]. We once again used the work of Hu et al. [136] to connect H₂S and SO₂ abundances to ϕ_s , and for consistency we assumed inventories of CO₂ and N₂ matching those assumed by Hu et al. [136] (their high-CO₂ case). Our radiative transfer calculations are insensitive to the atmospheric T/P profile, because atmospheric emission is negligible at UV wavelengths and our UV cross-sections vary minimally as a function of temperature [261]; consequently, we assume a simple exponential profile to the vertical number density of the atmosphere. We also used the work of Hu et al. [136] to estimate the total S₈ and H₂SO₄ aerosol loading in the atmosphere for each ϕ_s , and calculated aerosol optical parameters using the same size distributions and complex indices of refraction as they did. Lacking detailed atmospheric profiles of the aerosol abundance as a function of altitude, we assumed the aerosols were distributed exponentially, with a scale

⁶Our results are insensitive to the precise choice of albedo or solar zenith angle

height equal to the bulk atmosphere scale height (i.e. well-mixed). In practice, sulfur aerosols tend to form photolytically at higher altitudes, meaning our approach places more aerosol at low altitude and less aerosol at high altitude. Since the radiative impact of aerosol absorption is amplified lower in the atmosphere due to enhanced scattering, this means our treatment should slightly overestimate UV attenuation due to aerosols. Similarly, Hu et al. [136] assume an aerosol size distribution with surface area mean diameter $D_s = 0.1 \mu m$, at the lower end of the plausible $D_s = 0.1 - 1 \mu m$ range, which maximizes the possible radiative impact of the sulfur aerosols. Consequently, our results should be interpreted as a lower bound on the true UV fluence.

Fig. 3.3.4 presents the UV fluence available on the surface of the prebiotic Earth as a function of φ_s under these assumptions. For $\varphi_s \leq 1 \times 10^{11} \text{ cm}^{-2} \text{ s}^{-1}$, UV radiation remains abundant on the planet surface. Millimolar levels of SO_3^{2-} and HSO_3^- are available in aqueous reservoirs buffered to $pH \geq 7$ for $\varphi_s = 1 \times 10^{11} \text{ cm}^{-2} \text{ s}^{-1}$. Consequently, volcanism could supply prebiotically relevant levels of SO_3^{2-} and HSO_3^- without blocking off the UV radiation required by UV-dependent prebiotic pathways for sulfur emission fluxes up to $\varphi_s \leq 1 \times 10^{11} \text{ cm}^{-2} \text{ s}^{-1}$ (near the upper edge of what is considered plausible for major terrestrial volcanic episodes). On the other hand, for $\varphi_s \geq 3 \times 10^{11} \text{ cm}^{-2} \text{ s}^{-1}$, atmospheric sulfur-bearing gases and aerosols, especially the UV-absorbing S_8 , suppress surface UV radiation by an order of magnitude or more; this paucity of UV radiation may pose a challenge for UV-dependent prebiotic chemistry, but could create a very clement surface environment for UV-independent prebiotic chemistries. If one accepts the idea that the nucleobases show evidence of UV selection pressure [20, 62, 254, 275, 307], this suggests the biogenic nucleobases evolved in an epoch with $\varphi_s \leq 1 \times 10^{11} \text{ cm}^{-2} \text{ s}^{-1}$.

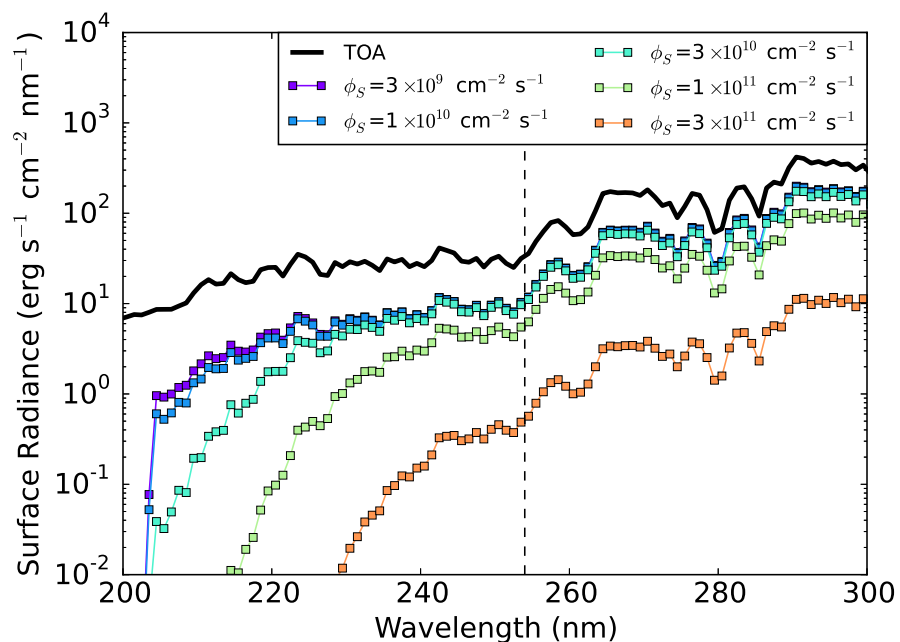


Figure 3.3.4: UV surface radiance for the early Earth as a function of ϕ_S , using the models of Hu et al. [136]. The black solid line indicates the top-of-atmosphere (TOA) flux, i.e. the irradiation incident at the top of the atmosphere from the young Sun. The vertical dashed line demarcates 254 nm, the wavelength at which the low-pressure mercury lamps commonly used in prebiotic chemistry experiments emit.

3.4 DISCUSSION

3.4.1 SULFIDIC ANION CONCENTRATIONS IN SURFICIAL WATERS ON EARLY EARTH

We have shown that terrestrial volcanism could have globally supplied the sulfidic anions SO_3^{2-} and HSO_3^- , derived from the dissolution of SO_2 into aqueous solution, to shallow surficial aqueous reservoirs on early Earth. These compounds would have been available at micromolar levels for volcanic outgassing rates comparable to the modern day. During episodes of high volcanism, such as those responsible for emplacement of basaltic plains ($\phi_s \approx 1 \times 10^{11} \text{ cm}^{-2} \text{ s}^{-1}$), these compounds could have built up to the millimolar levels in shallow aqueous reservoirs buffered to $\text{pH} \geq 7$. On the other hand, due to its lower solubility and unfavorable first dissociation, sulfidic anions derived from dissolving atmospheric H_2S can only be supplied at low concentrations (sub-micromolar) across the plausible range of pH_2S and pH ⁷. Therefore, other mechanisms must be invoked for supply of such anions, if required by a proposed prebiotic chemical pathway.

We conducted our calculations assuming a temperature of $T = 25^\circ\text{C}$. We investigate the sensitivity of our results to temperatures ranging from $T = 0 - 50^\circ\text{C}$ in Appendix 3.9, including temperature effects on both the reaction rate and the Henry's Law coefficient. While H_2S -derived anion concentrations are not significantly affected by temperature variations in this range, SO_2 -derived anion concentrations are. This is because H_{SO_2} decreases with temperature and $\text{pK}_{\text{aSO}_2,1}$ increases with temperature⁸; both effects favor increased concentrations of HSO_3^- and its derivatives, assuming a not-highly acidic ($\text{pH} > 2.5$) solution. We find that while our overall conclusions are unchanged, concentrations of the SO_2 -derived anions HSO_3^- and SO_3^{2-} are an

⁷Our results are relevant to shallow, aqueous bodies of water, like lakes. By contrast, in the ocean volcanoes vent directly into the water, and the turnover time can be long. Consequently, one could envision significant buildup of H_2S near deep-ocean volcanoes. This scenario is beyond the scope of this work, but may be worthy of consideration for HS^- -dependent chemistry

⁸The exothermic first dissociation of SO_2 is disfavored at higher temperatures.

order of magnitude higher for $T \approx 0^\circ\text{C}$ relative to $T = 25^\circ\text{C}$, and an order of magnitude lower for $T \approx 50^\circ\text{C}$, assuming a near-neutral reservoir. Consequently, cooler waters are more favorable environments for prebiotic chemistry which invokes HSO_3^- or SO_3^{2-} .

Sulfur-bearing gases and aerosols, in particular S_8 , are strong UV absorbers, and if present at high enough levels could suppress UV-sensitive prebiotic chemistry. For $\varphi_S \leq 1 \times 10^{11} \text{ cm}^{-2} \text{ s}^{-1}$, corresponding to most of the plausible range of sulfur emission fluxes on early Earth, surface UV fluxes (200-300 nm) are not significantly attenuated by atmospheric absorbers, meaning that in the steady state and for most volcanic eruptions, abundant UV light should have reached the Earth's surface to power UV-dependent prebiotic chemistry. However, for the very largest volcanic eruptions, corresponding to the uppermost end of the plausible range of sulfur outgassing fluxes during terrestrial basaltic flood plain emplacement ($\varphi_S = 3 \times 10^{11} \text{ cm}^{-2} \text{ s}^{-1}$), surface UV fluence (200-300 nm) may be reduced by an order of magnitude or more. Hence, the very largest volcanic events⁹ might create an especially clement surficial environment for UV-independent prebiotic chemistry

These results were derived using the high- CO_2 model of Hu et al. [136], which, while plausible, assumes more CO_2 and less N_2 than other models of prebiotic Earth (e.g., Rugheimer et al. 285), and is hence comparatively oxidizing. We explored the sensitivity of our results to this assumption via the the N_2 -rich model of Hu et al. [136]. This model assumes 1 bar of N_2 and negligible CO_2 , and is hence an unrealistic approximation to the early Earth, because an appreciable CO_2 inventory is expected due to climate constraints [150, 383], and due to volcanic outgassing of CO_2 . Hence, this model serves as an extreme bounding case. Assuming this model, we find that H_2S and SO_2 levels are lower

⁹However, even in this case there may be a window in which prebiotic chemistry experiences both elevated SO_2 levels and plenty of UV light, since aerosol formation is not instantaneous. Detailed photochemical modelling is required to determine the timescale of aerosol formation after a large volcanic eruption on early Earth; absent such modelling, we note that on modern Earth, formation of sulfate aerosols from volcanic eruptions occurs on a timescale of weeks [281]; we may speculate a similar timescale for aerosol formation on early Earth.

than for the high-CO₂ case. SO₂-derived anions remain available at micromolar levels over the plausible range of φ_s , but in order to build to millimolar levels require the assumption of reservoirs buffered to slightly alkaline pH (e.g., pH ~ 8.2, modern ocean). HS⁻ levels are even lower than in the CO₂-rich case. UV fluences are lower than in the CO₂-rich case, due to elevated levels of S₈ formation in this more reducing atmosphere; surface UV fluence (200-300 nm) is suppressed by an order of magnitude or more for $\varphi_s \geq 1 \times 10^{11} \text{ cm}^{-2} \text{ s}^{-1}$. Overall, this boundary case suggests that our finding that the atmosphere can supply prebiotically-relevant levels of SO₂-derived anions but not H₂S-derived anions in conjunction with UV light remains true across a broad range of CO₂ and N₂ abundances, though both sulfidic anion abundances and UV are lower for more reducing, N₂-rich atmospheres. However a detailed exploration of the pCO₂-pN₂ parameter space with photochemical models is required to be certain of these findings.

3.4.2 IMPACT OF OTHER SINKS

Our analysis is predicated on the assumption that [Z] is set by Henry equilibrium, i.e. that the aqueous reservoir is saturated in H₂S and SO₂. This assumes no major sinks other than outgassing to the atmosphere. In this section, we examine the sensitivity of our results to this assumption. Microbial sinks (e.g., Halevy 114) are not relevant since we are concerned with prebiotic Earth; neither are oxidic sinks, since the surface of early Earth was anoxic [90, 151, 154, 174, 241]. However, reactions with metal cations to produce insoluble precipitates and redox reactions could have been relevant; we explore these sinks.

PRECIPITATION REACTIONS WITH METAL CATIONS

We explored the possibility that reactions of S-anions with metal cations might lead to formation of insoluble precipitates, which would act as a sink on S-anion concentrations. Such cations might have been delivered to aqueous reservoirs via weathering of rocks and minerals.

Under standard conditions, Fe^{2+} and Cu^{2+} react with $\text{H}_2\text{S}(\text{aq})$ to generate insoluble precipitates, like CuS and FeS_2 [287]. Interaction of copper sulfides with cyanide solution can liberate HS^- [58], as invoked by Patel et al. [240]. In general high-Cu/Fe waters (e.g. due to interaction with ores) will be even more HS^- -poor than we have modeled, with the caveat that specific local environmental factors (like the presence of aqueous cyanide) can prevent sulfide depletion due to precipitation. This reinforces our conclusion that HS^- concentrations are unlikely to have reached prebiotically relevant levels on early Earth, absent unique local factors. For example, the aqueous cyanide required as a feedstock in the pathways of Patel et al. [240] would also permit elevated HS^- levels.

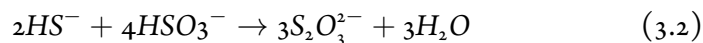
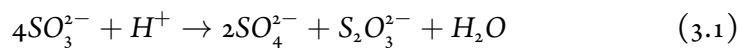
Ca^{2+} , produced by mineral weathering, reacts with sulfite to produce insoluble CaSO_3 . Studying the Ca^{2+} - SO_3^{2-} system requires considering the effects of carbonate (CO_3^{2-}) as well, because Ca^{2+} forms precipitate with this anion as well, and because high levels of carbonate are expected in natural waters on early Earth due to elevated levels of atmospheric CO_2 required to solve the faint young Sun paradox [154]. While precisely modeling this geochemical system requires use of a geochemical model capable of accounting for all reactions involving sulfites and carbonates and their kinetics, we can get a first-order estimate of the impact of Ca^{2+} , as follows. Assuming parameters from Hu et al. [136], the flux of carbonates into solution due to deposition and speciation of atmospheric CO_2 is $r_{\text{CO}_2} n_{\text{atm}} \nu_{\text{dep}, \text{CO}_2} = 2 \times 10^{15} \text{ cm}^{-2} \text{ s}^{-1}$ on the CO_2 -rich early Earth, which exceeds the mean flux of Ca due to mineral weathering ($1 - 5 \times 10^{10} \text{ cm}^{-2} \text{ s}^{-1}$; Taylor et al. 345, Watmough and Aherne 372) by 5 orders of magnitude; thus, it is reasonable to assume the solution is saturated in CO_2 with abundance dictated by Henry's law of $(3.3 \times 10^{-2} \text{ M}/\text{bar})(0.9 \text{ bar}) = 0.03 \text{ M}$ [296]. Then, $[\text{CO}_3^{2-}] = (0.03 \text{ M})(10^{7-6.35})(10^{7-10.33}) = 6 \times 10^{-5} \text{ M}$ at neutral pH (dissociation constants $K_{a_{\text{CO}_2,1}} = 6.35$ and $K_{a_{\text{CO}_2,2}} = 10.33$ from Rumble [287]¹⁰). Since

¹⁰Using pKas for CO_2 dissociation from modern seawater, e.g., Zeebe and Wolf-Gladrow [399], results in much higher carbonate levels, much lower Ca levels, and a much higher threshold for CaSO_3 saturation, so this treatment is conservative.

CaCO₃ ($K_{sp} = 3.36 \times 10^{-9} \text{ M}^2$, Rumble 287) is two orders of magnitude less soluble than CaSO₃ ($K_{sp} = 3.1 \times 10^{-7} \text{ M}^2$, Rumble 287) and the sulfite flux is much less than the carbonate flux, we can assume that [Ca²⁺] is dictated to first order by equilibrium with carbonate mineral, i.e. [Ca²⁺]
 $= 3.36 \times 10^{-9} \text{ M}^2 / 6 \times 10^{-5} \text{ M} = 6 \times 10^{-5} \text{ M}$. At this [Ca²⁺], CaSO₃²⁻ (s) will begin to form at [SO₃²⁻] = $3.1 \times 10^{-7} \text{ M}^2 / 6 \times 10^{-5} \text{ M} = 5 \times 10^{-3} \text{ M}$. The [SO₃²⁻] we calculate does not exceed this threshold value across the plausible range of sulfur outgassing fluxes in our calculation, meaning the solution is unsaturated in CaSO₃ and precipitate does not form. Were pCO₂ lower, e.g., pCO₂ = 0.2 bar¹¹, CaSO₃ precipitate formation begins at [SO₃²⁻] = $1 \times 10^{-3} \text{ M}$. However, if pH were low, the carbonate solubility would exceed sulfite solubility, and sulfite precipitates would form [117]; hence at low pH, sulfite and bisulfite concentrations will be below the values we calculate. Overall, our results are unaffected by CaSO₃ precipitation across most of parameter space, but CaSO₃ precipitation might be a significant sink on aqueous sulfite levels for acid solutions and/or for very low atmospheric CO₂-levels; calculations with a more thorough geochemical model (e.g., PHREEQC, Parkhurst and Appelo 237) are required to constrain S-anion concentrations in this regime.

REDOX REACTIONS

We explored the possibility that redox reactions (disproportionation, comproportionation) might have acted as sinks to S-anion concentrations in shallow aqueous reservoirs on prebiotic Earth, or might otherwise affect the distribution of sulfidic anions. We identified the following reactions that are spontaneous near standard conditions [114, 316]:



¹¹Corresponding to the lower limit suggested by Kasting [154] from climate considerations.

The kinetics of Reaction 3.1 are not well characterized near standard temperature, and are an active topic of research [6, 207]. Meyer et al. [201] report sulfite and bisulfite are stable on timescales ≥ 1 year in anoxic conditions, while Guekezian et al. [112] report decay of sulfite in days at $\text{pH} \geq 12.8$. Halevy [114] propose that rate coefficients in the range $k_{3,1} = \exp\left(\frac{-50\text{kJmol}^{-1}}{RT}\right) - \exp\left(\frac{-40\text{kJmol}^{-1}}{RT}\right)$ s^{-1} are plausible; at 293K, this corresponds to $1 \times 10^{-9} - 7 \times 10^{-8} \text{ s}^{-1}$, which correspond to timescales of 0.5 – 30 years. The kinetics of Reaction 3.2 have been determined as a function of temperature at $\text{pH}=9$ and $I = 0.2\text{M}$ by Siu and Jia [316]. At 293K, the rate coefficient is $k_{3,2} = 4 \times 10^3 \text{ M}^{-2} \text{ s}^{-1}$. At the S-anion concentrations relevant to our work¹², the timescale of this reaction is $\gtrsim 1$ year. For comparison, putative prebiotic chemistry in laboratory studies often occurs on timescales of hours to days (e.g. Patel et al. [240], Xu et al. [384]).

We test the effects of redox reactions on S-anion concentrations by carrying out a dynamical equilibrium calculation for a shallow lake buffered to $\text{pH}=7$, with source the atmosphere and sink these redox reactions. Following the treatment of Halevy [114], the equilibrium equations can be written:

$$r_{\text{H}_2\text{S}} n_{\text{atm}} v_{\text{dep}, \text{H}_2\text{S}} A_{\text{catch}} = \left(\frac{2}{3} k_{3,2} [\text{HS}^-] [\text{HSO}_3^-]^2\right) A_{\text{lake}} d_{\text{lake}}$$

$$r_{\text{SO}_2} n_{\text{atm}} v_{\text{dep}, \text{SO}_2} A_{\text{catch}} = \left(\frac{4}{3} k_{3,2} [\text{HS}^-] [\text{HSO}_3^-]^2 + k_{3,1} [\text{S(IV)}]\right) A_{\text{lake}} d_{\text{lake}}$$

For consistency with Hu et al. [136], we adopt $v_{\text{dep}, \text{H}_2\text{S}} = 0.015 \text{ cm s}^{-1}$, $v_{\text{dep}, \text{SO}_2} = 1 \text{ cm s}^{-1}$, $T = 288\text{K}$, and $n_{\text{atm}} = \frac{1\text{bar}}{kT} = 2.4 \times 10^{19} \text{ cm}^{-3}$. Since we are concerned with shallow, well-mixed lakes, we take the lake depth $d_{\text{lake}} = 10^2 \text{ cm}$. A_{catch} is the catchment area of the lake and A_{lake} is the surface area of the lake; we conservatively adopt $A_{\text{catch}} = A_{\text{lake}}$, which likely underestimates sulfur supply since the catchment area is likely larger than the lake area. $[\text{S(IV)}]$ refers to the total concentration of S(IV) atoms in solution, and is calculated as $[\text{S(IV)}] = [\text{SO}_2] + [\text{HSO}_3^-] + [\text{SO}_3^{2-}] + 2[\text{HS}_2\text{O}_5^-] \approx [\text{SO}_2(\text{aq})] + [\text{HSO}_3^-] + [\text{SO}_3^{2-}]$ ¹³. Since we have specified $\text{pH}=7$ and know the relevant pKas, we can calculate

¹² $[\text{HS}^-] \lesssim 10^{-8}\text{M}$, $[\text{HSO}_3^-] \lesssim 10^{-3}\text{M}$
¹³ $[\text{HS}_2\text{O}_5^-]$ is negligible for dilute $[\text{SO}_2]$

$[\text{HSO}_3^-]$ from $[\text{S(IV)}]$ and vice versa. With $r_{\text{H}_2\text{S}}$ and r_{SO_2} specified from Hu et al. [136], we have a system of two equations in two variables that we can solve.

Figure 3.4.1 shows the resultant S-anion concentrations as a function of φ_S :

The dynamic calculation is very sensitive to the uncertainty in $k_{3,1}$, with sulfite and bisulfite concentrations varying by 2 orders of magnitude and hydrosulfide concentrations varying by 4 across the range of $k_{3,1}$ suggested by Halevy [114]. However, even with this uncertainty it is clear that prebiotically relevant levels ($\geq 1\mu\text{M}$) of SO_2 -derived anions are available across the range of plausible sulfur outgassing fluxes, with concentrations $\sim 1 - 10\mu\text{M}$ if sulfite disproportionation is fast and $\sim 100 - 1000\mu\text{M}$ if sulfite disproportionation is slow. Note depending on $k_{3,1}$, it is possible for $[\text{HS}^-]$ in the dynamic calculation to exceed the value calculated from solubility constraints; in reality, in well-mixed solution H_2S would degas when it reached the solubility limit, voiding equation 3.4.2. In these cases, $[\text{HS}^-]$ is lower than the value calculated from the dynamic method, modestly increasing sulfite and bisulfite concentrations since Reaction 3.2 is slower. S-anion concentrations increase as d_{lake} and T decrease, and are ultimately limited by gas solubility. Overall, our finding that prebiotically relevant levels of SO_2 -derived anions were available in shallow well-mixed lakes on early Earth is robust to the effect of redox reactions, but it is possible for the precise concentrations to be lower than from our equilibrium calculation depending on the depth and temperature of the lake, and especially on the rate of sulfite disproportionation $k_{3,1}$. Constraining $k_{3,1}$ is key to improved modelling of abiotic sulfur chemistry.

3.4.3 CASE STUDY: IMPLICATIONS FOR CYANOSULFIDIC SYSTEMS CHEMISTRY OF PATEL ET AL. [240]

The cyanosulfidic prebiotic chemistry of Patel et al. [240] requires cyanide and sulfur-bearing anions, both as feedstocks and as sources of hydrated electrons through UV-driven photoionization. Patel et al. [240] used HS^- as their sulfidic anion, and propose impact-derived sources of metal sulfides (both from the

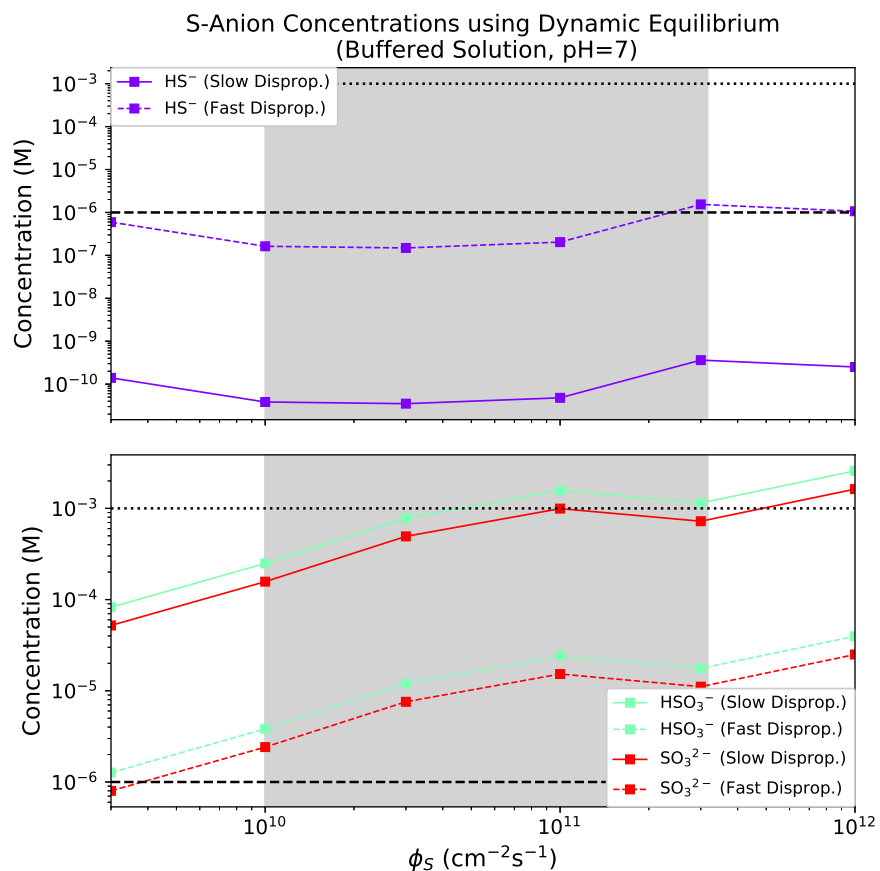


Figure 3.4.1: Speciation of sulfur-bearing molecules in a shallow lake buffered to pH=7 as a function of total sulfur emission flux ϕ_S , using a dynamic calculation with source atmospheric deposition and sink redox reactions. The range of ϕ_S highlighted by Halevy and Head [116] for emplacement of basaltic plains on Earth is shaded in grey. Horizontal dashed and dotted lines demarcate micromolar and millimolar concentrations, respectively. $[\text{HS}^-]$ would not be able to achieve the high concentrations calculated here for the slow disproportionation (low $k_{3.1}$) case due to solubility constraints.

impactor and from subsequent metallogenesis) and evaporatively concentrated iron sulfides as a source for HS^- . This postulated mechanism requires specific, local environmental conditions to function. By contrast, simple exposure of a non-acidic lake to the atmosphere anywhere on the planet would supply HSO_3^- and SO_3^{2-} at prebiotically relevant levels to either supplement the photochemical reducing capacity of HS^- , or function as sole sources of hydrated electrons in the Patel et al. [240] chemistry. Indeed, recent work by the same group suggests that HSO_3^- and SO_3^{2-} can replace HS^- as the source of hydrated electrons upon UV irradiation, and thus drive those parts of the reaction network that do not rely on HS^- as a feedstock [384]. Reducing or eliminating the dependence of the Patel et al. [240] chemistry on HS^- in favor of HSO_3^- or SO_3^{2-} increases the robustness of this chemistry, because no special local circumstances need to be invoked. This illustrates how geochemistry can inform improvements of the plausibility of prebiotic pathways.

Indeed, volcanism can be a source of more than sulfidic anions. Volcanism can also be a source of phosphates through partial hydrolysis of volcanically outgassed polyphosphates [387], and a supplementary source of HCN through photochemical reprocessing of volcanically outgassed reducing species like CH_4 [397]¹⁴. Volcanism could thereby supply or supplement many of the C, H, O, N P & S-containing feedstock molecules and photoreductants required by the Patel et al. [240] chemistry. The UV light also required by the Patel et al. [240] chemistry would be available at Earth's surface for all but the largest volcanic episodes ($\phi_s \geq 3 \times 10^{11} \text{ cm}^{-2} \text{ s}^{-1}$). Hence, epochs of moderately high volcanism may have been uniquely conducive to cyanosulfidic prebiotic chemistry like that of Patel et al. [240], especially if they can be adapted to work with HSO_3^- or SO_3^{2-} instead of HS^- .

We considered alternate planetary sources for HS^- for the Patel et al. [240] chemistry. We explored whether shallow hydrothermal systems, such as hot springs, might provide prebiotically-relevant levels of HS^- . These sources are

¹⁴Though some concentration mechanism would be required to achieve prebiotically relevant levels of HCN via this pathway

high-sulfur systems on modern Earth, and, if shallow, prebiotic chemistry in them might retain access to UV light while accessing high concentrations of sulfidic anions. Surveys of modern hydrothermal systems reveal examples of surficial systems that exhibit micromolar or even millimolar concentrations of HS^- [147, 365, 386]. However, high concentrations of HS^- appear to only be achieved in hot systems¹⁵ ($T > 60^\circ \text{C}$, and typically higher). Similarly, studies of geothermal waters in Yellowstone National Park suggest sulfite availability at the $0.4 - 5\mu\text{M}$ level. However, such levels of sulfite were again accessed only in hot waters [148]. It is not clear how compatible such conditions are with prebiotic chemistry; for example, most of the cyanosulfidic chemistries of Patel et al. [240] and Xu et al. [384] were conducted at room temperature (25°C), and in general many molecules thought to be relevant to the origin of life, such as ribozymes, RNA and their components, are more stable and function better at cooler temperatures [2, 10, 164, 172]. However, for hot origin-of-life scenarios, hydrothermal systems may be compelling venues for cyanosulfidic reaction networks like that of Patel et al. [240], reinforcing the utility of volcanism for prebiotic chemistry.

3.5 CONCLUSION & NEXT STEPS

Constraining the abundances of trace chemical species on early Earth is important to understanding whether postulated prebiotic pathways which are dependent on them could have proceeded. Here, we show that prebiotically-relevant levels of certain sulfidic anions are globally available in shallow, well-mixed aqueous reservoirs due to dissolution of sulfur-bearing gases that are volcanically injected into the atmosphere of early Earth. In particular, anions derived from SO_2 are available at $\geq 1\mu\text{M}$ levels in non-acidic reservoirs for SO_2 outgassing rates corresponding to the modern Earth and higher. During episodes of intense volcanism, like the emplacement of basaltic fields like the

¹⁵We speculate that HS^- -rich shallow hydrothermal systems tend to be hot because the same volcanism that supplies elevated levels of HS^- also supplies elevated levels of heat.

Deccan Traps, SO_2 -derived anions may be available at $\geq 1\text{mM}$ levels for reservoirs buffered to $\text{pH} \geq 7$ (e.g., the modern ocean at $\text{pH} = 8.2$) and at a temperature of $T = 25^\circ\text{C}$, though sulfite disproportionation may have ultimately limited concentrations to the $\sim 10\mu\text{M}$ level; better constraints on sulfite disproportionation reaction rates are required to constrain this possibility. At cooler temperatures, even higher concentrations of these anions would have been available. Formation of mineral precipitate should not inhibit sulfite concentrations until $\geq 1\text{mM}$ concentrations so long as the reservoir is not acidic, but might suppress sulfite levels in acidic waters. On the other hand, anions derived from H_2S would not have been available at micromolar levels across the plausible range of volcanic outgassing due to low solubility of H_2S and an unfavorable dissociation constant, and prebiotic chemistry invoking such anions must invoke local, specialized sources. Radiative transfer calculations suggests that NUV radiation will remain abundant at the planet surface for $\varphi_{\text{S}} \leq 1 \times 10^{11} \text{ cm}^{-2} \text{ s}^{-1}$, but will be suppressed for $\varphi_{\text{S}} \geq 3 \times 10^{11} \text{ cm}^{-2} \text{ s}^{-1}$; such epochs may be especially clement for surficial, UV-independent prebiotic chemistry. We applied our results to the case study of the proposed prebiotic reaction network of Patel et al. [240]. The prebiotic plausibility of this network can be improved if it can be adapted to use SO_2 -derived anions like HSO_3^- or SO_3^{2-} instead of HS^- , since the atmosphere is capable of supplying prebiotically-relevant levels of the former directly but more localized sources must be invoked for adequate supply of the latter. Coupled with the potential for volcanogenic synthesis of feedstock molecules like HCN and phosphate [387, 397], it appears that episodes of moderately intense volcanism ($\varphi_{\text{S}} \approx 1 \times 10^{11} \text{ cm}^{-2} \text{ s}^{-1}$) might have been especially clement for cyanosulfidic prebiotic chemistry which exploits SO_2 -derived anions (e.g., HSO_3^-). Avenues for future work include simulating these scenarios experimentally and/or with a large general purpose aqueous geochemistry code, improving measurements of the sulfite disproportionation reaction rate constant, and further photochemical modelling to improve constraints on the expected concentrations of SO_2 and H_2S on early Earth.

Acknowledgements We thank A. Levi for his insight regarding equilibrium

chemistry, and D. Catling, I. Halevy, M. Claire, J. Szostak, I. Halevy, T. Bosak, and T. Vick for answers to many questions and/or comments on the manuscript. We especially thank J. Toner for extensive discussion and feedback. We thank M. Claire for sharing sulfur aerosol cross-sections for validation purposes. This research has made use of NASA’s Astrophysics Data System Bibliographic Services, and the MPI-Mainz UV-VIS Spectral Atlas of Gaseous Molecules. S. R., Z. R. T., D. D. S., and J. D. S. gratefully acknowledge support from the Simons Foundation (S. R., Z. R. T., D. D. S.: grant no. 290360; S.R., grant no. 495062; J. D. S.: grant no. 290362).

3.6 APPENDIX A: ATMOSPHERIC SULFUR SPECIATION

We use the work of Hu et al. [136] to connect the sulfur emission flux φ_S to the speciation of atmospheric sulfur. Table 3.6.1 presents H_2S and SO_2 mixing ratios as a function of φ_S from Hu et al. [136] (their Fig. 5, CO_2 -dominated atmosphere case).

Table 3.6.1: Column-integrated mixing ratios of H_2S and SO_2 as a function of φ_S from Hu et al. [136] (their Fig. 5, CO_2 -dominated case).

φ_S ($cm^{-2} s^{-1}$)	r_{H_2S}	r_{SO_2}
3×10^9	4×10^{-10}	3×10^{-10}
1×10^{10}	1×10^{-9}	9×10^{-10}
3×10^{10}	9×10^{-9}	3×10^{-9}
1×10^{11}	5×10^{-8}	7×10^{-9}
3×10^{11}	2×10^{-7}	1×10^{-8}
1×10^{12}	7×10^{-7}	3×10^{-8}
3×10^{12}	2×10^{-6}	8×10^{-8}
1×10^{13}	9×10^{-6}	3×10^{-7}

3.7 APPENDIX B: ACTIVITY COEFFICIENT CALCULATION

This appendix describes the calculation of the activity coefficients of the ions involved in equilibria reactions for SO₂ and H₂S.

We use the Extended Debye-Huckel (EDH) Theory to calculate activity coefficients (γ_i) for the ions in our study. EDH is valid for ionic strengths up to 0.1M, which is the highest ionic strength we consider, motivated by the fact that lipid vesicle formation is inhibited at ionic strengths above 0.1M [193].

Extended Debye Huckel theory states that:

$$\log\gamma_i = -Az_i^2 \frac{I^{0.5}}{1 + Ba_i I^{0.5}} \quad (3.3)$$

where A and B depend on the temperature, density, and dielectric constant of the solvent (in our case water), and a_i is an ion-specific parameter. We took $A = 0.5085 \text{ M}^{-1/2}$ and $B = 0.3281 \text{ M}^{-1/2-1}$, corresponding to $T = 25^\circ\text{C}$; Appendix 3.9 describes the sensitivity of our analysis to this assumption. Table 3.7.1 summarizes the a_i used in our study, taken from Misra [208]. We were unable to locate a value of a_C for HS_2O_5^- , and consequently take $\gamma_{\text{HS}_2\text{O}_5^-} = 1$ throughout (i.e., we do not correct for its activity). Since in our analysis the supply of SO₂ is not limited (the atmosphere is treated as an infinite reservoir), $\text{pKa}_{\text{SO}_2,3}$ affects only the abundance of H₂SO₅⁻, which is a trace compound in our analysis (see Fig. 3.3.2).

Table 3.7.2 shows the activity coefficients for the relevant ions at the two ionic strengths considered in our study:

3.8 APPENDIX C: SENSITIVITY OF HENRY'S LAW CONSTANTS TO SALINITY

This appendix describes our assessment of the sensitivity of the Henry's Law coefficients for SO₂ and H₂S to salinity.

Table 3.7.1: Values for the ion-specific parameter α (related to the hydration sphere of the ion) used to calculate activity coefficients.

Ion	α_i (angstroms)
HSO_3^-	4.0
SO_3^{2-}	4.5
HS^-	3.5
S^{2-}	5.0
OH^-	3.5
H^+	9.0

Table 3.7.2: Per-ion activity coefficients for different ionic strengths.

Ion	I=0 M	I=0.1 M
HSO_3^-	1.0	0.770
SO_3^{2-}	1.0	0.364
HS^-	1.0	0.762
S^{2-}	1.0	0.377
OH^-	1.0	0.762
H^+	1.0	0.826

We account for the effect of salinity on H_G using the Schumpe-Sechenov method, as outlined in Burkholder et al. [36]:

$$\log H_o/H = \sum_i (h_i + h_G) * c_i, \quad (3.4)$$

where H_o is the Henry's Law constant in pure water, H is the Henry's law constant in saline solution, c_i is the concentration of the ion i , h_i is an ion-specific constant, and h_G is a gas-specific constant. h_G is temperature dependent, via $h_G = h_o + h_T(T - 298.15K)$. NaCl is the dominant salt in Earth's oceans; we approximate NaCl as the sole source of salinity in our calculations. Table 3.8.1 summarizes the values of these parameters used for this study, all taken from the

compendium of Burkholder et al. [36]. We were unable to locate a value for h_T for H_2S in our literature search, and assumed $h_T = 0$ for this case.

Table 3.8.1: Parameters used to estimate the dependence of Henry's Law constants on $[NaCl]$.

Parameter	H_2S	SO_2	Na^+	Cl^-
H_o (M/bar)	0.101	1.34	–	–
h_o (M^{-1})	-0.0333	-0.0607	–	–
h_T (M^{-1})	0 ^a	0.000275	–	–
h_i (M^{-1})	–	–	0.1143	0.0318

The Henry's Law constants for these gases as a function of $[NaCl]$ at $T = 298.15K$ is show in Fig. 3.8.1. In this study, we consider ionic strengths $I \leq 0.1M$, corresponding to $[NaCl] \leq 0.1M$. At such levels, salinity has a negligible effect on Henry's Law solubility, and we consequently neglect it in our calculations.

3.9 APPENDIX D: SENSITIVITY OF ANALYSIS TO TEMPERATURE

This appendix describes our assessment of the sensitivity of our calculations to the temperature of the aqueous reservoir in which the equilibrium chemistry proceeds.

3.9.1 SENSITIVITY OF HENRY'S LAW CONSTANTS TO TEMPERATURE

We calculated the effect of temperature on Henry's Law using the three-term empirical fit outlined in Burkholder et al. [36], i.e. $\ln(H) = A + B/T + C \ln(T)$, where H is in units of M/atm and A , B , and C are gas-specific coefficients of an empirical fit. The values of these coefficients for H_2S and SO_2 were taken from Burkholder et al. [36] and are summarized in Table 3.9.1. $H(T)$ for H_2S and SO_2 is plotted in Fig. 3.9.1. For temperatures ranging from $0 - 50^\circ$ ($273.15 - 323.15$

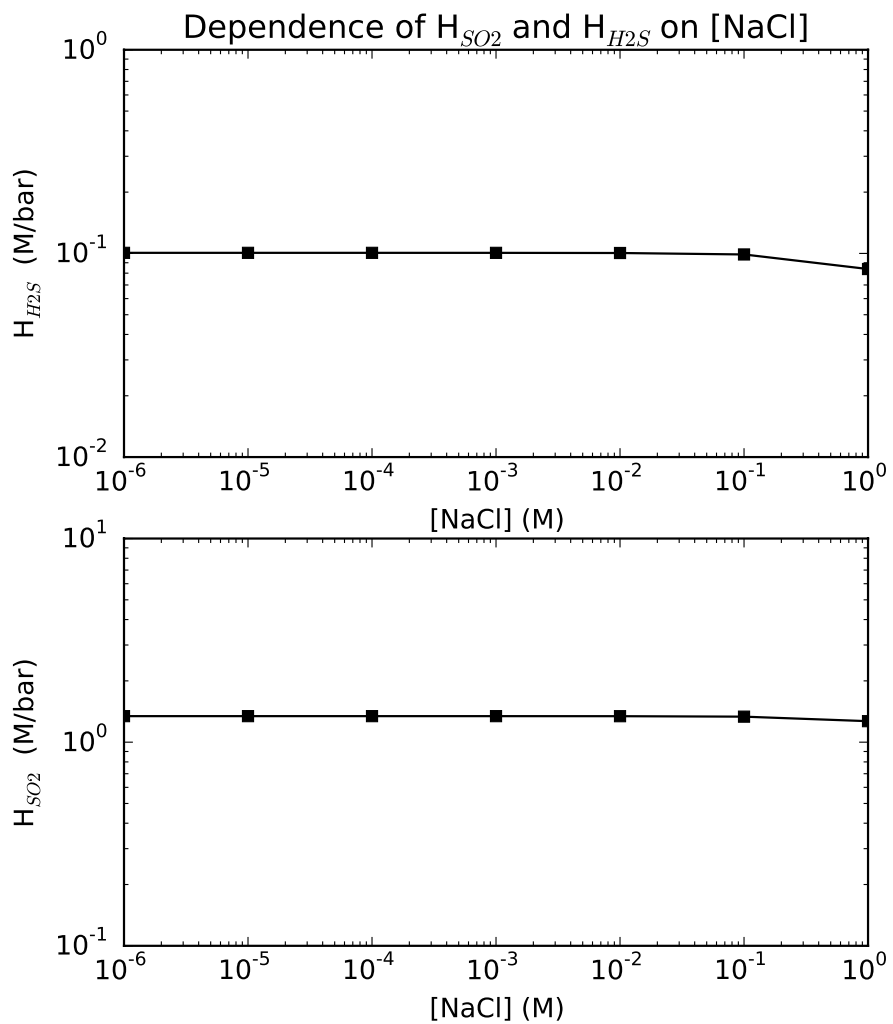


Figure 3.8.1: Dependence of Henry's Law constants for H_2S and SO_2 on $[NaCl]$, calculated using the formalism from Burkholder et al. [36]. H_{H_2S} and H_{SO_2} are insensitive to $[NaCl]$ for $[NaCl] < 1M$.

K), the Henry's Law constants vary by less than a factor of 2.5 relative to their values at 25°C (293.15K), which is small compared to the order-of-magnitude variations in concentration we focus on in this study. We also estimated the temperature dependence using the van't Hoff equation as outlined in Sander [296], and obtained similar results.

Table 3.9.1: Parameters used to estimate dependence of Henry's Law constant on temperature

Parameter	H ₂ S	SO ₂
A	-145.2	-39.72
B	8120	4250
C	20.296	4.525

3.9.2 SENSITIVITY OF REACTION RATES TO TEMPERATURE

In order to assess the temperature dependence of acid dissociation pKa's, we use the Van't Hoff Equation:

$$\frac{\partial[\ln K_o]}{\partial T} = \frac{\Delta H_o}{RT^2} \quad (3.5)$$

Where K_o is the equilibrium constant, T is temperature, ΔH_o is the change in enthalpy, and $R = 8.314 \times 10^{-3}$ kJ/mol/K. Solving this differential equation, assuming temperature-invariant enthalpy of solution¹⁶, gives:

$$\ln(K_2) = \ln(K_1) + \frac{-\Delta H_o}{R} \left(\frac{1}{T_2} - \frac{1}{T_1} \right) \quad (3.6)$$

With this equation, the acid dissociation constant K_2 can be estimated at a given temperature T_2 , provided its value K_1 is known at a reference temperature

¹⁶We expect this assumption to be reasonable because of the limited range of temperatures that are plausible for our surface aqueous reservoir scenario.

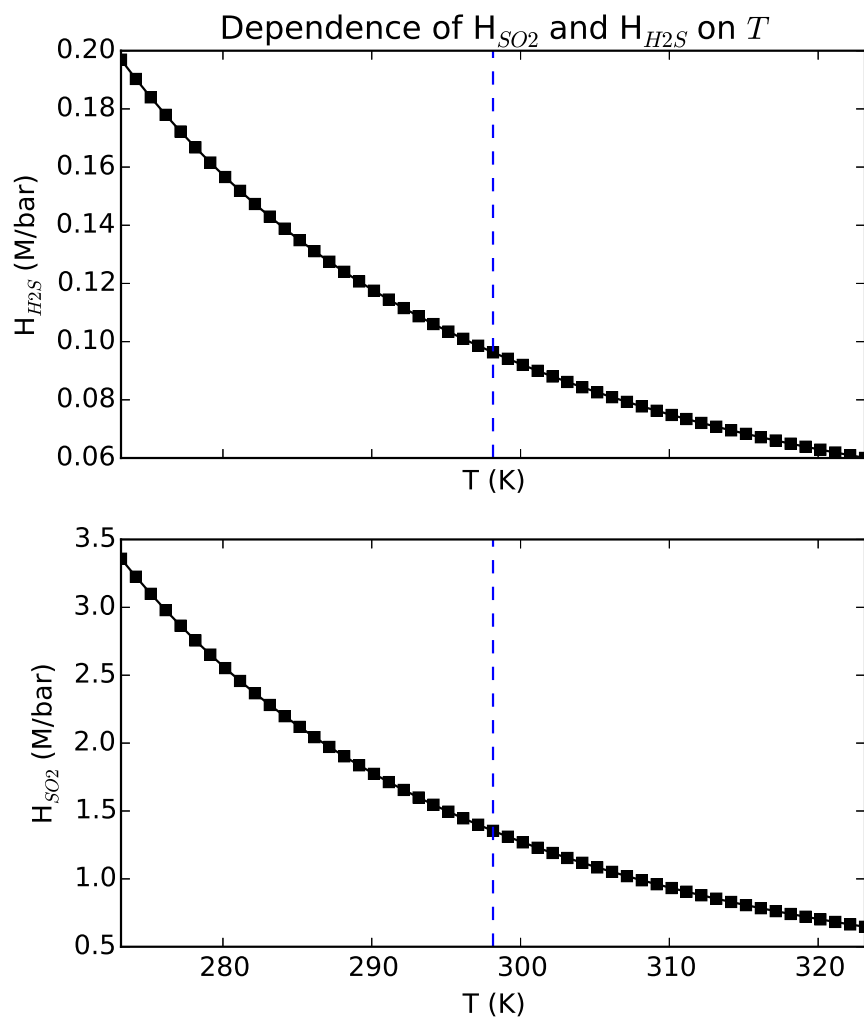


Figure 3.9.1: Temperature dependence of Henry's Law constants for H_2S and SO_2 , calculated using the formalism from Burkholder et al. [36]. Varying the temperature by 25K relative to the reference temperature of 298.15K (blue line) affects the value of H_{H_2S} and H_{SO_2} by less than a factor of 2.5.

T_1 . ΔH is the change in enthalpy of the reaction, given by:

$$\Delta H = \sum \Delta H_f^\circ(\text{products}) - \sum \Delta H_f^\circ(\text{reactants}) \quad (3.7)$$

The enthalpies of formation for the products and reactants of the first two acid dissociation reactions for H_2S and SO_2 are taken from [?], and are shown in Table 3.9.2. Note that $\Delta H_f^\circ = 0$ for H^+ , by definition. We were unable to locate an enthalpy of formation for H_2SO_5^- , and consequently are unable to calculate the temperature-dependence of $\text{pK}_{\text{aSO}_2,3}$. Since in our analysis the supply of SO_2 is not limited (the atmosphere is treated as an infinite reservoir), $\text{pK}_{\text{aSO}_2,3}$ affects only the abundance of H_2SO_5^- , which is a trace compound in our analysis (see Fig. ??).

Table 3.9.2: Enthalpies of formation used in the Van't Hoff Equation calculation.

Molecule	ΔH_f° (kJ/mol)
HSO_3^-	-626.2
SO_3^{2-}	-635.5
SO_2	-296.8
HS^-	-17.6
S^{2-}	33.1
H_2S	-20.6
H_2O	-285.8

Using these values and the Van't Hoff equation, we calculated the temperature dependence of the first two acid dissociation constants for aqueous H_2S and SO_2 . Table 3.9.3 shows these pK_a 's for SO_2 and H_2S at 0, 25, and 50°C.

The variation in pK_a is negligible for all reactions except the first dissociation of SO_2 ; $\text{pK}_{\text{aSO}_2,1}$ increases significantly with temperature. This implies that in non-acidic solutions, the concentrations of SO_2 -derived anions should decrease,

Table 3.9.3: pKa at temperatures of 0°C, 25°C, and 50°C and reaction enthalpies

	T=0 ° C	T=25 ° C	T=50 ° C	ΔH_{rxn}° (kJ/mol)
H ₂ S, pKa ₁	7.098	7.05	7.009	3.0
H ₂ S, pKa ₂	19.81	19.0	18.31	50.7
SO ₂ , pKa ₁	1.160	1.86	2.452	-43.6
SO ₂ , pKa ₂	7.051	7.2	7.326	-9.3

and conversely that as temperature decreases they should increase.

3.9.3 SENSITIVITY OF ACTIVITY COEFFICIENTS TO TEMPERATURE

Temperature dependence enters the calculation of the activity coefficients through the parameters A and B (see Appendix 3.7 for details). For water, at $T = 0^{\circ}\text{C}$, $A = 0.4883 \text{ M}^{-1/2}$ and $B = 0.3241 \text{ M}^{-1/2-1}$; at $T = 25^{\circ}\text{C}$, $A = 0.5085 \text{ M}^{-1/2}$ and $B = 0.3281 \text{ M}^{-1/2-1}$; and at $T = 50^{\circ}\text{C}$, $A = 0.5319 \text{ M}^{-1/2}$ and $B = 0.3321 \text{ M}^{-1/2-1}$ [208]. From $T = 0 - 50^{\circ}\text{C}$, the activity coefficients varied by $< 8\%$ for $I \leq 0.1$.

3.9.4 OVERALL SENSITIVITY OF ANALYSIS TO TEMPERATURE

We evaluated the overall sensitivity of our analysis to our assumption of $T = 25^{\circ}\text{C}$ by repeating our analysis at $T = 0^{\circ}$ and $T = 50^{\circ}$, and including the effects of temperature on Henry's Law constant, the reaction pKa's, and the activity coefficients, simultaneously. Across the tested range, temperature had a negligible impact on the abundances of the H₂S-derived anions, but a significant impact on the abundances of the SO₂-derived anions. H_{SO_2} decreases with temperature, and pKa_{SO₂,1} increases with temperature; both effects serve to increase the concentration of HSO₃⁻ and its derivatives in non-acidic (pH > 2.5) waters. At $T = 0^{\circ}\text{C}$, HSO₃⁻ and SO₃²⁻ concentrations are an order of magnitude higher than at $T = 25^{\circ}\text{C}$. Similarly, at $T = 50^{\circ}\text{C}$, HSO₃⁻ and SO₃²⁻

concentrations are an order of magnitude lower than at $T = 25^{\circ}\text{C}$. Our overall conclusions are robust to these variations. However, this study does imply that significantly higher concentrations of SO_2 -derived anions are available to prebiotic chemistry in cooler waters, and inversely that hotter waters would have access to lower levels of SO_2 -derived anions.

4

Nitrogen Oxides Concentrations in Natural Waters on Early Earth

Abstract

A key challenge in origins-of-life studies is estimating the abundances of species relevant to the chemical pathways proposed to have contributed to the emergence of life on early Earth. Dissolved nitrogen oxide anions (NO_x^-) in particular nitrate (NO_3^-) and nitrite (NO_2^-), have been invoked in diverse origins-of-life chemistry, from the oligomerization of RNA to the emergence of protometabolism. Recent work has calculated the supply of NO_x^- from the prebiotic atmosphere to the ocean and reported steady state $[\text{NO}_x^-]$ to be high across all plausible parameter space. These findings rest on the assumption that NO_x^- is stable in natural waters unless processed at a hydrothermal vent. Here, we show that NO_x^- is unstable in the reducing environment of early Earth. Sinks due

to ultraviolet photolysis and reactions with reduced iron (Fe^{2+}) suppress $[\text{NO}_x^-]$ by several orders of magnitude relative to past predictions. For $\text{pH} = 6.5\text{--}8$ and $T = 0\text{--}50^\circ\text{C}$, we find that it is most probable that $[\text{NO}_x^-] < 1\mu\text{M}$ in the prebiotic ocean. On the other hand, prebiotic ponds with favorable drainage characteristics may have sustained $[\text{NO}_x^-] > 1\mu\text{M}$. As on modern Earth, most NO_x^- on prebiotic Earth should have been present as NO_3^- , due to its much greater stability. These findings inform the kind of prebiotic chemistries that would have been possible on early Earth. We discuss the implications for proposed prebiotic chemistries and highlight the need for further studies of NO_x^- kinetics to reduce the considerable uncertainties in predicting $[\text{NO}_x^-]$ on early Earth.¹

4.1 INTRODUCTION

A KEY CHALLENGE FOR origin-of-life studies is determining the range of environmental conditions on early Earth under which life arose. Knowledge of these environmental conditions informs development of theories of the origin of life, and enables assessment of the plausibility and probability of postulated prebiotic chemistries (e.g., Bada et al. [12], Corliss et al. [61], Ruiz-Mirazo et al. [286], Todd et al. [350], Urey [360], Xu et al. [385]). Consequently, extensive work has been done to place constraints on the prebiotic environment, including but not limited to the availability of liquid water, the redox state of the atmosphere, the UV irradiation environment, the pH and temperature of the early oceans, the physico-chemical conditions at deep-sea hydrothermal vents, and the availability of sulfidic anions [89, 115, 162, 188, 211, 260, 263].

An important prebiotic environmental factor is the abundance of fixed nitrogen species in natural waters on early Earth. Dinitrogen's high-energy triple bond renders it highly nonreactive, meaning that nitrogen generally must be "fixed" into its reduced or oxidized forms (e.g., NO_2^- , NO_3^- , NH_4^+) to be useful

¹This thesis chapter was published as: S. Ranjan, Z. R. Todd, P. B. Rimmer, D. D. Sasselov, and A. R. Babbitt (2019) *Geochem. Geophys. Geosys.*, 20(4), 2021-2039.

to biology or prebiotic chemistry. Consequently, it is unsurprising that nitrogen fixation is thought to be ancient [39, 87, 331, 400, 402]. Prebiotic chemists have been especially interested in nitrate (NO_3^-) and nitrite (NO_2^-), the oxidized anions of nitrogen (NO_x^-). These molecules are high-potential electron acceptors, have played a key role in microbial metabolisms since at least the Archaean [39], and have been hypothesized to have been involved in the first metabolic pathways, e.g, the oxidation of methane and hydrogenation of CO_2 at deep-sea vents [81, 227, 311]. These molecules have also been invoked for the non-enzymatic synthesis and replication of oligonucleotides, in surficial (lake/pond) settings [184]. Crucially, NO_x^- can be abiotically synthesized by the thermal decay of molecules like HNO, which are produced by high-energy events like lightning in an N_2 - CO_2 atmosphere [8, 151, 183, 222], meaning these molecules may have been available for prebiotic chemistry on early Earth.

Motivated by the potential prebiotic relevance of NO_3^- and NO_2^- , a number of studies have aimed to constrain their concentrations on early Earth. Mancinelli and McKay [183] pointed out that atmospherically-generated NO_x^- would form NO_2^- and NO_3^- in the prebiotic ocean and accumulate, and that solubility concerns would not limit the accumulation. However, Mancinelli and McKay [183] did not quantify the concentrations to which NO_x^- could accumulate. Wong et al. [379] conducted atmospheric modeling, combining 3D General Circulation Model (GCM) estimates with 1D photochemical models to estimate the supply of NO_x^- to the oceans due to lightning. They identified the key variable controlling the NO_x^- supply to be the CO_2 partial pressure ($p\text{CO}_2$). Under the assumption that the sole sink on NO_x^- was destruction at high-temperature hydrothermal vents, Wong et al. [379] computed $[\text{NO}_x^-]$ in the bulk ocean to be $\geq 10\mu\text{M}$, and $[\text{NO}_x^-] = 20\text{ mM}$ for $p\text{CO}_2 = 1\text{ bar}$. Laneuville et al. [166] conducted a systems model of the prebiotic nitrogen cycle, including cometary delivery, impact synthesis, and lightning as sources of fixed nitrogen, and destruction at hydrothermal vents as the sole sink of oceanic NO_x^- . They calculated $[\text{NO}_x^-] \approx 1\mu\text{M} - 10\text{mM}$ in the bulk prebiotic oceans, depending on a number of variables including atmospheric nitrogen fixation rate.

These large ranges are due to the wide range of possible NO_x^- supply. Both Wong et al. [379] and Laneuville et al. [166] suggest that the prebiotic oceans should have had $\geq 1\mu\text{M}$ [NO_x^-], thought to be adequate for prebiotic chemistry. For comparison, on modern earth, bioavailable fixed NO_x^- achieves maximum concentrations of $\sim 40\mu\text{M}$ in the deep Pacific [230, 400]. NO_x^- in the modern ocean is almost exclusively in the form of NO_3^- , except where NO_2^- accumulates substantially within two depth horizons. The primary nitrite maximum, where nitrite concentrations reach hundreds of nanomolar to occasionally a few micromolar, is a global feature at the base of the photic zone, and formed by leaking algal cells [178] and/or an imbalance in the ammonium and nitrite oxidation steps of nitrification [299]. The secondary nitrite maximum is a broad feature in the oxygen deficient zones of the eastern tropical Pacific and Arabian Sea, where oxygen levels are reduced to $< 10\text{ nmol/L}$ [269]. These secondary nitrite maxima can achieve several micromolar in concentration (e.g., Babbitt et al. 11) and are indicative of active denitrification regimes.

Overall, previous work has concluded that high [NO_x^-] (micromolar to millimolar) was present in the prebiotic ocean, under the assumption that the only sink of NO_x^- in the prebiotic ocean was processing at hydrothermal vents, and that atmospherically-supplied NO_x^- was otherwise stable in prebiotic waters. However, in the anoxic prebiotic environment, NO_2^- and NO_3^- are vulnerable to reduction to less soluble forms due to UV photochemistry and reactions with reductants (e.g., Fe^{2+}). These reduced species (NO , N_2O , N_2) can then escape to the atmosphere, depleting the oceanic nitrogen pool [41].

In this paper, we explore the impact of these chemical sinks on the predicted concentrations of NO_x^- in prebiotic waters. In Section 4.2, we carry out a kinetic calculation, comparing the supply of NO_x^- to natural waters to the sinks of NO_x^- from reduction reactions and photochemistry to estimate the steady-state concentration of NO_x^- in oceans and ponds with $T = 0 - 50^\circ\text{C}$ and $\text{pH} = 6.5 - 8$. In Section 4.3, we examine the thermochemical stability of NO_3^- and NO_2^- in prebiotic conditions, finding results consistent with our kinetic calculations. In Section 4.4, we discuss our calculations and explore their

implications for prebiotic NO_X^- levels, postulated prebiotic chemistries, and origin-of-life scenarios. We summarize our conclusions in Section 4.5.

4.2 KINETIC STEADY-STATE

In this section, we calculate abiotic loss of aqueous NO_2^- and NO_3^- due to reduction by UV light and Fe^{2+} , and compare to the NO_X^- supply rate from processes such as lightning fixation and exogenous delivery, to estimate steady-state NO_X^- concentrations. We focus on these processes because they are dominant under the range of conditions available on early Earth. If abiotic NO_X^- destruction is slow compared to abiotic NO_X^- production, then it is possible for high levels of NO_X^- to build up in natural waters. If destruction is fast compared to production, then NO_X^- levels will be low.

4.2.1 NO_X^- PRODUCTION

On modern Earth, lightning fixation is the largest non-biological natural source of fixed nitrogen, via high-energy shocks which form free radicals and disrupt N_2 [183]. Wong et al. [379] used photochemical models calibrated with GCM results to model the supply of NO_X^- to the prebiotic surface due to lightning fixation. Most NO_X^- reached the surface in the form of HNO , which in aqueous settings would then undergo dissociation, homologation, and decay reactions, ultimately yielding soluble NO_2^- and NO_3^- , and gaseous N_2O [183, 335]. Stanton et al. [326] have recently demonstrated the reduction of NO to N_2O in ferrous waters; we may speculate similar chemodenitrification to occur with NO^- . It is difficult to calculate the fraction of fixed nitrogen that escapes back to the atmosphere as N_2O , because the kinetics of these transformations have not been quantified for NO^- . We follow Wong et al. [379] in neglecting the sink to N_2O formation and assuming all NO_X^- supplied to the surface from the atmosphere eventually yields NO_2^- and/or NO_3^- ; this means our calculations may overestimate NO_X^- supply and hence $[\text{NO}_X^-]$. Wong et al. [379] report a dominant factor controlling the surface flux of NO_X^- to be the partial pressure of

CO₂ in the atmosphere; the minimum NO_X⁻ flux, $\varphi_{NO_X^-}$, was

$$\varphi_{NO_X^-} = 2.5 \times 10^5 \text{ cm}^{-2} \text{ s}^{-1} \text{ for } pCO_2 = 0.1 \text{ bar, and the maximum was}$$

$$\varphi_{NO_X^-} = 6.5 \times 10^8 \text{ cm}^{-2} \text{ s}^{-1} \text{ for } pCO_2 = 1 \text{ bar.}$$

We used the lightning atmospheric chemistry model from Ardaseva et al. [8] to explore the production of NO_X⁻ by lightning as a function of pN₂, pCO₂, and lightning flash rate, to verify the upper bound in NO_X⁻ production rate identified by Wong et al. [379]. This model uses the freeze-out temperature approximation; a more sophisticated approach would involve shock modeling. We compare our lightning model calculations to the experimental results tabulated in Mvondo et al. [220], and find we reproduce these results well for CO₂ mixing ratios $\gtrsim 0.2$; at lower CO₂ concentrations, we overpredict NO_X⁻ production. We therefore only apply our model to atmospheres with CO₂ mixing ratios ≥ 0.2 .

We find NO_X⁻ production to be strong functions of pN₂/pCO₂ and pCO₂. NO_X⁻ production decreases as pN₂/pCO₂ increases, because the probability of N atoms recombining to N₂ is higher (as opposed to reacting with CO₂-derived oxygen to form NO_X⁻). We find NO_X⁻ production increases with pCO₂ over the range pCO₂ = 0.1 – 10 bar. This contrasts to Wong et al. [379], who report a maximum in NO_X⁻ production at pCO₂ = 1 bar; this is because Wong et al. [379] calculate lower lightning flash rates for high pCO₂ due to lack of moist convection in the warm troposphere they calculate for pCO₂ = 10 bar, while we fix the lightning flash rate. If we extrapolate the finding of Marty et al. [189] that pCO₂ ≤ 0.7 bar and pN₂ ≥ 0.5 bar from 3-3.5 Ga to the prebiotic era (c. 3.9 Ga) and assume lightning energies and flash densities similar to modern Earth, we find a tropospheric NO_X⁻ production rate of $\varphi_{NO_X^-} < 10^9 \text{ cm}^{-2} \text{ s}^{-1}$, in concordance with Wong et al. [379]. Biological fixation tends to decrease pN₂, suggesting that pN₂ was not lower in the prebiotic era than in the Archaean [143]. Krissansen-Totton et al. [163] calculate that weathering restricted pCO₂ ≤ 1 bar at 4 Ga. We consequently retain $6.5 \times 10^8 \text{ cm}^{-2} \text{ s}^{-1}$ of Wong et al. [379] as the upper bound on $\varphi_{NO_X^-}$, but caution that if pCO₂ were higher or pN₂ lower than what we consider, $\varphi_{NO_X^-}$ could have been up to an order of magnitude higher. For more details, see 4.9.

Comet delivery and impact fixation should also have supplied fixed nitrogen on prebiotic Earth; however, these mechanisms are thought to have supplied $\phi_{\text{NO}_x^-} < 2 \times 10^9 \text{ cm}^{-2} \text{ s}^{-1}$ and typically less, well within the range bracketed by lightning production [166]. Airapetian et al. [1] suggest that energetic protons from flares on the young Sun might also have powered nitrogen fixation and the supply of NO_x^- to the surface; however, they do not quantify the magnitude of this supply. We consequently focus on the NO_x^- production flux range defined by lightning production in the model of Wong et al. [379] in our work ($2.5 \times 10^5 - 6.5 \times 10^8 \text{ cm}^{-2} \text{ s}^{-1}$).

4.2.2 NO_x^- DESTRUCTION

We consider three processes in calculating NO_x^- destruction in natural waters: processing at hydrothermal vents, UV photolysis, and reactions with Fe^{2+} . Past work has focused on processing at vents; in this work, we consider the effects of UV and Fe^{2+} as well. Section 4.10 explores these processes in detail, along with other NO_x^- loss processes we neglected in this work because they are dominated by the processes we consider here.

The presence of UV light on early Earth is attested to by the sulfur mass-independent fractionation (SMIF) signal [90]. The presence of Fe^{2+} is attested by the presence of banded iron formations (BIFs) and other geological evidence [54, 159, 174, 369]. Recent estimates place $[\text{Fe}^{2+}] = 30 - 600 \mu\text{M}$ in early Archean oceans, with higher $[\text{Fe}^{2+}]$ in the aphotic deep oceans [115, 160, 352, 404]. In this work, we explore $[\text{Fe}^{2+}] = 10 - 600 \mu\text{M}$, bracketing this range. We do not consider reactions with other reductants, such as Mn^{2+} , owing to paucity of constraints on the kinetics of these processes; consequently, we may underestimate NO_x^- reduction rates in prebiotic natural waters.

The rates of NO_x^- photolysis by UV and reduction by Fe^{2+} are dependent on temperature and pH. In this work, we consider $\text{pH} = 6.5 - 8$ and $T = 273 - 323 \text{ K}$, motivated by modeling work which predicts the early ocean to have been circumneutral ($6.3 \leq \text{pH} \leq 7.2$) and temperate ($271 \leq T \leq 314 \text{ K}$)

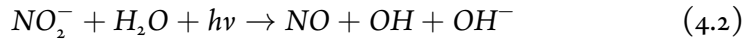
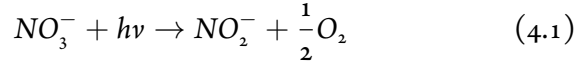
(Krissansen-Totton et al. [162]; see also Halevy and Bachan [115]). We consider the sensitivity of our conclusions to these assumptions in Section 4.2.4.

NO_X⁻ DESTRUCTION IN VENTS

The hot and acidic conditions at hydrothermal vents can destroy NO_X⁻ [26, 266, 333]. It is debated how extreme conditions need to be to consume NO_X⁻. Under the assumptions that NO_X⁻ is removed with unit efficiency at and only at black smoker-type vents ($T \lesssim 405^\circ \text{C}$, pH= 1 – 2, Martin et al. [188]), Wong et al. [379] propose NO_X⁻ destruction to be characterized by a first-order process with rate constant $k_{vents} = 8 \times 10^{-17} \text{ s}^{-1}$. Under the assumption that circulation through any hydrothermal vent would destroy 100% of NO_X⁻, Laneuville et al. [166] instead propose $k_{vents} = 1 \times 10^{-14} \text{ s}^{-1}$. We explore the range $k_{vents} = 8 \times 10^{-17} - 1 \times 10^{-14} \text{ s}^{-1}$ in this work.

NO_X⁻ DESTRUCTION BY UV

Irradiation by UV light in natural waters net photolyzes NO₃⁻ to NO₂⁻, and NO₂⁻ to NO, which escapes the ocean to the atmosphere or is reduced to N₂O [41, 88, 182, 322, 326]:



These processes are thought to be first order and have been measured both in the oceans and in lakes. In the modern surface ocean, these processes have median rate constants $k_{\text{NO}_3^-, hv} = 2.3 \times 10^{-8} \text{ s}^{-1}$ and $k_{\text{NO}_2^-, hv} = 1.2 \times 10^{-6} \text{ s}^{-1}$ for nitrate and nitrite, respectively [206, 392, 393]. In pure water, NO₂⁻ reacts with OH to reform NO₃⁻; however, in the presence of OH scavengers like bicarbonate or Br⁻, NO₂⁻ is lost with 20-100% efficiency [354, 389, 393, 394].

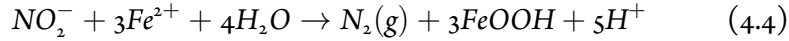
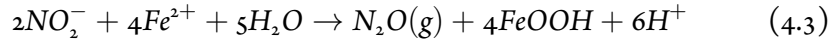
Nitrite and nitrite photolysis rates, as measured by OH production, depend

modestly on temperature. At $T = 0^\circ \text{C}$, photolysis rates are $\geq 0.5 \times$ the rates at $T = 25^\circ \text{C}$, and at $T = 50^\circ \text{C}$, photolysis rates are $\leq 2 \times$ the rates at $T = 25^\circ \text{C}$ [182, 401]. The reaction rates measured by Zafriou and True [393] and Zafriou and True [392] were measured at ambient temperature. Under the assumption that these ambient conditions corresponded to $T \approx 25^\circ \text{C}$, we explore $k_{\text{NO}_3^-, hv} = 1.1 - 4.6 \times 10^{-8} \text{ s}^{-1}$ and $k_{\text{NO}_2^-, hv} = 0.6 - 2.4 \times 10^{-6} \text{ s}^{-1}$, to account for the variation in photolysis rates with temperature for $T = 0 - 50^\circ \text{C}$.

We calculate the global rate of nitrate/nitrite photolysis following a procedure motivated by that of Zafriou and True [392] and Zafriou and True [393]. We assume that nitrate and nitrite are lost at rates equal to half their surface photolysis rates down to their photic depths, and that the loss rates are zero below this threshold. The modern photic depth for nitrate and nitrite at the equator are 5 m and 10 m, respectively; to average over latitude and obtain global mean photic depths, we scale these photic depths by $2/3$ [64, 392, 393]. In the modern ocean, intense consumption by phototrophic microbes depletes surficial NO_X^- , meaning that NO_X^- photolysis is only significant in upwelling areas where NO_X^- is maintained at high concentrations due to supply from below. In the absence of biology, surface NO_X^- would not be depleted, and NO_X^- would be photolyzed from 100% of the surface area of the ocean. When calculating the loss of NO_X^- in pond and lake environments, we assume the same photic depths, and continue to take NO_X^- to be lost from 100% of the surface area. We neglect possible enhancements in the conversion rate due to factors such as availability of shorter-wavelength UV radiation on early Earth and the anoxic nature of prebiotic natural waters, and we assume the lowest proposed efficiency for net loss of NO_2^- to photolysis (i.e., 20%). Consequently, our estimates of NO_X^- photolysis should be considered lower bounds.

REDUCTION OF NO_2^- BY Fe^{2+} TO NITROGENOUS GAS

Fe^{2+} reduces NO_2^- to yield nitrogenous gas [34]:



Recent kinetic studies of these reactions are consistent with first-order kinetics with respect to both reactants and second order kinetics overall, with rate constants that are dependent on pH [34, 110, 146]. From the data of Buchwald et al. [34] and Grabb et al. [110], we extract

$$k_{NO_2^-, Fe^{2+}} = 3 \times 10^{-5} - 1 \times 10^{-2} \text{ M}^{-1} \text{ s}^{-1} \text{ over pH}=6.5-8 \text{ and } T=25^\circ \text{ C} \quad (4.10).$$

$k_{NO_2^-, Fe^{2+}}$ depends on whether Fe^{2+} or NO_2^- is in excess, with reaction rates up to an order of magnitude lower if $[NO_2^-] > [Fe^{2+}]$ compared to if $[NO_2^-] < [Fe^{2+}]$ [146]. To account for the potential dependence on relative NO_2^- and Fe^{2+} concentrations, we assign

$$k_{NO_2^-, Fe^{2+}}([NO_2^-] > [Fe^{2+}]) = 0.1 k_{NO_2^-, Fe^{2+}}([NO_2^-] < [Fe^{2+}]).$$

Further, The activation energy E_A for NO_2^- reduction by dissolved Fe^{2+} has not been measured to our knowledge, but is 18.4 kJ mol^{-1} for NO_2^- reduction by mineralized Fe^{2+} , and is 70 kJ mol^{-1} for NO_3^- reduction by dissolved Fe^{2+} [235, 295]. Mineralized Fe^{2+} is a more effective reductant than dissolved Fe^{2+} , and NO_2^- is more reactive than NO_3^- , suggesting $18.4 \leq E_A \leq 70 \text{ kJ mol}^{-1}$. To ensure we do not underestimate the possible range of $k_{NO_2^-, Fe^{2+}}$, we take $E_A = 70 \text{ kJ mol}^{-1}$.

Combining these effects, in total we consider

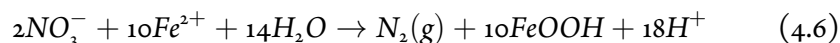
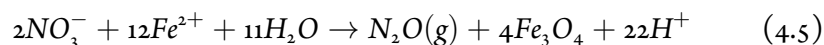
$$k_{NO_2^-, Fe^{2+}} = 2 \times 10^{-6} - 9 \times 10^{-2} \text{ M}^{-1} \text{ s}^{-1} \text{ if } [NO_2^-] < [Fe^{2+}] \text{ and}$$

$$k_{NO_2^-, Fe^{2+}} = 2 \times 10^{-7} - 9 \times 10^{-3} \text{ M}^{-1} \text{ s}^{-1} \text{ if } [NO_2^-] > [Fe^{2+}], \text{ corresponding to}$$

pH= 6.5 – 8 and $T = 0 - 50^\circ \text{ C}$.

REDUCTION OF NO_3^- BY Fe^{2+} TO NITROGENOUS GAS

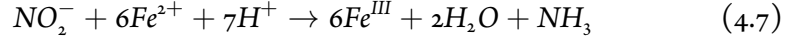
Fe^{2+} can reduce NO_3^- to nitrogenous gas, with proposed reactions [255, 295]:



The kinetics of uncatalyzed room-temperature reduction of NO_3^- by Fe^{2+} at room temperature are uncertain, because NO_3^- reduction is very slow under these conditions and hence difficult to characterize in the laboratory. Ottley et al. [235] reports the detection of uncatalyzed NO_3^- reduction by Fe^{2+} at room temperature over timescales of a week. However, Picardal [247] report nondetections of NO_3^- reduction by Fe^{2+} in sterile incubations carried out under conditions and timescales similar to those of Ottley et al. [235]. As we are unable to favor one study above the other from available information, we consider a range of $k_{\text{NO}_3^-, \text{Fe}^{2+}} = 0 - 9 \times 10^{-4} \text{ M}^{-1} \text{ s}^{-1}$. The lower bound is derived from the reported nondetections of Picardal [247]. The upper bound is derived from the study of Ottley et al. [235], and corresponds to $\text{pH} = 8$ and $T = 50^\circ \text{ C}$, which should be the maximum rate possible over $\text{pH} = 6.2 - 9$ and $T = 0 - 50^\circ \text{ C}$ [244]. We assume that the reduction of NO_3^- by dissolved Fe^{2+} is, like the reduction of NO_2^- , first-order with respect to both reactants, for a second-order reaction overall, motivated by the generally similar kinetics of NO_2^- and NO_3^- reduction by $\text{Fe}(\text{o})$, H_2 , and mineralized Fe^{2+} [295, 405]. This range of $k_{\text{NO}_3^-, \text{Fe}^{2+}}$ is very large; kinetic studies are required to constrain it.

OTHER REACTIONS OF NO_X^- WITH Fe^{2+}

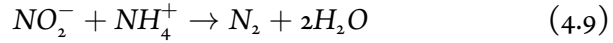
Fe^{2+} can also reduce NO_2^- to NH_3 , with proposed empirical reaction mechanism and rate law [334]:



$$\frac{d[\text{NH}_3]}{dt} = k_{4.7}[\text{NO}_2^-][\text{Fe}^{2+}]^{1.8} (\text{pH} = 7.9) \quad (4.8)$$

This reaction should be a negligible sink on $[\text{NO}_2^-]$ compared to Fe^{2+} reduction of NO_2^- to nitrogenous gas; to demonstrate this, we evaluate it for $k_{4.7} = 4.2 \times 10^{-5} \text{ s}^{-1} \text{ M}^{-1.8}$, corresponding to the maximum rate (pH= 7.6, $T = 40^\circ\text{C}$) measured by Summers and Chang [334]. UV photolysis and reduction by Fe^{2+} dominate this process over the $[\text{NO}_2^-]$ range we consider here (Figure 4.2.1).

Similarly, the anaerobic ammonium oxidation by NO_2^- (anammox) to N_2 is negligible compared to other processes; to illustrate this, we compute its rate for $[\text{NH}_3] = 6 \times 10^{-7} \text{ M}$ and pH= 6.5, $T = 50^\circ\text{C}$, corresponding to conditions maximize the reaction rate while conforming to the constraints Kasting [149] and Krissansen-Totton et al. [162]. We take the rate law from Nguyen et al. [226] following Laneuville et al. [166]:



$$\frac{d[\text{N}_2]}{dt} = A \exp(-E/RT)[\text{NH}_3][\text{HNO}_2]^2 \quad (4.10)$$

With $A = \exp(37.8) \text{ M}^{-2} \text{ s}^{-1} = 2.6 \times 10^{16} \text{ M}^{-2} \text{ s}^{-1}$ and $E = 65.7 \text{ kJ mol}^{-1}$. At $T = 50^\circ\text{C}$, this corresponds to a rate constant of $k_{4.9} = A \exp(-E/RT) = 6 \times 10^5 \text{ M}^{-2} \text{ s}^{-1}$. UV photolysis and reduction by Fe^{2+} dominate this process over the $[\text{NO}_2^-]$ range we consider here (Figure 4.2.1).

We note that the results of Nguyen et al. [226] were based on experiments with reactant concentrations $\geq 0.05 \text{ M}$. We assume this rate law to hold at lower concentrations as well; experimental studies are required to confirm this extrapolation. Our overall conclusions do not depend on these kinetics since

Process	Rate Law	Rate Constant
Hydrothermal Vents	$\frac{d[NO_X]}{dt} = k_{vents}[NO_X]$	$k_{vents} = 8 \times 10^{-17} - 1 \times 10^{-14} \text{ s}^{-1}$
NO_2^- UV Photolysis	$\frac{d[NO_2^-]}{dt} = k_{NO_2^-,hv}[NO_2^-]$	$k_{NO_2^-,hv} = 0.6 - 2.4 \times 10^{-6} \text{ s}^{-1}$
NO_3^- UV Photolysis	$\frac{d[NO_3^-]}{dt} = k_{NO_3^-,hv}[NO_3^-]$	$k_{NO_3^-,hv} = 1.1 - 4.6 \times 10^{-8} \text{ s}^{-1}$
NO_2^- Reduction by Fe^{2+} to N_2, N_2O	$\frac{d[NO_2^-]}{dt} = k_{NO_2^-,Fe^{2+}}[Fe^{2+}][NO_2^-]$	$= k_{NO_2^-,Fe^{2+}} = 2 \times 10^{-6} - 9 \times 10^{-2} \text{ M}^{-1} \text{ s}^{-1},$ $([Fe^{2+}] > [NO_2^-]); k_{NO_2^-,Fe^{2+}} = 2 \times 10^{-7} - 9 \times 10^{-3} \text{ M}^{-1} \text{ s}^{-1},$ $([Fe^{2+}] < [NO_2^-])$
NO_3^- Reduction by Fe^{2+} to N_2, N_2O	$\frac{d[NO_3^-]}{dt} = k_{NO_3^-,Fe^{2+}}[NO_3^-][Fe^{2+}]$	$= k_{NO_3^-,Fe^{2+}} = 0 - 9 \times 10^{-4} \text{ M}^{-1} \text{ s}^{-1}$
NO_2^- Reduction by Fe^{2+} to NH_3	$\frac{d[NH_3]}{dt} = k_{4.7}[NO_2^-][Fe^{2+}]^{1.8}$	$k_{4.7} = 4.2 \times 10^{-5} \text{ M}^{-1.8} \text{ s}^{-1}$ (Max.)
Anammox of NO_2^- and NH_3	$\frac{d[N_2]}{dt} = k_{4.9}[NH_3][HNO_2]^2$	$k_{4.9} = 6 \times 10^5 \text{ M}^{-2} \text{ s}^{-1}$ ($T = 50^\circ\text{C}$)

Table 4.2.1: Summary of NO_X^- loss process kinetics

these reactions are negligible compared to other processes.

4.2.3 CALCULATION OF $[NO_X^-]$ IN KINETIC STEADY-STATE

We calculate the concentrations of NO_3^- and NO_2^- under the assumption of kinetic steady-state, i.e. that the loss rates of these molecules due to the destruction processes specified in Section 4.2.2 and summarized in Table 4.2.1 equals their supply from the atmosphere (Section 4.2.1).

To compare loss rates to the supply flux of NO_X^- ($\text{cm}^{-2} \text{ s}^{-1}$), we integrate over the water column, giving us a loss flux ($\text{cm}^{-2} \text{ s}^{-1}$). We consider both ocean and pond environments, corresponding to different families of postulated prebiotic

chemistries (e.g., Patel et al. [240] vs. Shibuya et al. [311]). For the ocean, we adopt a depth of $d_{ocean} = 3.8 \times 10^5$ cm, corresponding to the mean depth of the modern ocean [287]. Figure 4.2.1 presents the column-integrated destruction rates of oceanic NO_2^- and NO_3^- as functions of $[\text{NO}_2^-]$ and $[\text{NO}_3^-]$, as well as the range of plausible atmospheric supply rates from Wong et al. [379]. The point at which the supply flux equals the destruction flux for a given process corresponds to the steady-state concentration for that process.

For pond environments, a broad range of depths is possible. Larger depths correspond to lower $[\text{NO}_X^-]$, since more column is available over which NO_X^- is destroyed (or, equivalently, input NO_X^- flux is distributed over a larger column). To obtain an upper limit on plausible $[\text{NO}_X^-]$, we choose $d_{pond} = 10$ cm, corresponding approximately to the summer depths of Don Juan Pond in Antarctica, which hosts millimolar abiotic NO_X^- [185, 295]. Figure 4.2.2 presents the column-integrated destruction rate of pond NO_2^- and NO_3^- as a function of $[\text{NO}_2^-]$ and $[\text{NO}_3^-]$, as well as the range of plausible atmospheric supply rates from Wong et al. [379]. Pond catchment areas can be much larger than their surface areas, meaning that ponds can concentrate atmospherically-delivered NO_X^- if the drainage timescale is short enough that the NO_X^- does not decay en route). The catchment area/surface area ratio is often termed the drainage ratio (DR). A study of catchment areas in southern England indicates means DR= 14 for lakes and DR= 500 for ponds [71]. We therefore also present the supply fluxes scaled by a factor of 100, to simulate the potential concentrating effects of high DR.

Figures 4.2.1 and 4.2.2 show that UV photolysis and reduction by Fe^{2+} to nitrogenous gas are the dominant sinks on NO_X^- in natural waters; at a given $[\text{NO}_X^-]$, the loss rates due to these processes are higher than the others, including processing at vents. We calculate $[\text{NO}_2^-]$ and $[\text{NO}_3^-]$ in the ocean as a function of $\phi_{\text{NO}_X^-}$ including UV photolysis and reduction by Fe^{2+} as sinks, and exploring the full range of reaction rate coefficients identified in Table 4.2.1. We assume

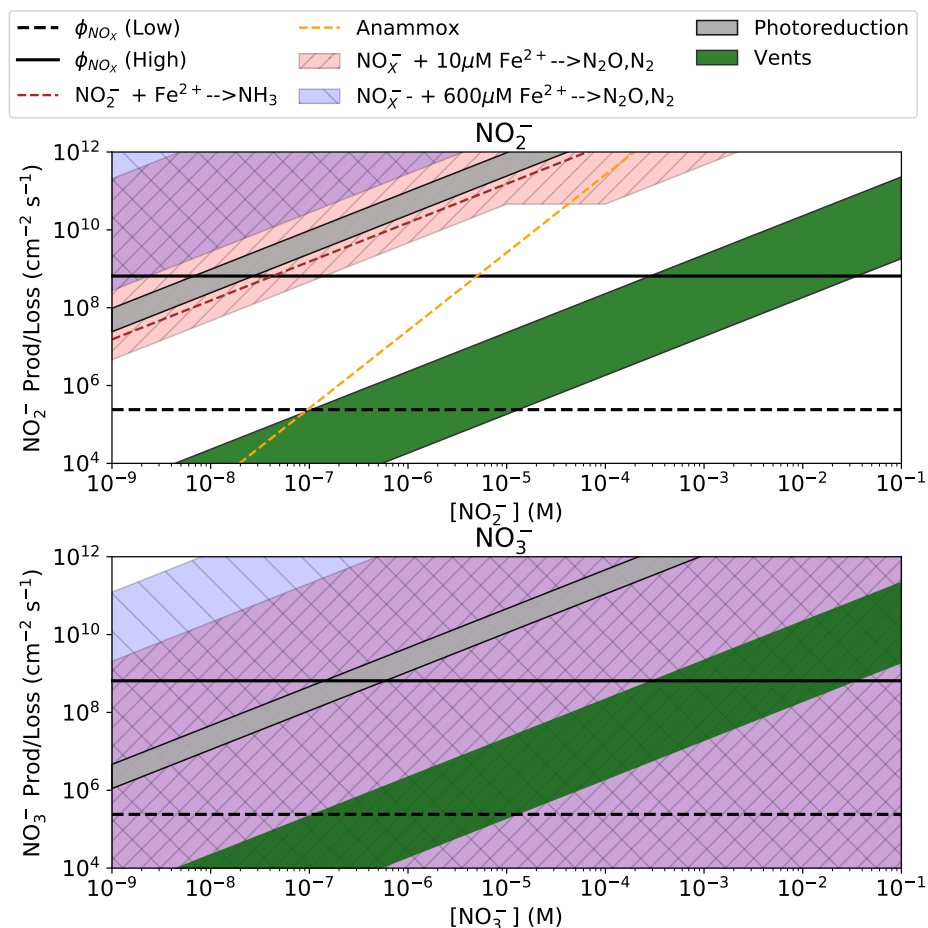


Figure 4.2.1: Kinetic loss rates for oceanic NO_2^- (top) and NO_3^- (bottom) for the processes summarized in Table 4.2.1, as a function of $[\text{NO}_2^-]$ and $[\text{NO}_3^-]$. Also plotted are the extremal ϕ_{NO_x} calculated by Wong et al. [379]. The point at which the supply flux equals the destruction flux for a given process corresponds to the steady-state concentration for that process; the largest destruction flux (leftmost curve at given ϕ_{NO_x}) dominates the system. Note that NO_3^- reduction by Fe^{2+} cannot be used to set an upper limit on $[\text{NO}_3^-]$, because we consider the possibility that $k_{\text{NO}_3^-, \text{Fe}^{2+}} = 0$.

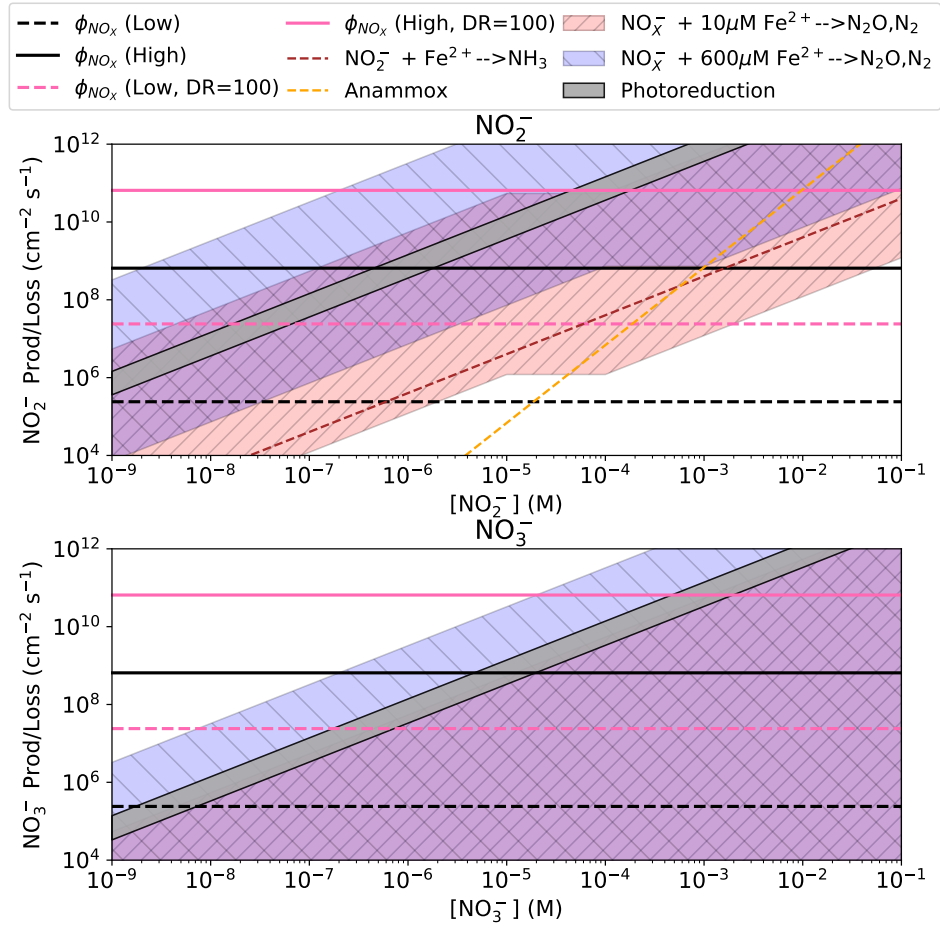


Figure 4.2.2: Kinetic loss rates for pond NO_2^- (top) and NO_3^- (bottom) for the processes summarized in Table 4.2.1, as a function of $[\text{NO}_2^-]$ and $[\text{NO}_3^-]$. Also plotted are the extremal $\phi_{\text{NO}_x^-}$ calculated by Wong et al. [379], as well as these $\phi_{\text{NO}_x^-}$ scaled by $100\times$ to simulate a lake/pond with a large DR and fast drainage. The point at which the supply flux equals the destruction flux for a given process corresponds to the steady-state concentration for that process; the largest destruction flux (leftmost curve at given $\phi_{\text{NO}_x^-}$) dominates the system. Note that NO_3^- reduction by Fe^{2+} cannot be used to set an upper limit on $[\text{NO}_3^-]$, because we consider the possibility that $k_{\text{NO}_3^-, \text{Fe}^{2+}} = 0$.

the NO_X^- is supplied as 80% NO_3^- and 20% NO_2^- , following the experimental work of Summers and Khare [335]; however, our results are not strongly sensitive to this assumption. We repeat this calculation for the case of a shallow pond with high drainage ratio and fast drainage ($d = 10$ cm, $\text{DR} = 100$), corresponding to a highly favorable scenario for NO_X^- accumulation. Hence, this should be considered an approximate upper bound on plausible NO_X^- . From this calculation, the upper bound on oceanic NO_X^- is $< 10\mu\text{M}$, and typically $< 1\mu\text{M}$ across most of parameter space. Ponds with favorable drainage characteristics can accumulate much more NO_X^- (Figure 4.2.3).

4.2.4 SENSITIVITY TO pH

We have focused on $\text{pH} = 6.5 - 8$, motivated by the findings of Halevy and Bachan [115] and Krissansen-Totton et al. [162] that the early ocean was circumneutral. However, this finding is a model prediction. Additionally, lakes/ponds can be buffered by local factors to an even wider range of pH; on modern Earth, lake pH ranges from $\text{pH} < 1$ to $\text{pH} > 11$ [111, 177]. Here, we consider the sensitivity of our results to our assumption of circumneutral pH.

As measured by OH production, NO_2^- photolysis rates vary by $\leq 2\times$ from $\text{pH} = 4 - 11$, and nitrate photolysis rates by $\leq 3\times$ from $\text{pH} = 2 - 14$, suggesting this process should be insensitive to pH [66, 390, 401]. However, for water with low concentrations of OH scavengers, nitrite photolysis should be reduced, since the OH can react with the photolysis products to reform the nitrite [389, 393]. Carbonate and bicarbonate are efficient OH scavengers. Consequently, achieving low OH scavenger concentrations requires $\text{pH} < 6$, such that dissolved inorganic carbon is present primarily as CO_2 as opposed to bicarbonate or carbonate at higher pH. At such pH, NO_2^- is unstable. Hence, our choice of photolysis rate constants are valid from $\text{pH} = 4 - 11$.

$k_{\text{NO}_2^-, \text{Fe}^{2+}}$ increases with pH for $\text{pH} = 6 - 8.5$ [212, 321]. For $\text{pH} < 6$, nitrite protonates and self-decomposes [236, 266]. Brown and Drury [31] report fast reduction of NO_2^- by Fe^{2+} in alkaline solution [88] (though the experimental

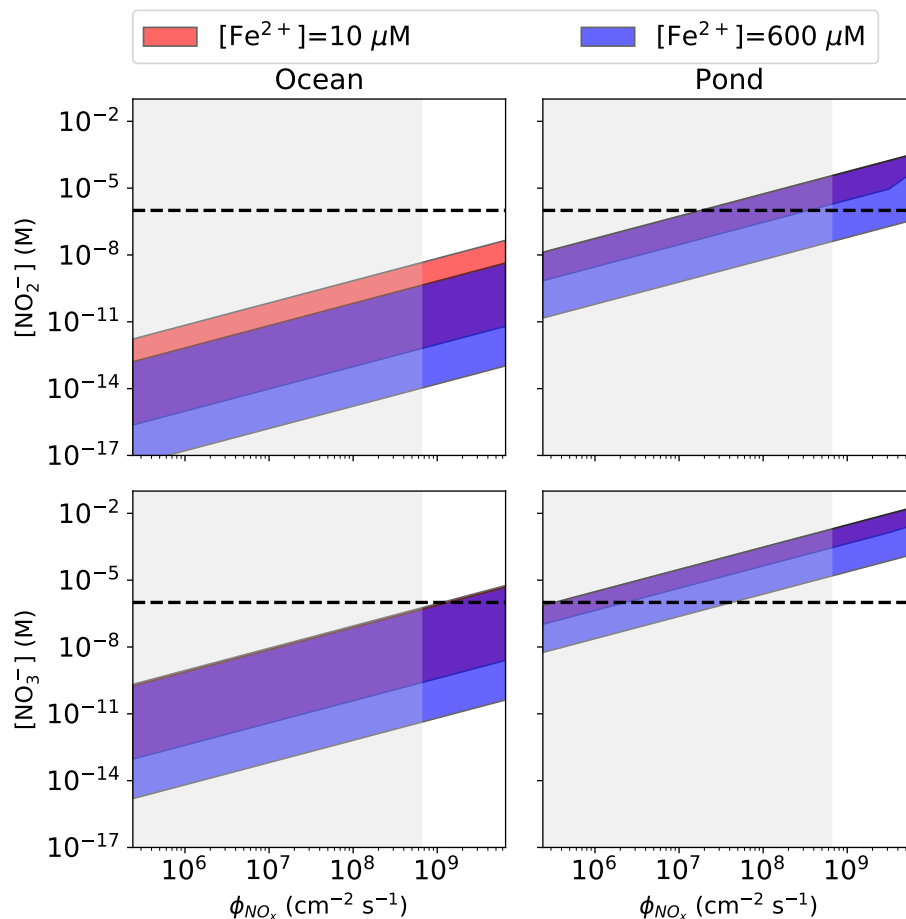


Figure 4.2.3: Steady-state concentrations of NO_2^- and NO_3^- as a function of atmospheric supply flux with UV photolysis and reduction by Fe^{2+} to nitrogenous gas as the sinks, in the ocean and in a pond. The pond parameters ($d = 10 \text{ cm}$, $\text{DR} = 100$) are favorable for NO_x^- accumulation, and hence should be considered an optimistic scenario. The horizontal dashed line demarcates micromolar concentrations, the putative boundary concentration for prebiotic relevance. The grey shaded area corresponds to the range of $\phi_{\text{NO}_x^-}$ calculated by Wong et al. [379].

temperature is unclear). Thus, $\text{pH} \approx 6$ probably represents a minimum on thermal loss of NO_2^- .

4.3 THERMOCHEMICAL EQUILIBRIUM

In this section, we examine the stability of NO_3^- and NO_2^- in the anoxic early Earth environment under the assumption of thermal equilibrium. The purpose of this analysis is to test the implicit assumption of previous work that these molecules are stable in prebiotic waters absent processing at vents. Whether or not thermal equilibrium is achieved depends upon kinetic considerations. However, while our understanding of nitrogen kinetics in prebiotic natural waters may be incomplete (since we do not have an anoxic, prebiotic Earth-analog atmosphere-ocean system to study to confirm we have identified all relevant reactions), our equilibrium analysis depends only on known thermodynamic parameters, and hence is robust.

We consider the general speciation of nitrogen in a reducing atmosphere-ocean system as present on early Earth, with H_2 as our reductant ($\text{pH}_2 \geq 1 \times 10^{-3}$ bar on early Earth; Kasting [155]). We balance the nitrogen-converting redox half reactions with H_2 oxidation and take this to physically represent the amount of "reducing power" in the environment, even though the system could obtain its reducing power from other half reactions, e.g., Fe(II) oxidation. pN_2 on early Earth is known to have been comparable to present-day levels ($0.5 < \text{pN}_2 < 1.1$ bar, Marty et al. [189]). We consider an initial atmosphere-ocean system with atmospheric $\text{pN}_2 = 1.1$ bar, oceanic $[\text{N}_2]$ in equilibrium with the atmosphere (i.e. saturated in N_2), and no other initial carrier of N. We assume an N_2 -dominated atmosphere and ocean volume equal to modern. Then, the total inventory of nitrogen atoms N_N in the atmosphere/ocean system is:

$$N_N = 2 \times ([\text{N}_2]V_{\text{ocean}} + \left(\frac{\text{pN}_2}{\mu\text{g}}\right)(4\pi R_{\text{Earth}}^2)) \quad (4.11)$$

Species	ΔG_f° (kJ/mol)	Reference
NO_3^- (aq)	-111.3	Rumble [287]
NO_2^- (aq)	-32.2	Rumble [287]
NH_4^+ (aq)	-79.5	Rumble [287]
NO (g)	87.6	Rumble [287]
N_2O (g)	103.7	Rumble [287]
N_2 (g)	0	Rumble [287]
N_2 (aq)	18.8	Amend and Shock [5]
O_2 (g)	0	Rumble [287]
O_2 (aq)	16.54	Amend and Shock [5]
H_2 (g)	0	Rumble [287]
H_2 (aq)	17.72	Amend and Shock [5]
H_2O	-237.1	Rumble [287]
H^+	0	Rumble [287]

Table 4.3.1: Gibbs free energies of formation under standard conditions (ΔG_f°) for the species considered in this work.

Here, $V_{ocean} = 1.4 \times 10^{21}$ L is the volume of the ocean [248], $\mu = 28$ g/mol is the mean molecular mass of the N_2 -dominated atmosphere, and $g = 981$ cm s⁻² is the acceleration due to gravity. From Henry's Law, $[\text{N}_2] = H_{\text{N}_2} p_{\text{N}_2}$, where $H_{\text{N}_2} = 6.4 \times 10^{-4}$ M bar⁻¹ (Table 4.3.4). Then, $N_{\text{N}} = 4 \times 10^{20}$ mol, comparable to present atmospheric N [144].

We allow this N_2 to relax to equilibrium under a range of pH_2 and pH , and calculate the speciation of nitrogen compounds at equilibrium. To do this, we consider the possible reactions between the nitrogen species by balancing the individual half reactions for interconverting nitrogen species with H_2 oxidation, and calculate cell potentials and logK for each reaction (see also 4.7). We identified the reactions of each species with H_2 with the largest logK; they are tabulated in Table 4.3.2. The Gibbs free energies of formation used in this study, ΔG_f° , are compiled in Table 4.3.2.

We use these reactions to set up equations for concentrations at equilibrium using the definition of the equilibrium constant:

Reaction	ΔG_{rxn}° (kJ/mol)	E_{cell}° (V)	log K
$2NO_3^- + 12H^+ + 10e^- \rightarrow N_2 + 6H_2O$			
$2NO_3^- + 2H^+ + 5H_2 \rightarrow N_2 + 6H_2O$	-1202	1.25	210.4
$2NO_2^- + 8H^+ + 6e^- \rightarrow N_2 + 4H_2O$			
$2NO_2^- + 2H^+ + 3H_2 \rightarrow N_2 + 4H_2O$	-879.6	1.52	154.0
$NO + 6H^+ + 5e^- \rightarrow NH_4^+ + H_2O$			
$2NO + 2H^+ + 5H_2 \rightarrow 2NH_4^+ + 2H_2O$	-403.3	0.84	141.9
$N_2O + 10H^+ + 8e^- \rightarrow 2NH_4^+ + H_2O$			
$N_2O + 2H^+ + 4H_2 \rightarrow 2NH_4^+ + H_2O$	-499.7	0.65	87.5
$N_2 + 8H^+ + 6e^- \rightarrow 2NH_4^+$			
$N_2 + 2H^+ + 3H_2 \rightarrow 2NH_4^+$	-159.0	0.27	27.8

Table 4.3.2: Half reactions and full cell reactions (balanced with H_2 oxidation) with the maximum logK's for the nitrogen species considered in this study. ΔG_{rxn}° , E_{cell}° , and log K were calculated using the standard expressions.

$$K_1 = \frac{[N_2]}{[NO_3^-]^2[H^+]^2[H_2]^5} \quad (4.12)$$

$$K_2 = \frac{[N_2]}{[NO_2^-]^2[H^+]^2[H_2]^3} \quad (4.13)$$

$$K_3 = \frac{[NH_4^+]^2}{[NO]^2[H^+]^2[H_2]^5} \quad (4.14)$$

$$K_4 = \frac{[NH_4^+]^2}{[N_2O][H^+]^2[H_2]^4} \quad (4.15)$$

$$K_5 = \frac{[NH_4^+]^2}{[N_2][H^+]^2[H_2]^3} \quad (4.16)$$

NO_3^- , NO_2^- , and NH_4^+ undergo further acid/base equilibration, with partitioning governed by the reaction pKa's (Table 4.3.3):



$$K_a = \frac{[H^+][A^-]}{[HA]} = 10^{-pKa} \quad (4.18)$$

Where A^- is the acid and HA its conjugate base.

Aqueous HNO_3 , HNO_2 , NO , N_2O , N_2 , NH_3 exist in equilibrium with their gaseous forms, with partitioning specified by Henry's Law (Table 4.3.4; Sander [296]):

Reaction	pKa	Reference
$HNO_3 \leftrightarrow H^+ + NO_3^-$	-1.38	Dean [73]
$HNO_2 \leftrightarrow H^+ + NO_2^-$	3.25	Rumble [287]
$NH_4^+ \leftrightarrow H^+ + NH_3$	9.25	Rumble [287]

Table 4.3.3: pKa's for relevant dissociations of acids/bases in the redox network to their corresponding conjugate base/acid.

$$[X] = H_X pX \quad (4.19)$$

Where H_X is the Henry's Law constant for species X , and pX its partial pressure.

Species	H (M/bar)	Reference
HNO_3	2.6×10^6	Chameides [43]
HNO_2	5×10^1	Chameides [43]
NO	1.9×10^{-3}	Schwartz and White [304]
N_2O	2.4×10^{-2}	Sander [296]
N_2	6.4×10^{-4}	Sander [296]
H_3	6×10^1	Kavanaugh and Trussell [157]
O_2 (g)	1.3×10^{-3}	Sander [296]
H_2 (g)	7.8×10^{-4}	Sander [296]

Table 4.3.4: Henry's Law constants (H) under standard conditions and zero salinity for the species considered in this analysis in aqueous solution.

Finally, we have the mass balance constraint that the sum of nitrogen atoms across all species equals the initial nitrogen inventory N_N :

$$\begin{aligned}
N_N = & ([NO_3^-] + [NO_2^-] + [NO] + 2[N_2O] + 2[N_2] + [NH_4^+] \\
& + [HNO_3] + [HNO_2] + [NH_3])V_{ocean} \\
& + \frac{pHNO_3 + pHNO_2 + pNO + 2pN_2O + 2pN_2 + pNH_3}{\mu g} (4\pi R_{Earth}^2) \quad (4.20)
\end{aligned}$$

Taken together, this system provides us with 15 equations, 15 unknowns ($[NO_3^-]$, $[NO_2^-]$, $[NO]$, $[N_2O]$, $[N_2]$, $[NH_4^+]$; $[HNO_3]$, $[HNO_2]$, $[NH_3]$; $pHNO_3$, $pHNO_2$, pNO , pN_2O , pN_2 , pNH_3), and 3 prescribed conditions ($[H^+]$, $[H_2]$, N_N). We solve this system of equations for a range of pH ($[H^+]$) and reducing powers ($[H_2]$) for $N_N = 4 \times 10^{20}$ mol. We compute the fraction of atoms of N stored in each species (Figure 4.3.1).

Figure 4.3.1 shows the speciation of nitrogen by redox state. The two oxidation states of nitrogen favored under plausible hydrogen concentrations are (-3) and (0), corresponding to NH_3/NH_4^+ and N_2 , respectively. N_2 , which is favored at $[H_2] \leq 10^5$ M, will partition mostly into the atmosphere. The distribution of NH_4^+ , NH_3 (aq), and NH_3 (g) depends on the pH of the aqueous solution. The concentration of NO_3^- and NO_2^- is sub-picomolar over the scenarios considered here. These findings are insensitive to variations in pK, pKa, and H_X from $T = 2 - 45^\circ$ C, and variations in H_X due to salinity from $[NaCl] = 0 - 1$ M; see SI Section S3 for details.

Overall, nitrate and nitrite are thermally unstable in the reducing conditions available on early Earth. If allowed to reach equilibrium, under most conditions NO_X^- will relax to a gaseous species like N_2 . This result is consistent with Van Cleemput and Baert [361], who concluded that NO_2^- in anoxic soils should decay, generally to N_2 . The situation on reducing prebiotic Earth is very different from the situation on oxidizing modern Earth, where in equilibrium NO_X^- is thermodynamically favored [161]. Our thermochemical analysis confirms our kinetic analysis that previous work has overestimated prebiotic $[NO_X^-]$, increasing our confidence in this conclusion.

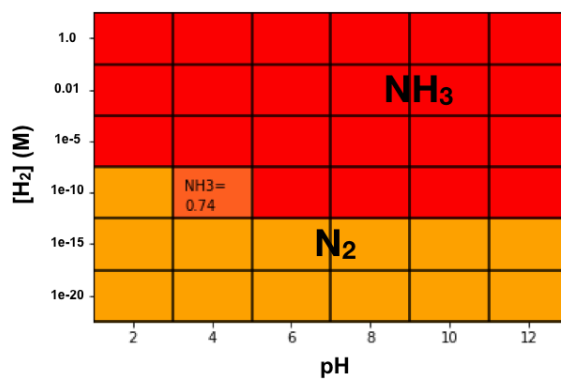


Figure 4.3.1: Favored nitrogen species as a function of pH and hydrogen concentration. At high reducing powers ($\geq 10^{-5}$ M H₂), at thermodynamic equilibrium, nitrogen will go to the (-3) oxidation state, i.e. NH₃ or NH₄⁺. Below this reducing power, the favored state of nitrogen is N₂, which partitions mainly to the atmosphere. At pH= 4 and [H₂]= 10⁻¹⁰ M, N₂ and NH₃ coexist. Lower H₂ concentrations are disfavored in conventional models of early Earth and not included in the analysis [150].

4.4 DISCUSSION

4.4.1 $[\text{NO}_X^-]$ IN THE PREBIOTIC OCEANS

Previous work has concluded that $[\text{NO}_X^-]$ in the prebiotic oceans was high, on the assumption that the dominant sink of NO_X^- in the prebiotic ocean was processing at hydrothermal vents and that it was otherwise stable in the ocean [166, 379]. However, NO_X^- is thermodynamically unstable in reducing environments. UV photolysis and reduction by Fe^{2+} are much stronger sinks than processing at vents, and restrict NO_X^- to orders of magnitude lower concentrations than previously suggested. Reduction by Fe^{2+} and UV photolysis suppresses NO_X^- to sub-micromolar concentrations across most of the plausible parameter space. $> 1 \mu\text{M } \text{NO}_X^-$ requires $\phi_{\text{NO}_X^-} > 1 \times 10^9 \text{ cm}^{-2} \text{ s}^{-1}$, higher than has been suggested in the literature. Achieving such high $\phi_{\text{NO}_X^-}$ requires some combination of a high lightning flash rate, high $p\text{CO}_2$, and low $p\text{N}_2/p\text{CO}_2$. The required $p\text{CO}_2$ and $p\text{N}_2$ are not favored by the available geochemical evidence, and we lack a robust prescription for global lightning flash rates, leading us to disfavor this possibility. Consequently, prebiotic oceanic NO_X^- was likely sub-micromolar.

Wong et al. [379] point out that Fitzsimmons et al. [100] have detected dissolved iron thousands of kilometers from hydrothermal sources, and suggest that the survival of this iron for such large distances on NO_X^- rich modern Earth means that Fe^{2+} oxidation, by NO_X^- and other oxidants is inefficient. However, Fitzsimmons et al. [100] also point out that only 0.02 – 1% of hydrothermal Fe survives transport over these distances in the dissolved phase, meaning that the vast majority of hydrothermal Fe is oxidized. Moreover, the Fe that does avoid oxidation is thought to do so by forming colloids and/or by complexing with organic ligands [100, 124, 297, 344]. In other words, hydrothermal Fe appears to survive long-distance transport because it is protected by complexing, mineralization, and colloidation, not because its reactions with oxidants are inefficient. Additionally, mineralized Fe^{2+} is typically a more effective reductant

than dissolved Fe^{2+} [78, 121, 321]. We consequently argue that it is not possible to dismiss reduction by Fe^{2+} as a sink on NO_x^- , especially in light of evidence that Fe^{2+} levels were high on early Earth.

4.4.2 $[\text{NO}_x^-]$ IN PREBIOTIC PONDS

As in the oceans, reduction by Fe^{2+} and photochemical loss are major sinks of NO_x^- . However, since ponds are much shallower than oceans, the impact of thermal reactions is muted, and UV photolysis is proportionated more important.

$[\text{NO}_x^-]$ could have been above oceanic in shallow ponds ($d \lesssim 3$ m) with large DR and short transit times. Shallow ponds permit higher NO_x^- buildup because NO_x^- destruction processes have a shorter column over which to operate. Large drainage ratios permit ponds to collect NO_x^- rainout from a larger area. Short transit times minimize the probability the NO_x^- will decay en route due to encounters with reductants in the soil. For a pond with $d = 10$ cm, $\text{DR} = 100$, and fast drainage, $[\text{NO}_x^-]$ can build up to micromolar concentrations for $\phi_{\text{NO}_x^-} \geq 4 \times 10^7 \text{ cm}^{-2} \text{ s}^{-1}$, and at lower $\phi_{\text{NO}_x^-}$ if the pond is cold and acidic. For $\phi_{\text{NO}_x^-} = 6.5 \times 10^8 \text{ cm}^{-2} \text{ s}^{-1}$, $[\text{NO}_x^-]$ can build up to near-millimolar concentrations in such a lake.

We consider whether such a pond is plausible. A study of water bodies in southern England indicated that the ratio between the total catchment area and total surface area for lakes and ponds was 14 and 500, respectively, and a study of boreal lakes in Sweden found DR as high as 1000, indicating $\text{DR} = 100$ to be plausible [71, 319]. Assuming neutral, room-temperature groundwaters with $[\text{Fe}^{2+}] \leq 10^{-4} \text{ M}$, the lifetime of NO_x^- is ≥ 400 days, implying transit times ≤ 400 days are required to ensure negligible decay of NO_x^- during transport. Catchment transit times ≤ 400 days exist, particularly for smaller catchments, but are not universal, indicating that only a subset of ponds will meet this criterion [30, 32, 197, 282]. Further, if present, mineralized Fe^{2+} in the ground may more efficiently reduce NO_x^- [78]. These challenges will be avoided in terrain where rain is immediately lost to the pond as surface runoff; this is especially likely to

occur in catchments in bare, rocky terrain [175]. Ponds with high concentrations of NO_x^- do exist on modern Earth, as predicted from our modeling; an example is Don Juan Pond, which is thought to be abiotic and which features $[\text{NO}_x^-] = 6$ mM [295]. In summary, ponds with high $[\text{NO}_x^-]$ should have existed on early Earth, but were probably not typical; hence, pond prebiotic chemistries which require high NO_x^- must specify such a pond as part of their scenario.

4.4.3 IMPLICATIONS FOR PREBIOTIC CHEMISTRY

Oceanic NO_x^- could only have achieved prebiotically relevant levels if atmospheric supply rates were very high. Achieving $[\text{NO}_x^-] \geq 1 \mu\text{M}$ requires $\phi_{\text{NO}_x^-} \geq \times 10^9 \text{ cm}^{-2} \text{ s}^{-1}$, which requires some combination of high flash rates, high $p\text{CO}_2$, and low $p\text{N}_2/p\text{CO}_2$. These conditions are not at present favored in the literature (Krissansen-Totton et al. [162], Marty et al. [189], Wong et al. [379]). Consequently, oceanic NO_x^- -dependent origin-of-life scenarios (e.g., those that invoke NO_x^- as electron acceptors at deep-sea hydrothermal vents; Ducluzeau et al. [81], Nitschke and Russell [227], Shibuya et al. [311]) must invoke either extreme planetary parameters, or local circumstances which can concentrate $[\text{NO}_x^-]$ levels beyond the oceanic mean.

NO_x^- could have achieved above-oceanic concentrations in favorable pond environments, i.e. ponds with large DR and short catchment transit times. Low temperatures and acidic pH would also favor NO_x^- buildup, especially as NO_3^- . $[\text{NO}_x^-]$ could be even higher at polar latitudes where photolysis rates are suppressed by low UV surface radiances due to larger solar zenith angles [260]. Such a pond would be able to sustain $[\text{NO}_x^-] \geq 1 \mu\text{M}$ across most of the range of $\phi_{\text{NO}_x^-}$ calculated by Wong et al. [379]. Such ponds are plausible but not typical, and hence must be explicitly invoked when considering NO_x^- -dependent pond prebiotic chemistries. Their non-universality must also be considered when estimating the plausibility of NO_x^- -dependent prebiotic chemistries.

NO_3^- is orders of magnitude more stable than NO_2^- . This suggests that in both lake and oceanic environments, prebiotic NO_x^- should have existed primarily as

NO_3^- , as in natural waters on modern Earth and in experimental studies of abiotic nitrogen fixation [335]. Consequently, NO_3^- -utilizing prebiotic chemistries are more plausible than NO_2^- -dependent prebiotic chemistries, and prebiotic chemists should consider using NO_3^- instead of NO_2^- in their studies.

In this work, we have focused on concentrations of NO_2^- and NO_3^- , under the broad category of NO_X^- . We have ignored more complex derivatives of these compounds. For example, Mariani et al. [184] point out that under UV irradiation, NO_3^- , Fe, and HCN combine to yield nitroprusside, a compound in which NO_X^- is protected from reduction by Fe^{2+} and which is stable in the dark on a timescale of ≥ 5 months. However, nitroprusside is unstable to irradiation by the visible light which accompanies UV irradiation, though this may be due to the more rapid degradation of nitric oxide (NO) following photodissociation of nitroprusside in the oxygenic atmosphere of modern Earth [301, 363, 364, 378]. Measurements of the kinetics of nitroprusside formation and destruction under prebiotically relevant conditions are required to determine the range of plausible steady-state concentrations of nitroprusside in prebiotic natural waters.

We note in passing that the prospects for abiotic NO_X^- buildup may be enhanced on planets orbiting M-dwarfs, due to their much lower surface UV irradiation and consequently much slower NO_X^- photolysis rate [262]. Consequently, NO_X^- -dependent prebiotic chemistries may proceed especially well on such worlds relative to early Earth.

4.4.4 VALIDITY OF SIMPLIFYING ASSUMPTIONS

In this work, we have approximated the activity of ionic species (e.g., NO_3^- , H^+) by their concentrations, neglecting the effects of ion-ion and ion-water interactions on their reactivity. For the species relevant to this work, the activity coefficient $\gamma_c \geq 0.26$ for solutions with ionic strengths $I \leq 1$ (see 4.6). For context, the ionic strength of the modern oceans is $I = 0.7$, and studies of fluid inclusions in quartz suggests that Archean ocean salinity was \lesssim modern [191, 287]). Our order-of-magnitude conclusions are insensitive to such

variations, motivating this simplifying assumption.

Van Cleemput and Baert [362] suggest that the kinetics of NO_2^- reduction by Fe^{2+} are second-order with respect to nitrite concentrations at acidic pH. We repeated our analysis assuming second-order dependence on $[\text{NO}_2^-]$; our conclusions were unchanged, indicating our analysis is insensitive to this possibility.

Our photolysis calculations assume photolysis rate constants equal to the modern value. While shortwave surface UV irradiation (200 – 300 nm) on anoxic early Earth was much higher than on modern Earth, surface UV irradiation over the full UV range (200 – 400 nm) was 20% lower on prebiotic Earth compared to modern Earth, suggesting we may slightly overestimate the photolysis rate [260]. However, (1) our conclusions are robust to variations in photolysis rate of a few tens of percent, and (2) the magnitude of NO_x^- photolysis is sensitive to the action spectrum of NO_x^- photolysis; if shorter wavelengths are much more effective at photolyzing NO_x^- , then our methods may underestimate photolysis rates [50, 56, 259]. Further measurements of the action spectrum of NO_x^- photolysis are required to rule on this possibility.

Our calculations assumes all NO_x^- entering the ocean goes to NO_x^- and neglects reactions of NO_x^- with other reductants which may have been abundant on early Earth, such as H_2 , CH_4 , or Mn^{2+} [98, 347, 398]. Consequently, our estimates should be considered upper bounds on prebiotic $[\text{NO}_x^-]$.

This box-model approach we have taken averages over the entire natural water body under consideration. This approach permits us to place bounds on the mean concentrations of NO_x^- in prebiotic natural waters with minimal assumptions, and is in line with past work (e.g., Laneuville et al. [166], Wong et al. [379]). This approach is a good approximation to well-mixed shallow lakes and ponds. However, the oceans are not necessarily well-mixed; $[\text{NO}_x^-]$ may be a function of depth. Resolved, 1D models are required to probe this effect; mean oceanic concentration should be similar, but NO_x^- concentrations should be higher at the surface where it is supplied and lower at depth. In summary, our approach suffices for NO_x^- estimates in ponds, and for estimates of the mean

NO_x^- concentration in the ocean, but resolving the heterogeneity of the ocean requires higher-dimensional models.

4.4.5 IMPORTANCE OF BETTER KINETIC CONSTRAINTS

Measurements of NO_x^- kinetics under conditions relevant to the early Earth are scarce. While our calculations are motivated by and consistent with available data, improved measurements of these kinetics can decrease the uncertainty in these calculations and improve the confidence of these results. In particular: (1) the literature contains contradictory reports as to whether uncatalyzed NO_3^- reduction by Fe^{2+} is significant at room temperature [235, 247]. Experimental studies are required to resolve the dichotomy between these studies; if this process is indeed significant, as Ottley et al. [235] report, then oceanic NO_3^- concentrations would be suppressed to concentrations lower than we model here. (2) The activation energy for reduction of NO_2^- by Fe^{2+} is not known; knowledge of this quantity would enable tighter constraints on $k_{\text{NO}_2^-, \text{Fe}^{2+}} > 0$. (3) The rate constants for Fe^{2+} reduction used in this work are generally derived from measurements made at larger $[\text{Fe}^{2+}]$ than thought to have been available on early Earth. Determination of these rate constants at prebiotically plausible $[\text{Fe}^{2+}]$ (10 – 600 μM) under early Earth conditions (e.g., anoxia) could confirm the applicability of these rate constants at lower $[\text{Fe}^{2+}]$. The extension of studies like Stanton et al. [326] for NO kinematics to NO_x^- kinematics could improve the precision and potentially accuracy of this work. (4) Measuring the rate constant of NO_x^- photolysis in simulated prebiotic natural waters, under irradiation by a source simulating the prebiotic UV environment in both magnitude and spectral shape, could directly verify our extrapolation from modern photolysis rates, and in particular could confirm whether the shorter-wavelength UV radiation available on early Earth would affect overall reaction rates.

4.5 CONCLUSIONS

Constraining the abundance of trace chemical species on early Earth is relevant to understanding the plausibility and guiding the development of proposed prebiotic chemistries. In this work, we have used box-model kinetic calculations to constrain the plausible range of NO_2^- and NO_3^- concentrations in oceans and ponds on prebiotic Earth.

Prebiotic oceanic NO_X^- was likely much lower than calculated in previous work [166, 379] due to UV photolysis and reactions with Fe^{2+} . Oceanic NO_X^- could only have built up to $\geq 1 \mu\text{M}$ in an extremal realm of parameter space, in particular if the NO_X^- supply flux was much higher than currently favored in the literature. Consequently, origins-of-life scenarios which require elevated NO_X^- in the ocean must invoke either an extremal planetary conditions, or specialized local conditions which concentrate NO_X^- above the oceanic mean. NO_X^- was not an inevitable part of the prebiotic milieu, and the prebiotic plausibility of oceanic origin-of-life scenarios can be improved by utilizing alternative feedstocks, e.g. an alternative electron donor for protometabolism [81].

Prebiotic NO_X^- could have built above oceanic levels in shallow ponds with large, fast-draining catchment areas. Such environments should have been extant but likely uncommon. In these environments, NO_X^- could have built up to prebiotically relevant levels ($\geq 1 \mu\text{M}$) over a much broader range of planetary parameters than in the ocean, and in particular over most (but not all) of the proposed range of NO_X^- supply flux. Consequently, NO_X^- -dependent prebiotic chemistries which can function in shallow ponds (e.g., Mariani et al. [184]) are prebiotically plausible, with the caveat that they impose requirements on the environment. Near-millimolar NO_X^- concentrations are possible if the NO_X^- supply flux was at the upper end of what has been proposed in the literature ($\phi_{\text{NO}_X^-} \geq 6.5 \times 10^8 \text{ cm}^{-2} \text{ s}^{-1}$), and if the pond were cool and mildly acidic. This finding is in line with past work which suggests shallow lakes/ponds to be especially compelling venues for origin-of-life chemistry [217, 240, 263]. We emphasize that our estimates are upper bounds; if a significant fraction of input

NO_X^- failed to go to NO_X^- , or reactions with other reductants present on early Earth were significant compared to the processes considered here, $[\text{NO}_X^-]$ would have been proportionately lower.

For both oceanic and pond environments, NO_X^- -dependent prebiotic chemistries that can function at lower $[\text{NO}_X^-]$ are more prebiotically plausible. Similarly, prebiotic chemistries that utilize NO_3^- are more plausible than those which utilize NO_2^- , since most NO_X^- should be present as NO_3^- due to its greater stability.

Our analysis could be most improved by better characterization of NO_X^- reaction kinetics under prebiotically-relevant conditions, especially its reduction by Fe^{2+} and Mn^{2+} and its reduction by UV in prebiotic natural waters (e.g., the extension of studies like Stanton et al. [326] to NO_X^-). Studies with higher-dimensional models could also help determine if there exist areas in the ocean which should have concentrated NO_X^- above the oceanic mean, perhaps to prebiotically-relevant levels.

Acknowledgements We thank Jonathan Toner for help with PHREEQC and insights regarding activity coefficients and diffusion. We thank Joshua Krissansen-Totton for a tutorial on his code and discussions about thermal equilibrium. We thank Scott Wankel, Taylor Perron, Sam Goldberg, William Bains, Craig Walton, and Sara Seager for helpful discussions. We thank Peter Gao, Matthie Laneuville, and Oliver Zafiriou for answers to questions. We thank the MIT Libraries for heroic efforts in uncovering very old, very obscure papers. We thank Jim Kasting, Jennifer Glass, Chris McKay, and Janne Blichert-Toft for feedback which substantively improved this paper. Z. R. T. and D. D. S. thank the Harvard Origins of Life Initiative. This research has made use of NASA's Astrophysics Data System. This work was supported by grants from the Simons Foundation (SCOL grant 495062 to S. R.; grant 290360 to D. D. S.) and support from an MIT startup (A. R. B.). P. B. R. thanks the Simons Foundation and Kavli Foundation for funding. The software used to carry out our calculations is available for validation and extension at the website (<https://github.com/sukritranjan/nox.git>).

4.6 APPENDIX A: ACTIVITY COEFFICIENT CALCULATION

This section describes the activity coefficient calculation of ions considered during the reactions of nitrogen species with each other and other environmental ions.

The activity coefficients (γ_i) are calculated using various theories for different ionic strength regimes. Extended-Debye Huckel (EDH) Theory is used for ionic strengths up to 0.1 M, while Davies theory extends to 0.5 M, and Truesdell-Jones (TJ) can be used up to 1 M. The Extended Debye-Huckel Theory states:

$$\log(\gamma_i)^- = Az_i^2 \frac{I^{0.5}}{1 + Ba_i I^{0.5}} \quad (4.21)$$

Davies theory states:

$$\log(\gamma_i)^- = Az_i^2 \frac{I^{0.5}}{1 + I^{0.5}} - 0.3I \quad (4.22)$$

Truesdell-Jones theory states:

$$\log(\gamma_i)^- = Az_i^2 \frac{I^{0.5}}{1 + Ba_i^{\circ} I^{0.5}} + b_i I \quad (4.23)$$

where A and B are constants that depend on the temperature, density, and dielectric constant of the solvent (e.g. water). a_i is the effective radius of an ion, which varies from species to species. a_i° and b_i are ion-specific parameters measured for Truesdell-Jones theory. These parameters are not easily available for the ions we consider, so we assume that $b_i \approx 0.1^2$ and that $a_i = a_i^{\circ}$. We use $A = 0.5085M^{-1/2}$ and $B = 3.281M^{-1/2}nm^{-1}$, the values for $T = 25^{\circ}C$. Table 4.6.1 shows the a_i for EDH theory, from Misra (2012) and the activity coefficients at $I=1$ M, calculated from Truesdell-Jones theory given our assumptions. $\gamma_i \geq 0.26$ for the species considered in our study (Figure 4.6.1); our results are robust to

²<http://www.aqion.de/site/101>, accessed June 21, 2018

such variations, motivating us to neglect activity corrections in our calculations.

4.7 APPENDIX B: REDOX CALCULATION

In this section, we describe the details of the redox calculations, including the set of reactions considered and the ΔG_{rxn}° , E_{cell}° , and $\log K$ used in calculating the thermodynamics of these reactions.

The ΔG_{rxn}° can be calculated from the Gibb's free energy of formation (ΔG_f°) as:

$$\Delta G_{rxn}^\circ = \Sigma \Delta G_{f,products}^\circ - \Sigma \Delta G_{f,reactants}^\circ \quad (4.24)$$

From ΔG_{rxn}° the reaction cell potential can be calculated as:

$$\Delta G = -nFE_{cell}^\circ, \quad (4.25)$$

where n is the number of moles of electrons transferred in the balanced redox reaction, F is Faraday's constant ($96,485\text{C/mol}$), and E_{cell}° is the cell potential in volts.

The equilibrium constant can be related to the cell potential through the Nernst Equation (at $T = 25^\circ\text{C}$):

$$\log K = \frac{nE^\circ}{0.0592\text{V}} \quad (4.26)$$

We use the above equations to calculate the ΔG_{rxn}° , E_{cell}° , and $\log K$. A negative ΔG_{rxn}° and positive E_{cell}° indicate spontaneous reactions. The larger the $\log K$, the more favored the reaction.

Ion	a_i (nm)	γ_i
NO_3^- , NO_2^-	0.3	0.70
NH_4^+	0.25	0.66
Fe^{2+}	0.6	0.26
H^+	0.9	0.94

Table 4.6.1: List of relevant ions and their EDH parameters used in activity coefficient calculations, when relevant. We also show the activity coefficient at the highest ionic strength ($I=1$ M) that we consider here (as calculated by Truesdell-Jones theory and with the above-specified assumptions).

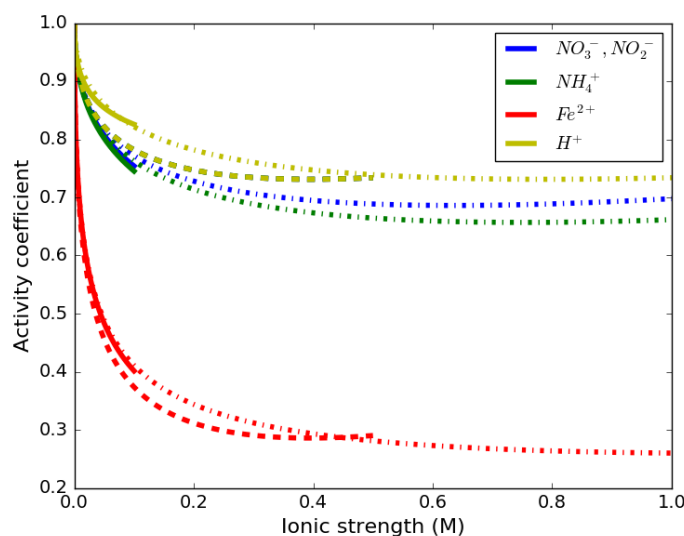


Figure 4.6.1: Activity coefficients as a function of ionic strength for the various species considered here. The solid lines show EDH theory (valid to 0.1 M); the dashed lines show Davis theory (valid to 0.5 M); and the dot-dash lines show Truesdell-Jones theory (valid to 1 M). At higher ionic strengths, the activity of ions decreases. Various ions have different effective radii, leading to distinct activity coefficients for ions of different radius.

4.8 APPENDIX C: REDOX CALCULATION SENSITIVITY ANALYSIS

The analysis presented in 4.3 was performed under the assumptions of standard conditions and zero salinity. Here, we explore the sensitivity of our results to these assumptions, and show that our results are robust to $T = 2 - 45^\circ \text{C}$ and $[\text{NaCl}] = 0 - 1 \text{ M}$.

4.8.1 SENSITIVITY ANALYSIS TO TEMPERATURE

To assess the sensitivity of our calculations to temperature, we repeat our Gibbs free energy calculations at temperatures spanning $T = 2 - 45^\circ \text{C}$.

Table 4.8.1 tabulates $\Delta G_f^{T,P_{\text{sat}}}$ for the species in our analysis at various temperatures, from Amend and Shock [5]:

In 4.8.2, we calculate the equilibrium constants of our reactions we identified from their $\Delta G_{\text{rxn}}^{T,P_{\text{sat}}}$, following the procedure described in SI Section S??:

Figures 4.8.1 and ?? show the results of the thermodynamic calculation at 2 and 45°C , respectively. The only case where temperature makes a difference in the speciation of nitrogen at redox equilibrium is the $[\text{H}_2 = 1.0 \times 10^{-10} \text{ M}]$, $\text{pH}=4$ case. In this state, nitrogen coexists in the (-3) and (0) oxidation states. The fraction of each species depends on temperature, with higher temperatures favoring N(0). $[\text{NO}_X^-]$ remains in the picomolar range across each of these scenarios.

4.8.2 SENSITIVITY OF pKa TO TEMPERATURE

We investigate the dependence of pKa on temperature. We tabulate the Gibbs free energies of formation for the relevant species as a function of temperature and then calculating the ΔG_{rxn} and pKa. Table 4.8.3 shows these values, all taken from Amend and Shock [5].

Species	$T = 2^{\circ}\text{C}$	$T = 18^{\circ}\text{C}$	$T = 37^{\circ}\text{C}$	$T = 45^{\circ}\text{C}$
NO_3^- (aq)	-107.5	-109.9	-112.7	-113.8
NO_2^- (aq)	-29.3	-31.4	-33.7	-34.6
NO (aq)	104.6	102.9	100.6	99.5
N_2O (aq)	115.8	114.2	111.9	110.9
N_2 (aq)	20.2	18.8	17.0	16.12
NH_4^+ (aq)	-77.0	-78.7	-80.8	-81.7
H_2 (aq)	18.9	18.1	17.0	16.5
H_2O (l)	-235.6	-235.7	-238.0	-238.6
H^+ (aq)	0	0	0	0

Table 4.8.1: $\Delta G_f^{T,P_{\text{sat}}}$ (kJ/mol) for the species considered in this analysis, at various temperatures, from Amend and Shock [5].

Reaction	$T = 2^{\circ}\text{C}$	$T = 18^{\circ}\text{C}$	$T = 37^{\circ}\text{C}$	$T = 45^{\circ}\text{C}$
1	222.9	222.7	222.5	222.4
2	161.2	161.0	160.9	160.8
3	162.6	162.3	161.7	161.4
4	101.7	101.7	101.5	101.3
5	40.4	40.4	40.2	40.1

Table 4.8.2: logK of selected dominant reactions as a function of temperature.

Species	$T = 2^{\circ}\text{C}$	$T = 18^{\circ}\text{C}$	$T = 25^{\circ}\text{C}$	$T = 37^{\circ}\text{C}$	$T = 45^{\circ}\text{C}$
NO_3^-	-107.45	-109.87	-110.91	-112.66	-113.82
HNO_3	-99.44	-102.23	-103.47	-105.64	-107.1
NO_2^-	-29.28	-31.35	-32.22	-33.67	-34.62
HNO_2	-47.53	-49.68	-50.63	-52.26	-53.36
NH_3	-24.30	-25.96	-26.71	-28.02	-28.92
NH_4^+	-76.96	-78.68	-79.45	-80.81	-81.72
H^+	0	0	0	0	0

Table 4.8.3: $\Delta G_f^{T,P_{\text{sat}}}$ for the species considered in this analysis, at various temperatures, from Amend and Shock [5].

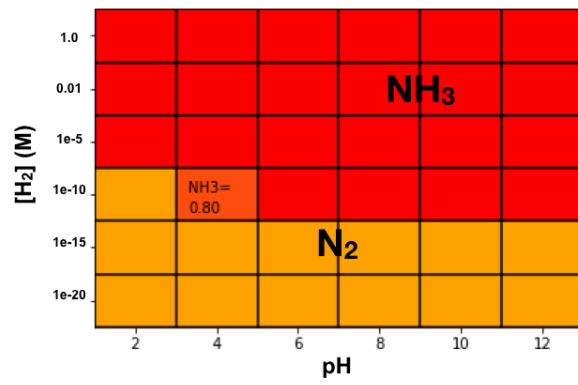


Figure 4.8.1: Speciation of N at $T = 2^\circ\text{C}$.

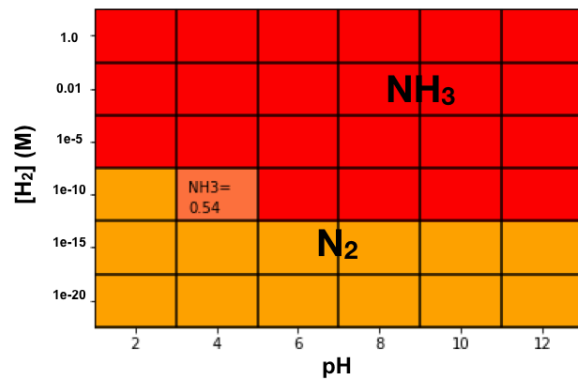


Figure 4.8.2: Speciation of N at $T = 45^\circ\text{C}$.

From the values in Table 4.8.3, we calculated the ΔG_{rxn} and hence the pKa's for the acid dissociation reactions of HNO_3 , HNO_2 , and NH_4^+

$$K_a = \exp\left(\frac{-\Delta G}{RT}\right) \quad (4.27)$$

The pKa's for these three acid dissociations are tabulated as a function of temperature in table 4.8.4. These values differ slightly from the literature values at $T = 25^\circ\text{C}$ from Rumble [287]. Our results are insensitive to these small variations.

4.8.3 SENSITIVITY OF HENRY'S LAW CONSTANTS TO SALINITY

Salinity decreases the solubility of gases. We parametrize the impact of salinity on H via the Schumpe-Sechenov method (e.g. Burkholder et al. [36]).

$$\log H_o/H = \sum_i (h_i + h_G) \times c_i, \quad (4.28)$$

where H_o and H are the Henry's law constants in pure water and a saline solution, respectively, c_i is the concentration of ion i , h_i is constant for a given ion, and h_G is constant for a given gas. The h_G parameter can in principle, depend on temperature, as $h_G = h_o + h_T(T - 298.15\text{K})$; since the purpose of this study was to understand the impact of salinity alone, we neglected the temperature dependence of h_G and set $h_G = h_o$ for all species. Table 4.8.5 shows the values of these parameters, from Burkholder et al. [36].

We assume that NaCl is the only source of salinity, as this species dominates in Earth's oceans. Figure ?? shows the fractional dependence of the Henry's Law constant of gas X , H_X , on salinity, over up to an ionic strength of 1 M, exceeding $[\text{NaCl}] = 0.6\text{M}$ in the modern ocean. H_X decreases with increasing salinity for each of the gaseous species considered, but the effect is $< 20\%$ at the extreme;

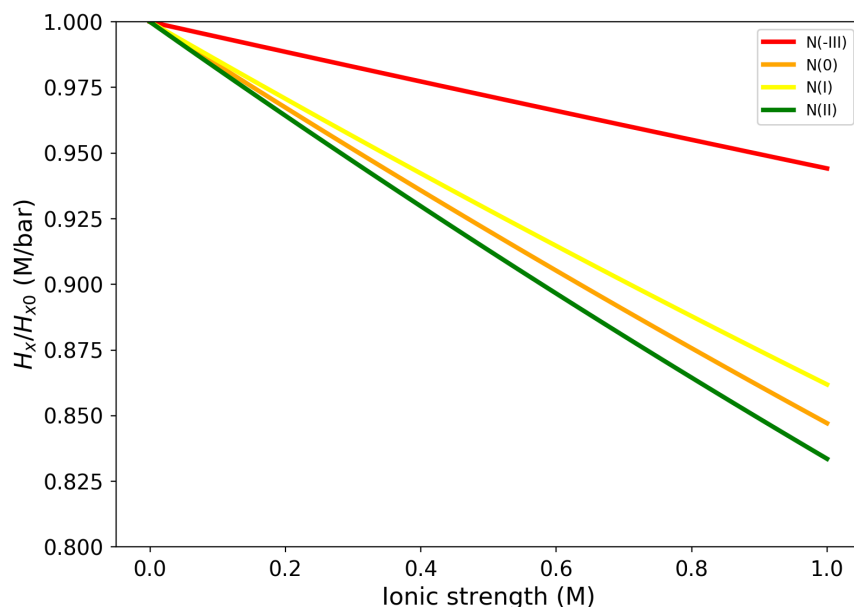


Figure 4.8.3: Fractional change in H_G as a function of ionic strength, assuming a temperature of 25°C and only NaCl contributing to the salinity.

our conclusions are insensitive to variations of this magnitude. Moreover, the band of possible ionic strength is likely narrower than the $0 < I < 1$ we consider here. We therefore neglect the dependence of H_X on salinity.

4.8.4 SENSITIVITY OF HENRY'S LAW CONSTANTS TO TEMPERATURE

To calculate the sensitivity of Henry's law constants to temperature, we use the empirical formalism from Burkholder et al. [36]:

$$\ln(H) = A + B/T + C\ln(T), \quad (4.29)$$

where H is the Henry's law constant in M/atm, and A , B , and C are empirically-fitted gas-specific coefficients. We took the values of these parameters from Burkholder et al. [36]; they are shown in table 4.8.6. The parametrization

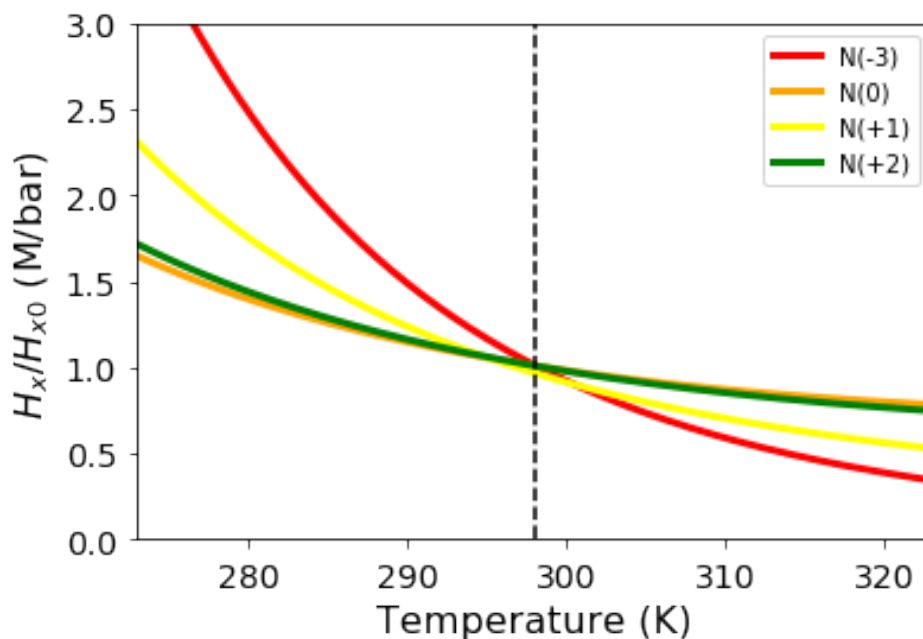


Figure 4.8.4: Henry's law constant dependence on temperature for the various species considered here. Henry's law parameters have been normalized to the standard value at 298 K for each gas.

for NO from Burkholder et al. [36] yielded erroneous results at 298K compared to literature measurements of H_{NO} ; consequently, for this molecule we used the parametrization from Gevantman [106], which takes form

$$\ln(H) = A + B/\left(\frac{T}{100K}\right) + C \ln\left(\frac{T}{100K}\right)$$

Of the gases we consider, only NH_3 shows significant variation with temperature (Figure 4.8.4). This affects the partitioning of N(-3) between the aqueous and gaseous states, but does not affect our overall results that the concentrations of oxidized N in general and NO_3^- and NO_2^- in particular are low in equilibrium.

Acid	$T = 2^{\circ}\text{C}$	$T = 18^{\circ}\text{C}$	$T = 25^{\circ}\text{C}$	$T = 37^{\circ}\text{C}$	$T = 45^{\circ}\text{C}$
HNO_3	-1.52	-1.37	-1.30	-1.18	-1.10
HNO_2	3.47	3.29	3.23	3.13	3.08
NH_4^+	10.0	9.46	9.24	8.90	8.67

Table 4.8.4: pKa as a function of temperature for the three acid dissociation reactions we consider.

Parameter	NH_3	N_2	N_2O	NO	Na^+	Cl^-
H_o (M/bar)	60	6.4×10^{-4}	2.4×10^{-2}	1.90×10^{-3}	-	-
h_o (M^{-1})	-4.81×10^{-2}	-1.00×10^{-3}	-8.50×10^{-3}	6.00×10^{-3}	-	-
h_T ($M^{-1}K^{-1}$)	-	-6.05×10^{-4}	-4.79×10^{-4}	-	-	-
h_i (M^{-1})	-	-	-	-	0.1143	0.0318

Table 4.8.5: Parameters for determining the dependence of Henry's law constants on salinity.

Species	A	B	C
NH_3	-9.84	4160	-
N_2	-177.1	8640	24.71
N_2O	-148.1	8610	20.266
NO	-62.8	82.3	22.816

Table 4.8.6: Parameters for determining the dependence of Henry's law constants on temperature. For NO, the parametrization is from Gevantman [106], and is different in form.

4.9 APPENDIX D: LIGHTNING PRODUCTION CALCULATION

The global lightning flash rate on Earth today is about $4 \text{ km}^{-2} \text{ year}^{-1}$ [130]. The flash rate on the Early Earth is not well constrained. Wong et al. [379] provide some constraints for the Early Earth by invoking the proportionality between the lightning flash rate and the convective available potential energy Romps et al. [283]. This captures some of the relationship between lightning rates and climate, but there are more variables to be considered than climate.

Cloud cover, height and structure play a large role in lightning rates, as can be seen from the order of magnitude difference between lightning rates over land vs. over the ocean [130]. This is important for the Early Earth because it is uncertain what fraction of the Earth was above the ocean at this time, and whether these differences in lightning rates only apply when 70% of the Earth is covered by water. Also, cloud cover may have been very different on the Early Earth, owing to a lack of biogenic and anthropogenic production of nucleation particles for cloud growth [355], but at the same time may have been enhanced by the larger amount of volcanic ash possibly present at this time [135, 245]. The physical mechanism of lightning strikes is also important. It may be that energetic particles are required to initiate the electron avalanche that results in a lightning strike [113], and far more energetic particles would have been impinging on the Earth's atmosphere due to a more active sun [1]. These factors could change the global average lightning flash rates by an order of magnitude [128], and some of these changes will increase the rate, and some will decrease it. Therefore we treat the global-average flash rate as a free parameter that can be varied by one order of magnitude about the modern rate.

The amount of NO_x produced by lightning depends on both the flash rate and the partial pressures of N_2 ($p\text{N}_2$) and CO_2 ($p\text{CO}_2$). In order to predict the effect of these lightning flashes on atmospheres with different $p\text{N}_2$ and $p\text{CO}_2$ on the NO_x production, we used the lightning atmospheric chemistry model from Ardaseva et al. [8] using the STAND2018 chemical network [272, 274], and ran it for a suite of atmospheres of a range of $p\text{N}_2$ and $p\text{CO}_2$. We calculate the

abundance of NO and NO₂ generated, and relate that to the energy by the equation [272]:

$$P(\text{NO}_x)(2.4 \times 10^{22} \text{K/J}) \frac{X(\text{NO}_x)}{T_f}$$

where $X(\text{NO}_x)$ is the volume fraction of NO and NO₂ generated, T_f [K] is the freeze-out temperature for NO and NO₂, identifiable from the model output, and $P(\text{NO}_x)$ is the production of NO_x in units of molecules/J. We can then estimate the flux of NO_x:

$$\Phi(\text{NO}_x) = P(\text{NO}_x)E_f\nu_f$$

where E_l [J] is the energy of a lightning flash, ν_f [cm⁻² s⁻¹] is the global average flash rate, and $\Phi(\text{NO}_x)$ [cm⁻² s⁻¹] is the global average surface flux of NO_x. We assume the flash energy to be the same then as today, or $E_f = 5 \times 10^9$ J. It would be useful in the future to model Hadean lightning flashes to see if this assumption is justified. The resulting NO_x surface fluxes are shown in Fig. 4.9.1.

The ratio between $p\text{N}_2$ and $p\text{CO}_2$ has a profound effect on the NO_x flux. Much more NO_x is generated when $p\text{CO}_2 > p\text{N}_2$. This is because when nitrogen is more abundant, then nitrogen atoms produced by dissociating N₂ will readily react with other available nitrogen atoms to reform N₂. With more available oxygen, a great deal more NO_x is formed. For an atmosphere with 10 bar CO₂ and 0.1 bar N₂, one can generate $\approx 5 \times 10^9$ through $\approx 5 \times 10^{11}$ cm⁻² s⁻¹ fluxes of NO_x, depending on the global-average lightning flash rate.

4.10 APPENDIX E: NO_x LOSS PROCESSES

Here, we expand on 4.2.2 to discuss NO_x⁻ loss process kinetics in greater detail.

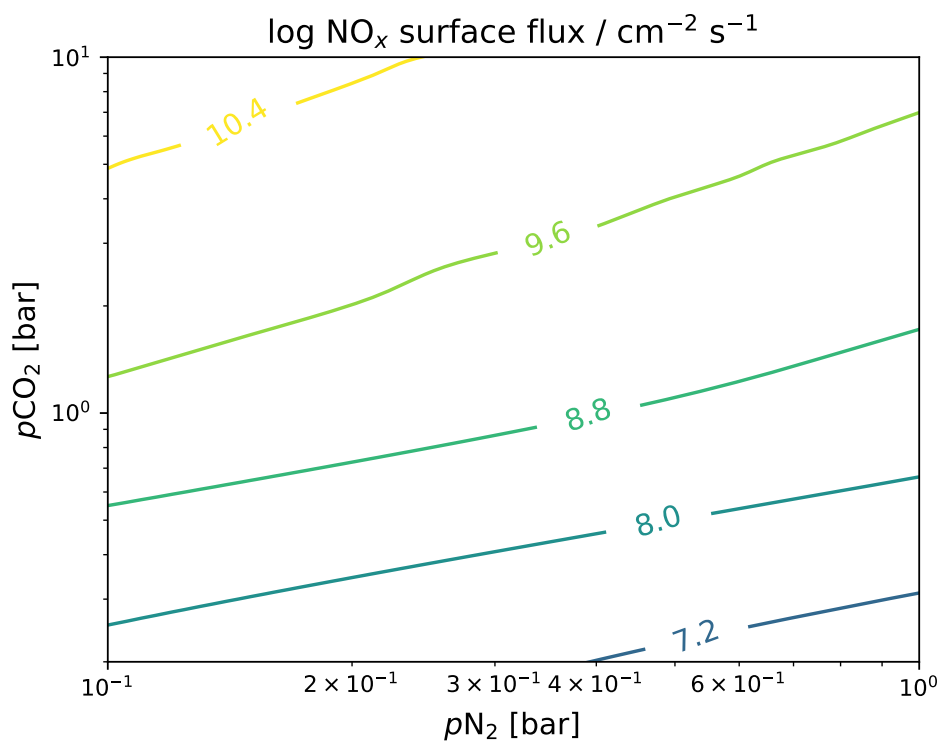


Figure 4.9.1: φ_{NO_x} predicted from model atmospheres exposed to a simulated lightning shock based on partial pressure of N_2 ($p\text{N}_2$, bar, x-axis) and CO_2 ($p\text{CO}_2$, bar, y-axis), assuming a modern-Earth global-average lightning flash rate of $4 \text{ km}^{-2} \text{ year}^{-1}$ [130]. The values scale linearly with the global-average lightning flash rate.

4.10.1 NO_x LOSS AT VENTS

Wong et al. [379] assume that NO_x⁻ is destroyed with 100% efficiency at only at hot (~ 400°C), acidic black smoker vents. They assume the water mass flux from prebiotic high-temperature vents to be the same as modern (7.2 × 10¹² kg yr⁻¹; ?] and assume an ocean volume of 3 × 10¹⁸ m³. Assuming a seawater density of 1 × 10³ kg m⁻³, this corresponds to a first-order rate constant of

$$k_{vents} = \frac{7.2 \times 10^{12} \text{ kg yr}^{-1}}{(1 \times 10^3 \text{ kg m}^{-3})(3 \times 10^{18} \text{ m}^3)} = 8 \times 10^{-17} \text{ s}^{-1}.$$

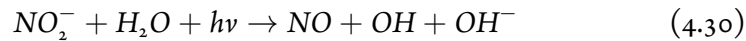
By contrast, Laneuville et al. [166] assume processing at any hydrothermal system would destroy 100% of NO_x⁻. The maximum hydrothermal circulation they consider corresponds to $k_{vents} = 3 \times 10^7 \text{ year}^{-1} = 1 \times 10^{-14} \text{ s}^{-1}$.

Overall, the range $k_{vents} = 8 \times 10^{-17} - 1 \times 10^{-14} \text{ s}^{-1}$ brackets the first-order rate constants for NO_x⁻ destruction at vents proposed by previous works, and we explore this range in our work. The heat flux from the terrestrial interior in the Archaean is thought to have been 2 – 3 × modern [271]. Under the assumption that hydrothermal water flux scales linearly with heat flux, this corresponds to an enhancement in k_{vents} of a factor of a few; our conclusions are robust to such variations in k_{vents} .

4.10.2 NO_x PHOTOCHEMISTRY

NO₂ PHOTOCHEMISTRY

Under irradiation by near-UV (NUV) radiation (~ 300 – 370 nm), NO₂⁻ undergoes reaction 4.30 [41, 182, 206, 390]:



The overall impact of UV depends on the composition of the aqueous reservoir in which the nitrite is contained. In pure water, OH and NO rapidly recombine to restore NO₂⁻, and no net loss of nitrite takes place [354]. However, in the presence of OH scavengers whose concentration exceeds nitrite, the OH is

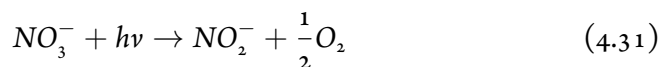
consumed before it can react with NO to restore nitrite, and nitrite is net lost. For example, in modern seawater, concentrations of the OH scavenger bromide (Br^-) [Br^-] \gg [NO_2^-], and UV photolysis is hence a net sink of NO_2^- level [389, 391, 393]. The nitrite loss rate in nitrite-rich waters in the central Pacific was measured by Zafiriou and True [393] to be

$k_{\text{NO}_2^-,hv} = 0 - 0.25 \text{ day}^{-1} = 0 - 2.9 \times 10^{-6} \text{ s}^{-1}$, with a median value of $k_{\text{NO}_2^-,hv} = 0.1 \text{ day}^{-1} = 1.2 \times 10^{-6} \text{ s}^{-1}$; this is approximately consistent with later work [41, 391]. It is also possible for NO and NO_2 to backreact to nitrate/nitrite via N_2O_3 . However, overall Zafiriou and True [393] report that 20-100% of NO formed from nitrite photolysis in seawater does not reform nitrite. Hence, in the modern ocean photolysis net converts NO_2^- to NO [394], which is much less soluble than nitrite and degasses to the atmosphere [391]. For example, Wong et al. [379] calculate $p\text{NO} = 1 \times 10^{-7} \text{ bar}$ for $p\text{CO}_2 = 1 \text{ bar}$, and the solubility constant for NO is $2 \times 10^{-3} \text{ M bar}^{-1}$ [296], meaning that NO degases for $[\text{NO}] > 2 \times 10^{-10} \text{ M}$. Overall, UV photolysis is a net sink of NO_2^- in the ocean.

One might imagine that prebiotic ponds with extremely pure water might have existed, with Br^- levels so low that it could not scavenge the OH and prevent nitrite regeneration. However, bicarbonate and carbonate (HCO_3^- , CO_3^{2-}) are also OH scavengers, with bicarbonate the next most reactive ion with OH in modern seawater [389]. Early Earth is thought to have had elevated levels of CO_2 relative to present to reconcile the lower bolometric output of the young Sun with evidence for a global hydrologic cycle (the Faint Young Sun problem; Holland [131], Kasting [150, 155], Mojzsis et al. [211], Sagan and Mullen [292], Wilde et al. [376]). In this case, pond waters must have had high HCO_3^- and CO_3^{2-} levels. These would have reacted with OH and inhibited reformation of nitrite, and photolysis would remain a sink on nitrite until [NO_2^-] exceeded [HCO_3^-] and [CO_3^{2-}]. We note that observations of nitrite photolysis in modern lakes indicate a nitrite loss rate only $2 - 3 \times$ slower than expected from direct photolysis, suggesting that it is typical for UV photolysis to be a sink on NO_2^- levels even in relative low ionic-strength lake/pond waters [206].

NO₃ PHOTOCHEMISTRY

In modern natural waters, interaction with UV light photolyzes nitrate to nitrite, with peak conversion at ~ 305 nm and net reaction given by Equation 4.31 [41, 182, 206, 322, 392].



(4.32)

In the modern equatorial Pacific, the net nitrate-nitrite conversion rate coefficient is estimated to be $k_{\text{NO}_3^-,h\nu} = 0.7 - 6.2 \times 10^{-3} \text{ day}^{-1}$, with median value $k_{\text{NO}_3^-,h\nu} = 2 \times 10^{-3} \text{ day}^{-1} = 2.3 \times 10^{-8} \text{ s}^{-1}$ [392]. If radical scavengers are present, the nitrate conversion rate may be higher than estimated here, as high scavenger levels increase conversion to nitrite [66, 120, 182].

For $\lambda \geq 280$ nm, which are the only wavelengths accessible naturally on modern Earth due to the UV-shielding ozone layer, the coproducts of nitrite photolysis are O^- , which protonates to form OH, and $\text{O}(^3\text{P})$; for irradiation at 305 nm, the formation of OH is $9\times$ as common as the formation of $\text{O}(^3\text{P})$. In the modern ocean, $\text{O}(^3\text{P})$ can react with dissolved O_2 to form ozone, which can then react with nitrite to reform nitrate [41, 108, 182]. This pathway should be suppressed in the anoxic oceans of prebiotic Earth, suggesting nitrate conversion rates somewhat higher on prebiotic Earth than modern Earth. The photoconversion of nitrate to nitrite can be catalyzed by dissolved organic matter (DOM), but we postulate DOM levels to be low on prebiotic Earth due to the absence of biogenic carbon fixation [322]. Finally, the quantum yield of nitrite formation under 300 nm irradiation is roughly constant from pH= 2 – 8, but increases by a factor < 4 from pH= 8 – 14 [66]. This suggests nitrate photolysis rates in the prebiotic ocean comparable to the present day ocean, and nitrate photolysis rates in prebiotic ponds \geq oceanic rates for pH ≥ 2 .

For $\lambda < 280$ nm, irradiation of nitrate leads to formation of peroxyxynitrite

(ONOO^-), which can decay to nitrite. Nitrate absorbs even more strongly at these shorter wavelengths, with a stronger absorption feature at 200 nm than at 302 nm, and on early Earth, UV radiation at wavelengths down to 204 nm would have been available due to the anoxic early atmosphere [108, 182, 260]. Consequently, one might expect nitrate photolysis rates to have been higher in natural waters on early Earth. However, high $[\text{CO}_2(\text{aq})]$ levels catalyze decomposition of peroxyxynitrite back to nitrate instead of nitrite, and elevated $[\text{CO}_2]$ is expected on early Earth due to elevated CO_2 required to compensate for the fainter young Sun, decreasing the nitrite yield [108, 155, 359]. Further, the fate of the peroxyxynitrite depends on pH. In its protonated form ($\text{pH} < \text{pK}_a = 6.5 - 6.8$), this molecule quickly decays back to nitrate. In its deprotonated form ($\text{pH} > \text{pK}_a = 6.5 - 6.8$), it decomposes to nitrite and O_2 [108, 182]. Consequently, nitrite yield increases with pH for $\lambda < 280$ nm irradiation [108, 309]. Overall, while it is likely that nitrate photolysis rates were somewhat higher in prebiotic natural waters compared to the modern ocean due to the penetration of 204 – 280 nm radiation through the atmosphere, the magnitude of the increase depends on the pH. In natural waters buffered to alkaline pH, nitrate photolysis rates may have been significantly higher, whereas in waters buffered to acidic pH the impact should have been minimal.

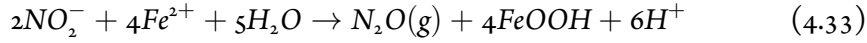
4.10.3 NO_x THERMAL CHEMISTRY

REDUCTION OF NO_2^- BY Fe^{2+} TO NITROGENOUS GAS

Fe^{2+} can reduce NO_2^- to N_2O . While this process is faster with mineralized Fe^{2+} or in the presence of catalysts, it nevertheless proceeds with aqueous Fe^{2+} [34, 78, 110, 146, 321, 333, 362]. The net reaction is thought to proceed by Equation 4.33, though Jones et al. [146] note that only 15 – 40% of the nitrite consumed emerged as N_2O in their studies. The reaction is first-order in both $[\text{Fe}^{2+}]$ and $[\text{NO}_2^-]$, and second-order overall, with the consumption of $\text{NO}_2^-:\text{Fe}^{2+}$ in a 1:2 ratio [34, 110, 146]. However, note that the study of Van Cleemput and Baert [362] reported second-order kinetics with respect to

NO_2^- at acidic pH.

Fe^{2+} reduces NO_2^- to yield nitrogenous gas [34]:



The reaction rate is dependent on pH and on whether NO_2^- or Fe^{2+} is in excess. Reaction rates are higher at pH= 8 compared to pH= 7, pH= 6, and pH= 6.5 Buchwald et al. [34], Grabb et al. [110], Jones et al. [146], Moraghan and Buresh [212]. We extract the second-order rate constant $k_{\text{NO}_2^-, \text{Fe}^{2+}}$ from the rates and concentrations reported in the literature. From Grabb et al. [110], we infer $k_{\text{NO}_2^-, \text{Fe}^{2+}} = 0.1 \text{ M}^{-1} \text{ hour}^{-1} = 3 \times 10^{-5} \text{ M}^{-1} \text{ s}^{-1}$ at pH~ 6.5. From Jones et al. [146], we infer

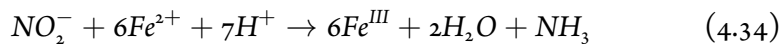
$k_{\text{NO}_2^-, \text{Fe}^{2+}} = 0.4 - 4 \text{ M}^{-1} \text{ hour}^{-1} = 1 \times 10^{-4} - 1 \times 10^{-3} \text{ M}^{-1} \text{ s}^{-1}$ at pH=7, with higher reaction rates corresponding to an excess of Fe^{2+} over NO_2^- . From Buchwald et al. [34], we infer

$k_{\text{NO}_2^-, \text{Fe}^{2+}} = 1.2 - 12 \text{ M}^{-1} \text{ hour}^{-1} = 3.3 \times 10^{-4} - 3.3 \times 10^{-3} \text{ M}^{-1} \text{ s}^{-1}$ for pH=7, and $k_{\text{NO}_2^-, \text{Fe}^{2+}} = 50 - 56 \text{ M}^{-1} \text{ hour}^{-1} = 1.4 \times 10^{-2} - 1.6 \times 10^{-2} \text{ M}^{-1} \text{ s}^{-1}$ for pH=8, with larger $k_{\text{NO}_2^-, \text{Fe}^{2+}}$ at larger $[\text{Fe}^{2+}]$. Since we expect $[\text{Fe}^{2+}] \leq 600\mu\text{M}$ in natural waters and most of these experiments were conducted at higher $[\text{Fe}^{2+}] \geq 600\mu\text{M}$, we take the $k_{\text{NO}_2^-, \text{Fe}^{2+}}$ derived from measurements at the lowest $[\text{Fe}^{2+}]$ at each pH. Hence, $k_{\text{NO}_2^-, \text{Fe}^{2+}} = 3 \times 10^{-5} \text{ M}^{-1} \text{ s}^{-1}$ (pH= 6.5, $[\text{Fe}^{2+}] = 12\text{mM}$, Grabb et al. [110]); $k_{\text{NO}_2^-, \text{Fe}^{2+}} = 3 \times 10^{-4} \text{ M}^{-1} \text{ s}^{-1}$ (pH= 7, $[\text{Fe}^{2+}] = 600\mu\text{M}$, Buchwald et al. [34]); and $k_{\text{NO}_2^-, \text{Fe}^{2+}} = 1 \times 10^{-2} \text{ M}^{-1} \text{ s}^{-1}$ (pH= 8, $[\text{Fe}^{2+}] = 600\mu\text{M}$, Buchwald et al. [34]).

REDUCTION OF NO_2^- BY Fe^{2+} TO NH_3

Summers and Chang [334] demonstrated that Fe^{2+} can also reduce NO_2^- to

NH₃, with reaction consistent with Equation 4.34:

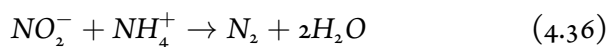


$$\frac{d[\text{NH}_3]}{dt} = k_{22}[\text{NO}_2^-][\text{Fe}^{2+}]^{1.8} (\text{pH} = 7.9) \quad (4.35)$$

$k_{22} = 35 \times 10^{-6} \text{ min}^{-1} \text{ M}^{-1.8} = 5.8 \times 10^{-7} \text{ s}^{-1} \text{ M}^{-1.8}$ (pH=7.9, T=22°C). They also report the reaction rate to depend on temperature, pH, and the presence of background anions and cations at near-oceanic concentrations. For T=0 – 40°C, pH=7.5 – 8.4, and varying levels of added ions, they reported reaction rates to vary between 1 – 72× the rate at T=22°C, pH=7.9, and no additional ions. The reaction proceeds at an undetectable rate for pH ≤ 7.3, maximal rate for pH= 7.6, and decreases slowly for pH > 7.6.

ANAMMOX OF NO₂⁻ WITH NH₃

Laneuville et al. [166] point out that nitrite and ammonium can also react in an irreversible, exothermic anammox reaction, producing N₂ as a byproduct. The reaction mechanism and kinetics have been determined by Nguyen et al. [226] for reactant concentrations ≥ 0.05M, over pH= 3 – 7 and T = 4 – 50°C, and are given by Equation 4.36:



$$\frac{d[\text{N}_2]}{dt} = A \exp(-E/RT)[\text{NH}_3][\text{HNO}_2]^2 \quad (4.37)$$

In calculating the reaction rate, we must specify the ammonia concentration. While the ammonia concentration in prebiotic natural waters is not known, an upper bound on atmospheric ammonia concentrations of pNH₃ < 10⁻⁸ bar suggested by photochemistry considerations [149]. The Henry's Law constant for NH₃ is 60 M/bar [296, 298], corresponding to a limit of [NH₃] < 6 × 10⁻⁷ M for solutions in equilibrium with the atmosphere.

We follow Laneuville et al. [166] in using the kinetics of Nguyen et al. [226] to calculate the anammox rate, but we note that the reactant concentrations we study here are well below the reactant concentration range ($\geq 0.05\text{M}$) of the study of Nguyen et al. [226]. Nguyen et al. [226] note that Dusenbury and Powell [84] reported first-order kinetics with respect to total nitrite species at low nitrite concentrations and low pH (as opposed to second-order kinetics Nguyen et al. [226] report), but suggest that experimental inaccuracies are at the root of this difference as opposed to a change in the reaction mechanism. Nevertheless, our extension of the Nguyen et al. [226] kinetics to lower concentrations is a significant caveat.

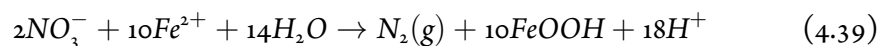
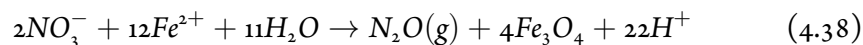
NO_2^- DECAY

For $\text{pH} < 6$, nitrite becomes unstable, decaying to produce N-bearing gases (e.g., N_2 , N_2O , and NO) in ways that are dependent on a broad range of environmental factors such as pH, presence of metallic cations, and organic matter [236, 321, 361]. One major pathway for nitrite loss is nitrous acid decomposition, $3\text{HONO} \rightarrow 2\text{NO} + \text{H}^+ + \text{NO}_3^-$; this reaction limits nitrite to a half-life of 14 hours at 0°C [145, 236, 266]. Overall, in acid solution nitrite is unstable, and faces a strong sink due to self-decay. We note that the latest estimates for early ocean pH call for $\text{pH} > 6.5$ [115, 162], suggesting this process should not affect prebiotic nitrite concentrations in oceanic waters, though it would in lake or pond waters buffered to acidic pH.

REDUCTION OF NO_3^- BY Fe^{2+}

Reduction of nitrate by Fe^{2+} to N-bearing gases (N_2O , N_2) is thermodynamically favored but kinetically slow; as a result, studies conducted over short timescales ($\lesssim 1$ day) generally do not detect uncatalyzed nitrate reduction by dissolved ferrous iron, while studies conducted over longer time periods ($\gtrsim 1$ week) do detect nitrate reduction [35, 235, 244, 255, 295, 405, 406]. Ottley et al. [235] estimate an activation energy of 70 kJ/mol for abiotic nitrate loss due to

uncatalyzed reduction by ferrous iron. Reactions 4.38 and 4.39 have been proposed to describe these reactions.



REDUCTION OF NO_3^- BY MINERALIZED Fe^{2+}

Nitrate may also be reduced to ammonium by green rust and by FeS suspensions [121, 333], and to N-bearing gases by Fe^{2+} bearing mineral catalysts [78, 255, 258, 295]. The reductive step is generally much faster with mineralized, surface-complexed Fe^{2+} [78]. The presence of elevated temperatures, trace oxygen, and certain metals (e.g., Cu^{2+}) can also catalyze nitrate reduction [35, 235, 244].

5

Solvated-electron production by cyanocuprates is compatible with the UV-environment on a Hadean-Archaeon Earth

Abstract

UV-driven photoredox processing of cyanocuprates can generate simple sugars necessary for prebiotic synthesis. We investigate the wavelength dependence of this process from 215 to 295 nm and generally observe faster rates at shorter wavelengths. The most efficient wavelengths are accessible to a range of potential prebiotic atmospheres, supporting the potential role of cyanocuprate

photochemistry in prebiotic synthesis on the early Earth.¹

5.1 INTRODUCTION

MANY PREBIOTIC SYNTHESSES of simple biomolecules, including ribonucleotides, amino acids, and lipid precursors [240] require the simple 2- and 3-carbon sugar feedstock molecules, glycolaldehyde and glyceraldehyde. Past suggestions for synthesis of simple sugars include the formose reaction [37], atmospheric photochemical production and subsequent transport to the surface [123], and delivery from space [47, 48, 194]. However, unspecific products [37] and large threshold concentrations [105, 267, 303] (formose reaction), and low yields [123] (atmospheric production) are all drawbacks. Alternatively, Ritson and Sutherland [276] demonstrated that hydrogen cyanide can be converted to the glycolaldehyde and glyceraldehyde oxazolidinone derivatives via a Kiliani-Fisher homologation mechanism using cyanocuprate photoredox chemistry. This mechanism uses UV light to photooxidize the cyanocuprates, producing aqueous solvated electrons, which are capable of reducing HCN and 2-hydroxynitriles to imines, which can then hydrolyze to give rise to formaldehyde and α -hydroxy aldehydes in a stepwise fashion.

Glyceraldehyde is the first sugar that contains a chiral center and can thus influence the stereochemistry in downstream synthesis. Glycolaldehyde and formaldehyde can form enantiomerically enriched glyceraldehyde under chiral amino acid catalysts [28, 29, 126]. Similarly, stereoselective tetrose [252, 373] and pentose [253] sugars were demonstrated under chiral amino acid catalysts and plausible prebiotic conditions. Steer et al. [327] showed the selective synthesis of 2-deoxy-D-ribose from glycolaldehyde and formaldehyde under the influence of proteinogenic amino esters and amino nitriles. Plausible syntheses of glycolaldehyde and glyceraldehyde may thus be intimately connected with the

¹This thesis chapter was published as: Z. R. Todd, A. C. Fahrenbach, C. J. Magnani, S. Ranjan, A. Bjorkbom, J. W. Szostak and D. D. Sasselov (2018) *Chem. Commun.*, 54, 1121-1124.

issue of homochirality. In the Ritson and Sutherland system, UV light photooxidizes the cyanocuprates, producing aqueous (solvated) electrons, which are key for putting into motion the reaction network capable of producing glycol- and glyceraldehyde. (See Figure 5 of Ritson and Sutherland [276] for a detailed mechanism.) Additional work by Ritson and Sutherland [277] modified this cycle to include hydrogen sulfide as the stoichiometric reductant and produced free sugars upon 254 nm irradiation. The UV-wavelength dependence of the system with the addition of sulfide may not necessarily be the same as for the cyanocuprate cycle alone. Further work [240] expanded upon the cyanosulfidic chemistry in Ritson and Sutherland [276] and found that sugars, amino acids, ribonucleotides, and lipid precursors can be generated under UV irradiation at 254 nm. In this system, copper is not strictly necessary, but can increase the overall efficiency.

Cyanocuprate photochemistry has only been studied at limited wavelengths (254 nm [133, 134, 276] and 266 nm [328]), which are poor approximations of the spectral radiance illuminating the surface of the prebiotic Earth [259]. The young Sun is thought to have been on average about 20–30% dimmer than today, but with a larger fraction of its radiation in the UV range [50, 270]. The early atmosphere (typically considered to be 1 bar of N₂ and CO₂ [285]) was anoxic [90, 241], providing ample radiation at wavelengths >200 nm, which are not screened out by likely prebiotic atmospheric constituents [28].

UV light is a potentially important source of energy to drive prebiotic reactions [46, 243, 291]. Since photochemical reactions are generally wavelength-dependent [32], it is necessary to study suggested prebiotic photochemistry at multiple wavelengths and fluxes more relevant to the prebiotic Earth. The flux from our experimental apparatus is consistent with the flux expected on the surface of the early Earth in the wavelength range 235–255 nm to within an order of magnitude; our lamp provides roughly 6–9 times as much flux in this wavelength interval. Here, we investigate the wavelength dependence of the cyanocuprate photochemical process (5.1.1) and assess if this reaction is plausible on the early Earth; other systems, such as the cyanosulfidic chemistry,

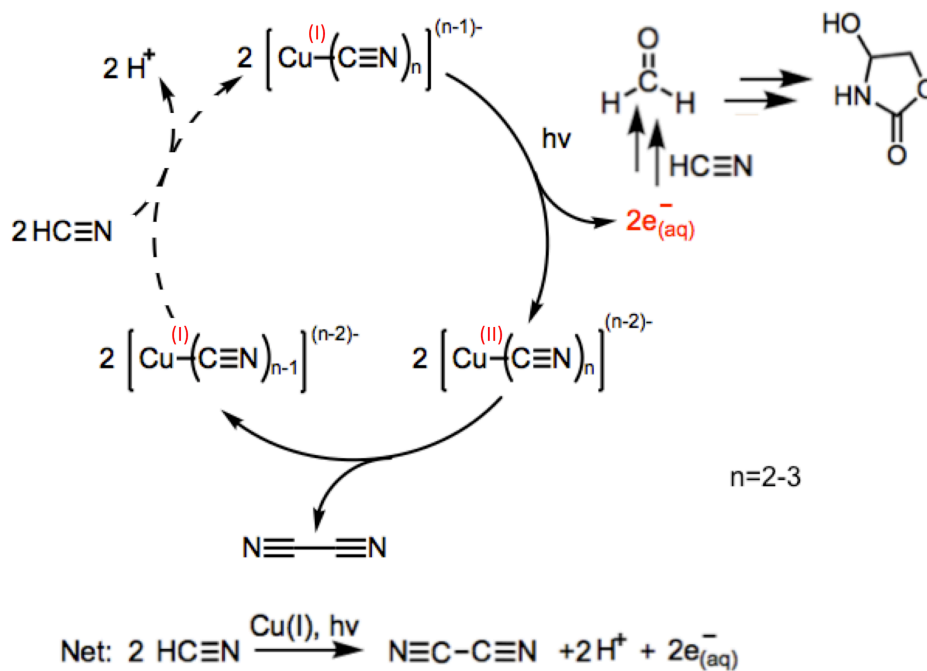


Figure 5.1.1: The cyanocuprate photoredox process results in the production of solvated electrons, cyanogen, and protons and depletion of HCN. The reduction of HCN by solvated electrons yields formaldehyde after a few steps. This process is driven by UV-light, studied in the past at 254 nm, and in this study, at a range of wavelengths from 215–295 nm. The dashed lines indicate that some forms of the cyanocuprate complexes may not be replenished efficiently by HCN when HCN is limiting.

will be addressed in future work. Studying the cyanocuprate photoprocess can act as a valuable test case for more complex chemical systems, such as those described in Ritson and Sutherland [277] and Patel et al. [240].

5.2 RESULTS AND DISCUSSION

We began by testing how the relative rates and quantum yields of the photoprocess depend on irradiation wavelengths from 215–295 nm (10 nm

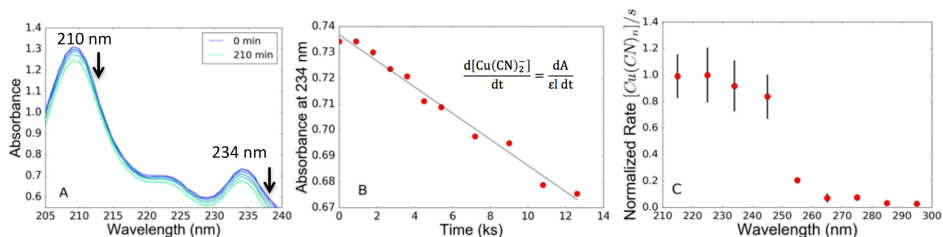


Figure 5.2.1: A. Absorption spectra of an aqueous solution of cyanocuprates ($63 \mu\text{M CuCN}$, $125 \mu\text{M KCN}$) during UV-irradiation. Arrows indicate the two absorption maxima at 210 and 234 nm decrease as a function of irradiation time. B. Absorbance at 234 nm as a function of irradiation time. The slope of the trendline measures the rate. C. Action spectrum with maximum value set to 1. Each wavelength was tested in triplicate, with the values representing the averages and errors the standard deviation. The rates are faster at wavelengths below roughly 250 nm.

intervals, 10 nm bandwidths). These wavelengths of light (roughly 200-300 nm, or mid-range UV) were selected according to conditions expected on the surface of the early Earth. Aqueous solutions of dilute cyanocuprate complexes ($63 \mu\text{M}$ copper (I) with three equivalents of cyanide) were prepared at neutral pH anaerobically. The absorption spectra of these solutions (Fig. 5.2.1a) display peaks at 210 and 234 nm, indicating that the solution is primarily composed of dicyanocuprate complexes. The tricyanocuprate species has absorption maxima at 205 nm and 239 nm. As the number of equivalents of cyanide per copper center is increased, the absorption spectrum changes from that characteristic of the dicyanocuprate to the tricyanocuprate (Fig 5.7.3). Irradiation of the solutions resulted over time in a decrease in the absorption intensity across the spectrum, the rate of which depended on the irradiation wavelength.

We attribute the decreases in absorbance due to the following mechanism: photoexcitation by UV light of cyanocuprates releases solvated electrons, a fraction of which are scavenged by HCN to eventually yield sugar products. The cyanide ligands of the oxidized copper(II) cyanide complexes undergo reductive elimination, forming cyanogen and regenerating the copper(I) state. Each turn of

the cyanocuprate photoprocess removes multiple HCN molecules per copper complex, causing the cyanocuprate distribution to favor complexes with lower coordination numbers and the observed decrease in absorbance. The relative rates of the reaction at different wavelengths were also monitored with a cyanide-selective electrode (Fig 5.8.1) to confirm the overall trend from rates determined by absorbance measurements. LC-MS studies also confirmed the production of an oxazolidinone end product at all wavelengths tested (Figure 5.9.1). This detection indicates that the production of simple sugars can occur even at more prebiotically relevant sub-millimolar concentrations of copper and cyanide, while previous experiments used higher initial concentrations (200 mM KCN, 10 mM CuCN)[276].

The decrease in absorbance of the cyanocuprate solution with irradiation time allows us to determine an apparent rate (Fig. 1b) for the overall photochemical process, which serves as a proxy for the relative rate of solvated electron production at each irradiation wavelength studied. In order to compare reaction rates at different irradiation wavelengths, we normalize the apparent rates by incident photon fluxes (Fig. 5.2.1c). The normalized rate is larger at irradiation wavelengths <250 nm.

We calculated the relative quantum yields (number of reactions per absorbed photon) at the various irradiation wavelengths tested and normalized all quantum yields such that the maximum yield (at 245 nm irradiation, near the absorption maxima of the cyanocuprates) was set to 1 (Figure 5.2.2). Two different mechanisms have been proposed for this process: 1) The Ritson and Sutherland [276] mechanism postulates a photoionization as the underlying photoprocess, suggesting that any photon with energy greater than the activation energy of the process should be sufficient, and 2) Banerjee et al. [14] use theoretical calculations of electronic structures and a mechanism involving dipole-bound forms of HCN to predict a Gaussian efficiency centered at 265 nm. Our results do not support this mechanism, given that the relative quantum yield at 265 nm is roughly a tenth of the maximum value at 245 nm.

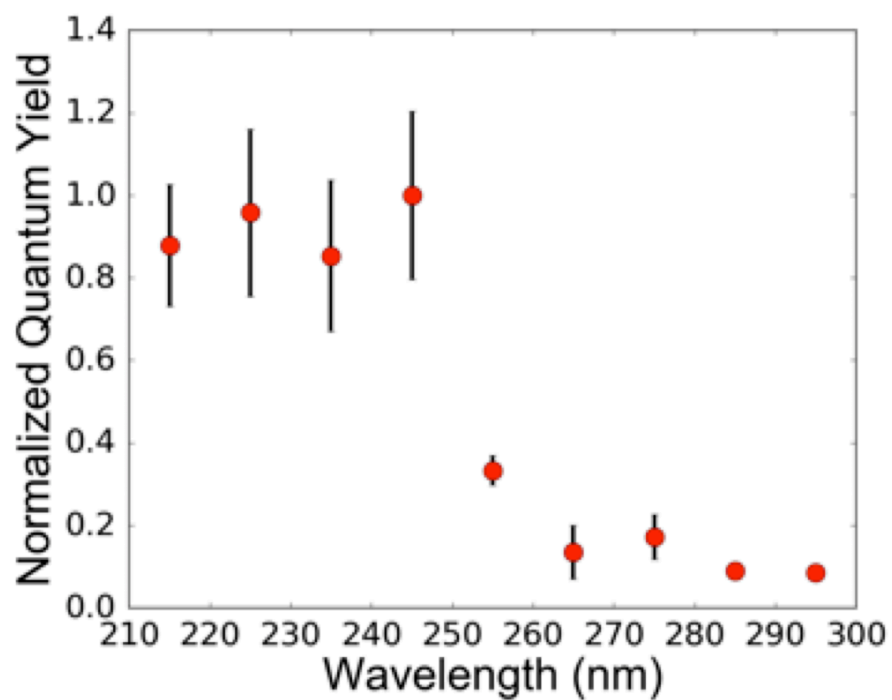


Figure 5.2.2: Relative quantum yield (normalized such that the maximum is 1) as a function of irradiation wavelength. The quantum yield is greatest at a wavelength of 245 nm.

We next studied how the wavelength-dependent reaction rates compare to the spectral irradiation on the modern and prebiotic Earth. The relative rates determined herein suggest that the process proceeds more efficiently at wavelengths below 250 nm; but, shorter wavelengths are less accessible on the surface of a planet due to shielding by atmospheric gases and decreased solar output. We compute the intensity of light reaching the surface of Earth as a function of wavelength by convolving the solar flux with the spectral screening by atmospheric gases (see section 5.10). We compute the relative rate of solvated-electron production as a function of wavelength by multiplying the action spectrum and integrated surface radiance at each wavelength³⁴. The resulting curve is shown in Figure 5.2.3b (red dots); the area under it is commonly referred to as the relative dose rate^[259].

The modern surface of the Earth receives low levels of UV light (due to UV-shielding O₂ and O₃) leading to a UV flux inadequate to drive this photochemistry. Even when including the effects of atmospheric attenuation and stellar spectral slope, we find that the most productive wavelength of irradiation remains 245 nm for the early Earth. Energy at the relevant wavelengths should be accessible on the early Earth for a range of plausible atmospheres, suggesting that this mechanism for simple sugar generation is viable. The peak wavelength does not precisely correspond with the 254 nm light that is typically used in prebiotic experiments, exemplifying the importance of wavelength dependence considerations. Our study, though carried out at specific individual wavelengths that do not mimic the spectrum of the Sun, when combined with information about the spectral flux on the early Earth, can provide insight as to the plausibility of the process in the overall context of the UV environment on the early Earth.

5.3 CONCLUSIONS

In summary, we performed a wavelength-dependent analysis to assess the plausibility of the synthesis of 2- and 3-carbon sugar building blocks (necessary

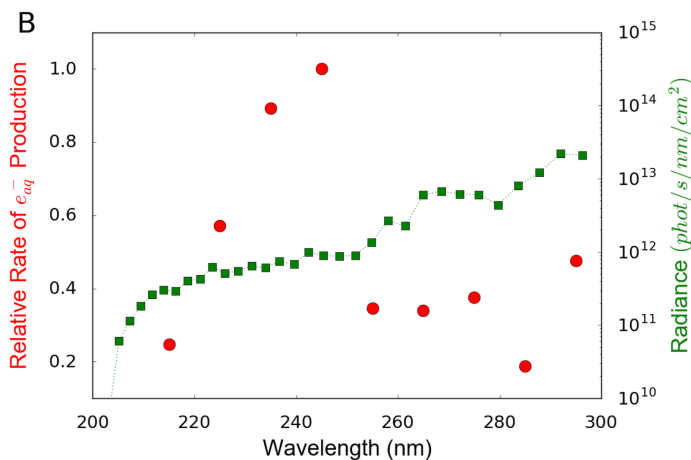
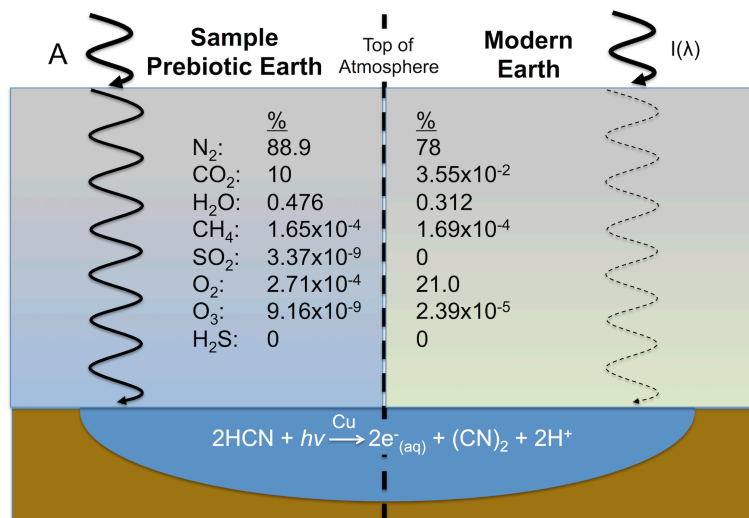


Figure 5.2.3: A. Schematic of the UV light reaching the surface of the Earth for a proposed prebiotic (left) and modern atmosphere (right), both with 1 bar and atmospheric compositions as noted. B. The relative rate of solvated-electron production occurring from the cyanocuprate photoprocess as a function of wavelength for a hypothetical prebiotic atmosphere (red circles; normalized so that the maximum is 1); for the modern Earth the rate is essentially zero and not shown. The highest relative rate occurs at 245 nm. The Earth surface radiance (green squares) is shown for the early atmosphere. The UV wavelengths necessary for driving the cyanocuprate photochemical production of solvated electrons should be accessible on the early Earth and under a variety of atmospheres.

for simple biomolecule synthesis) from photoredox processing of cyanocuprates. Past studies of the cyanocuprate photoprocess used monochromatic emission at 254 nm, which is a poor proxy of the surface irradiation on early Earth. In order to assess the prebiotic plausibility of this pathway, we measured the wavelength dependence and found that the process is more efficient at wavelengths <250 nm. The wavelength with highest quantum yield (245 nm) should be accessible not only in the atmosphere we tested here, but in other plausible early Earth atmospheres. Thus, we argue that the photochemical cycling of cyanocuprates is a prebiotically plausible source of 2- and 3- carbon sugar building blocks on the early Earth, across a diversity of possible atmospheric states. This process should also work on early Mars (unless high levels of dust are present^[259]) or exoplanets analogous to the young Earth orbiting stars with UV emission similar to the Sun.

5.4 EXPERIMENTAL

Wavelength-dependent experiments employed solutions of 63 μM CuCN and 125 μM KCN prepared from concentrated stocks. The pH was adjusted to 7.4 using HCl. All preparations were done anaerobically, inside a glove box filled with an inert gas mixture (98% N_2 , 2% H_2). The final samples were placed inside gas-tight screw-top Spectrosil cuvettes (Starna cells part number 9-Q-10-GL14-C) to ensure anaerobic conditions. For each experiment, 0.7 mL of cyanocuprate solution was irradiated. Every 15 minutes for the first two hours, and every 30 minutes thereafter (210 minutes total), UV-Vis absorption spectra were recorded in order to monitor the reaction and determine the rate.

Acknowledgements We thank C. P. Tam and F. Ng for experimental and laboratory assistance. We thank R. Szabla and D. Bucher for helpful comments and discussions. We thank S. Trauger and others at the Harvard Small Molecule Mass Spectrometry facility. This work was supported in part by grants from the Simons Foundation (290363 to J. W. S and 290360 to D. D. S.) and we acknowledge the Harvard Origins of Life Initiative. J. W. S. is an Investigator of

the Howard Hughes Medical Institute. A. B. was supported by a grant from the Academy of Finland. A. B. is currently located at Statens Serum Institut, Artillerivej 5, DK-2300 Copenhagen S, Denmark. C. J. M. is currently at the School of Medicine, Stanford University, 291 Campus Drive, Palo Alto CA, 94305.

5.5 APPENDIX A: GENERAL METHODS

Potassium cyanide (KCN; 98%) and copper cyanide (CuCN; 99%) were purchased from Sigma-Aldrich. The solutions for the irradiation experiments all contained 0.0625 mM CuCN and 0.125 mM KCN. All solutions were prepared anaerobically in a glove box (Coy Labs PureLab 2GB Glovebox System) filled with an inert gas mixture (98% N₂, 2% H₂). To bring materials and solutions in and out of the glove box, an airlock system was used, with two cycles of purging to ensure oxygen removal. One cycle of purging constitutes 3 times of purging with nitrogen and one time with the nitrogen-hydrogen gas mixture. To make the solutions, a stock solution of 1 M KCN, 0.5 M CuCN was prepared. The pH of the solution was adjusted to 7.4 by using concentrated HCl. This stock solution was then diluted 100x to a concentration of 5 mM CuCN and 10 mM KCN. This solution was then diluted again to prepare 50 mL of a solution containing 0.0625 mM CuCN and 0.125 mM KCN. The pH was checked and adjusted to 7.4, using 1 M HCl. Aliquots (1 mL) were transferred to Eppendorf tubes and frozen at -30° C in the dark until time of use.

In order to carry out an irradiation experiment, one of the samples contained in the Eppendorf tubes was first sonicated and then 0.7 mL of this solution was transferred anaerobically to a Spectrosil quartz cuvette with a screw top (Starna Cells part number 9-Q-10-GL14-C). A micro-stirbar was placed inside the cuvette. An initial UV-Vis absorption spectrum (200–350 nm) was taken before irradiation, using an Amersham Sciences Ultrospec 3100 pro. The cuvette was then placed in the tunable lamp setup, set at the appropriate wavelength and bandwidth (215-295 nm in 10 nm intervals, with 10 nm bandwidths), with

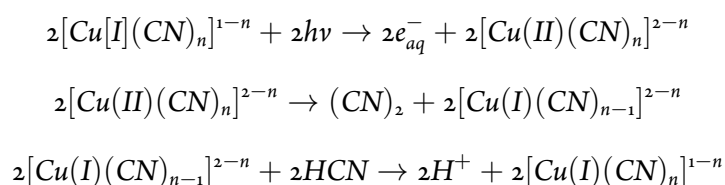
stirring on. Every fifteen minutes for the first two hours, the cuvette was removed briefly from the lamp and a UV-Vis absorption spectrum was recorded. Subsequent timepoints were taken every half hour until 3.5 hours of total irradiation had elapsed.

The tunable lamp setup consists of a 75 W Tunable PowerArc, made by Optical Building Blocks (OBB). Figure 5.5.1 shows the lamp setup. This apparatus uses a xenon arc lamp and a monochromator to allow for tunable wavelength selection. The monochromator is a diffraction grating that separates the spectrum of the lamp by wavelength. Changing the relative position of the grating and the exit slit allows for precise wavelength selection. The cuvette is held in the enclosed housing capable of magnetic stirring. The bandwidth of irradiation can also be adjusted as desired.

Several of our control experiments were performed with irradiation from a Rayonet photochemical reactor (RPR-200, Figure 5.5.2). The lamps used here output the same type of irradiation used by Ritson and Sutherland [276]. This system only allows for irradiation at a wavelength specified by the lamps, which in this case were mercury emission lamps, with primary emission at 254 nm. While the wavelength selection of such systems is rather poor at simulating a prebiotic UV-environment, these systems have the advantage of delivering high fluxes, which can increase reaction rates.

5.6 APPENDIX B: CYANOCUPRATE MECHANISM

Taking the aqueous solutions to be composed of cyanocuprate species with n cyanides per copper(I), we can write the steps of the cycle as:



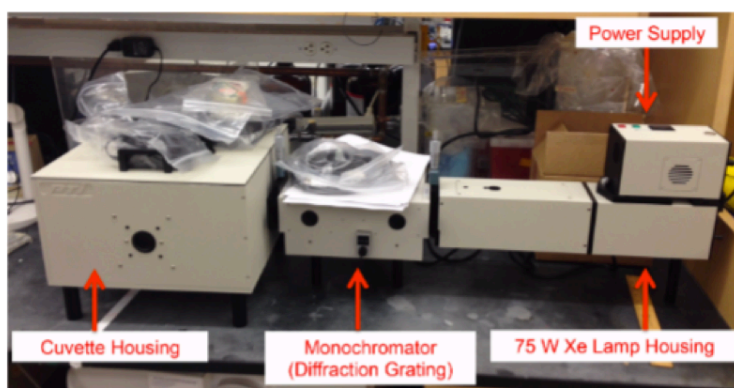


Figure 5.5.1: Optical Building Blocks 75W Tunable PowerArc lamp used for irradiation experiments with varying wavelengths. A xenon arc lamp is used in conjunction with a diffraction grating to split the light into its spectrum. Adjusting the position of the grating with respect to the exit slit allows for tunable wavelength selection.

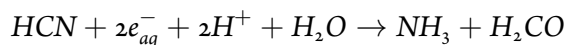


Figure 5.5.2: The Rayonet RPR-200 Photochemical Reactor has a maximum of 16 lamps surrounding a central reaction chamber. The lamps used in this study were mercury emission lamps, with primary emission at 254 nm. This reactor is the same system as used by Ritson and Sutherland [276].

The net reaction is:



The free HCN present in solution at equilibrium acts as a scavenger for the solvated electrons, preventing their recombination with the oxidized copper centers, according to the following equation.



As a consequence of the fact that HCN is limiting and is being depleted from solution as the photoprocess progresses, reaction (iii) becomes inhibited, and the concentration of the cyanocuprate species with higher coordination numbers of cyanide begins to decrease. By monitoring the concentration of cyanocuprate species over time, we can quantify the apparent rate of the cycle. The absorbance and concentration of cyanocuprate species are related by:

$$A = \epsilon cl$$

, where A is the absorbance, ϵ is the extinction coefficient, l is the path length, and c is the concentration. Differentiating with respect to time gives:

$$\frac{dA}{dt} = \epsilon l \frac{dc}{dt}$$

Thus, the change in concentration with time is related to the change in absorbance with time as:

$$\frac{dc}{dt} = \frac{dA/dt}{\epsilon l}$$

The initial rates of the reactions were all measured in this fashion. We monitored the reaction at 234 nm. We used a standard curve to relate absorbance at 234 nm to concentration of cyanocuprate complexes. The extinction coefficients of the evolving compounds, like cyanogen and formaldehyde, are negligible in this region, in comparison with those of the cyanocuprates. We then

assumed that the rate of solvated electron production is proportional to the observed decrease in cyanocuprate complexes.

5.7 APPENDIX C: UV/VIS SPECTROSCOPY

5.7.1 IRRADIATION EXPERIMENTS ANALYSIS

For the irradiation wavelength experiments, UV-Vis spectra were obtained with an Amersham Science Ultrospec 3100 Pro over the span of 3.5 hours of irradiation, as described in 5.5. The absorption spectrum of the copper cyanide solution contains maxima at 210 and 234 nm. We elected to use the 234 nm feature to look at the kinetics of the reaction. The concentration, as determined by the absorption at 234 nm, was plotted as a function of time. This plot gave a linear trend, which was fit using a python fitting routine. The slope of this trendline corresponds to the negative rate of the photochemical process. This analysis was performed for each of the irradiation wavelength experiments, which included triplicate studies of each wavelength in the 215–295 nm range in 10 nm intervals. The rates from the triplicate set were averaged to obtain the overall rate, and errors were calculated from the standard deviation of the set. These rates for each irradiation wavelength, however, are not yet comparable, due to varying photon fluxes emitted by the lamp at different wavelengths. The photon flux at each wavelength was calculated by measuring the power from the lamp at a given wavelength with a ThorLabs power detector. The photon flux is then calculated as the power divided by the energy of a photon at that wavelength. We thus find the photon fluxes for each irradiation wavelength.

In a control experiment, we held the irradiation wavelength constant and varied the photon flux by changing the bandwidth of the tunable lamp setup. This experiment was done with 0.0625 mM copper cyanide, and 0.125 mM potassium cyanide at 235 nm. The rate of the reaction was plotted against the photon flux, and the trend was consistent with an approximate linear dependence (Figure 5.7.1). Nonlinear behavior of the rate with photon flux is possible, but this

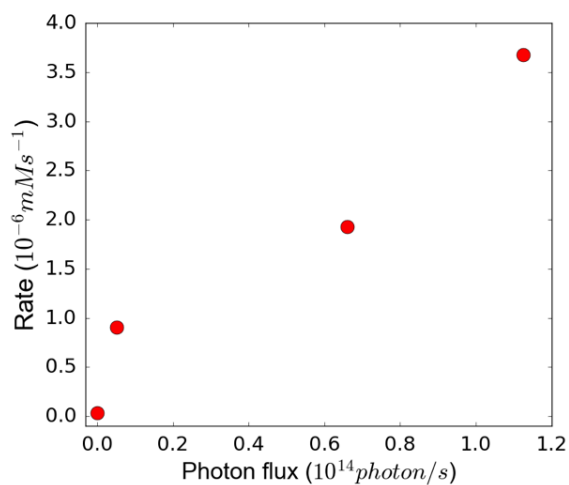


Figure 5.7.1: Rate of the cyanocuprate photochemical process, as determined by UV-Vis absorption spectra, for a constant irradiation wavelength of 235 nm, with photon flux varied by changing the bandwidth.

experiment suggested the effect, if any, would be negligible under the range of photon fluxes investigated here. The reaction rates were then normalized by dividing out the incident photon flux, resulting in reaction rates that could be accurately compared.

5.7.2 DICYANOCUPRATE VS. TRICYANOCUPRATE

The number of cyanide ligands coordinated to the copper(I) metal center can vary, generally between zero and four. Past studies of cyanocuprates find that the amount of tetracyanocuprate in solution is exceedingly low², so we neglect this species. Furthermore, the monocyano cuprate is insoluble and is assumed to precipitate out of solution rapidly when the CN^- anion is limiting. Thus, we

restrict ourselves to di- and tricyanocuprates. Past studies on the photoactivity of each species have produced ambiguous and conflicting results. We wanted to understand the composition of our solutions, so we carried out a series of titrations. To do these titrations we first prepared a solution of $63 \mu\text{M}$ CuCN and $63 \mu\text{M}$ KCN, and titrated in increasing amounts of potassium cyanide using a 110 mM solution of KCN. This solution also contained $63 \mu\text{M}$ of copper(I) in order to keep the concentration of copper(I) constant throughout the titration. We monitored the UV-Vis absorption spectrum from two to ten equivalents of cyanide to copper(I). The spectra of varying equivalences of cyanide to copper are shown in Figure 5.7.2.

We found two morphologically different spectra, which agree with past literature claims of the spectra of dicyanocuprate and tricyanocuprate⁴. The transition point between these two spectra occurred around six equivalents of potassium cyanide. At lower equivalents of potassium cyanide, the spectrum shows maxima at 210 and 234 nm , with another feature around 220 nm . The tricyanocuprate spectrum has maxima at 205 and 239 nm , with no feature in between. Figure ?? shows the ratio of absorbance at 234 nm to that at 239 nm , as a function of the number of equivalents of potassium cyanide, in order to constrain where the transition point occurs. We find that the ratio of absorbances decreases from roughly $3-6$ equivalents of potassium cyanide, before leveling off. This observation indicates that cyanide-to-copper ratios >6 are primarily tricyanocuprate, while those <3 are primarily dicyanocuprate. In the $3-6$ range, there is a mixture of the two species. Our solutions for the irradiation wavelength experiments have a cyanide-to-copper ratio of 3 . These solutions should contain a majority of dicyanocuprate species, but with some amount of tricyanocuprate, as indicated by this titration. Further experiments are needed to determine if there are differences in the photoactivities of the two species.

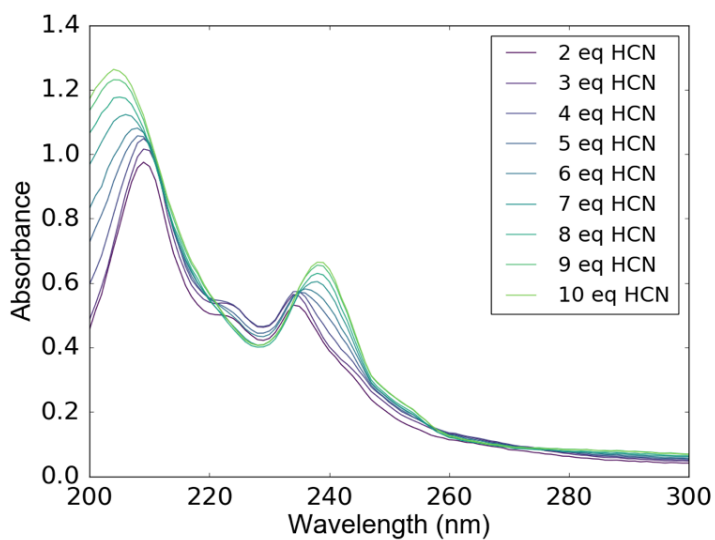


Figure 5.7.2: Absorption spectra of cyanocuprate complexes at a range of cyanide to copper(I) ratios. The concentration of copper(I) cyanide was held constant at 0.0625 mM, while the cyanide concentration was varied through titration from 2–10 equivalents of cyanide in total. The pH of the solutions was adjusted to 7.4 and temperature was held constant at 25°C. There are two main morphological spectra found in this range, which are attributed to the dicyanocuprate and tricyanocuprate. The dicyanocuprate spectrum (e.g. 3 equivalents of HCN per copper(I)) has absorption maxima at 210 and 234 nm, with another feature near 220 nm. The tricyanocuprate spectrum (e.g. 8 equivalents of HCN per copper(I)) has absorption maxima at 205 and 239 nm, with the feature at 220 nm gone.

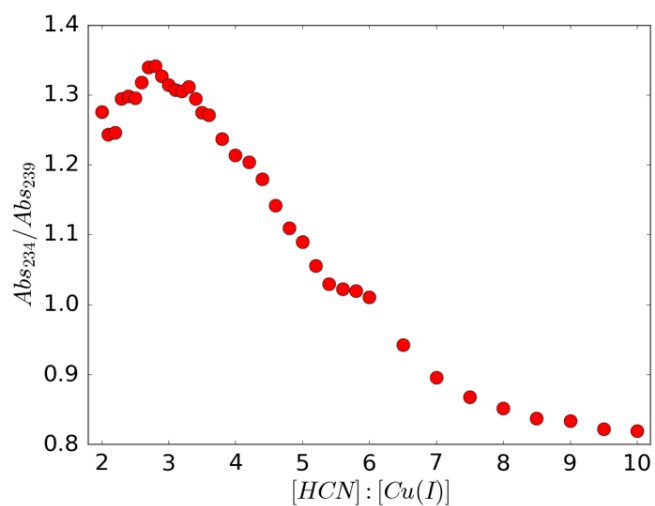


Figure 5.7.3: Ratio of absorbances at 234 nm and 239 nm as a function of cyanide-to-copper ratio. The 234 nm feature is attributed to the di-cyanocuprate species, while the 239 nm feature is due to the tricyanocuprate. At increasing cyanide-to-copper ratios, the tricyanocuprate feature becomes stronger, as is expected. The transition between species occurs from a cyanide-to-copper ratio of approximately 3–6. The concentration of copper (I) cyanide in these solutions was held at 0.0625 mM, while the total cyanide concentration ranged from 2-10 equivalents of cyanide per copper. The pH was adjusted to 7.4 and temperature was held constant at 25°C.

5.7.3 COPPER CONTROL EXPERIMENTS

In order to make sure that direct photolysis of HCN was not resulting in decreases in the UV-Vis absorption spectrum and being mistaken for the progress of the reaction, we performed a control experiment. In this experiment, a sample of 0.3125 mM HCN (made by adjusting the pH of a 0.3125 mM solution of KCN to pH = 7.4) was prepared and separated into two fractions. One fraction was irradiated in the tunable lamp at 235 nm, while the other was kept in the dark. After 25 hours of irradiation, copper(II) sulfate was added (0.0625 mM) to both the irradiated and dark samples. Copper(II) sulfate was used because it is a more soluble form of copper when the cyanide anion is limiting. When copper(II) is added to the solution, the copper(II) cyanide complexes that form are unstable and undergo elimination of cyanogen in a bimolecular fashion in order to restore the copper(I) oxidation state. Thus, when copper(II) sources are added, one equivalent of cyanide per copper(II) atom should be consumed in cyanogen production. The remaining cyanide forms copper(I) cyanide complexes, which we measure by UV-Vis absorption spectra. The UV-Vis absorption spectra of these two solutions and found that they were nearly identical (See Figure ??). This observation indicated that there was very little direct photolysis of cyanide during the irradiation. If a significant amount of cyanide had been photolyzed directly, there would not have been enough cyanide ligand in solution to complex the copper species and create similar amounts of absorption as the unirradiated sample. Given that the two spectra are nearly identical, we conclude that hydrogen cyanide photolysis was not of concern on the order of 25 hours of irradiation. Thus, the decreases in the absorption spectrum when solutions of copper cyanide were irradiated are not due to cyanide photolysis and instead are attributed to the progress of the cyanocuprate photochemical process.

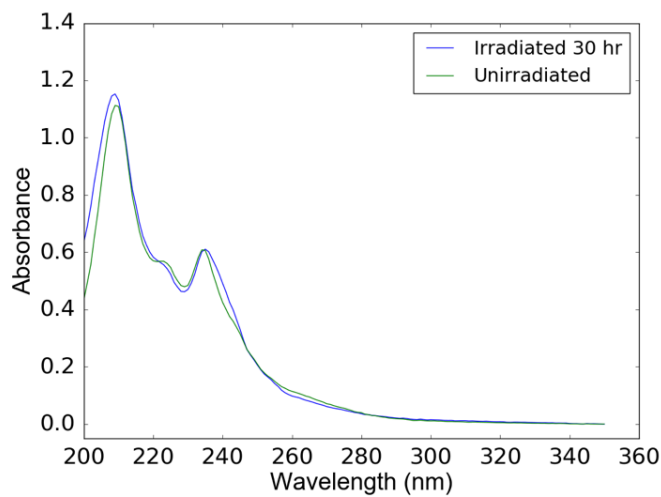


Figure 5.7.4: Absorption spectra of the control experiment to test for the photolysis of cyanide. A 0.3125mM KCN solution, pH 7.4, was separated into two fractions; one was irradiated in the tunable lamp at 245 nm for 30 hours while the other was kept in the dark. Then, copper(II) sulfate was added to each sample to give a concentration of 0.0625mM Cu(II). Copper(II) sulfate was used as a more soluble source of copper at low cyanide concentrations. The copper(II) centers eliminate cyanogen in a bimolecular fashion to convert into copper(I) centers. The baselines were adjusted such that the absorbance at 350 nm was set to 0. The absorption spectra of the two samples are very similar, indicating that very little photolysis of cyanide occurs throughout irradiation.

5.8 APPENDIX D: CYANIDE ELECTRODE MONITORING

In order to further confirm our measurement of the reaction rates with UV-Vis absorption, we additionally monitored the apparent reaction rate as a function of wavelength using both UV-Vis spectroscopy and a cyanide-selective electrode (Fisher Scientific Cyanide Solid-State Combination ISE; BNC connector; catalog number 13-620-538). We repeated experiments in triplicate at the same wavelengths tested previously (215-295 nm, 10 nm intervals, 10 nm bandwidth), monitoring by both UV-Vis absorption and the cyanide probe. For these experiments, solutions of 63 μM CuCN and 125 μM KCN, pH 7.4, were prepared anaerobically and frozen until use. For each timepoint (0, 30, 60, and 120 minutes), 0.7 mL of solution were thawed and transferred anaerobically to the quartz cuvette for irradiation. An initial UV-Vis absorption spectrum was taken prior to irradiation for the appropriate amount of time. After that time elapsed, a final UV-Vis absorption spectrum was taken and the cuvette was then transferred anaerobically into the oxygen-free glove box. Next, the solution was diluted two-fold to give a total volume of 1.4 mL. We followed the procedure outlined in the cyanide probe manual for dealing with complexes of metal cyanides. Namely, 25 μL of acetic acid were added to the 1.4 mL solution to bring it to pH 4. Then, 56 μL of 0.5 M EDTA, pH 8 were added to bring the total EDTA concentration to 0.02 M. The solution was vortexed and allowed to sit for 20 minutes to allow for chelation of the copper ions. At this point, the majority of the cyanide was assumed to be free from copper complexes. A standard curve made from cyanide solutions of known concentrations was used to calibrate the total amount of cyanide in the solutions. The samples prior to irradiation generally had cyanide concentrations of 0.11-0.12 mM, as measured by the probe. The total amount of cyanide initially put in the solutions was 0.1875 mM, so roughly 2/3 of the cyanide is detected by the probe. The difference may be due to an equilibrium between chelated and free cyanide or losses brought on by the chelating procedure. Letting the solution sit for longer amounts of time did not significantly change the concentration of cyanide reported by the probe. We also

tested for cyanide loss due to volatilization from the acidification step and found this to contribute negligible loss of cyanide. After adding EDTA and allowing time for chelation, 250 μ L of 10 M KOH were then added to bring the pH of the solution to roughly 10. The cyanide concentration was then determined from the cyanide probe, which had been calibrated with a standard curve of known potassium cyanide concentrations. The same procedure was repeated for each time point, which began from a fresh sample of the initial solution. Rates were determined from the UV-Vis data as described previously. These rates were in agreement with our past determinations of rates from UV-Vis absorption monitoring at these irradiation wavelengths. Rates were also determined from the cyanide probe readings, which were converted to a free cyanide concentration using a standard curve and corrected for the appropriate dilution factor.

The cyanide probe measures the rate of consumption of cyanide, while the UV-Vis absorption measures the concentration of cyanocuprate species. Depending on the detailed mechanism of the cyanocuprate cycle, a range of number of cyanides per cyanocuprate can be consumed. We estimate that this ranges from 0.5-2 cyanides per cyanocuprate complex, based on the suggested mechanism in Ritson Sutherland¹. This factor will influence the difference between the rates measuring the cyanocuprate vs. free cyanide concentrations. Since the detailed mechanism of the cycle is not definitively known, we do not adopt a correction factor for this fact and instead directly compare the measured rates, with the assumption that these rates should not agree precisely.

These experiments were performed in triplicate at all wavelengths. The probe consistently measured higher rates than the absorbance method, which is consistent with our expectations due to the consumption of multiple cyanide molecules per cyanocuprate as the cycle turns. Figure S7 shows the relative rate at each wavelength as determined by both the absorbance and probe methods. While the numerical values are not precisely correlated, the overall trend is consistent; namely, the cyanocuprate protoprocess is more efficient at shorter wavelengths. Wavelengths below 250 nm are 2.8 and 4.0 times faster than those above 250 nm for the probe and absorbance methods, respectively. Furthermore,

the rates we monitored with the two different methods show the same overall wavelength trend and are in general agreement when considering the unknown correction factor from the details of the mechanism and the errors inherent in the experiments.

5.9 APPENDIX E: LC-MS

While we used UV-Vis absorption spectroscopy to analyze the kinetics of the reaction, we also monitored the products of the reaction by LC-MS (Agilent 6460 Triple Quad LC/MS with Agilent 1290 Infinity HPLC). Ritson and Sutherland¹ identify the major products of the reaction after prolonged irradiation as the glycolaldehyde and glyceraldehyde derived 4-hydroxyoxazolidin-2-one and 4-hydroxy-5-(hydroxymethyl)oxazolidin-2-one, respectively (5.9.1). The 4-hydroxyoxazolidin-2-one (**6**) should always be produced in higher yields, so we elected to detect that compound. We synthesized a standard of **6** using the procedure of Ritson and Sutherland¹. We calibrated the concentration of this standard using ¹H-NMR with an NMR tube containing a coaxial insert filled with triethylamine as a standard for integration. An LC-MS method was developed to detect the product using a 4.6 x 50 mm Gemini C18 5 μm column. The flow rate was 0.3 mL/min and an injection volume of 5 μL was used and eluting solvents were A) water with 0.1% formic acid, and B) acetonitrile with 0.1% formic acid. We submitted samples (0.25 mM CuCN, 0.75 mM KCN, pH 7.4) for LC-MS analysis after prolonged irradiation (70–76 hours) at each irradiation wavelength. The [M+H]⁺ parent compound, C₃H₆NO₃⁺ (mass of 104) produced two fragments: CH₂NO⁺ (the “qualifier” compound, mass of 44) and C₂H₅O₂⁺ (mass of 61), which was used for quantitative analysis (Figure 5.9.2). The quantifier was chosen due to its higher abundance. The qualifier is used as a measure of enhanced selectivity and to reduce the chance of false positives. The synthesized standard was analyzed under the above conditions, and found to have a retention time of roughly 2.93

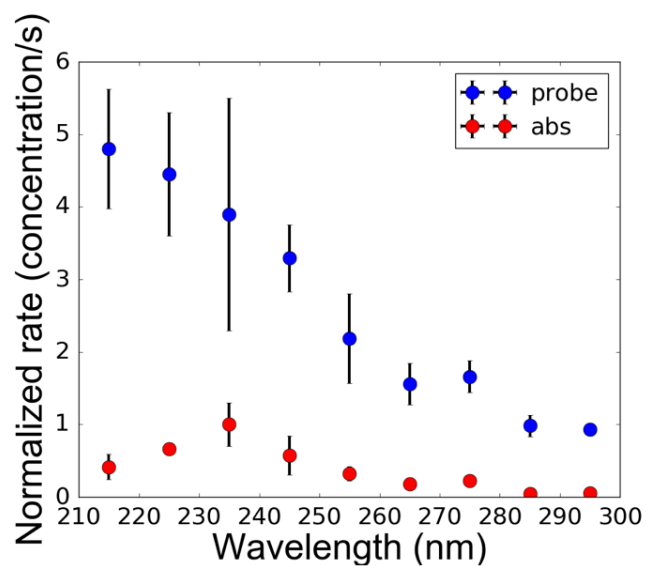


Figure 5.8.1: Relative rate of the reaction as a function of incident wavelength, normalized by photon flux, as determined by both the cyanide electrode (blue) and absorbance measurements (red). Each experiment was completed in triplicate (as described above). The points represent the average of the triplicate set, and the error bars are the error from the triplicate set. The cyanide electrode consistently measures a higher rate, due to detecting the total cyanide concentrations, while the absorbance method measures the concentration of cyanocuprate complexes. The overall wavelength dependence from the two methods is broadly consistent: the relative rate of the reaction is generally larger at lower wavelengths.

minutes (Figure 5.9.3). Irradiated samples produced peaks at the same retention time, followed by a closely eluting background peak. The peak from the target compound was integrated to avoid interference from the background peak, as shown in Figure 5.9.4. The results showed the detection of the target compound above the threshold detection limit for all irradiation wavelengths, except for the negative control of 320 nm. This set of experiments confirmed that the reaction proceeds in the same manner towards producing the same products at all irradiation wavelengths between 200 and 300 nm.

5.10 APPENDIX F: ATMOSPHERIC MODELING

When carrying out the calculation of weighted surface intensity, we used code produced and described in Ranjan and Sasselov [259]. This code takes as input a user-specified atmospheric profile (composition, temperature, and pressure), and runs it through a two-stream clear-sky radiative transfer model to compute relevant spectral quantities, including total surface flux and total surface intensity. The total surface radiance from the model was integrated in 10 nm wavelength bins to get the total surface radiance value to multiply by the normalized relative reaction rates, in order to get the relative rate of solvated-electron production. These values were normalized such that the maximum was equal to 1. The normalized rates plotted against irradiation wavelength are often referred to as an action spectrum, which is a measure of the activity of a reaction as a function of wavelength. The two atmospheres selected for use in this study include the modern Earth atmosphere and a sample prebiotic atmosphere, from Rugheimer et al. [285] The exact chemical compositions of these atmospheres can be found in Figure 5.2.3.

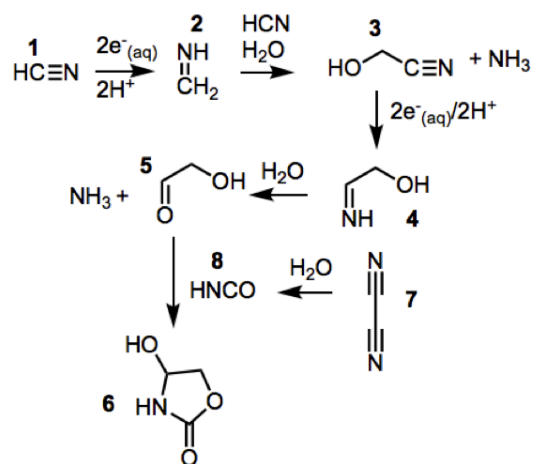


Figure 5.9.1: The systems chemistry process that occurs during this reaction reduces hydrogen cyanide 1 first to methanimine 2 by action of solvated electrons. Methanimine hydrolyzes to formaldehyde which reacts with HCN to yield cyanohydrin 3, and this product undergoes further reduction by solvated electrons to imine 4. Glycolaldehyde 5 is produced by another round of homologation. Oxazolidinone 6 forms by cycloaddition of glycolaldehyde with cyanic acid 8, a product produced by hydrolysis of cyanogen 7. 6 accumulates in solution and is the product we detect by LC-MS.

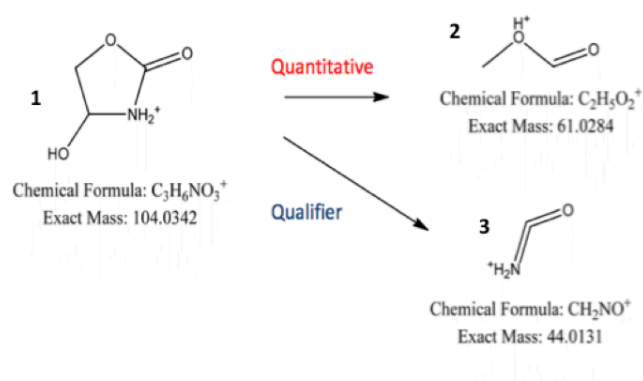


Figure 5.9.2: Fragmentation of the protonated oxazolidinone (mass of 104) to the fragment used for quantification ($C_2H_5O_2^+$, mass of 61) and the qualifier fragment (CH_2NO^+ , mass of 44). The target compound, 1, was fragmented into 2 and 3. Quantification was performed using compound 2.

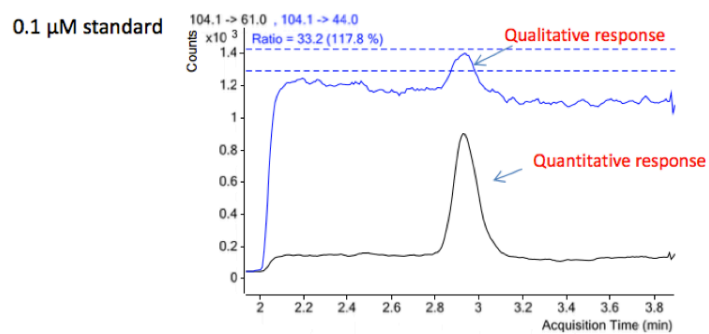


Figure 5.9.3: LC-MS chromatogram for a synthetically prepared standard of 0.1 μM of 6. The black curve shows the trace for the quantifying fragment (mass of 61), while the blue shows that of the qualifier fragment (mass of 44).

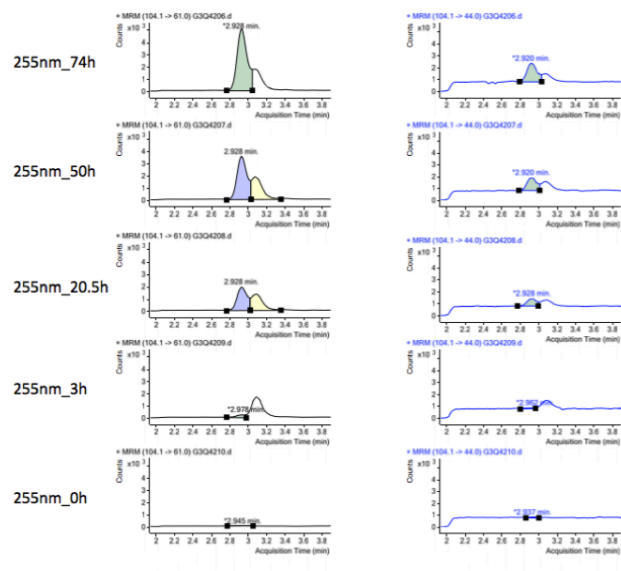


Figure 5.9.4: Sample LC-MS chromatograms for 255 nm irradiation. The experiment was sampled at times of 0, 3, 20.5, 50, and 74 hours. The black curves show the quantifying fragment (mass of 61), while the blue curves show the qualifier fragment (mass of 44). The appropriate peak was identified and calibrated by standards of synthesized oxazolidinone 6 ($C_3H_6NO_3^+$). The peak eluting behind the peak of the target is likely due to a background molecule and does not affect the results.

6

UV-driven deamination of cytidine ribonucleotides under planetary conditions

Abstract

A previously proposed synthesis of pyrimidine ribonucleotides makes use of UV light to convert β -d-ribocytidine-2',3'-cyclic phosphate to β -d-ribouridine-2',3'-cyclic phosphate, while simultaneously selectively degrading synthetic byproducts. Past studies of the photochemical reactions of pyrimidines have employed mercury arc lamps, characterized by narrowband emission centered at 254 nm, which is not representative of the UV-environment of the early Earth. To further assess this process under more realistic circumstances, we have investigated the wavelength dependence of the

UV-driven conversion of β -d-ribocytidine-2',3'-cyclic phosphate to β -d-riouridine-2',3'-cyclic phosphate. We use constraints provided by the planetary environments to assess the implications for pyrimidine nucleotides on the early Earth. We find that the wavelengths of light (255-285 nm) that most efficiently drive the deamination of β -d-ribocytidine-2',3'-cyclic phosphate to β -d-riouridine-2',3'-cyclic phosphate are accessible on the surface of the Hadean-Archaeon Earth for CO₂-N₂ dominated atmospheres. However, continued irradiation could eventually lead to low levels of ribocytidine in a low-temperature, highly irradiated environment, if production rates are slow. ¹

6.1 INTRODUCTION

THE ELUCIDATION OF A POTENTIALLY prebiotic synthetic pathway for activated pyrimidine ribonucleotides [256] from simple starting materials provided one possible solution to a long-term issue with the RNA world: the synthesis of pyrimidine monomers. Recently, substantial progress has been made toward the potentially prebiotic synthesis of canonical and non-canonical RNA nucleosides [18] and nucleotides [19, 158, 256, 325, 384]. Powner et al. [256] achieved the synthesis of β -d-ribocytidine-2',3'-cyclic phosphate (denoted hereafter as C>p) from simple precursors, i.e. glycolaldehyde, d-glyceraldehyde, cyanamide, cyanoacetylene, and phosphate. The irradiation of the mixture that forms C>p selectively degrades non-canonical ribonucleotide byproducts and affords partial conversion of C>p into β -d-riouridine-2',3'-cyclic phosphate (denoted as U>p). Later work also utilized partial conversion of C>P to U>p under UV irradiation, while additionally harnessing advantageous photoanomerization chemistry at an earlier synthetic step to increase the yield of the biologic β -anomer via photoanomerization of α -2-thioribocytidine at a 76% efficiency [384]. Powner et al. [256] and Xu et al. [384] used mercury arc lamps (primary emission at 254

¹This thesis chapter is in press as: Z. R. Todd, A. C. Fahrenbach, S. Ranjan, C. J. Magnani, J. W. Szostak and D. D. Sasselov (2020) *Astrobiology*, *In press*.

nm) as a source of UV light, but such narrowband emission is not consistent with the spectral flux of the Sun on the surface of the early Earth. The lack of O₂ and O₃ in the atmosphere would have allowed mid-range UV light (200-300 nm) to penetrate to the surface of the planet [55, 260]. This atmospheric scenario begs the question posed by Ranjan and Sasselov [259]: would the UV photochemistry (here, specifically the partial conversion of C>p into U>p) actually occur at a realistic rate under the UV environment on the Hadean Earth? In this study, we address the photochemistry of C>p over a range of UV wavelengths and use this data to model the lifetime and concentrations of C>p under various environmental conditions.

The effect of UV irradiation on the pyrimidine nucleotides/nucleosides/nucleobases has been the focus of intense study, mostly due to an interest in DNA/RNA damage. In addition to the UV-induced formation of pyrimidine dimers, UV light can cause chemical changes to individual nucleobases, nucleosides, and nucleotides. Early work revealed that UV irradiation of uridine produces a hydrated species, namely 6-hydroxy-5,6-dihydrouridine [82, 374]. This photo-generated hydrate can be converted back into uridine thermally or under highly acidic conditions [315]. Similarly, the product of UV-irradiation of cytidine was postulated to be 6-hydroxy-5,6-dihydrocytidine based on hydrolysis to the uridine hydrate derivative [141] and borohydride reduction [204]. The irradiation product of cytidine was confirmed to be 6-hydroxy-5,6-dihydrocytidine by direct NMR characterization [176].

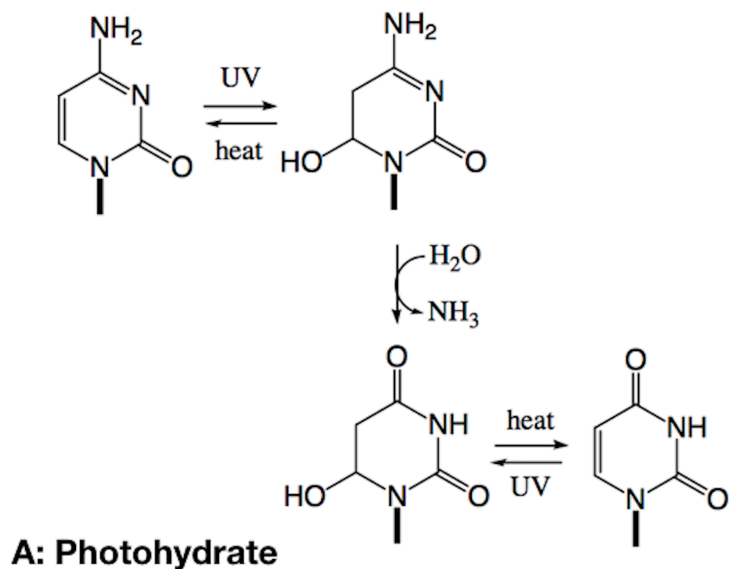
Upon UV irradiation, the 270 nm band in the absorption spectrum of cytidine decreases, while a band at 240 nm appears [314, 371, 375], resulting from absorption of the photohydrate, 6-hydroxy-5,6-dihydrocytidine (see Figure 6.1.1A). This photohydrate is unstable and can either revert back to cytidine, or alternatively, deaminate to generate the uridine photohydrate [302]. The photohydrate of uridine, 6-hydroxy-5,6-dihydrouridine, then reverts back to uridine, but on longer timescales than the cytidine photohydrate [74].

Though cytosine, cytidine, and 5'-CMP form a photohydrated intermediate

upon UV irradiation, C>p was hypothesized by Powner et al. [256] to form a different intermediate, in which the 5-hydroxyl adds intramolecularly to C6 to give a bridged ether (Figure 6.1.1B). Powner et al. [256] hypothesized that elimination of the 5-OH in the postulated photoproduct is a slower process in comparison to the dehydration of the analogous photohydrate, causing the C>p to undergo fewer cycles of photoexcitation, allowing some degree of protection from UV damage. Powner et al. [256] observed that C>p is more stable to UV photodegradation than other cytosine nucleotides and nucleosides, including α -ribocytidine-5'-phosphate, β -arabinocytidine, β -arabinocytidine-5'-phosphate, and α -ribocytidine-2',3'-cyclic phosphate, suggesting that UV may have played a role in selecting the canonical nucleotide stereochemistry due to increased stability. This is not the only suggestion of UV light playing a role in selection; in addition, the canonical nucleobases have shorter excited state lifetimes upon UV irradiation than some other non-canonical bases [20]. Again, this promotes increased stability towards photoreactions of the canonical nucleobases, suggesting that UV potentially acted as a selection pressure on the early Earth [170, 275, 384].

In this study, we do not attempt to differentiate between the two possible intermediates, the photohydrate or the bridged 5-6 cyclic molecule (Figure 6.1.1), as the identity of the intermediate is not critical to the overall implications for the final products of the reaction and will not change our results. We focus on the UV-mediated partial conversion of β -d-ribocytidine-2',3'-cyclic phosphate to β -d-ribouridine-2',3'-cyclic phosphate. In particular, we examine the UV wavelength dependence of this reaction in the context of the UV environment on the early Earth to assess the planetary implications for this reaction. We then use this data to model the concentrations and lifetimes of C>p for different environments on the early Earth.

To investigate the UV-driven conversion of C>p, a 50 μ M solution of C>p in degassed, deionized water was prepared. Aliquots of this solution were irradiated from 215-295 nm individually in 10 nm intervals with a 10 nm bandwidth. To



B: 6,5'-ether linked intermediate

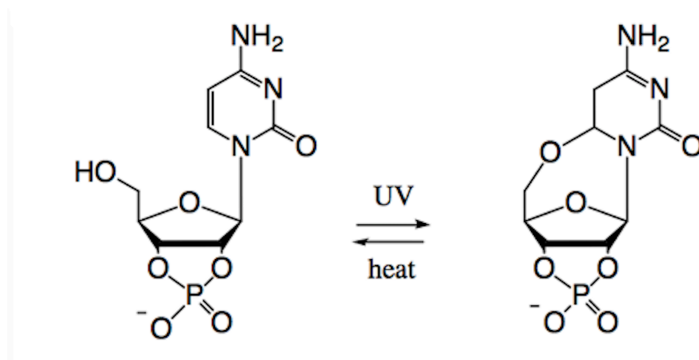


Figure 6.1.1: Two potential mechanisms for the photochemical processing of β -d-ribocytidine-2',3'-cyclic phosphate. (A) Mechanism for cytidine, cytosine, and 5-CMP, where UV irradiation produces the photohydrate (e.g. 6-hydroxy-5,6-dihydrocytosine). This photohydrate can undergo deamination to the corresponding uridine photohydrate. Both photohydrates can be converted into the canonical nucleobase through thermal dehydration (the rate of thermal recovery of C is much greater than that of U). (B) Structure of the hypothesized intermediate upon UV irradiation of β -d-ribocytidine-2',3'-cyclic phosphate, suggested by Powner et al. (2009). Similarly, this intermediate could undergo deamination and then thermal recovery to β -d-ribo-uridine-2',3'-cyclic phosphate.

perform the irradiation, a xenon arc lamp coupled with a diffraction grating acting as a monochromator to allow for tunable wavelength selection was used (as in Todd et al. [350]). The flux from the lamp over the wavelength interval 265-285 nm is within an order of magnitude of the surface flux expected over the same wavelength range on the surface of the early Earth [260].

Solutions were monitored by UV-Vis spectroscopy at 15 minute intervals throughout irradiation, for a total duration of 2 hours. Upon irradiation, the absorption band centered at 270 nm from C>p decreases and an absorption band at 240 nm grows in. These spectral changes were used to determine the concentrations of the starting material and photogenerated intermediate as a function of irradiation time, through experimentally determined extinction coefficients for both species (with concentrations determined by ³¹P-NMR, see section 6.5). Once extinction coefficients were determined, the concentrations of the two species were determined from the UV absorption at the maximum wavelengths for the intermediate and starting material by solving a system of two equations, as described below:

$$A_{240nm} = \epsilon_{C>p,240nm}c_{C>p}l + \epsilon_{int,240nm}c_{int}l$$

$$A_{270nm} = \epsilon_{C>p,270nm}c_{C>p}l + \epsilon_{int,270nm}c_{int}l$$

We then determined the observed rate constant of the reaction by plotting the logarithm of concentration against time for each wavelength. Irradiations at each wavelength were performed in triplicate, in order to obtain an average rate constant and error. In order to compare reaction rates at different wavelengths, the observed rate constants were normalized by photon flux to get the rate constant, since the lamp used does not provide constant fluxes at all wavelengths. To do this normalization, powers at each wavelength were measured with a Newport power detector, then converted to a photon flux through the relation between wavelength and energy of a photon.

For experiments testing the thermal reversion of the photoproduct of C>p, solutions of 50 μM C>p were irradiated in a Rayonet reactor (RPR-200, 254 nm,

mercury lamps), for 15 minutes. Cuvettes were then placed in a Cary UV-Vis spectrometer with adjustable temperature control. Temperatures were varied from 25-45^{circ} Celsius, in 5° intervals. Each temperature tested was monitored for >16 hours. UV-Vis absorption spectra were recorded and used to calculate concentrations to then determine reversion rates.

To study the partitioning of the photochemically-generated intermediate between C>p and U>p, solutions of 50 μM β-ribocytidine-2',3'-cyclic phosphate were irradiated for varying irradiation times (0, 10, 30, 60, 90, and 120 minutes) in the Rayonet reactor at 254 nm. After the set irradiation time elapsed, the samples were placed in a Cary UV-Vis spectrometer with adjustable temperature control. Cuvettes were heated at 60°C for 100 hours total, with UV-Vis monitoring every 30 minutes. The concentrations of C>p, U>p, and the photochemically generated intermediate were determined from solving a system of three equations from the absorption values at the maximum absorption wavelengths of the three species (240, 260, and 270 nm for the intermediate, U>p, and C>p, respectively):

$$A_{240nm} = \epsilon_{C>p,240nm}c_{C>p}l + \epsilon_{int,240nm}c_{int}l + \epsilon_{U>p,240nm}c_{U>p}l$$

$$A_{260nm} = \epsilon_{C>p,260nm}c_{C>p}l + \epsilon_{int,260nm}c_{int}l + \epsilon_{U>p,260nm}c_{U>p}l$$

$$A_{270nm} = \epsilon_{C>p,270nm}c_{C>p}l + \epsilon_{int,270nm}c_{int}l + \epsilon_{U>p,270nm}c_{U>p}l$$

We note that the reaction likely contains another species: the uridine form of the intermediate. C>p photochemically generates the cytidine intermediate (either cytidine photohydrate or cytidine bridged ether intermediate, see Fig. 6.1.1). This structure then deaminates to give the uridine form of the intermediate. Thermal recovery generates U>p from any deaminated intermediate while regenerating C>p from any cytidine intermediate that did not deaminate. The uridine form of the intermediate does not absorb significantly in the 230-300 nm range (section 6.6), so it should not interfere with the concentration determinations through UV absorption measurements.

6.2 RESULTS

6.2.1 WAVELENGTH-DEPENDENT UV CONVERSION

Irradiation of $50 \mu\text{M}$ C>p causes the initial absorption feature at 270 nm to decrease, while a band at 240 nm grows in (see Figure 6.2.1a). A clear isosbestic point is observed at 250 nm. This observation suggests that C>p is directly converted to the photoproduct, and only one photoproduct is formed initially. ^{31}P NMR spectroscopy supports this supposition by the fact that irradiation of C>p initially results only in one detectable ^{31}P resonance other than the starting material. These spectral changes, coupled with experimentally determined extinction coefficients for the starting material and photoproduct (section ??) can be used to determine their concentrations during irradiation. The slope of the best fit line for $\ln([\text{C>p}])$ as a function of time gives the observed rate constant (Figure 6.2.1B). Solutions were irradiated at 215-295 nm (10 nm interval, 10 nm bandwidth) in triplicate. Figure 6.2.2 shows the rate constant (for a constant photon flux of 5×10^{14} phot/s/cm², expected from 210-300 nm based on the baseline early Earth scenario from Ranjan and Sasselov [260], which uses atmospheric profiles from Rugheimer et al. [285]) across a range of irradiation wavelengths, with the points representing the average of the triplicate set and the errors estimated by the standard deviation. The rate constant is maximum at 265 nm, which is consistent with expectations based on the absorption maximum of the starting material. The rate constant decreases significantly at wavelengths shorter than 245 nm and longer than 275 nm.

We next sought to compare the experimentally determined rate constants at various irradiation wavelengths with the spectral flux available on the surface of the early Earth from the Sun. A two-stream radiative transfer model produced and described in Ranjan and Sasselov [260] was used to calculate the surface spectral radiance through a sample N₂/CO₂-dominated (0.9 bar N₂, 0.1 bar CO₂) prebiotic atmosphere; the surface UV environment is robust to the

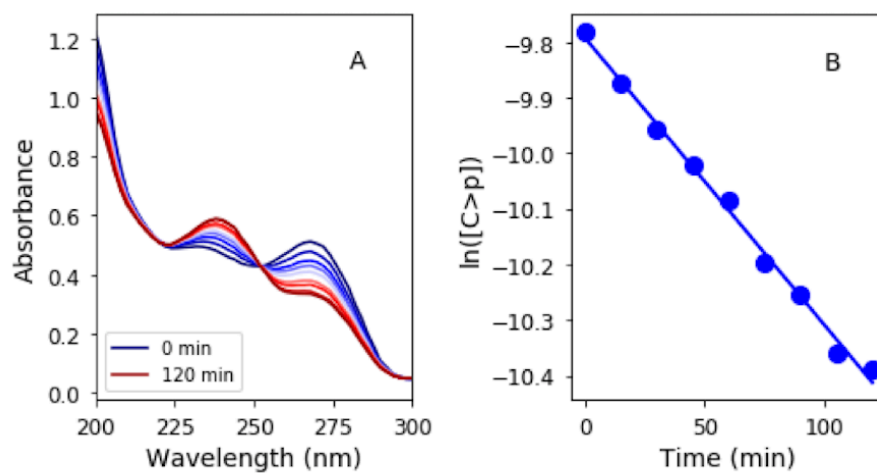


Figure 6.2.1: (A) UV absorption spectrum with irradiation at 265 nm in the tunable lamp setup. As irradiation is continued, the absorption at 240 nm increases while that at 270 nm decreases. This observation is due to the accumulation of intermediate and depletion of starting material, respectively. The concentrations of starting material and intermediate can be calculated for each time point from the UV-Vis absorption spectra. (B) Plot of logarithm of concentration of $C>p$ with irradiation time. The slope of the best-fit line gives the observed rate constant.

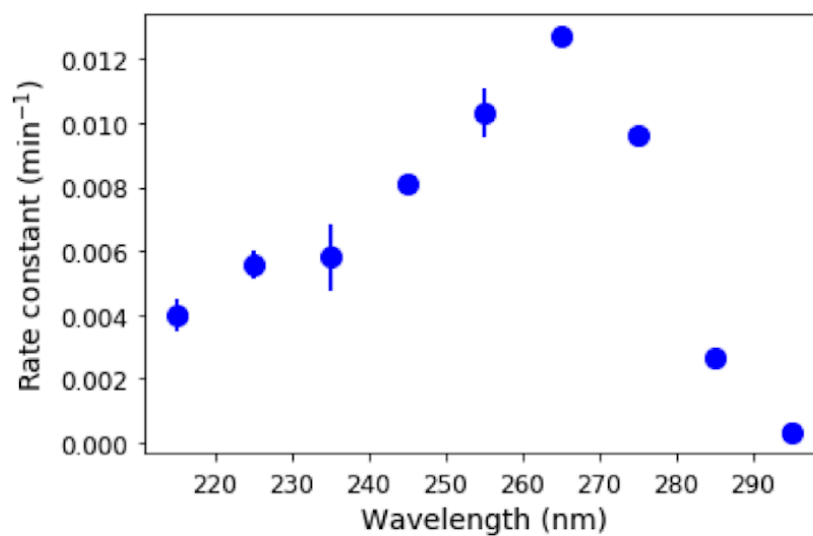


Figure 6.2.2: Rate constant of UV-driven reaction of C>p to the intermediate photoproduct as a function of irradiation wavelength, for a constant photon flux from 210–300 nm. The rate constant is greatest at a wavelength of 265 nm, as might be expected from the maximum absorption of C>p near this wavelength.

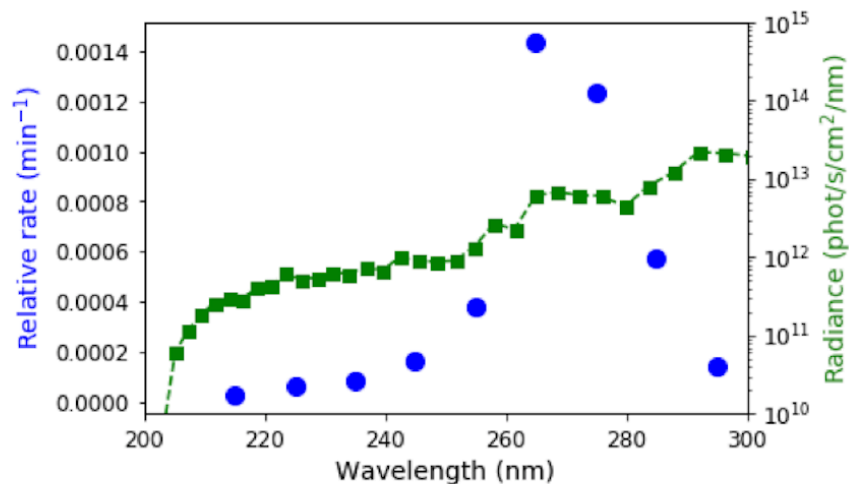


Figure 6.2.3: The relative rate of the conversion of C>p into the photochemically generated intermediate, taking into account the spectral surface flux (green squares) and the relative rate constants at varying wavelengths are shown in the blue points. The relative rate is maximum at 265 nm. The effective range of radiation for driving this reaction is from roughly 255-285 nm.

uncertainties in early Earth's atmospheric state as a result of saturation of absorption of wavelengths <204 nm due to CO₂, resulting in mid-range UV wavelengths from ≈ 200 -300 nm present on the surface of the planet [259, 260]. The intensities of longer wavelength UV light are greater than that of shorter wavelengths on the surface of the planet (see green line in Figure 6.2.3). We then integrated the surface radiance using the same 10 nm bins that the experiments employed, and calculated the relative rate of the reaction, defined as the product of the experimental rate and the integrated surface radiance (blue points in Figure 6.2.3). The relative rate is still maximum at 265 nm, and the most productive wavelengths for driving this photochemical reaction in our model for the surface of the early Earth are 255-285 nm.

6.2.2 THERMAL REVERSION

Upon continued UV-irradiation of C>p, the photochemically generated intermediate can either revert back to C>p thermally, deaminate to form the uridine-derivative of the photochemically generated intermediate, or possibly undergo a second photochemical reaction. The photochemically generated uridine intermediate is more thermally stable than the cytidine photochemically generated intermediate [74], and hence the production of U>p requires prolonged heating. We investigated the thermal reversion of the UV-generated intermediate back to C>p at different temperatures to determine the activation energy for this reaction. 50 μ M C>p solutions were irradiated in a RPR-200 Rayonet reactor (254 nm) for 15 minutes, until converted to at least 90% intermediate (as determined by UV-Vis spectroscopy). Then, solutions were incubated in the dark at temperatures from 25-45°C, in 5° intervals for 16-24 hours, while being monitored every 15-30 minutes by UV-Vis absorption spectroscopy. Concentrations of the starting material and UV-generated intermediate were determined and fit with exponentials as a function of incubation time. Figure 6.2.4A shows the concentration of the intermediate and starting material during heating at 35°C. The rates for thermal reversion to C>p were determined for various temperatures to generate an Arrhenius plot (Figure 6.2.4B). The activation energy for this reaction was determined from both the appearance of C>p and the disappearance of the intermediate, as 84.0 ± 10.5 kJ/mol and 86.2 ± 11.7 kJ/mol, respectively, i.e. the same within error. These were determined in the same reaction, with rates and activation energies calculated from the increase in C>p and the decrease in the intermediate, respectively. We did not see the appearance of U>p during the course of these experiments, since this requires elevated temperatures for longer amounts of time.

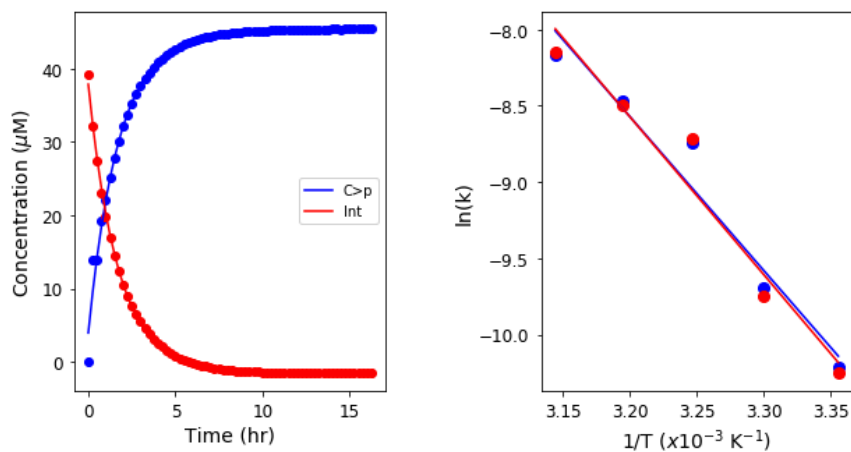


Figure 6.2.4: (A) Concentrations of $C_{>p}$ and the photo-generated intermediate during thermal recovery at 35°C . The concentrations are fit by exponential functions, which allow the rate constant of recovery to be calculated for a given temperature. (B) Arrhenius plot for both the rate of recovery of C and the rate of disappearance of the intermediate. The logarithm of the rate constant is plotted as a function of inverse temperature. The activation energies can be calculated from the slopes of the trendlines, giving activation energies of and kJ/mol for $C_{>p}$ and the intermediate, respectively, i.e. the same within error.

6.2.3 CYTIDINE-DERIVATIVE VS. URIDINE-DERIVATIVE PARTITIONING

Upon UV irradiation of C>p, the photochemically generated intermediate can deaminate to give the uridine form of the intermediate, which is more thermally stable to dehydration and subsequent recovery to the canonical nucleotide than the cytidine intermediate. Accordingly, we next attempted to see the generation of U>p by irradiating C>p and then incubating the solution for a prolonged period at elevated temperatures. A solution of 50 μ M C>p was irradiated for 90 minutes in the Rayonet RPR-200 reactor (254 nm), then allowed to sit in the dark at 60°C for 100 hours. Figure 6.2.5A shows the UV-Vis absorption spectra of this solution during the heating period following irradiation. The concentrations of C>p, the photochemically-generated cytidine intermediate, and U>p were extracted from the UV-Vis spectra throughout the incubation and are shown in Figure 6.2.5B. The intermediate is quickly returned to C>p, while it takes longer for U>p to appear, likely due to the fact that the uridine photochemically-generated intermediate is more thermally stable. We do not attempt to quantify the uridine intermediate, as it does not show a clear absorption peak. It does not absorb significantly in the 230-300 nm window (see section 6.6), so the presence of this species in the reaction should not affect our overall determinations of the concentrations of the other species which do absorb through the UV spectra. After 100 hours at 60°C, the fractions of C>p and U>p reach a constant ratio. To better understand the partitioning between C>p and U>p and the role of irradiation, we allowed the initial irradiation time prior to incubation to vary. After irradiation (for 0, 10, 30, 60, 90, or 120 min), samples were incubated at 60°C for 100 hours and monitored by UV-Vis. Figure 6.2.6 shows the final concentration of C>p and U>p after heating (100 hr, 60°C) at various irradiation times. C>p is depleted more with increasing irradiation times, while the level of U>p after incubation seems to be approximately constant across different irradiation times. At the longer irradiation times, the proportion of C>p and U>p reaches a value of roughly 61% C and 33% U, though the total amount of material decreases with increasing irradiation times. This indicates

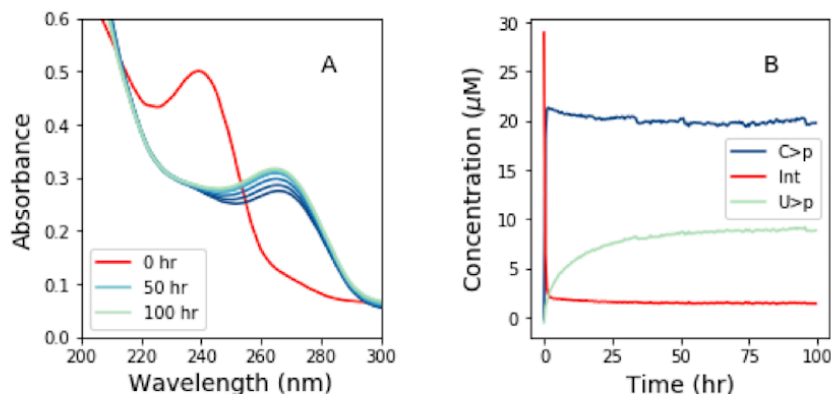


Figure 6.2.5: (A) Absorption spectra for various incubation times at 60° C after irradiation at 254 nm for 90 minutes. (B) Concentration of intermediate, C>p, and U>p as a function of incubation time, extracted from the absorption spectra. As heating is continued, the absorption spectra show increasing absorption at 260 nm, consistent with a thermal recovery of the deaminated intermediate to β -d-ribose-2',3'-cyclic phosphate.

that prolonged irradiation will deplete C>p, and may also limit the amount of U>p generated, if production rates are slow.

6.2.4 MODEL DAY/NIGHT CYCLE

We next studied what happens to C>p under repeated photocycling/thermocycling. We began with 50 μ M C>p and alternated between irradiating in the Rayonet reactor (254 nm) for 15 minutes, and incubating at 35° C for 24 hours, repeating for a total of eight cycles. Figure 6.2.7A shows the absorption spectra for the solution immediately after each irradiation cycle, with the absorption spectrum of the starting material (before irradiation) shown by the dashed black line. Figure 6.2.7B shows the absorption spectra after the completion of the thermal step (24 hours at 35° C after irradiation). With repeated cycles of irradiation and thermal recovery, material is

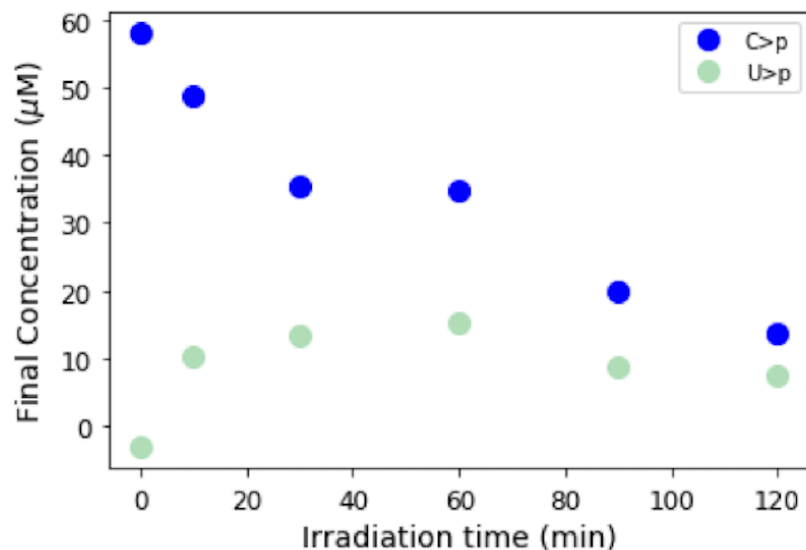


Figure 6.2.6: Final concentration of C>p and U>p after 100 hours of incubation at 60° C, following irradiation for varying amounts of time (0, 10, 30, 60, 90, 120 minutes). During this longer heating step, the absorption spectra show increasing absorption at 260 nm, which indicates a recovery of the uridine-intermediate to U>p. Longer irradiation times lead to loss of overall material likely due to irreversible photodamage. At longer irradiation times, the ratios of C>p to U>p appear to plateau near 61% C>p and 33% U>p, after 100 hours of incubation at 60°C.

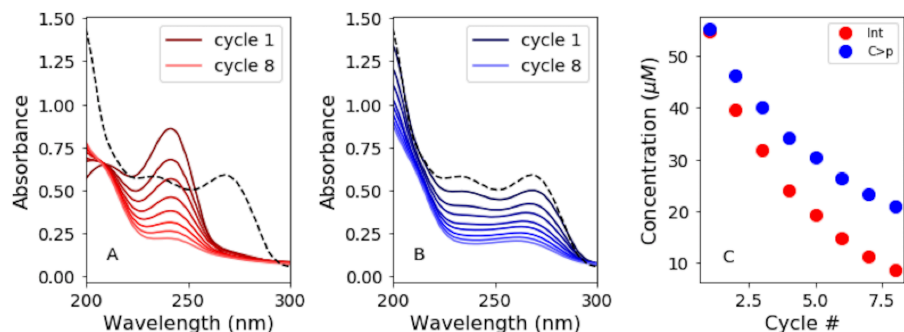


Figure 6.2.7: Degradation of material over repeated cycles of irradiation and thermal recovery. (A) Absorption spectra of the irradiated species (primarily intermediate) after each 15 minute irradiation cycle. Each irradiation is followed by thermal recovery to make one full cycle. (B) Absorption spectra of the recovered (primarily starting) material as a function of cycle, after 24 hours at 35°C. The black dotted line shows the absorption spectrum of the initial material (before irradiation). (C) Concentration of the intermediate and C>p after irradiation and thermal recovery, respectively, as a function of cycle number. With repeated cycles, material is lost; leaving roughly 88% of C>p recovered with each successive cycle.

lost, as seen by the decreasing absorption intensities. These spectra were converted to concentrations of C>p and the photochemically-generated intermediate after each cycle (Figure 6.2.7C). On average, only 88% of the material is recovered after a given cycle, leading to significant depletion of C>p by the end of the eighth cycle. The lost material is likely converted to the corresponding uridine intermediate or other irreversible photodamage. U>p is not observed under these experimental conditions, since generation of U>p from the uridine intermediate requires elevated temperatures for prolonged periods.

This loss of material leads to a potential limitation of UV-deamination of pyrimidine ribonucleotides. If a fixed stock of C>p undergoes repeated cycles of irradiation, it will ultimately be lost to U>p or other photoproducts, limiting the overall amount of C>p that could be available for prebiotic chemistry. This situation would be mitigated if the production of C>p occurs at a similar rate to

the UV-induced loss. We asked what production rates of C>p are needed to sustain a steady state under a variety of planetary environmental conditions by simulating a day-night cycle expected on the early Earth (16 hours total, e.g. Lathe [168]). Figure 6.2.8 shows the concentration of C>p (initially assumed to be 1 mM) under simulated day-night cycles. The net irradiation loss rate is calculated by weighting the experimentally-determined rate constants by the solar irradiation flux calculated for the surface of the early Earth, and integrating over 210-300 nm. The photochemical rate is assumed to be temperature-independent, while the dark reaction is not. The thermal recovery during the dark is modeled at three temperatures: 15, 25, and 35°C. With each cycle, we impose a maximum recovery of 88% β -d-riboctidine-2',3'-cyclic phosphate, as indicated by our experimental results. This repeated photocycling depletes the initial stock of C>p on varying timescales depending on the temperature, where higher temperatures are more favorable for longer residence times of C>p. The yellow shaded region in Figure 6.2.8 indicates levels of C>p > 1 μ M, which is the threshold where prebiotic chemistry is thought to be plausible. C>p (initially at 1 mM) is expected to be > 1 μ M for 68, 130, and 1010 hours for T=15, 25, and 35°C, respectively. We find these results to be insensitive to the assumed length of the day.

This model can also be used to determine the production rates necessary in order to sustain a steady state of C>p at various concentrations, by equating the production and destruction rates. In order to maintain 0.1 mM C>p, production rates need to be from 0.3–4.4 μ M/hr, depending on temperature (see Table 1). The required production rate scales linearly with steady state concentration, e.g. to obtain 1 mM C>p at steady state, production rates need to be 3.0–44 μ M/hr for the temperature range of 15–35°C. Past work on the prebiotic synthesis of molecules including these nucleotides has generally not focused on rates, but rather yields. These production rates offer a rough guideline as to what is required in order for the prebiotic chemistry to maintain a fairly constant stock of material without significant depletion under self-consistent conditions, and

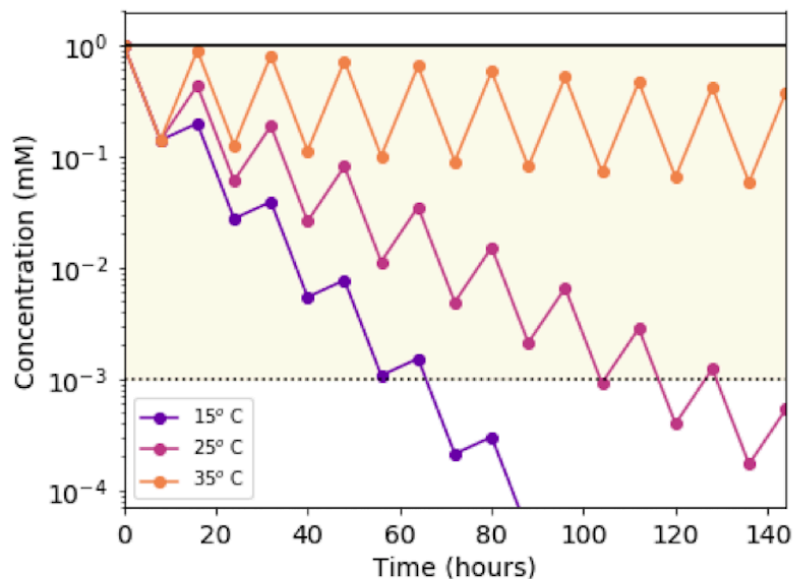


Figure 6.2.8: Model of the concentration of C>p through successive day/night cycles (16 hours) from the experimentally-determined wavelength- and temperature-dependent rates. The concentration of C>p is calculated as a function of time for temperatures of 15, 25 and 35°C. The irradiation degradation rate is determined by weighting the measured rate constants by the solar irradiation flux expected on the surface of the early Earth and integrating from 210-300 nm. We include degradation, by only allowing 88% of C>p to return with each successive cycle, leading to an overall loss with time. During these successive irradiation cycles, we would expect accumulation of the corresponding uridine intermediate, which could then be recovered as U>p upon prolonged heating. The yellow shaded region indicates concentrations above 1 μ M, which may be enough for prebiotic chemistry to occur.

without invoking additional environmental constraints.

6.3 DISCUSSION

Given that the spectral surface radiance on the early Earth is quite broad, and thus not well represented by narrowband irradiation sources typically used in irradiation experiments, it is important to analyze potential prebiotic photochemical reactions for their plausibility in the context of the UV-environment on the early Earth. Previous studies showed a prebiotically plausible synthesis of β -d-riboctidine-2',3'-cyclic phosphate and subsequent UV-driven conversion to β -d-ribouridine-2',3'-cyclic phosphate. The UV light (254 nm narrowband emission) also acted to destroy other synthetic co-products, enriching the relative concentration of the canonical ribonucleotides used by life today. In order to assess the prebiotic plausibility of the conversion of the C>p to U>p, we first studied the wavelength dependence of the reaction rate, as monitored by UV-Vis absorption spectroscopy. This analysis showed that the photochemical step proceeded best at an irradiation wavelength of 265 nm. In the context of the spectral flux available on the surface of the early Earth, generally, longer wavelengths are more accessible, meaning the reaction is more efficient under more realistic conditions. In order to quantify the effect of varying amounts of surface radiation at different wavelengths, we computed the weighted surface intensity, which accounts for the rate of the reaction as a function of wavelength and the intensity of the radiation available on the surface of the early Earth at each wavelength. 265 nm is still the most efficient wavelength, with the window of usable radiation for this reaction occurring around 255–285 nm. Outside this window, either the reaction rate or the radiation intensity drops low enough that the weighted surface intensity suffers significantly. It is fortuitous that the most efficient wavelengths for this reaction are those that are not significantly screened out by plausible prebiotic atmospheric constituents and are available at sufficient intensity from the early Sun to drive the reaction. Our study demonstrates that the wavelengths necessary

to drive this reaction would likely be available on the surface of the early Earth.

We further investigated the second step of the reaction, which is the thermal reversion of the photochemically-generated intermediate back into the starting material. We determined the rate of the back reaction as a function of temperature and found the activation energy to be kJ/mol. On the prebiotic Earth, materials would be subjected to repeated cycles of light and dark during the day/night cycles. We modeled this by determining the net photochemical rate weighted over the wavelength intensities expected on the early Earth. After the irradiation step, we then modeled the dark reaction at various temperatures. Included in this model was the experimentally determined recovery of, on average, 88% of the starting material with each cycle. This ultimately leads to a limit on how long C>p would have been available on the early Earth, if C>p was only present in a finite amount. This calculation can conversely be used to constrain the necessary production rate of C>p in order to maintain steady state concentrations. We find that a stock of 1 mM C>p will last from 70–1000 hours at temperatures of 15–35 °C, and that production rates of 3–44 μM/hr are needed to maintain a 1 mM stock of C>p (depending on temperature). These considerations can help constrain the environmental conditions in order for the prebiotic chemistry to be self-consistent and plausible. In particular, if future experiments can quantify typical production rates under plausible planetary conditions, these can be compared to our findings to assess the overall consistency of the proposed chemistry. We also note that the deaminated product that forms as a result of UV light requires a significant amount of heating to return to U>p. This step would need to occur in the dark on the early Earth in order to not drive the reaction back to the UV-generated intermediate state. This condition again may imply constraints and requirements on the prebiotic environment if both C>p and U>p nucleotides are to be obtained through this UV-driven method. In particular, if both C>p and U>p are to be obtained through UV-driven deamination, the products would need to be incubated in the dark or exposed to significant durations of heating in order to recover the canonical ribonucleotides.

With these experimental constraints on this prebiotic chemical reaction, we can begin to envision an environmental scenario in which photochemistry can generate both cytidine and uridine nucleotides, but still have protection from overall UV degradation of both materials. If we invoke the geochemical scenario postulated by Patel et al. [240], our analysis shows that the UV-environment found on the surface of the early Earth in a shallow pond or lake would allow for conversion of β -d-riboctidine-2',3'-cyclic phosphate into β -d-ribouridine-2',3'-cyclic phosphate on appropriate timescales. The production rates of C>p are currently not well constrained, but if production rates are non-negligible, the UV-driven conversion of C>p into U>p could lead to pools of both canonical pyrimidine ribonucleotides available on the prebiotic Earth. Even if production rates are slow, the material might be protected from further loss by UV light. Potential mechanisms for UV protection could include sinking deeper into a body of water, or being otherwise shielded by other UV absorbers (e.g. Sagan [290]). We only examined the C>p to U>p photoreaction in isolation in this study; in actuality on the early Earth, other potentially UV-absorbing molecules may be present. These molecules could act to shield C>p and U>p from UV light, or could increase the rate of degradation through various photoredox or other chemical processes. These effects are beyond the scope of this study, but worth noting.

UV-driven photoconversion is not the only possible way to obtain both pyrimidine ribonucleotides on the early Earth. Reaction of cytidine derivatives with nitrous acid in the dark can generate uridine derivatives [179, 308]. Recent work has suggested that nitrate and nitrite (collectively called NO_x) may have been available in prebiotically relevant concentrations in shallow lake environments on the early Earth [264]. Thus, there are seemingly multiple plausible ways in which to convert cytidine nucleotides into uridine nucleotides on the early Earth. Possibly one or more could have been at play to provide both canonical ribonucleotides for the origins of life or the development of the genetic code. Multiple ways to achieve this conversion could make it easier for uridine production to be a larger-scale process, and less confined to a specific local

geochemical environment.

6.4 CONCLUSIONS/IMPLICATIONS

Our study determined the prebiotic plausibility of the conversion of β -d-riboctidine-2',3'-cyclic phosphate into a photochemically-generated intermediate that can partially convert to β -d-ribouridine-2',3'-cyclic phosphate, in the context of the UV light available on the surface of the early Earth. Radiation at wavelengths from 255–285 nm is most efficient at driving this reaction; such irradiation was available on the early Earth. The relative proportion of C>p and U>p after UV irradiation appears to depend modestly on the length of irradiation time, with longer times reaching similar amounts of both. However, we find that continued irradiation (1 hour in Rayonet RPR-200, 254 nm) leads to significant loss of the overall amount of C>p and U>p that can be recovered upon heating. Proposed prebiotic chemistries for the accumulation and retention of C>p and U>p at e.g. 1 mM concentrations in the surficial environment must have production rates of several to tens of micromolar per hour in order to be plausible. If production rates are smaller, another mechanism for UV protection must be invoked in order to maintain these threshold concentrations for origins of life scenarios.

Acknowledgements

We thank R. Szabla and D. Bucher for helpful discussions and comments. We would also like to thank V. S. Lelyveld, C. P. Tam, T. S. Walton and S.-Y. Ng for experimental and laboratory assistance. This work was supported in part by grants from the Simons Foundation (290363 to J. W. S. and 290360 to D. D. S.) and a fellowship from the Simons Foundation (495062 to S. R.). J. W. S. is an investigator of the Howard Hughes Medical Institute. D. D. S., S. R., and Z. R. T. would like to acknowledge funding from the Harvard Origins of Life Initiative. C. J. M. is currently at Stanford University.

6.5 APPENDIX A: DETERMINATION OF EXTINCTION COEFFICIENTS

In order to convert the observed absorbances into concentrations of both the starting material and the intermediate, the extinction coefficients for these species need to be known. We assumed that the extinction coefficients for the starting material (β -d-riboctidine-2,3-cyclic phosphate) were the same for cytidine monophosphate (8814 and 9000 $\text{M}^{-1} \text{cm}^{-1}$ for 240 and 270 nm, respectively). In order to determine the extinction coefficients for the intermediate, we obtained $^3\text{1P}$ NMR spectra of a solution of 1 mM β -d-riboctidine-2',3'-cyclic phosphate before and after irradiation (254 nm, Rayonet reactor). The solution was monitored with UV-Vis absorption spectroscopy both before and after irradiation. An aliquot of the solution was spiked with a fixed concentration of trimethyl phosphate (TMP) as an internal standard to use for integration and concentration determination. The remaining unspiked solution was then irradiated in a Rayonet reactor (RPR-200, at 254 nm) and monitored by UV-Vis absorption until there was some conversion to the intermediate. We then spiked this sample with the same amount of TMP and took $^3\text{1P}$ NMR spectra (Varian Inova 400 MHz spectrometer). The TMP peaks in the irradiated and unirradiated samples were used as an internal standard and to integrate the phosphorous signals from the sample. The unirradiated sample showed one peak at 17.09 ppm, while the irradiated sample showed two (17.09 and 17.35 ppm). Integrations of the signals were used to calculate the concentrations of the starting material and intermediate in the irradiated sample. We confirmed the identity of the starting material signal by sample spiking. With the concentrations of starting material and intermediate, as well as the absorption spectra, we could then solve for the extinction coefficients by solving the following set of equations for $\epsilon_{int,240nm}$ and $\epsilon_{int,270nm}$:

$$A_{240} = \epsilon_{C,240nm}c_C l + \epsilon_{int,240nm}c_{int} l$$

$$A_{270} = \epsilon_{C,270nm}c_C l + \epsilon_{int,270nm}c_{int} l$$

From this, we find that $\epsilon_{int,240nm} = 15875M^{-1}cm^{-1}$ and $\epsilon_{int,270nm} = 2528M^{-1}cm^{-1}$.

6.6 APPENDIX B: IRRADIATION OF U>P

In order to test the properties of the uridine form of the photochemically generated intermediate, we irradiated a solution of 50 μ M U>p (254 nm, Rayonet reactor) over a span of 7 minutes. The UV absorption spectrum was recorded at various time intervals during the irradiation (Fig 6.6.1). The initial U>p has an absorption maximum at 260 nm, but this feature quickly disappears with irradiation. By 7 minutes, almost no U>p remained. The photo-generated intermediate does not absorb significantly in the 230–300 nm range, which indicates we can effectively ignore the contribution of this species to the absorption of solutions of irradiated and heated C>p. The only three species that should be detectable by UV spectroscopy are C>p, U>p, and the cytidine intermediate (absorption maxima at 270, 260, and 240 nm, respectively).

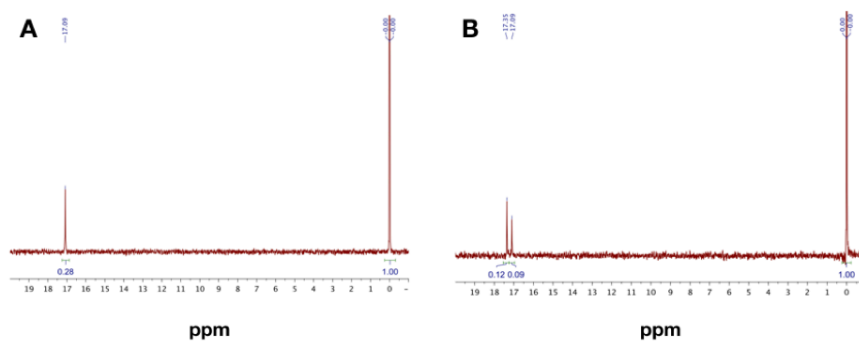


Figure 6.5.1: (A) ^{31}P NMR spectrum of initial 2 mM β -d-ribocytidine-2',3'-cyclic phosphate, with TMP added as an internal standard. The starting material has a phosphorous signal at 17.09 ppm. (B) ^{31}P NMR spectrum of 2 mM β -d-ribocytidine-2',3'-cyclic phosphate irradiated for 90 minutes in the Rayonet reactor at 254 nm. TMP was spiked in after irradiation as an internal standard. Two signals (17.09 and 17.35 ppm) are observed; the 17.09 ppm signal was confirmed to be the initial material by sample spiking. Integration of the two signals allowed for calculation of concentration and then extinction coefficients for the intermediate.

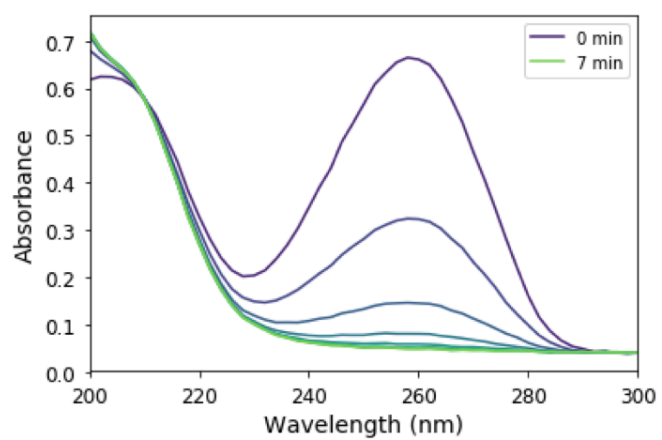


Figure 6.6.1: UV spectra of U>p during irradiation (7 minutes total) in the Rayonet RPR-200 (254 nm). The uridine photo-generated intermediate does not absorb significantly in the 230–300 nm region.

7

UV Photostability of three 2-aminoazoles with key roles in prebiotic chemistry on the early Earth

Abstract

Three related molecules in the 2-aminoazole family are potentially important for prebiotic chemistry: 2-aminooxazole, 2-aminoimidazole, and 2-aminothiazole, which can provide critical functions as an intermediate in nucleotide synthesis, a nucleotide activating agent, and a selective agent, respectively. Here, we examine the wavelength-dependent photodegradation of these three molecules under mid-range UV light (210–290 nm). We then assess the implications of the observed degradation rates for the proposed prebiotic roles of these compounds. We find that all three 2-aminoazoles degrade under UV light, with half lives

ranging from $\approx 7-100$ hours under a solar-like spectrum. 2-Aminooxazole is the least photostable, while 2-aminoimidazole is the most photostable. The relative photostabilities are consistent with the order in which these molecules would be used prebiotically: AO is used first to build nucleotides and AI is used last to activate them.¹

7.1 INTRODUCTION

RECENT ADVANCES IN PREBIOTIC cyanosulfidic chemistry informed by the environmental constraints on the Hadean-Archaeon Earth suggest that a robust chemical network may have generated all four major types of building blocks of life: sugars, amino acids, ribonucleotides, and lipid precursors [240]. In this network, critical roles are played by three molecules in the 2-aminoazole family: 2-aminooxazole (AO), 2-aminoimidazole (AI), and 2-aminothiazole (AT). 2-aminooxazole is a key intermediate in the pathway towards synthesizing pyrimidine ribonucleotides [256] and a complete set of arabino nucleotides [280]. 2-aminoimidazole is capable of activating ribonucleotides so that they are able to copy RNA templates non-enzymatically with greater efficiency than previously observed with other leaving groups [173]. Finally, 2-aminothiazole has been shown to be a potentially important selecting agent, allowing for stabilization and purification of simple sugars as their crystalline aminated derivatives. These derivatives enable nucleotide synthesis from a complex mixture of starting products as well as a pathway to amino acids without formation of non-canonical $\alpha - \alpha$ -disubstituted derivatives [138]. All three of these 2-aminoazoles could have potentially been synthesized prebiotically in the same or similar environments. Recent results show a divergent synthesis of 2-aminooxazole and 2-aminoimidazole from cyanamide and glycolaldehyde in the presence or absence of ammonia [86]. 2-aminothiazole can similarly be

¹This thesis chapter was published as: Z. R. Todd, R. Szabla, J. W. Szostak and D. D. Sasselov (2019) *Chem. Commun.*, 55, 10388-10391.

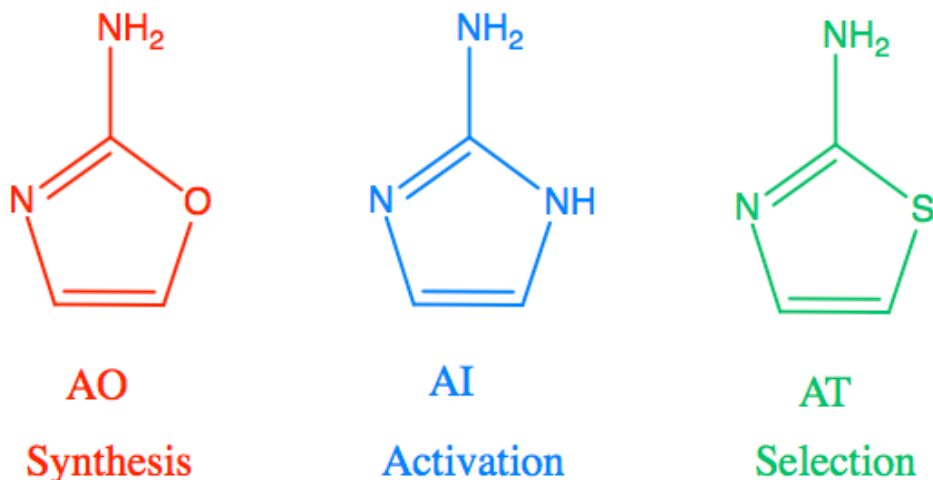


Figure 7.1.1: 2-aminooxazole (AO), 2-aminoimidazole (AI), and 2-aminothiazole (AT) are related molecules in the 2-aminoazole family with distinct potential roles in prebiotic chemistry. AO is a key intermediate in the synthesis of pyrimidine ribonucleotides. AI can activate RNA monomers to allow for efficient non-enzymatic replication, and AT can help to sequester, stabilize, and crystallize molecules.

synthesized from cyanamide and β -mercaptoacetaldehyde [138].

UV light has been suggested to be a potentially important source of energy for driving prebiotic chemistry [46, 243, 291]. Indeed, UV light is required in key steps of the chemistry yielding pyrimidine nucleosides and nucleotides under prebiotically plausible conditions. For instance, the UV irradiation of ferrocyanide and sulfite generates the solvated electrons that drive the cyanosulfidic redox chemistry that could generate simple sugars and amino acids from one-carbon feedstock molecules [274, 385]. Additionally, the selective conversion of C to U ribonucleotides and the degradation of non-canonical nucleotide stereoisomers is also driven by UV [256]. Alternative nucleobase analogs such as 2-aminopurine or 5-hydroxyuracil exhibit lower photostability than canonical nucleobases, potentially indicating why they were not incorporated into DNA [?]. Consequently, UV light may have been both an

important source of energy and a powerful selection factor in the prebiotic era.

The UV light used in laboratory experiments simulating prebiotic chemistry has typically been limited to 254 nm UV from a mercury lamp,[240, 256, 276, 385] but the wavelength range of UV light available on the surface of the early Earth is not well represented by monochromatic emission at 254 nm and instead would have reached down to roughly 200 nm [259]. The fact that photochemical reactions typically display a dependence on the irradiation wavelength (e.g. Matsunga et al. [192]) has inspired us to study these reactions as a function of wavelength[350].

Furthermore, UV-induced damage (and in some cases, self-repair) of RNA and/or DNA strands has been extensively studied[15, 33, 83, 268, 403]; however, much less effort has been put into studying the photostability of prebiotically credible precursors of nucleotides such as the three 2-aminoazoles. Here, following the recent investigation of the photostability of oxazoline precursors of RNA,[139] we investigate the wavelength-dependent UV photostability of the three 2-aminoazoles. We then discuss whether these rates allow for a self-consistent network of reactions, in order to place constraints on the relevant prebiotic environment.

7.2 RESULTS AND DISCUSSION

To perform these studies, a xenon lamp was coupled with a diffraction grating to allow tunable wavelength selection, as in Todd et al. [350]. We used experimental irradiation wavelengths of 215-285 nm, in 10 nm intervals with a 10 nm bandwidth, to irradiate 0.1 mM solutions of each of the 2-aminoazoles for 1-8 hours (depending on the rate of the reaction). We observed decreases in the UV-Vis absorption spectra of each species as a function of irradiation time (Figure 7.1.2) and converted the absorbances into concentrations of each molecule (see section 7.5). The photodegradation reactions are first order (see

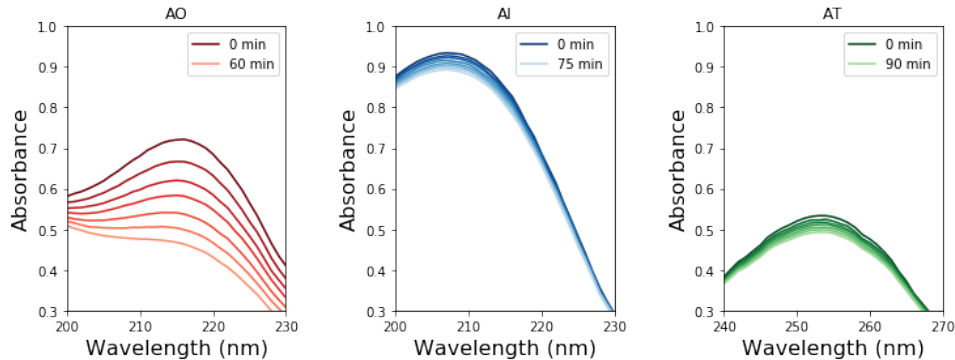


Figure 7.1.2: Absorption spectra of AI, AO, and AT as a function of irradiation time at irradiation wavelengths of 215, 215, and 255 nm, respectively. These wavelengths were chosen to be near the absorption maxima for each molecule, which will have larger changes in absorption. The decreasing absorption intensities with irradiation time allow for the destruction rate to be calculated.

section 7.7), so the logarithm of the concentration vs. time gives a linear trend, with the rate constant given by the slope (Figure 7.1.3). Destruction rates were measured for irradiation wavelengths from 215-285 nm. These rates were then normalized by the incident photon flux (determined by measuring the power at each wavelength) so that rates could be compared across wavelength for a constant photon flux expected on the surface of the early Earth (see section 7.6 for details). The wavelength dependencies and comparative photostability of the three molecules are shown in Figure 7.1.4. AO and AI are less photostable at shorter irradiation wavelengths compared to longer wavelengths, as would be expected from the maxima in their absorption spectra. It is also worth noting that we have recorded the highest photodestruction rate for AO at 215 nm, which indicates that short irradiation wavelengths (high energies) are necessary to efficiently trigger destructive photorelaxation mechanisms in this molecule. AT has an approximately constant rate of photodestruction at wavelengths below 255 nm and is more photostable at longer wavelengths. Comparing the three species to each other shows that AO is much less photostable than either AI or AT. The comparative photostability of AI and AT depends on the wavelength of light

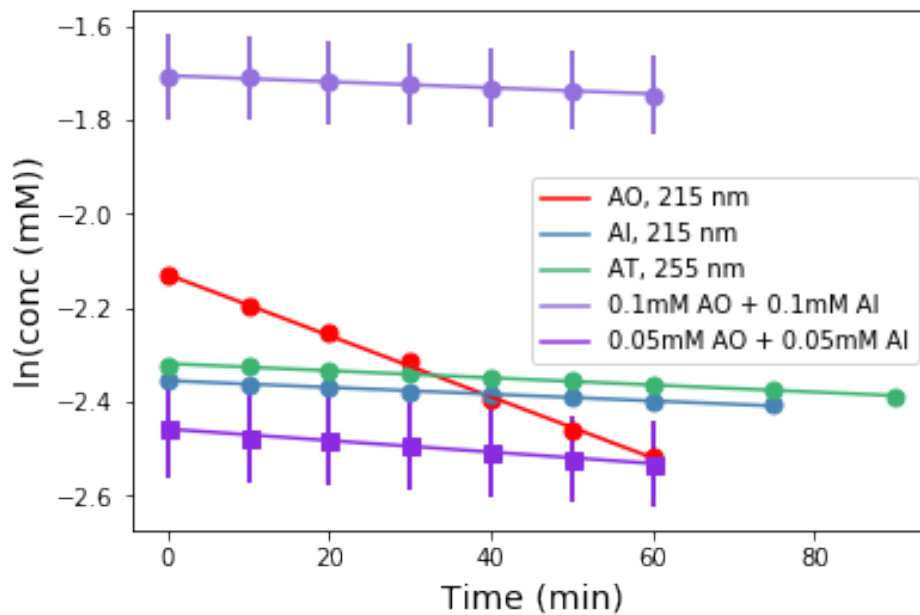


Figure 7.1.3: Concentration as a function of irradiation time for AI, and AO at 215 nm, and AT at 255 nm. Concentrations were calculated from the absorption spectra shown in figure 7.1.2. A mixture of 0.05mM AO + 0.05mM AI was also irradiated at 215 nm for comparison (purple points). The rate of degradation of the mixture is less than that of AO alone, indicating that AO can perhaps be protected by co-irradiation with a more UV-photostable molecule.

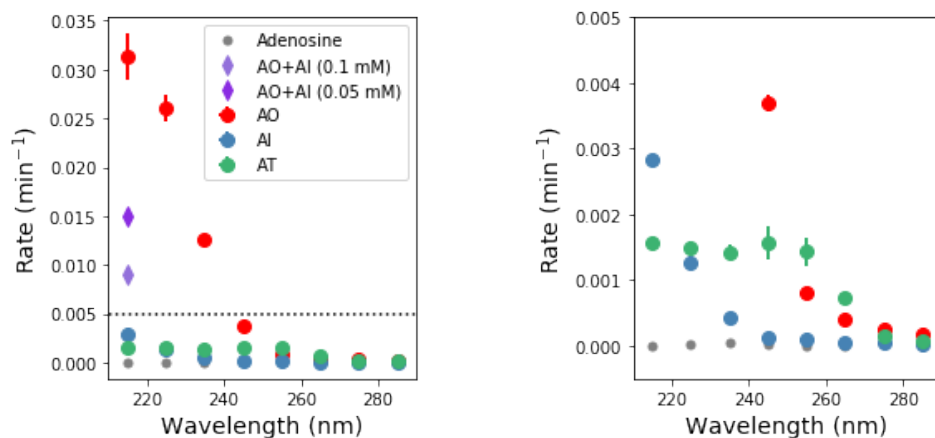


Figure 7.1.4: Destruction reaction rate normalized by incident photon flux as a function of irradiation wavelength. The right hand panel shows a zoomed in view of the left hand panel, to show the wavelength dependence of Al and AT. AO has the highest relative rate of photodegradation, especially at short wavelengths. Al and AT are more photostable, but Al is susceptible only to short wavelengths, while AT is most affected by short-to-mid-range wavelengths. We repeated each irradiation wavelength for each molecule in duplicate. Points show the average rates, while error bars represent the 1σ standard deviation.

considered (AI is less stable at the shortest wavelengths, while AT is less stable at wavelengths >230 nm). Co-irradiation of AO and AI (0.05mM) at 215 nm is shown in Figure 7.1.3 (see section 7.10 for details). The rate of degradation of the AO + AI mixture is less than that of AO alone but more than that of AI alone (see Figure 7.1.4, purple points), indicating a potential protection of AO when irradiated in the presence of another more UV-photostable molecule.

Quantum chemical simulations and pump-probe spectroscopic techniques revealed important details of the excited state dynamics of model azole chromophores, including AO and AI [40, 140, 279, 337, 338]. These studies demonstrated a significant contribution of repulsive $\pi\sigma^*$ states to their overall photochemistry [40, 140, 279, 337, 338]. In particular, $\pi\sigma_{\text{NH}}^*$ excitations were shown to promote an ultrafast two stage electron-driven proton transfer (EDPT) photorelaxation mechanism which is initiated with photoinduced electron transfer to neighbouring water molecules. The subsequent proton transfer from the amino group in the direction of the hydrated electron can be treated as an example of photoacidity and enables efficient photorelaxation through the $\pi\sigma^*/S_0$ state crossing. It was suggested that after the repopulation of the S_0 state the hydrogen atom could be readily returned to the chromophore and EDPT could be a photostabilizing deactivation mechanism. The very high photostability of AI reported here corroborates this computational prediction, since EDPT was found as the dominant, if not the only photodeactivation mechanism in this microhydrated chromophore [40, 140, 279, 337, 338]. In contrast, excited-state dynamics simulations revealed a considerable contribution from photoinduced ring-opening mechanism (C–O bond breaking) to the photochemistry of AO, which was observed in one third of photoexcitation events [140, 279, 337, 338]. The repulsive $\pi\sigma^*$ state responsible for the ring-opening mechanism is present in the higher energy range of the spectrum, which is also consistent with our observation that AO is most efficiently decomposed at shorter irradiation wavelengths [337, 338]. Consequently, we anticipate that the relatively high rate of photodestruction observed for AO could be the result of photochemical opening of its heteroaromatic ring. Photochemical opening and destruction of

thiazole rings has also been observed in past work [210, 358].

We note that we did not observe the appearance of new absorption bands in the monitored UV ranges throughout the irradiation period that could correspond to any photoproducts and could affect our estimated photodegradation rates. The open-ring photoproducts of AO and AI are not expected to absorb in similar regions. If any of the possible photoproducts of AT contains a thiocarbonyl group it might absorb between 210 and 290 nm. Nevertheless, we see a linear decrease in absorbance of the AT sample and no new spectral features (see Fig. 7.1.2 and 7.1.3), which indicates that the initial photoproducts formed from AT are also prone to photodegradation or do not absorb within the studied wavelength range either.

Based on our measured wavelength-dependent rates of degradation, we can then ask how stable these molecules would have been in the environment of the early Earth. We used the two-stream radiative transfer model described in Ranjan and Sasselov [260] to calculate the surface radiance of the Sun on the surface of the early Earth through a model prebiotic atmosphere. The yellow dashed line in Figure 5 shows the spectral surface radiance for this model, which is consistent within an order of magnitude with the flux from our experimental apparatus. In the absence of oxygen and ozone in the atmosphere, UV light all the way down to 200 nm reaches the surface of the planet; however, the shorter wavelengths have a much lower intensity than the longer wavelengths. We then integrated the spectral surface intensity in the same 10 nm intervals as the experimental conditions and calculated the relative rate of the reaction on the surface of the planet as the product of the integrated surface radiance and the experimental photon-flux normalized rate (Figure 7.2.1 circles, see section 7.1.1 for details). Under the UV environment on the surface of the early Earth, AO (red) has the highest rate of photodestruction, peaking at a wavelength of 225 nm. AI has a maximum rate at 215 nm, even though there is much less light coming at this wavelength, indicating that AI is especially susceptible to short-wavelength UV irradiation. The relative rate for AT destruction is maximum at 265 nm.

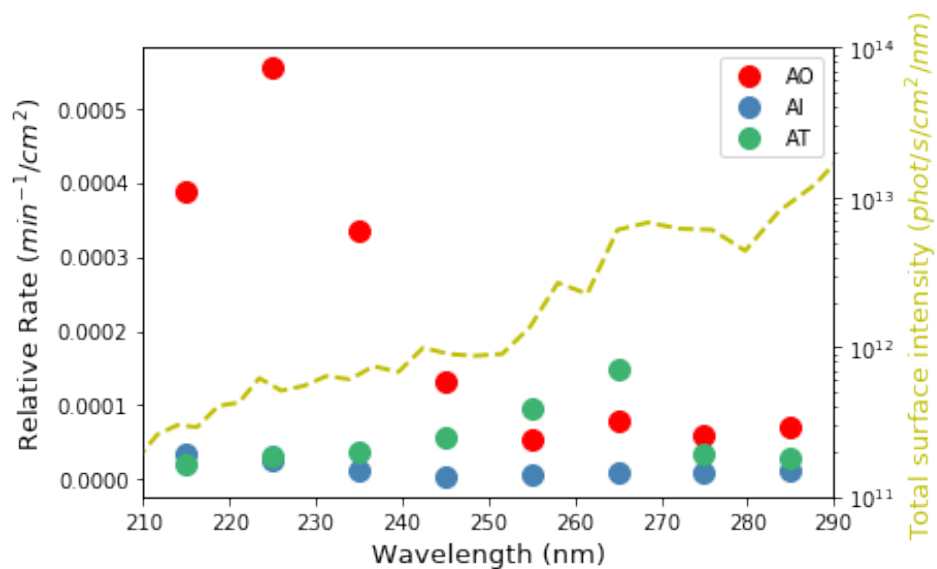


Figure 7.2.1: Calculated relative rates of UV degradation on the surface of the early Earth, derived from the product of experimentally determined rates and integrated surface intensity in the given wavelength ranges. The yellow dashed line shows the total surface intensity from the young Sun through a 1 bar N₂/CO₂-dominated atmosphere. The lower fluxes at shorter wavelengths help mitigate somewhat the higher experimental rates of destruction of AI and AO at these wavelengths.

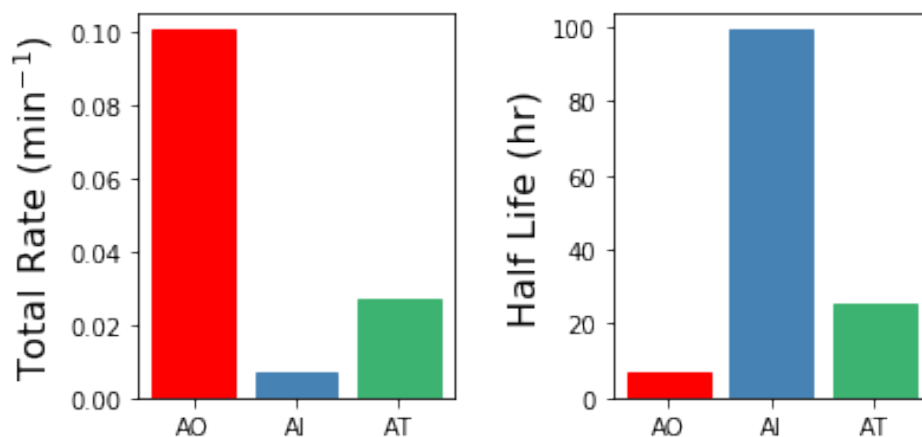


Figure 7.2.2: Total rate of degradation when integrating over all wavelengths from 210-290 nm for each molecule, and half-life of each molecule to photodegradation under a solar-like spectrum passing through a N_2/CO_2 -dominated atmosphere.

We then integrated the relative rates of photodestruction over wavelengths from 210-290 nm to obtain an estimate of the total rate of destruction, assuming a solar like flux. Figure 7.2.2 shows the total destruction rates and half lives for the three molecules. AO has the shortest half life, of approximately 6.9 hours. AT has an intermediate half life of ≈ 26 hr, and AI has the longest half life (≈ 99 hr). Interestingly, AI is less photostable than other imidazoles under select irradiation conditions (e.g. 2-methylimidazole and 2-ethylimidazole, see section 7.9). From these estimates, this family of prebiotically relevant molecules would only be stable if exposed to the surface UV flux expected on the early Earth for on the order of 7-100 hours. Further exposure to irradiation would significantly deplete the reservoir of these materials. These estimates for the photodestruction rates can help to constrain the relevant concentrations, timescales, and environments necessary for making and using these molecules in a prebiotically relevant manner.

7.3 CONCLUSIONS

The relative stabilities of the three aminoazoles are of interest in the context of their potential roles in nucleotide synthesis. As described above, AO, the key intermediate in the prebiotic synthesis of the pyrimidine ribonucleotides is the least photostable. This may not be an issue if the key chemical step involving AO, namely its reaction with glyceraldehyde to form pentose aminooxazolines, which then form anhydronucleosides and ultimately the pyrimidine ribonucleotides [256], proceeds rapidly and efficiently. In the original synthesis proposed by Powner *et al.*, [256] the reaction of AO and glyceraldehyde gives a 70% yield over 16 hours at 40° C at concentrations that are significantly higher than the concentrations we used for photostability measurements (1 M vs. 0.1 mM). We measured the rate of reaction of AO and glyceraldehyde at reduced concentrations (10, 1, and 0.1 mM each), and saw the reaction proceed over tens of hours for concentrations of 10 mM and 1 mM (see SI section 5). At 0.1 mM AO, 0.1 mM glyceraldehyde, AO has a half life of > 1200 hr for reaction with glyceraldehyde, which is significantly longer than the photodestruction half life of 6.9 hours for AO. This potentially places a constraint on the environmental scenario in order for the UV degradation of AO not to hinder the overall pathway. At higher concentrations, AO is consumed faster by reaction with glyceraldehyde while the rate of UV degradation could be slower as the optical depth is decreased, allowing for self-shielding from UV photons. Furthermore, the pentose aminooxazoline products of this reaction were demonstrated to be much more photostable than AO [139].

In summary, we have constrained the UV photostability of three key molecules for prebiotic chemistry under conditions in which they might form and be used. AI is the most photostable, while AO is the least. The comparatively low UV photostability of AO may or may not be an issue for this prebiotic chemical network, depending on the concentrations and timescales under which it is produced and used and the presence of other more UV-photostable molecules that could act as sunscreens, such as AI. It is also encouraging that AI, which

would be needed to activate already synthesized nucleotides [184] and facilitate nonenzymatic RNA template copying [173] has the longest lifetime under UV irradiation.

Acknowledgements We thank F. Ng for laboratory assistance, C. Giurgiu and C. Kufner for helpful comments and discussions. This work was supported in part by grants from the Simons Foundation (290363 to J.W.S. and 290360 to D.D.S. and 494188 to R.S.) and by the Foundation for Polish Science (FNP, START 2019 Fellowship to R.S.). Z.R.T and D.D.S acknowledge support from the Harvard Origins of Life Initiative. J.W.S. is an investigator of the Howard Hughes Medical Institute.

7.4 APPENDIX A: GENERAL METHODS

2-aminooxazole (97%) and 2-aminoimidazole hemisulfate (98%) were purchased from CombiBlocks. 2-aminothiazole (97%) was purchased from Sigma Aldrich. For irradiation experiments, a 0.1 mM solution of the molecule of interest was prepared in deionized water. The sample was transferred to a Spectrosil quartz cuvette with a screw top (Starna Cells part number 9-Q-10-GL14-C) and a micro-stirbar was added. Before irradiation, an initial UV-Vis absorption spectrum (200-350 nm) was taken using an Amersham Sciences Ultrospec 3100 pro. The sample was then irradiated in the tunable lamp setup, with irradiation wavelengths from 215-285 nm in 10 nm intervals, with a 10 nm bandwidth. The sample was continuously stirred. At periodic intervals, the sample was briefly removed from the lamp to record the UV-Vis absorption spectrum. For the more stable molecules at less destructive wavelengths, typical time points were taken every 30 minutes. For the most unstable wavelengths and molecules, time points were around 10 minutes. The duration of irradiation lasted from 1-8 hours, depending on the overall rate of the degradation.

The tunable irradiation setup uses a 75W Xenon Tunable PowerArc lamp made by Optical Building Blocks (OBB). The xenon lamp coupled with a diffraction grating (acting as a monochromator) allows for tunable wavelength

selection over the UV mid-range (roughly 200-300 nm). In order to allow tunable wavelength selection, the relative position of the grating with respect to the exit slit is adjusted. The sample-containing cuvette is placed on a mount with stirring capability. Irradiation experiments used a bandwidth of 10 nm, though the bandwidth is also adjustable in the setup.

7.5 APPENDIX B: STANDARD CURVES

In order to convert the observed absorption spectra to concentration throughout the course of an irradiation experiment, we compiled standard curves relating absorbance to concentration for the three molecules (Figure 7.5.1). The maximum absorbance for AO, AI, and AT occurred at wavelengths of 207, 215, and 254 nm, respectively. Figure 7.5.2 shows the absorbance (at the maximum) as a function of concentration for each molecule. The equations relating these absorption values to concentrations of each molecule are:

$$conc_{AI} = 0.120A_{AI,207nm} - 0.0175$$

$$conc_{AO} = 0.153A_{AO,215nm} - 0.0162$$

$$conc_{AT} = 0.211A_{AT,254nm} - 0.0165$$

From these relations, the measured absorption values can be converted into a concentration of the given molecule throughout an irradiation experiment.

7.6 APPENDIX C: IRRADIATION EXPERIMENTS ANALYSIS

During irradiation experiments, we monitored the photodestruction reaction by UV-Vis absorption using an Amersham Science Ultrospec 3100 Pro. Irradiations were carried out for durations of 1-8 hours, with variable timepoints depending on the total length of the experiment. We then used the standard curves from

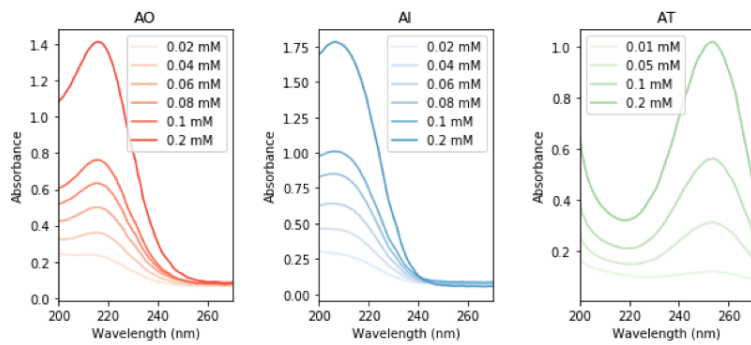


Figure 7.5.1: Standard curves for AO, AI, and AT, used to relate measured absorbances to a concentration.

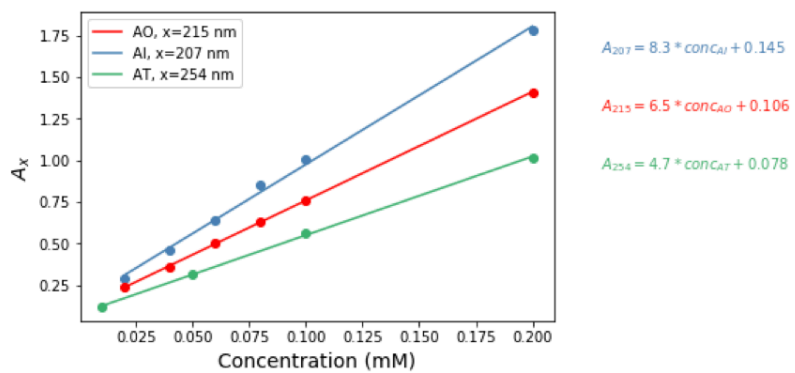


Figure 7.5.2: Absorption at the maximum wavelength for each molecule as a function of concentration. These relations can be used to calculate the concentration from measured absorption values.

section 7.5 to convert the absorbance at the absorption maximum for each molecule into a corresponding concentration. The destruction rate constant was determined by plotting $\ln(\text{concentration})$ as a function of irradiation time, which gave a linear trend. The slope of the linear trend line gives the rate constant for the destruction reaction, and was calculated from a python fitting routine. Each irradiation wavelength for all molecules was analyzed the same way. Additionally, all irradiation wavelengths and molecules were repeated in duplicate over the range of 215-285 nm, in 10 nm intervals with 10 nm bandwidths. The duplicate wavelength rates were averaged to obtain the estimated rate, and errors were estimated from the standard deviation of the duplicate pair. However, the tunable xenon lamp emits different powers at various irradiation wavelengths, so these rates cannot yet be compared as a function of irradiation wavelength.

In order to allow for irradiation wavelength comparison, we determined the incident photon flux as a function of irradiation wavelength. To do this, the power from the apparatus was measured with a Newport power meter during each experiment. The photon flux could then be calculated by dividing the incident power by the energy of a photon at that specific irradiation wavelength (through the relation $E = hc/\lambda$).

To then compare reaction rates as a function of irradiation wavelength, we took the raw reaction rates determined from the linear plot of $\ln(\text{concentration})$ vs. time, and normalized by the incident photon flux. These photon flux-normalized rates were then multiplied by a constant photon flux of 2.5×10^{14} phot/s to generate the normalized reaction rate (Figure 7.2.1). This photon flux is the expected solar photon flux from 210-290 nm on the surface of the early Earth (see section 7.11), which is also consistent with the typical experimental photon flux.

7.7 APPENDIX D: IRRADIATION EXPERIMENTS CONCENTRATION DEPENDENCE

We next analyzed the concentration dependence of irradiation experiments in order to determine the order of the reaction. For each molecule, we irradiated

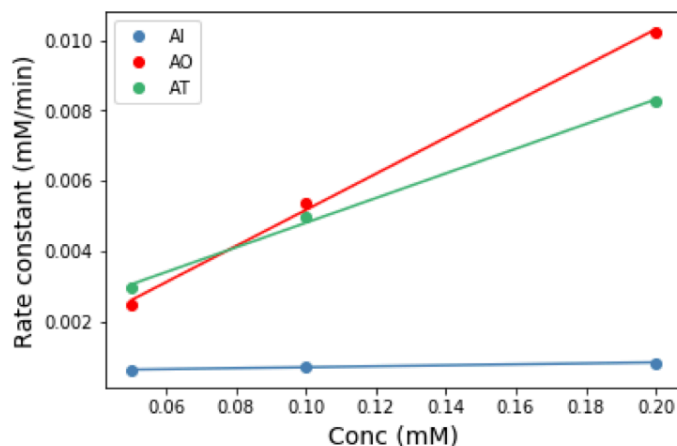


Figure 7.7.1: Concentration dependence of the photo destruction rate of each molecule. The linear trend between rate constant and concentration is indicative of first order kinetics.

0.05, 0.1, and 0.2 mM solutions in a Rayonet RPR-200 (254 nm) reactor for 10 minutes and monitored the reaction by UV-Vis spectroscopy. The rate constant for each reaction was determined as described above. Figure 7.7.1 shows the rate constant as a function of concentration for each molecule. We find a linear trend between rate and concentration, suggesting that the irradiation reactions are first order.

7.8 APPENDIX E: REACTION OF AO AND GLYCERALDEHYDE

We attempted to compare the rate at which AO reacts on the pathway to nucleotides in a prebiotic context to the photodestruction rate, in order to

determine if the presence of UV light in such a prebiotic chemical network is self-consistent. Powner et al. (2009) showed that AO can react with glyceraldehyde to form pentose aminooxazolines. The arabinose aminooxazoline undergoes further reaction to eventually yield activated pyrimidine ribonucleotides. Under the Powner et al. (2009) reaction conditions, AO is formed from reaction of glycolaldehyde (1M) and cyanamide (1M) in 1.0M phosphate (pH 7), in 3 hours at 60°C. 1M rac-glyceraldehyde was added, and the reaction was heated at 40°C for another 16 hours. Powner et al. (2009) found an overall 70% conversion to products including AO, arabinose aminooxazoline, ribose aminooxazoline, and other pentose aminooxazolines (xylose aminooxazoline, lyxofuranose aminooxazoline, lyxopyranose aminooxazoline), and pentose oxazoles (rac-[3R,4R]-pentose oxazole and rac-[3S,4R]-pentose oxazole).

We sought to determine the rate of the reaction of AO and glyceraldehyde at lower concentrations, so as to better compare to our experimental photodegradation timescales. We allowed unbuffered solutions of equal concentrations of AO and glyceraldehyde in D₂O to react at 40°C and monitored the reaction progress by ¹H-NMR. We tested concentrations of 10 mM AO + 10 mM glyceraldehyde, 1 mM AO + 1 mM glyceraldehyde, and 0.1 mM AO + 0.1 mM glyceraldehyde. The 10 mM and 1 mM experiments were heated for 16 hours, while the 0.1 mM experiment was heated for 200 hours. An aliquot of the initial sample was saved, then spiked with an internal standard, and monitored by NMR. After heating, samples were spiked with the internal standard to allow for quantitative comparison to the initial sample. We integrated the aromatic protons of AO (6.63 and 7.16 ppm) with respect to the internal standard to get a quantitative measure of the progress of the reaction (see figure 7.8.1). The internal standards were used to obtain the concentration of the aromatic protons of AO (7.16 and 6.63 ppm) at both the initial and final timepoints, as shown in Table 7.8.1.

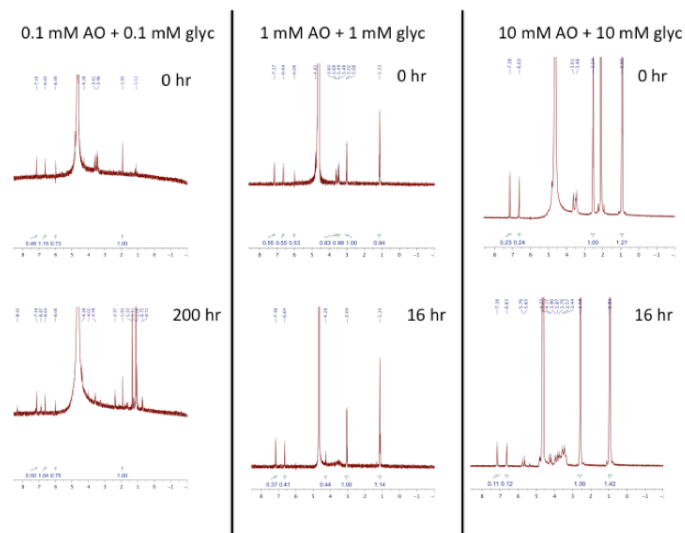


Figure 7.8.1: NMR spectra for initial and final timepoints for experiments of 0.1 mM, 1 mM, and 10 mM each of AO and glyceraldehyde. TEA was used as an internal standard in the 1 and 10 mM experiments, while acetonitrile was used for the 0.1 mM experiment. Integrating the initial and final aromatic AO proton signals (7.16 and 6.63 ppm) against the internal standard allowed for quantitative analysis of the reaction rates.

10mM AO + 10mM glyceraldehyde					
Time (hr)	7.16 ppm integral	Conc (mM)	6.63 ppm integral	Conc (mM)	
0	0.23	13.8	0.24	14.4	
16	0.11	6.6	0.12	7.2	
1mM AO + 1mM glyceraldehyde					
Time (hr)	7.16 ppm integral	Conc (mM)	6.63 ppm integral	Conc (mM)	
0	0.55	1.65	0.55	1.65	
16	0.37	1.11	0.41	1.23	
0.1mM AO + 0.1mM glyceraldehyde					
Time (hr)	7.16 ppm integral	Conc (mM)	6.63 ppm integral	Conc (mM)	
0	0.48	0.072	1.15	0.173	
200	0.50	0.075	1.04	0.156	

Table 7.8.1: Reaction of AO and glyceraldehyde at various concentrations. An internal standard was used to integrate the aromatic AO proton peaks at 7.16 and 6.63 ppm and allow for calculation of the concentration. With concentrations determined, we could then calculate a rate of the reaction.

Conc (mM)	Rate (mM/hr)	Half life (hr)
0.1	-8.3×10^{-5}	>1200
1	-0.030	33
10	-0.45	22

Table 7.8.2: Rates and half-lives for the reaction of AO and glyceraldehyde at different concentrations. AO and glyceraldehyde are used in equal concentrations in each experiment.

From the change in concentration with time, we could determine the rate of the reaction for each concentration. The average rate was determined from the rates determined from the 7.16 and 6.63 ppm signals, with the exception of the 0.1 mM experiment. In this case, only the 6.63 ppm signal gave a decreasing concentration with time, so we adopted the rate from this signal as the overall reaction rate, and only use this as an upper limit to the rate.

If we then assume that the reaction is first order in both AO and glyceraldehyde (so second order overall), the rate law can be written as:

$$rate = k[AO][glyc]$$

From the rate, we can determine the half life for the reaction at each concentration (table 7.8.2). At the highest concentration of 10 mM reactants, the half life is 22 hours. At 1 mM, the half-life increases to 33 hr, while the lowest concentration (0.1 mM) has a half-life >1200 hr. These are the rough timescales on which we might expect AO and glyceraldehyde to react to form the aminooxazolines that come next in the pathway, though this is by no means a complete exploration of parameter space.

Due to our experimental irradiation setup, we performed irradiations at 0.1 mM concentrations. At higher concentrations, the optical depth of the solution becomes smaller, leading to less penetration of photons which can slow the reaction. Comparing the estimated 6.9 hour half-life of 0.1 mM AO photodegradation to the reaction timescale of 0.1 mM AO + 0.1 mM

glyceraldehyde (> 1200 hr) does indeed make the usefulness of AO in this prebiotic scheme somewhat bleak. However, we note that the AO + glyceraldehyde reaction proceeds on the order of tens of hours at higher concentrations. At elevated concentrations, the UV degradation of AO could be lower, as the optical depth of the solution increases and could thus provide for some self-shielding. So, even though we find that AO is the most susceptible to UV damage, this may not be an insurmountable roadblock toward this prebiotic pathway. Instead, more consideration will have to be placed on the relevant concentrations possible from synthesis, and the potential for UV-shielding mechanisms.

7.9 APPENDIX F: STABILITY OF AI VS. OTHER IMIDAZOLES

Though these three molecules potentially play important roles in prebiotic chemistry, they are not the only 2-aminoazole molecules in existence. We sought to compare the photostability of three various imidazoles as a test case to understand how these prebiotic molecules compare to non-prebiotic counterparts. We irradiated 0.1 mM solutions of 2-methylimidazole, 2-ethylimidazole, and 2-aminoimidazole at 254 nm in a Rayonet reactor for 30 minutes. Rate constants were determined from the plot of $\ln(\text{conc})$ vs. time (Figure 7.9.1), as described previously. We find that AI is considerably less photostable (rate constant of $1.05 \times 10^{-2} \text{ min}^{-1}$) under these conditions than both 2-methylimidazole and 2-ethylimidazole (rate constants of 1.73×10^{-3} and $1.88 \times 10^{-3} \text{ min}^{-1}$, respectively). It is interesting that the potentially prebiotically relevant 2-aminoazoles are less photostable than non-prebiotic counterparts studied here. A more complete investigation of photostabilities of various related molecules could be useful for further understanding of why these molecules may or may not be relevant and under what environments and circumstances they could be used.

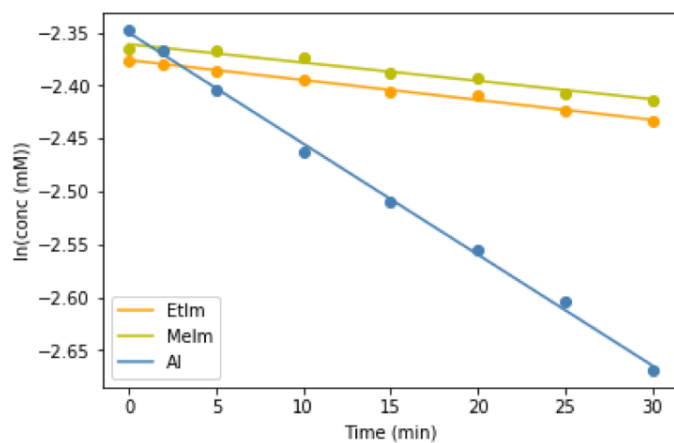


Figure 7.9.1: Irradiations of 2-methylimidazole (Melm) and 2-ethylimidazole (EtIm) compared to 2-aminoimidazole at 254 nm in a Rayonet reactor. The slope of the fits of the logarithm of concentration vs. time give the rate constants for Melm and EtIm of 1.73×10^{-3} and $1.88 \times 10^{-3} \text{ min}^{-1}$, respectively, compared to $1.05 \times 10^{-2} \text{ min}^{-1}$ for Al. Al is therefore less photostable than the other two imidazoles tested under these select irradiation conditions.

7.10 APPENDIX G: CO-IRRADIATION OF AI AND AO

Given the finding that AI is considerably more photostable than AO and the divergent synthesis and reactions of AO and AI, it becomes pertinent to ask if the simultaneous irradiation of the two compounds could allow for increased tolerance of AO to UV light. AI and AO can be synthesized simultaneously and have different reactivities towards glyceraldehyde, leading to a potential environment where both co-exist as they are being used for prebiotic reactions. To investigate this, we irradiated solutions of 0.1 mM AO + 0.1 mM AI and compared this to the individual irradiations. We tested this reaction in the Rayonet reactor (254 nm) and in the tunable setup at 215 nm. Figure 7.10.1 shows the logarithm of the maximum absorption of each solution as a function of time in the Rayonet reactor. AO and AI have very similar UV spectra, making it difficult to disentangle the two through UV-Vis measurements. For this reason, we use the absorption values at peak wavelengths (207, 215, and 210 nm for AI, AO, and AI+AO, respectively) and note that rate constants are not precisely constrained.

In the Rayonet reactor, AO and AI have pseudo-rates of 8.1×10^{-2} and $8.6 \times 10^{-3} \text{ min}^{-1}$, respectively. The combination of 0.1mM AO + 0.1mM AI has a pseudo-rate of $2.8 \times 10^{-2} \text{ min}^{-1}$ and 0.05mM AO + 0.05mM AI has a similar pseudo-rate of $2.9 \times 10^{-2} \text{ min}^{-1}$. AO degrades the fastest, and AI the slowest, while the mixture has an intermediate destruction rate.

We also irradiated mixtures of AO and AI (0.1mM each and 0.05mM each) in the tunable setup at 215 nm (see Figure 7.1.3). Again, given the very similar UV-Vis spectra of the two molecules, it is difficult to determine the concentration of each molecule throughout the irradiation. We instead calculated the concentrations assuming the absorption was due completely to AI and then completely due to AO. We took the average of these concentrations as a rough estimate, but show the ranges in potential net concentrations ($[AO]+[AI]$) with the error bars in Figure 7.1.3. At 215 nm irradiation, the relative rate of

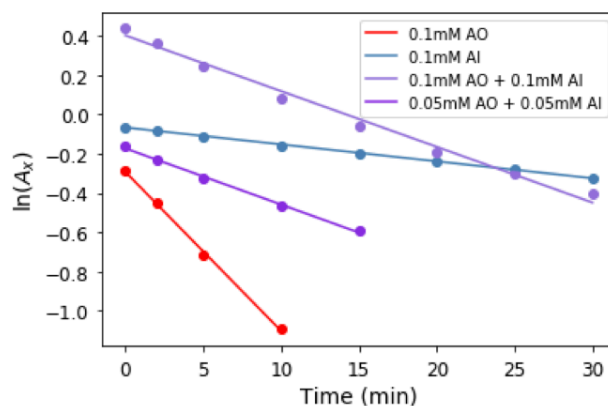


Figure 7.10.1: Logarithm of the absorbance at the peak wavelength (207, 215, and 210 nm) for solutions of AI, AO, and AO+AI with irradiation time in the Rayonet reactor. Pseudo-rates are calculated from the slopes (precise rates are difficult to determine for the AO+AI mixture due to the similar UV-Vis spectra of these two molecules). The mixtures of AO+AI have photodestruction rates in between those of AO and AI, indicating a partial protection of AO when co-irradiated with a more UV-photostable molecule, such as AI.

photodestruction of AO and AI alone are $3.13 \times 10^{-2} \text{ min}^{-1}$ and $2.84 \times 10^{-3} \text{ min}^{-1}$, respectively. The mixture of 0.1 mM AO + 0.1 mM AI has an approximate rate of $9.0 \times 10^{-3} \text{ min}^{-1}$, and the 0.05 mM AO + 0.05 mM AI solution has an approximate rate of $1.5 \times 10^{-2} \text{ min}^{-1}$ (see purple points on Figure 7.1.4). Mixtures of the two molecules show degradation rates slower than that of AO alone, suggesting some potential protection of AO when co-irradiated with AI. This observation is intriguing and suggests a potential possibility for mitigating the comparatively fast photodegradation of AO simply by invoking the presence of other more UV-stable molecules. More follow-up studies along these lines could provide more stringent constraints and understanding of the potential prebiotic environment, but this is beyond the scope of this paper.

7.1.1 APPENDIX H: ATMOSPHERIC MODELING

We calculated the relative rate of the reaction on the surface of the early Earth by taking the product of the experimentally determined reaction rates and the weighted surface intensity in each wavelength bin. To calculate the weighted surface intensity, we used the code described in Ranjan and Sasselov [260]. We provide an atmospheric profile containing composition, temperature, and pressure to the code, which then calculates spectral quantities like total surface flux and total surface intensity through a two-stream clear-sky radiative transfer model. We selected two atmospheres here: one for a sample prebiotic N_2/CO_2 -dominated atmosphere, and another for the modern Earth [285]. The exact chemical compositions of the atmospheres are listed in table 7.1.1.1. For the modern Earth, almost no light reaches the surface of the Earth from 200-300 nm, so we do not show the zero results. The total surface intensity through a prebiotic atmosphere was integrated in the same 10 nm intervals as experiments were carried out. These integrated surface intensities were then multiplied by the corresponding experimentally-determined photon flux-normalized reaction rate to generate the relative rate of the reaction on the surface of the planet as a function of irradiation wavelength. We then integrated these relative rates over

Gas	Sample Prebiotic Earth	Modern Earth
N ₂	88.9%	78%
CO ₂	10%	$3.6 \times 10^{-2}\%$
H ₂ O	0.48%	0.31%
CH ₄	$1.7 \times 10^{-4}\%$	$1.7 \times 10^{-4}\%$
SO ₂	$3.4 \times 10^{-9}\%$	0%
O ₂	$2.7 \times 10^{-4}\%$	21%
O ₃	$9.2 \times 10^{-9}\%$	$2.4 \times 10^{-5}\%$
H ₂ S	0%	0%

Table 7.11.1: Atmospheric compositions for a sample prebiotic atmosphere and the modern Earth, used for calculating the surface intensity of solar light on the planet.

irradiation wavelengths from 210-290 nm to estimate the total reaction rate expected on the surface of the early Earth, for a sample prebiotic atmosphere. This total rate could then be used to calculate the half life for each molecule under solar irradiation on the surface of a planet.

8

Shielding from UV photodamage: implications for surficial origins of life chemistry on the early Earth

Abstract

UV light has been invoked as a source of energy for driving prebiotic chemistry, but such high energy photons are also known to cause damage to molecules and biomolecules. One potential mechanism for increasing the lifetime of UV-photounstable molecules is to invoke a protection or shielding mechanism. UV shielding could either occur by the molecule in question itself (self-shielding) or by the presence of other UV-absorbing molecules nearby. We investigate these two shielding mechanisms as means to increase the lifetime of 2-aminooxazole, an example molecule that is fairly susceptible to UV photodamage and would

only be expected to have a half life of 7 hours on the early Earth. We find that this lifetime can be enhanced so that production and destruction rates are roughly equal, if AO is present in concentrations > 1 mM. AO can similarly be protected by the presence of UV-absorbing nucleosides; the amount of protection depends on the concentration and identity of the nucleoside. The purine nucleosides (A, G, and I) allow more protection than the pyrimidines (C and U). We find that 0.1mM of the purine ribonucleosides affords AO about the same protection as 1mM AO self-shielding. This suggests that only a modest yield of nucleosides is necessary to allow for protection of UV photounstable molecules, and therefore this could be a plausible mechanism for protecting sensitive molecules as prebiotic synthesis is simultaneously occurring.¹

8.1 INTRODUCTION

THE ROLE OF UV LIGHT for prebiotic chemistry and origins of life on Earth has been considered abundantly in the past, as UV light can both destroy organic molecules (e.g. Cockell and Knowland [57], Sagan [290]) and drive prebiotic processes, including the synthesis of ribonucleotides [256], and a wider cyanosulfidic network capable of synthesis all four major types of molecules [240, 384, 385]. UV light would have been abundant on the early Earth, given the larger fractional output of the young Sun in the UV [50, 270] and lack of the UV-absorbing oxygen and ozone gases responsible for screening out UV radiation in the modern atmosphere (e.g. Farquhar et al. [90], Kasting [154]). The energy from UV light on the early Earth is comparable or greater than that from lightning and atmospheric shocks, making the UV-driven synthesis of building blocks of life potentially very significant [46, 93]. Ranjan and Sasselov [259] find that UV light down to 200 nm would have been present on the early Earth, given a N_2 - CO_2 dominated atmosphere.

¹This thesis chapter represents unpublished, current work by Z. R. Todd, J. W. Szostak, and D. D. Sasselov.

UV light is also known to harm biomolecules. Nucleotides can undergo photodamage either as individual monomers (e.g. the pyrimidine bases form the photohydrates 6-hydroxy-5,6-dihydrocytidine/uridine, Liu and Yang [176], Wechter and Smith [374]) or as part of oligonucleotides. Adjacent pyrimidine bases in a strand of RNA or DNA will form cyclobutane pyrimidine dimers or 6-4 photoproducts [109]. Proteins, especially those with aromatic UV-absorbing residues, can be excited by UV light which potentially damages the protein structure [225]. It is also interesting to note that the nucleobases used by life today show shorter lifetimes after UV-excitation, giving them enhanced photostability and perhaps explaining their selection for use in early life [20].

It thus becomes important to contrast the helpful and harmful effects of UV light for building up a prebiotic chemical inventory for origins of life. Even if UV light is not invoked for prebiotic synthetic purposes and instead other methods (e.g. lightning discharge, impact delivery/synthesis) are used, any origins of life scenario occurring on the surface of the planet will have to assess the compatibility of the invoked chemistry with the presence of these high energy photons.

That is not to say that all surface prebiotic chemistry must be UV-photostable; indeed, various theories for UV protection or mitigation have been postulated in the past. Sagan [290] suggested that early life could be shielded from the damaging effects of UV light by the presence of layers of UV-absorbing purine and pyrimidine nucleotides. Prebiotic organic polymers (e.g. from HCN, Cleaves and Miller [53]), inorganic species (e.g. Cl^- , Br^- , Mg^{2+} , SH^- , Fe^{2+} , [53, 57]), or dissolved organic carbon [57] were suggested to have the potential for UV-shielding effects. The accumulation of longer oligonucleotides over monomers (which are favored by hydrolysis considerations) has also been suggested to be due to UV selection, where the nitrogenous bases absorb the UV light to protect the sugar-phosphate backbone from UV-induced cleavage [23, 216]. Furthermore, even if UV damage does occur, various mechanisms could repair these lesions. For example, charge transfer states from decay of photoexcited DNA can repair DNA photolesions [33, 339]. Life today

uses a number of means to repair UV damage, including photolyases and excision repair enzymes, but these would not have been available for the origin of life.

For any origin-of-life scenario occurring on the surface of a planet, UV protection may have been crucial for the more photo-unstable molecules. Here, we investigated the ability of shielding processes to enhance the lifetime of a marginally photo-unstable molecule under UV light. 2-aminooxazole (AO) is a key intermediate in the synthesis of pyrimidine ribonucleotides [256] and could plausibly have been synthesized on the early Earth, by making use of UV light [?](Ritson et al. 2018). We previously examined the photostability of three 2-aminoazoles (AO, 2-aminothiazole, and 2-aminoimidazole) potentially important for prebiotic chemistry and found AO to be the least photostable, with a half life of roughly 7 hours under a solar-like spectrum [351]. We thus decided that AO would make a good test molecule for UV-shielding experiments to see if its lifetime under UV irradiation could be enhanced. We specifically examined if 1) AO could be self-shielded from UV light, simply by being present at higher concentrations, or 2) AO could be shielded by co-irradiating it with various nucleosides.

8.2 EXPERIMENTAL

8.2.1 SELF-SHIELDING

AO was irradiated in varying concentrations (0.1, 0.5, 1, 5, 10, and 50 mM) in a RPR-200 reactor, with mercury emission lamps (254 nm) for times varying from 10 minutes to 4 hours. During the irradiation, small aliquots of the solution were removed and diluted such that the initial concentration of AO would have been 0.1 mM. The UV-Vis absorption spectra of the diluted solutions were measured and used to determine the concentration of AO as a function of time throughout the irradiation. The logarithm of the concentration plotted against time gives a straight line, the slope of which represents the rate constant of the reaction. We determined the rate constants for each initial concentration of AO.

8.2.2 NUCLEOSIDE CO-IRRADIATION

Solutions of AO (0.05mM or 0.1mM) were made with varying concentrations (0.01, 0.05, or 0.1mM) of different nucleosides (A, G, C, U, and I) and irradiated at 254 nm (RPR-200 reactor, mercury emission lamps). The UV-Vis absorption spectra were measured throughout the course of the irradiations (lasting from 10-30 min). The UV spectra were used to determine the concentration of AO over the course of the irradiation, which was then used to calculate the rate constant. Experiments were repeated in duplicate to obtain an average rate constant and the associated error.

8.3 RESULTS AND DISCUSSION

We first examined the rate of photodestruction of AO at varying concentrations to assess the efficiency of self-shielding as an efficient UV-blocking mechanism. We irradiated solutions of 0.1, 0.5, 1, 5, 10, and 50 mM AO in a Rayonet reactor (254 nm, mercury emission lamps) and determined the concentration of AO at various timepoints during the irradiation by diluting the solutions and measuring the UV-Vis absorption spectrum. The concentration of AO was calculated from a standard curve. The logarithm of the concentration of AO plotted against irradiation time gives a straight line (Figure 8.3.1), whose slope represents the rate constant of AO photodestruction.

Figure 8.3.2 shows the rate constants for varying concentrations of AO. The rate constant decreases for higher concentrations of AO, since the molecule absorbs more light at these higher concentrations. Increased absorption means the optical depth of the solution decreases, so less photons can reach the entire sample, causing the rate of photodestruction to be reduced. Experiments were repeated in duplicate; points represent the average and error bars show the standard deviation from each duplicate set. At the lowest concentration tested, the rate constant is 0.12 min^{-1} under these irradiation conditions (254 nm,

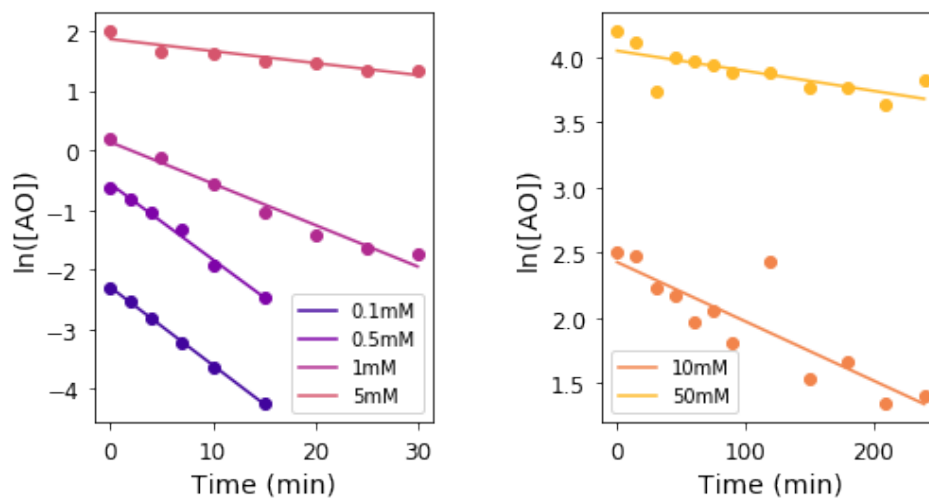


Figure 8.3.1: Logarithm of AO concentration as a function of irradiation time for various concentrations, as determined by UV-Vis spectroscopy. The slope of the best-fit lines represents the rate constant of the reaction.

RPR-200 reactor). At 1mM and 10mM, the rate constant becomes 7.2×10^{-2} and $5.0 \times 10^{-3} \text{ min}^{-1}$, leading to lifetime enhancements of a factor of 1.7 and 25, respectively. In Todd et al. (2019), we found that AO (0.1 mM) has a half life of 7 hours, taking into account the wavelength-dependence of the photodestruction and the spectrum of the Sun on the surface of the young Earth. It is important to note that the experiments presented here at different concentrations are not performed in a wavelength-dependent manner, and therefore we cannot determine an accurate lifetime for the UV-irradiation environment present on the early Earth. But, if the lifetime enhancement of AO under 254 nm irradiation at higher concentrations is directly comparable to the lifetime enhancement under a solar-like irradiation spectrum, 1mM and 10mM solutions of AO would have lifetimes of approximately 12 and 180 hours, respectively. The UV flux from the RPR-200 reactor is 48x greater than the flux from 250-260 nm in the tunable lamp.

The critical question then becomes, if UV light necessary to drive the prebiotic chemistry is present throughout the network, is the rate of production of AO

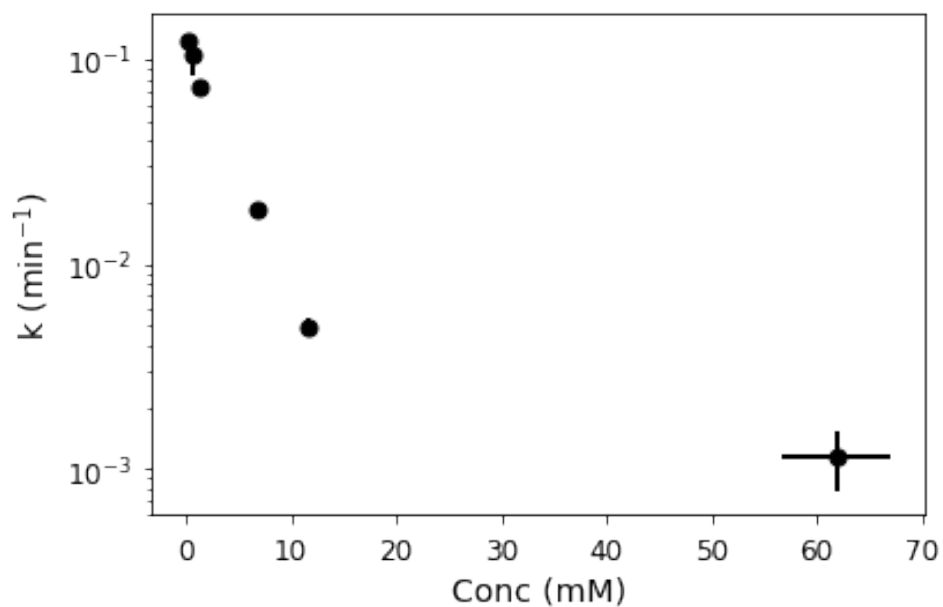


Figure 8.3.2: Rate constant of AO photodestruction for varying initial concentrations of AO. At higher concentrations, AO absorbs a larger amount of the UV light, leading to self-shielding and correspondingly lower rates of photodestruction.

faster than its rate of photodegradation under plausible conditions? If this is the case, then AO should be available to be used in the productive chemical pathway toward making pyrimidine ribonucleotides. If not, then AO will be degraded faster than it is produced, and this may act as a roadblock for the proposed prebiotic chemistry. We show here that the rate of degradation by UV light depends on the concentration of AO, with higher concentrations showing decreased rates of destruction. Previous work has shown an uninterrupted synthesis of AO using flow chemistry to get from simple precursors to AO without significant human intervention [278]. They report production of AO from simple compounds (glycolonitrile, sodium bisulfite, potassium ferrocyanide, and phosphate) when they undergo UV irradiation for 100 minutes followed by a dry down step. Redissolving the solution, subjecting it to calcium cyanamide and heat, followed by a cooling and sedimentation step yields $\approx 70\text{mM}$ AO. With a simplified calculation, we can estimate the production rate of AO under these conditions as follows: roughly 70 mmol of AO are produced from 100 minutes of irradiation, giving a rate constant of $\ln(70)/100 \text{ min} = 0.042 \text{ min}^{-1}$.

Comparing this value to our rates of photodestruction can constrain the relevant concentrations of AO in order for this prebiotic chemistry to be self-consistent and productive, given the presence of UV light and invoking the UV protection mechanism of self-shielding. We find that the photodestruction rate of AO exceeds 0.042 min^{-1} for concentrations roughly $< 1 \text{ mM}$. So, AO needs to be present in concentrations $> 1 \text{ mM}$ in order for the production rate to exceed UV destruction, when relying on self-shielding to protect AO from photodamage.

Such concentrations of AO may be plausible on the early Earth. Ritson et al. [278] find concentrations of 70mM after their continuous, uninterrupted synthesis), but perhaps there exists another alternative protective shielding mechanism in the form of other UV-absorbing molecules in the presence of AO [278]. We next tested whether nucleosides, which are fairly UV-absorbent molecules, could enhance the lifetime of AO to UV light when co-irradiated. In

these experiments, we tested concentrations of 0.05 and 0.1mM AO, where self-shielding is not significant enough to protect AO from degradation. We added varying concentrations (0.01, 0.05, and 0.1mM) of various nucleosides (G, C, U, A, and I) to these solutions and again performed the irradiations at 254 nm. The UV spectra were recorded throughout the irradiation to enable determination of the rate constants, as described below.

The purine nucleosides show a primary absorption feature around 260 nm. During irradiation, this absorption feature decreases and no new absorption signals are observed (Figure 8.3.3A). This allows for a simple extraction of the concentration of each species in solution as a function of irradiation time to enable determination of the rate constant as the slope of the best fit line in Figure 8.3.3B. The absorption at the maximum wavelengths for AO and the purine ribonucleoside (216 and 260 nm, respectively) are used to determine the concentration by solving a system of two equations:

$$A_{216} = \epsilon_{AO,216}c_{AO}l + \epsilon_{A/I/G,216}c_{A/I/G}l$$

$$A_{260} = \epsilon_{AO,260}c_{AO}l + \epsilon_{A/I/G,260}c_{A/I/G}l$$

This method does not work for the pyrimidine ribonucleotide experiments, because the pyrimidine ribonucleosides show increasing absorption at wavelengths < 240nm during irradiation, even as the 260 nm initial feature decreases. Given the overlapping of the AO band (maximum at 216 nm) and the new absorption feature that grows in with irradiation time, the extinction coefficients cannot be used disentangle the concentrations of the pyrimidine ribonucleosides and AO as is the case for the purine ribonucleosides. Therefore, for the pyrimidine ribonucleoside experiments, identical experiments were performed with only the ribonucleoside (without the addition of AO). The spectra at each timepoint were then subtracted from the corresponding spectra of the solution of both AO and the ribonucleoside (i.e. 0.1mM C spectra as a function of irradiation, Figure 8.3.4B, were subtracted from those of the 0.1mM

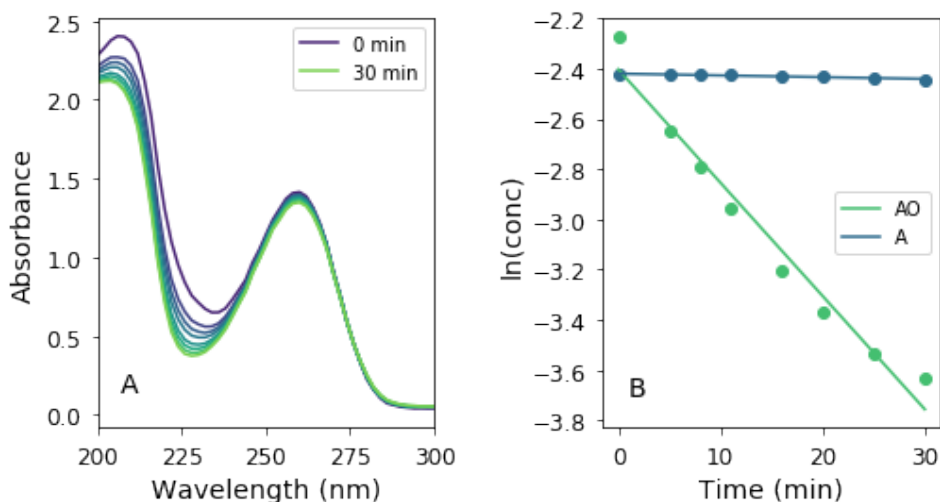


Figure 8.3.3: A. Absorption spectra of a solution of 0.1mM AO + 0.1mM A during irradiation. The AO and A spectral features are clearly separated and no new features appear, enabling the concentration of each species to be determined from the extinction coefficients. B. The logarithm of concentration as a function of irradiation time is used to determine the rate constants.

AO + 0.1mM C solution, Figure 8.3.4A). This enabled an effective destruction rate of AO to be calculated from converting the difference spectra (Figure 8.3.4C) into a concentration of AO with time (Figure 8.3.4D). We note that when this subtraction method is applied to the purine ribonucleoside experiments, similar rate constants are recovered as with the extinction coefficient method.

Now equipped with methods for determining the concentrations of AO with irradiation time for both purine and pyrimidine co-irradiation experiments, we then determined the rate constants for AO destruction. Figure 8.3.5 shows these rate constants for two different concentrations of AO, with and without the addition of nucleosides in varying concentrations. The rate constant for AO degradation alone at concentrations of 0.05 and 0.1mM is shown in shaded regions (red and blue, respectively). The degradation rate constant for 0.05mM AO and 0.1mM AO when co-irradiated with varying concentrations of different

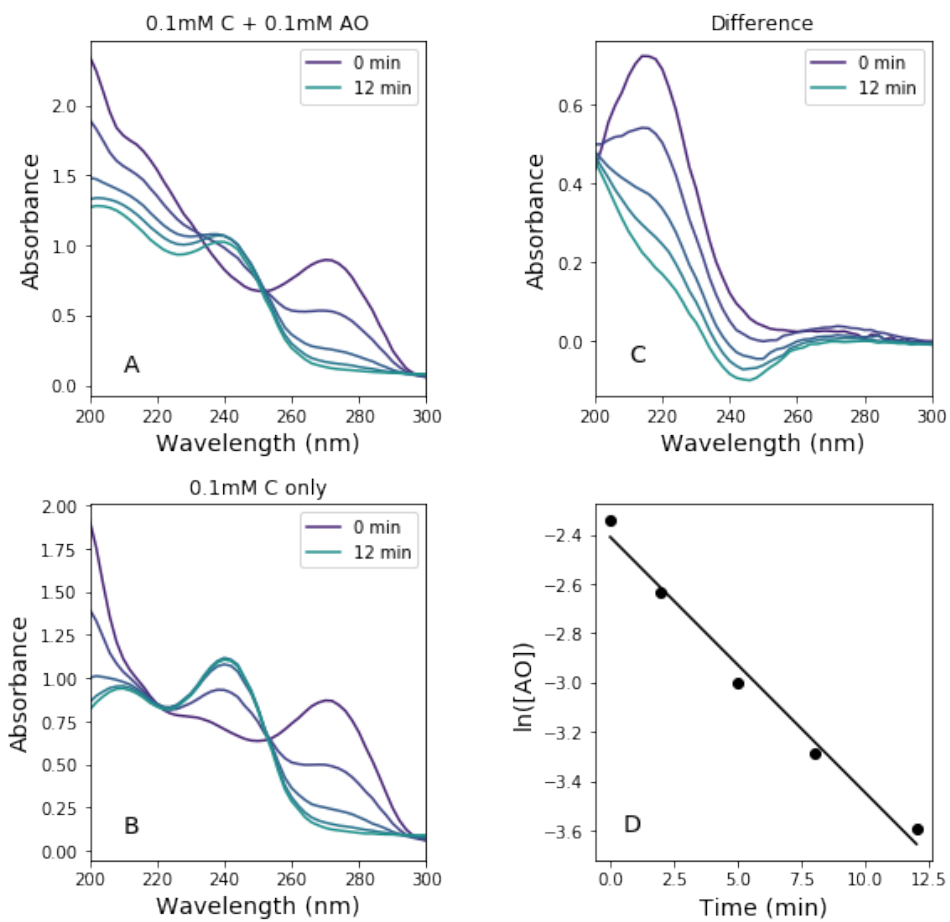


Figure 8.3.4: A. Absorption spectra of a solution of 0.1mM AO + 0.1mM C with irradiation time. B. Absorption spectra of a solution of 0.1mM C with irradiation time. C. Difference of the spectra in A and B at each respective timepoint to see the effects of irradiation of AO. D. Logarithm of calculated effective concentration of AO with irradiation time to get an estimated rate constant for AO destruction.

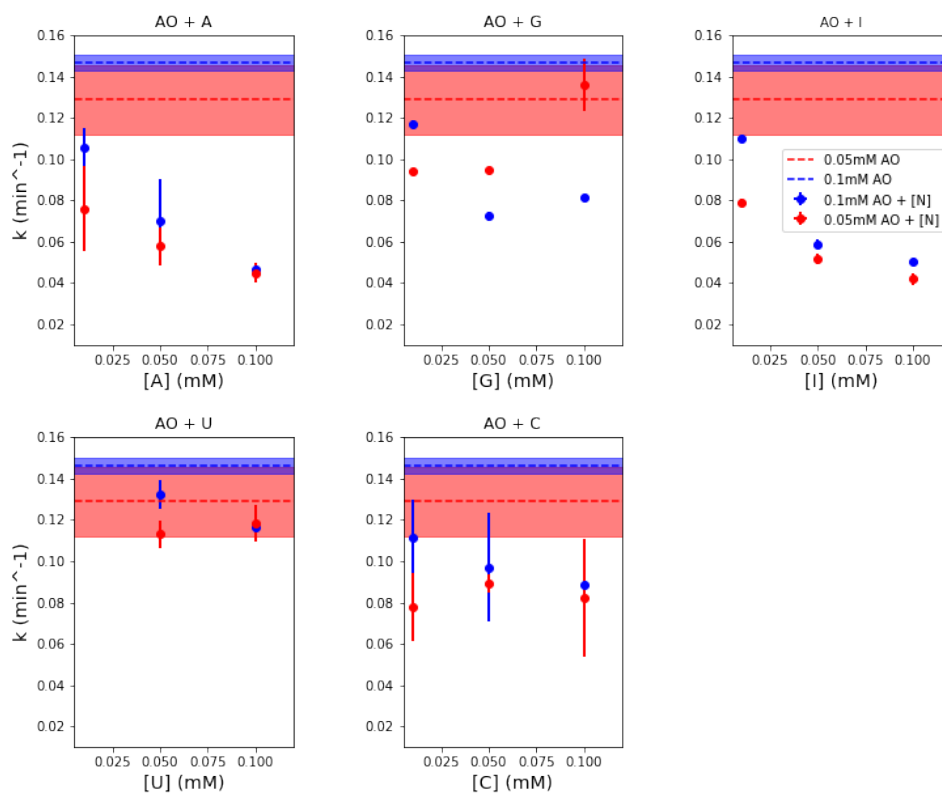


Figure 8.3.5: Rate constant for AO photodestruction alone (shaded regions) and with addition of various concentrations of nucleosides (points). AO was tested in two concentrations (0.05 and 0.1mM, red and blue, respectively). Nucleosides were added in concentrations of 0.01, 0.05, and 0.1mM. We find the addition of nucleosides can decrease the rate of photodestruction of AO. The purines were better at shielding AO, with the best protection provided by A. The pyrimidines may have marginally decreased the rate of AO photodestruction, but U was less efficient than C.

nucleosides is shown by the red and blue points, respectively. We find that the presence of nucleosides decreases the degradation rate of AO to varying degrees, depending on the identity and concentration of the nucleoside. Generally, higher concentrations of the nucleoside decrease the rate of photodestruction, as would be expected - the increased amount of nucleoside absorbs more UV light and has a stronger shielding effect for AO destruction by UV. The purine nucleosides (A, G, and I) show better protection capabilities, yielding lifetime enhancements of roughly a factor of two at the higher concentrations. The pyrimidine nucleosides are less effective at protecting AO: C shows marginal lifetime enhancements, but the effect of the U is not as significant. This is perhaps not surprising, given that the pyrimidines are also susceptible to their own UV photodamage in the form of photohydrates. Once pyrimidine photohydrates are formed, they absorb less UV light, and therefore may not provide as effective a shield for AO. It is worth pointing out that we find roughly the same amount of protection from the addition of 0.1 mM of purine nucleosides as the self-shielding of 1 mM AO. So, production of nucleosides does not have to reach as high concentrations as AO production in order to offer the same protective effects. In fact, the best protecting nucleoside addition (0.1 mM A) gives an AO photodestruction rate around 0.05 min^{-1} , which is comparable to the production rate from Ritson et al. (2018). Therefore, moderate concentrations of nucleosides could act as a sufficient UV shield to allow this borderline-photounstable molecule to survive longer, such that production and destruction are roughly equal. Figure 8.3.6 shows the relative lifetimes of 0.1 mM AO alone and with the addition of 0.1 mM A, as well as the lifetime of 1 mM AO. Modest (e.g. 2-3x) lifetime enhancements are seen with the addition of the nucleoside or when AO is present in higher concentrations such that it self-shields.

Here, we have used AO as an example of a UV-sensitive molecule in this study. AO plays a key role as an intermediate toward building up the pyrimidine ribonucleotides and was found to be the least photostable of three 2-aminoazoles, with a half life of 7 hours under the UV environment on the early

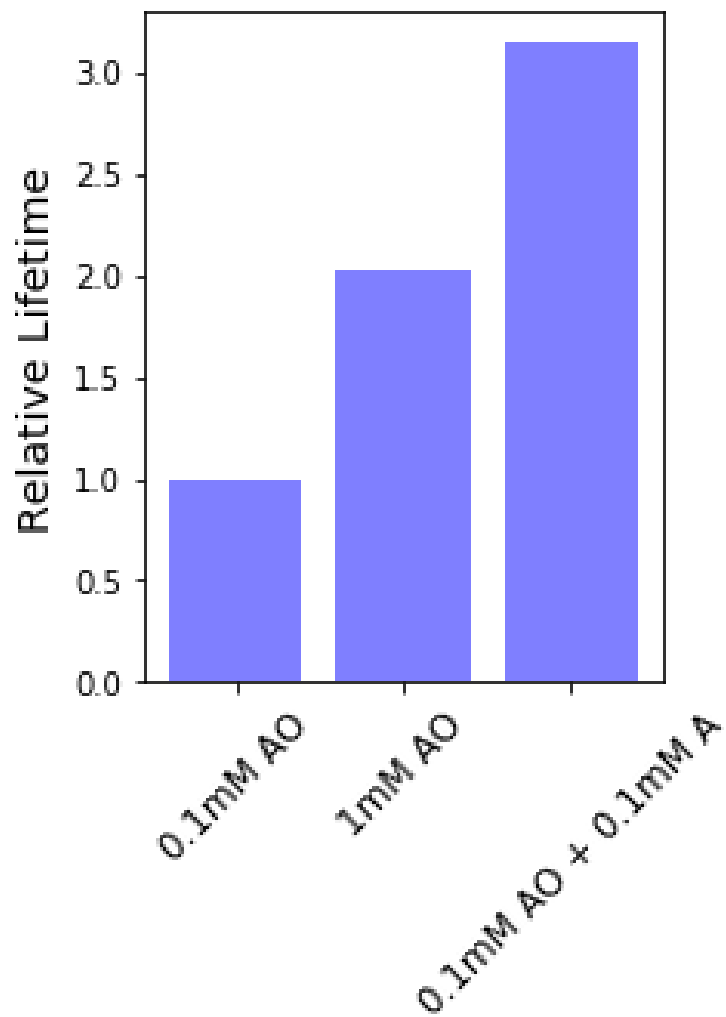


Figure 8.3.6: Lifetimes of AO with the addition of 0.1 mM A and at 1 mM, compared to the lifetime of the unshielded molecule at 0.1 mM. The lifetime of AO to UV light (as compared to 0.1 mM AO alone) is enhanced by a factor of 3 and 2 for the addition of 0.1 mM A and for 1 mM AO, respectively.

Earth (Todd et al. 2019). While we use AO as an example and find the results for protection and lifetime enhancement for this molecule, the shielding mechanisms investigated here should be robust across a variety of molecules. Our results for AO imply that UV photo-unstable molecules may find their lifetimes enhanced by being present in increasing concentrations. Alternatively, these UV-sensitive molecules could find protection from other UV-absorbing molecules present in solution, such as ribonucleosides. The effectiveness of these protection mechanisms depends on the concentrations of molecules used. The degree of shielding needed may vary from molecule to molecule, depending on its inherent UV photostability and the rates at which it is being produced. Here, AO was used as an example of the mechanism of shielding, but this could apply broadly to any range of molecules invoked in prebiotic chemistry scenarios.

One further caveat must be considered: some prebiotic chemistry relies on UV light as a source of energy to drive the synthesis of biomolecules. For example, in the cyanosulfidic network developed by the Sutherland lab [240, 384], UV light in particular is used as a source of solvated electrons, either from cyanocuprate complexes [276] or ferrocyanide and sulfite [385]. This is the driving source for the entire pathway leading towards all four major types of biomolecules [240]. It is possible that as the network builds up ribonucleotides, these UV-absorbing molecules could attenuate the UV light enough so that the generation of solvated electrons is no longer sufficient to continue driving the reaction network. So while on the one hand, increased UV shielding may be good for protecting UV-sensitive molecules created, it may at the same time pose a problem for the continued synthesis of these molecules. This remains an avenue of study that needs to be explored to assess the overall consistency of the network with regards to the presence of UV light.

8.4 CONCLUSIONS

UV light, though potentially an important source of energy on the early Earth for prebiotic synthesis, can also damage biomolecules. In order for surface

origins-of-life scenarios to be considered plausible, they must contend with the presence of potentially damaging UV photons. Various mechanisms of protection have been suggested in the past, and here we investigate mitigation of UV photodamage either through self-shielding or shielding from the presence of additional UV-absorbing molecules. We find that AO, a marginally photounstable molecule under a solar-like UV environment, is capable of shielding itself at higher concentrations, with its lifetime increasing by a factor of 25 at 10mM compared to 0.1mM. We also find that co-irradiation of moderate concentrations (0.05-0.1mM) of nucleosides, especially purines, can reduce the rate of AO photodestruction. Under such scenarios, the photodestruction rate of AO is similar to the rate of production found in Ritson et al. (2018), suggesting that these shielding mechanisms could be sufficient for allowing AO to continuously exist in a UV-irradiated environment without photodamage causing significant depletion of the key intermediate. While our results are encouraging for the particular UV-driven prebiotic chemistry scenario outlined by the Sutherland group (e.g. Patel et al. [240], Powner et al. [256], etc.), our work has wider implications beyond this specific chemistry. Any surficial prebiotic chemistry will experience exposure to UV light, and if any of those molecules are susceptible to UV damage, this could be an issue. However, we find that shielding by nucleosides could be a fairly robust mechanism for decreasing the rate of destruction of photo-unstable molecules. Any similar set of molecules with a pi electron system would likely act as a good UV screen as well, making this shielding process more generic beyond just nucleosides. In addition, if concentrations of molecules are sufficiently high, this may be enough to attenuate damaging UV light and prolong the lifetimes of molecules under UV irradiation.

9

Conclusions and Future Directions

9.1 CONCLUSIONS

IN THIS WORK, we sought to better understand the circumstances surrounding the origins of life on Earth, both from the chemical and planetary perspectives. We aimed to piece together various suggested steps in the process of origins of life to start to find a consistent and coherent picture for the origins of life. While there are still many gaps in our knowledge and much work remains to be done, we have made some substantial conclusions.

In Chapter 2, we studied the possibility of delivery of the hydrogen cyanide, a molecule of prebiotic interest, from impacts of comets. HCN is invoked in numerous schemes and ideas regarding prebiotic chemistry, and here, we addressed impact delivery of HCN. We found that, while on a global scale, the

amount of HCN delivered in comet impacts was probably not a significant source, under favorable circumstances, local impacts could provide prebiotically-relevant amounts of HCN for substantial amounts of time. We showed that the most favorable environments for significant HCN delivery are low-impact, smaller, slower impacts, where cometary delivered material is contained locally. The lifetime of HCN is longest in moderately acidic, low temperature environments, where it can remain in prebiotically-relevant concentrations for up to several million years. Our work has demonstrated a potentially significant source of HCN that does not depend on the reducing state of the atmosphere, like both photochemical and lightning generation do. In a relatively oxidizing atmosphere, impact delivery may exceed levels of HCN expected from lightning and photochemical generation.

In chapter 3, we looked at the atmosphere as a source of sulfur-containing compounds that may have been necessary for prebiotic chemistry. Volcanoes outgas both H_2S and SO_2 , which can dissolve in surface waters and form sulfidic anions. We found that the higher solubility and lower pKa of the SO_2 -derived anions, HSO_3^- and SO_3^{2-} , can give prebiotically-relevant concentrations (i.e. micromolar to millimolar) in surface waters. Alternatively, the decreased solubility and less favorable dissociation constant for H_2S -derived anions, HS^- and S^{2-} , limit these ions to insufficient concentrations for prebiotic chemistry on a global scale, though local production mechanisms are possible. As a result of this project, we were able to suggest an alternative sulfur-containing compound for origins of life experiments and better constrain the environmental circumstances that could be relevant and consistent for prebiotic chemistry.

In chapter 4, we similarly considered the levels of nitrogen oxides available on the early Earth. Nitrogen oxides, created primarily in the atmosphere through lightning chemistry, can reach surface waters to be potentially used in prebiotic chemistry. In this project, we revisited the potential levels of nitrogen oxides by considering an increased set of sinks, including photochemical loss and reduction by ferrous iron. We found that past estimates of nitrogen oxide concentrations were too high, once these sinks were taken into account. From this project, we

were able to determine globally available concentrations of nitrogen oxides, which can be used to inform prebiotic chemistry experiments. If higher concentrations of these molecules are found to be necessary, this suggests another, more specific environment, must be invoked.

Chapters 2-4 addressed planetary sources of simple feedstock molecules that can act as inputs to prebiotic chemistry networks leading to the synthesis of more complex biomolecules necessary for the origins of life. In the subsequent chapters, we shifted to focus on the prebiotic chemistry that makes use of these feedstock molecules, and specifically examined the role of UV light in this process.

In chapter 5, we examined the role of the UV-environment expected on the early Earth for driving the photochemical synthesis of simple sugars from hydrogen cyanide and cyanocuprates. Past work had determined that such sugars could be synthesized using 254 nm UV light, but this light is not representative of the UV environment present on the early Earth. We experimentally examined the rate of the reaction at various wavelengths and coupled these results to the expected spectral fluxes. We determined that the photochemical production of sugars from cyanocuprates is most efficient at wavelengths < 250 nm, but that the process should overall work under the UV environment present on the early Earth. In this study, we also decreased the concentrations of reactants from tens-to-hundreds of millimolar to sub-millimolar, which again increases the prebiotic plausibility of the process.

In chapter 6, we investigated the photochemical conversion of the ribonucleotide C into the ribonucleotide U. This process had again been studied in the past at 254 nm and under the most ideal laboratory conditions. We placed this reaction in the appropriate planetary context by analyzing its wavelength dependence and the effects of varying temperatures and day/night cycles. We found that the most efficient wavelengths for driving the reaction are 255-285 nm and that C should be able to be converted into U photochemically on the early Earth. However, we found that continued irradiation will deplete the supply of C if production rates are low. Finally, we also determined that substantial amounts

of heating are required to return C and U to their canonical, undamaged forms. Understanding the chemistry of the system in these respects allows us to constrain the planetary environment that would have favored such a reaction to be relevant on the early Earth.

In chapter 7, we studied the potential drawbacks to UV light by examining the photostability of three key molecules in the 2-aminoazole family invoked in the prebiotic chemical network suggested by Patel et al. [240]. The reaction studied in chapter 5 occurs at the beginning of this chemistry, while that in chapter 6 occurs near the end. Both make use of UV light as a productive driver of the chemistry, so it is simplest to assume that UV light would be present throughout the network. The three 2-aminoazoles studied in chapter 7 occur at intermediate points in this chemical network and therefore, their stability to UV light is crucial to understand. We found that these molecules have lifetimes of 7-100 hours under the UV-environment expected on the early Earth. Interestingly, the molecule used first in the network had the shortest half-life, while the last-used molecule had the longest half-life. This work suggests that the chemical network may be consistent with respect to the presence of UV light, provided that reactions using these molecules occur quickly enough, or production rates are comparable to destruction. By understanding the photodegradation, we can begin to piece together a picture of the chemical network and better understand the environmental conditions necessary for such a chemical network to function consistently.

Finally, in chapter 8, we addressed the question of, if the lifetime of 7 hours to UV light found in chapter 7 is not sufficient to allow the chemistry to function, what other mechanisms might be possible to extend this lifetime. We investigated self-shielding and shielding of photo-sensitive molecules either by themselves or another UV-absorbing molecule. We found that the lifetime of the marginally photo-unstable molecule, 2-aminooxazole (half-life of 7 hours) could be extended by 2-3 times under shielded or self-shielded conditions. This is ongoing work and a wider range of potential shielding mechanisms yet to be investigated could potentially extend this lifetime even further. In this way, we are able to offer

potentially simple mechanisms for increasing the lifetime with respect to UV light for photo-sensitive molecules, thus perhaps offering a more consistent set of conditions for prebiotic chemistry to occur.

9.2 FUTURE DIRECTIONS

As with most science, for each question we attempted to answer here, many new questions and ideas were prompted. Regarding sources of simple feedstock molecules, we plan to extend our impact delivery work in the future to address not only HCN, but other molecules contained in comets, including NH_3 , H_2CO , etc. The goal of these studies would be to determine the chemical composition of a "comet pond" to assess the molecules available for prebiotic chemistry following an impact. We hope to include not only intact delivery from impacts, but also impact synthesis from reactions in the atmosphere.

As a follow-up to some of the photochemistry work, we are similarly investigating the wavelength-dependence of a modified chemistry making use of ferrocyanide and sulfite instead of cyanocuprates and HS^- . The switch to sulfite by the experimental chemists was in part motivated by our work on sulfidic anions (chapter 3). Both sulfite and ferrocyanide are more geochemically plausible, making this process more relevant for the early Earth.

However, with all the good that UV light can do for driving prebiotic chemistry, it can also do significant damage, especially to the more complex polymers such as RNA. We are also investigating the potential of lipid vesicles to shield UV-sensitive molecules from photodamage through scattering or absorption. The hope is that UV-dependent prebiotic synthetic chemistry could take place outside of vesicles to make for example RNA monomers. Then, once RNA polymerizes and is potentially more susceptible to UV damage, perhaps encapsulation in a lipid vesicle could mitigate some of this damage. The move to lipid vesicles is also attractive from the point of view of creating a simple protocell. Ultimately, the goal would be to have simple, robust planetary conditions that could allow for the synthesis of the building blocks of life from

available feedstocks, then polymerize these molecules to make more complex biomolecules such as RNA and peptides, and finally have a self-replicating system enclosed by lipid protocells. Once this goal is attained, we will have a better understanding as to how life on Earth could have originated and what this implies for the possibility of life on other worlds.

- [8] A. Ardaseva, P. B. Rimmer, I. Waldmann, M. Rocchetto, S. N. Yurchenko, C. Helling, and J. Tennyson. Lightning chemistry on Earth-like exoplanets. *Monthly Notices of the Royal Astronomical Society*, 470: 187–196, September 2017. doi: 10.1093/mnras/stx1012.
- [9] Aristotle. *Aristotle's history of animals: In ten books*. London, 1862.
- [10] J. Attwater, A. Wochner, V. B. Pinheiro, A. Coulson, and P. Holliger. Ice as a protocellular medium for RNA replication. *Nature Communications*, 1: 76, September 2010. doi: 10.1038/ncomms1076.
- [11] A. R. Babbin, R. G. Keil, A. H. Devol, and B. B. Ward. Organic matter stoichiometry, flux, and oxygen control nitrogen loss in the ocean. *Science*, 344(6182):406–408, 2014.
- [12] J. L. Bada, C. Bigham, and S. L. Miller. Impact Melting of Frozen Oceans on the Early Earth: Implications for the Origin of Life. *Proceedings of the National Academy of Science*, 91:1248–1250, February 1994. doi: 10.1073/pnas.91.4.1248.
- [13] R. D. Ballard. The discovery of hydrothermal vents. *Oceanus*, 20(3), 1977.
- [14] A. Banerjee, G. Ganguly, R. Tripathi, N. N. Nair, and A. Paul. Unearthing the mechanism of prebiotic nitrile bond reduction in hydrogen cyanide through a curious association of two molecular radical anions. *Chem. Eur. J.*, 20(21):6348–6357, 2014.
- [15] A. Barlev and D. Sen. Dna's encounter with ultraviolet light: an instinct for self-preservation. *Acc. Chem. Res.*, 51(2):526–533, 2018.
- [16] N. G. Barlow. Estimating the terrestrial crater production rate during the late heavy bombardment period. *Meteorite Impact on the Early Earth, LPI Contribution*, 746:4, 1990.
- [17] D. L. Baulch, D. D. Drysdale, D. G. Horne, and A. C. Lloyd. *Evaluated Kinetic Data for High Temperature Reactions*.
- [18] S. Becker, C. Schneider, H. Okamura, A. Crisp, T. Amatov, M. Dejmek, and T. Carell. Wet-dry cycles enable the parallel origin of canonical and non-canonical nucleosides by continuous synthesis. *Nat. Commun.*, 9: 163, 2018.

- [19] S. Becker, J. Feldmann, S. Wiedemann, H. Okamura, C. Schneider, K. Iwan, A. Crisp, M. Rossa, T. Amatov, and T. Carell. Unified prebiotically plausible synthesis of pyrimidine and purine rna ribonucleotides. *Science*, 366:76–82, 2019.
- [20] A. A. Beckstead, Y. Zhang, M. S. de Vries, and B. Kohler. Life in the light: nucleic acid photoproperties as a legacy of chemical evolution. *Phys. Chem. Chem. Phys.*, 18(35):24228–24238, 2016.
- [21] S. A. Benner, H.-J. Kim, M.-J. Kim, and A. Ricardo. Planetary organic chemistry and the origins of biomolecules. *Cold Spring Harb. Perspect. Biol.*, 2(7):a003467, 2010.
- [22] J. G. Blank, B. T. Liu, I. N. Lomov, and T. H. Antoun. Modeling comet-earth collisions to assess survivability of organic materials during impact. *Lunar and Planetary Science XXXIX*, page 2237, 2008.
- [23] A. C. Borin. Light and nucleobases: A good interaction for everybody. *Journal of Luminescence*, 198:433–437, 2018.
- [24] W. J. Borucki, L. P. Giver, C. P. McKay, T. Scattergood, and J. E. Parris. Lightning production of hydrocarbons and hcn on titan: laboratory measurements. *Icarus*, 76:125–134, 1988.
- [25] W. F. Bottke, D. Vokrouhlicky, D. Minton, D. Nesvorny, A. Morbidelli, R. Brasser, B. Simonson, and H. F. Levison. An archaean heavy bombardment from a destabilized extension of the asteroid belt. *Nature*, 485:78–81, 2012.
- [26] J. A. Brandes, N. Z. Boctor, G. D. Cody, B. A. Cooper, R. M. Hazen, and H. S. Yoder Jr. Abiotic nitrogen reduction on the early earth. *Nature*, 395(6700):365, 1998.
- [27] R. Brasser, S. J. Mojzsis, S. C. Werner, S. Matsumura, and S. Ida. Late veneer and late accretion to the terrestrial planets. *Earth Planet. Sci Lett.*, 455:85–93, 2016.
- [28] R. Breslow and Z.-L. Cheng. L-amino acids catalyze the formation of an excess of d-glyceraldehyde, and thus other d-sugars, under credible prebiotic conditions. *Proc. Natl. Acad. Sci. USA*, 107:5723–5727, 2010.

- [29] R. Breslow, V. Ramalingam, and C. Appayee. Catalysis of glyceraldehyde synthesis by primary or secondary amino acids under prebiotic conditions as a function of pH. *Orig. Life Evol. Biosph.*, 43:323–329, 2013.
- [30] K. Brosig, T. Geyer, A. Subah, and M. Sauter. Travel time based approach for the assessment of vulnerability of karst groundwater: the transit time method. *Environmental Geology*, 54(5):905–911, 2008.
- [31] L. L. Brown and J. S. Drury. Nitrogen-isotope effects in the reduction of nitrate, nitrite, and hydroxylamine to ammonia. i. in sodium hydroxide solution with Fe(II). *The Journal of Chemical Physics*, 46(7):2833–2837, 1967.
- [32] P. D. Broxton, P. A. Troch, and S. W. Lyon. On the role of aspect to quantify water transit times in small mountainous catchments. *Water Resources Research*, 45(8), 2009.
- [33] D. B. Bucher, C. L. Kufner, A. Schlueter, T. Carell, and W. Zinth. Uv-induced charge transfer states in dna promote sequence selective self-repair. *J. Am. Chem. Soc.*, 138(1):186–190, 2016.
- [34] C. Buchwald, K. Grabb, C. M. Hansel, and S. D. Wankel. Constraining the role of iron in environmental nitrogen transformations: dual stable isotope systematics of abiotic NO₂-reduction by Fe(II) and its production of N₂O. *Geochimica et Cosmochimica Acta*, 186:1–12, 2016.
- [35] R. J. Buresh and J. T. Moraghan. Chemical reduction of nitrate by ferrous iron. *Journal of Environmental Quality*, 5(3):320–325, 1976.
- [36] J. B. Burkholder, J. P. D. Abbatt, R. E. Huie, C. E. Kolb, V. L. Orkin, P. H. Wine, S. P. Sander, J. R. Barker, M. J. Kurylo, and D. M. Wilmouth. Chemical kinetics and photochemical data for use in atmospheric studies: Evaluation number 18. Technical report, NASA Jet Propulsion Laboratory, 2015.
- [37] A. Butlerow. Bildung einer zuckerartigen substanz durch synthese. *Liebigs Ann. Chem.*, 120:295–298, 1861.
- [38] B. J. Cafferty and N. V. Hud. Was a pyrimidine-pyrimidine base pair the ancestor of Watson-Crick base base? insights from a systematic approach to the origins of RNA. 2015, 55:891–905, 2015.

- [39] D. E. Canfield, A. N. Glazer, and P. G. Falkowski. The Evolution and Future of Earth's Nitrogen Cycle. *Science*, 330:192, October 2010. doi: 10.1126/science.1186120.
- [40] J. Cao, Z.-Z. Xie, and X. Yu. Excited-state dynamics of oxazole: A combined electronic structure calculations and dynamic simulations study. *Chem. Phys.*, 474:25–32, 2016.
- [41] L. J. Carpenter and P. D. Nightingale. Chemistry and release of gases from the surface ocean. *Chemical reviews*, 115(10):4015–4034, 2015.
- [42] T. C. Chamberlin and R. T. Chamberlin. Early terrestrial conditions that may have favored organic synthesis. *Science*, 28:897–911, 1908.
- [43] W. L. Chameides. The photochemistry of a remote marine stratiform cloud. *Journal of Geophysical Research: Atmospheres*, 89(D3):4739–4755, 1984.
- [44] W. L. Chameides and J. C. G. Walker. Rates of fixation by lightning of carbon and nitrogen in possible primitive atmospheres. *Orig. Life*, 11: 291–302, 1981.
- [45] S. Charnoz, A. Morbidelli, L. Dones, and J. Salmon. Did saturn's rings form during the late heavy bombardment? *Icarus*, 199:413–428, 2009.
- [46] C. Chyba and C. Sagan. Endogenous production, exogenous delivery and impact-shock synthesis of organic molecules: an inventory for the origins of life. *Nature*, 355:125–132, 1992.
- [47] C. F. Chyba, C. Sagan, L. Brookshaw, and P. J. Thomas. Impact delivery of prebiotic organics to the early earth. *Orig. Life Evol. Biosph.*, 19:467–468, 1989.
- [48] C. F. Chyba, P. J. Thomas as L. Brookshaw, and C. Sagan. Cometary delivery of organic molecules to the early earth. *Science*, 249:366–373, 1990.
- [49] S. Civis, A. Knizek, O. Ivanek, P. Kubelik, M. Zikalova, L. Kavan, and M. Ferus. The origin of methane and biomolecules from a CO₂ cycle on terrestrial planets. *Nat. Astron.*, 1:721–726, 2017.

- [50] M. W. Claire, J. Sheets, M. Cohen, I. Ribas, V. S. Meadows, and D. C. Catling. The evolution of solar flux from 0.1 nm to 160 μm : quantitative estimates for planetary studies. *Astrophys. J.*, 757(1):95, 2012.
- [51] M. W. Claire, J. F. Kasting, S. D. Domagal-Goldman, E. E. Stüeken, R. Buick, and V. S. Meadows. Modeling the signature of sulfur mass-independent fractionation produced in the Archean atmosphere. *Geochimica Cosmochimica Acta*, 141:365–380, September 2014. doi: 10.1016/j.gca.2014.06.032.
- [52] H. J. Cleaves. *Formose reaction*. Springer, Berlin, Heidelberg, 2011.
- [53] H. J. Cleaves and S. L. Miller. Oceanic protection of prebiotic organic compounds from uv radiation. *Proc. Natl. Acad. Sci. USA*, 95(13): 7260–7263, 1998.
- [54] P. Cloud. Paleocological significance of the banded iron-formation. *Economic Geology*, 68(7):1135–1143, 1973.
- [55] C. Cockell. The ultraviolet history of the terrestrial planets: implications for biological evolution. *Planet. Space Sci.*, 48:203–214, 2000.
- [56] C. S. Cockell. The ultraviolet history of the terrestrial planets - implications for biological evolution. *Planetary and Space Science*, 48: 203–214, February 2000. doi: 10.1016/S0032-0633(99)00087-2.
- [57] C. S. Cockell and J. Knowland. Ultraviolet radiation screening compounds. *Biol. Rev. Camb. Philos. Soc.*, 74(3):311–345, 1999.
- [58] F. Coderre and D. G. Dixon. Modeling the cyanide heap leaching of cupiferous gold ores: Part 1: Introduction and interpretation of laboratory column leaching data. *Hydrometallurgy*, 52(2):151–175, 1999.
- [59] G. D. Cody. Transition metal sulfides and the origin of metabolism. *Annu. Rev. Earth Planet. Sci.*, 32:569–599, 2004.
- [60] N. Cohen and K. R. Westberg. Chemical kinetic data sheets for high-temperature chemical reactions. *Aerospace Corporation Report*, ATR-82(788):3, 1982.
- [61] J. B. Corliss, J. A. Baross, and S. E. Hoffman. A hypothesis concerning the relationships between submarine hot springs and the origin of life on earth. *Oceanologica Acta, Special issue*, 1981.

- [62] C. E. Crespo-Hernández, B. Cohen, P. M. Hare, and B. Kohler. Ultrafast excited-state dynamics in nucleic acids. *Chemical reviews*, 104(4): 1977–2020, 2004.
- [63] J. R. Cronin and C. B. Moore. Amino acid analyses of the murchison, murray, and allende carbonaceous chondrites. *Science*, 172:1327–1329, 1971.
- [64] T. W. Cronin. On the Choice of Average Solar Zenith Angle. *Journal of Atmospheric Sciences*, 71:2994–3003, August 2014.
- [65] B. Damer and D. Deamer. The hot spring hypothesis for an origin of life. *Astrobiology*, 20(3), 2020. URL <http://doi.org/10.1089/ast.2019.2045>.
- [66] M. Daniels, R. V. Meyers, and E. V. Belardo. Photochemistry of the aqueous nitrate system. i. excitation in the 300-m. mu. band. *The Journal of Physical Chemistry*, 72(2):389–399, 1968.
- [67] C. Darwin. *On the origin of species by means of natural selection or preservation of favored races in the struggle for life*. London, 1859.
- [68] N. Dauphas, F. Robert, and B. Marty. The late asteroidal and cometary bombardment of earth as recorded in water deuterium to protium ratio. *Icarus*, 148:508–512, 2000.
- [69] D. F. Davidson, A. Y Chang, and R. K. Hanson. Laser photolysis shock tube for combustion kinetic studies. *Proceedings of the Combustion Institute*, 22:1877–1885, 1988.
- [70] D. F. Davidson, A. J. Dean, M. D. DiRosa, and R. K. Hanson. Shock tube measurements of the reactions of cn with o and o2. *Int. J. Chem. Kinet.*, 23: 1035–1050, 1991.
- [71] B. R. Davies, J. Biggs, P. J. Williams, J. T. Lee, and S. Thompson. A comparison of the catchment sizes of rivers, streams, ponds, ditches and lakes: implications for protecting aquatic biodiversity in an agricultural landscape. *Hydrobiologia*, 597(1):7–17, 2008.
- [72] D. W. Deamer and P. Dworkin, J. *Prebiotic Chemistry*. Springer, 2005.

- [73] J. A. Dean, editor. *Lange's Handbook of Chemistry*, pages 5–16. McGraw-Hill Book Co., New York, NY, 13 edition, 1985.
- [74] G. DeBoer, O. Klinghoffer, and H. E. Johns. Reversal mechanisms for the photohydrates of cytosine and its derivatives. *Biochim. Biophys. Acta*, 213(2):253–268, 1970.
- [75] P. Debye and E. Huckel. On the Theory of Electrolytes. I. Freezing point depression and related phenomena. *Physik Z*, 24:185–206, 1923.
- [76] J. W. Delano. Redox History of the Earth's Interior since ~3900 Ma: Implications for Prebiotic Molecules. *Origins of Life and Evolution of the Biosphere*, 2001.
- [77] A. H. Delsemme. The cometary connection with prebiotic chemistry. *Orig. Life*, 14:51–60, 1984.
- [78] P. Dhakal. *Abiotic nitrate and nitrite reactivity with iron oxide minerals*. PhD thesis, University of Kentucky, 2013.
- [79] G. Dixon-Lewis and D. J. Williams. *Comprehensive Chemical Kinetics*, volume 17, page 1. Elsevier, Amsterdam, 1977.
- [80] R. A. Duce, V. A. Mohnen, P. R. Zimmerman, D. Grosjean, W. Cautreels, R. Chatfield, R. Jaenicke, J. A. Ogren, E. D. Pellizzari, and G. T. Wallace. Organic material in the global troposphere. *Rev. Geophys.*, 21(4):921–952, 1983.
- [81] Anne-Lise Ducluzeau, Robert Van Lis, Simon Duval, Barbara Schoepp-Cothenet, Michael J Russell, and Wolfgang Nitschke. Was nitric oxide the first deep electron sink? *Trends in biochemical sciences*, 34(1):9–15, 2009.
- [82] R. Ducolomb, J. Cadet, C. Taieb, and R. Teoule. Isomerisation and conformation studies of (+)- and (-)-6-hydroxy-5,6-dihydrouridine. *Biochim. Biophys. Acta*, 432(1):18–27, 1976.
- [83] B. Durbeej and L. A. Eriksson. On the formation of cyclobutane pyrimidine dimers in uv-irradiated dna: Why are thymines more reactive? *Photochem. Photobiol.*, 78:159–167, 2003.

- [84] J. H. Dusenbury and R. E. Powell. Reactions of nitrous acid. i. ammonium nitrite decomposition. *J. Am. Chem. Soc.*, 73(7):3266–3268, 1951.
- [85] A. Eschenmoser. Chemistry of potentially prebiological natural products. *Orig. Life Evol. Biosph.*, 24:389–423, 1994.
- [86] A. C. Fahrenbach, C. Giurgiu, C. P. Tam, L. Li, Y. Hongo, M. Aono, and J. W. Szostak. Common and potentially prebiotic origin of precursors of nucleotide synthesis and activation. *J. Am. Chem. Soc.*, 139(26):8780–8783, 2017.
- [87] R. Fani, R. Gallo, and P. Lio. Molecular evolution of nitrogen fixation: the evolutionary history of the *nifD*, *nifK*, *nifE*, and *nifN* genes. *J. Mol. Evol.*, 51(1):1–11, 2000.
- [88] J. C. Fanning. The chemical reduction of nitrate in aqueous solution. *Coordination Chemistry Reviews*, 199(1):159–179, 2000.
- [89] J. Farquhar, H. Bao, and M. Thiemens. Atmospheric Influence of Earth's Earliest Sulfur Cycle. *Science*, 289:756–759, August 2000.
- [90] J. Farquhar, J. Savarino, S. Airieau, and M. H. Thiemens. Observation of wavelength-sensitive mass-independent sulfur isotope effects during formulaSO₂ photolysis: Implications for the early atmosphere. *Journal of Geophysics Research*, 106:32829–32840, December 2001. doi: 10.1029/2000JE001437.
- [91] C. I. Fassett and D. A. Minton. Impact bombardment of the terrestrial planets and the early history of the solar system. *Nat. Geosci.*, 6:520–524, 2013.
- [92] E. C. Fayolle, K. I. Oberg, J. K. Jorgenson, K. Altwegg, H. Calcutt, H. S. P. Muller, M. Rubin, M. H. D. van der Wiel, P. Bjerkeli, T. L. Bourke, A. Coutens, E. F. van Dishoeck, M. N. Drozdovskaya, R. T. Garrod, N. F. W. Ligterink, M. V. Persson, S. F. Wampfler, and the ROSINA team. Protostellar and cometary detections of organohalogens. *Nat. Astron.*, 1:703–708, 2017.
- [93] J. P. Ferris and C. T. Chen. Photosynthesis of organic compounds in the atmosphere of jupiter. *Nature*, 258:587–588, 1975.

- [94] J. P. Ferris, A. R. Hill, R. Liu, and L. E. Orgel. Synthesis of long prebiotic oligomers on mineral surfaces. *Nature*, 1996.
- [95] M. Ferus, D. Nesvorny, J. Sponer, P. Kubelik, R. Michalcikova, V. Shestivska, J. E. Sponer, and S. Civiš. High-energy chemistry of formamide: A unified mechanism of nucleobase formation. *Proc. Natl. Acad. Sci. USA*, 112(3):657–662, 2015.
- [96] M. Ferus, P. Kubelik, A. Knizek, A. Pastorek, J. Sutherland, and S. Civiš. High energy radical chemistry formation of hcn-rich atmospheres on early earth. *Sci. Rep.*, 7(6275), 2017.
- [97] M. Ferus, F. Pietrucci, A. M. Saitta, A. Knizek, P. Kubelik, O. Ivanek, V. Shestivska, and S. Civiš. Formation of nucleobases in a miller-urey reducing atmosphere. *Proc. Natl. Acad. Sci. USA*, 114(17):4306–4311, 2017.
- [98] W. W. Fischer, J. Hemp, and J. S. Valentine. How did life survive earth's great oxygenation? *Current opinion in chemical biology*, 31:166–178, 2016.
- [99] P. M. Fishbane, S. G. Gasiorowicz, and S. T. Thornton. *Physics for Scientists and Engineers*. Prentice-Hall, 3 edition, 2005.
- [100] J. N. Fitzsimmons, E. A. Boyle, and W. J. Jenkins. Distal transport of dissolved hydrothermal iron in the deep South Pacific Ocean. *Proceedings of the National Academy of Science*, 2014.
- [101] G. J. Flynn. The delivery of organic matter from asteroids and comets to the early surface of mars. *Earth, Moon and Planets*, 72:469–474, 1996.
- [102] J. G. Forsythe, S.-S. Yu, I. Mamajanov, M. A. Grover, R. Krishnamurthy, F. M. Fernández, and N. V. Hud. Ester-mediated amide bond formation driven by wet–dry cycles: A possible path to polypeptides on the prebiotic earth. *Angewandte Chemie International Edition*, 54(34):9871–9875, 2015.
- [103] G. Friedrichs, J. T. Herbon, D. F. Davidson, and R. K. Hanson. Quantitative detection of hco behind shock waves: the thermal decomposition of hco. *Phys. Chem. Chem. Phys.*, 4:5778–5788, 2002.
- [104] W. D. Fuller, R. A. Sanchez, and L. E. Orgel. Studies in prebiotic synthesis. vi. synthesis of purine nucleosides. *J. Mol. Biol.*, 67(1):25–33, 1972.

- [105] N. W. Gabel and C. Ponnampereuma. Model for origin of monosaccharides. *Nature*, 216:453–455, 1967.
- [106] L. H. Gevantman. *CRC Handbook of Chemistry and Physics*, chapter Solubility of Selected Gases in Water. CRC Press, Boca Raton, FL, 91 edition, 2010.
- [107] W. Gilbert. The rna world. *Nature*, 319, 1986.
- [108] S. Goldstein and J. Rabani. Mechanism of nitrite formation by nitrate photolysis in aqueous solutions: the role of peroxyxynitrite, nitrogen dioxide, and hydroxyl radical. *J. Am. Chem. Soc.*, 129(34):10597–10601, 2007.
- [109] D. S. Goodsell. The molecular perspective: Ultraviolet light and pyrimidine dimers. *Stem Cells*, 19(4):348–349, 2001.
- [110] K. C. Grabb, C. Buchwald, C. M. Hansel, and S. D. Wankel. A dual nitrite isotopic investigation of chemodenitrification by mineral-associated Fe(II) and its production of nitrous oxide. *Geochimica et Cosmochimica Acta*, 196:388–402, 2017.
- [111] W. D. Grant and B. E. Jones. *Alkaline environments*, volume 1, pages 126–133. Academic Press, London and New York, 2000.
- [112] M. Guekezian, N. Coichev, M. Encarnacion, V. Suarez-Iba, and E. de Almeida Neves. Stability of sulfur(IV) solutions in the presence of amines and the tendency of sulfite ions to disproportionate in stock solutions. *Analytical Letters*, 30(7):1423–1436, 1997.
- [113] A. V. Gurevich, K. P. Zybin, and R. A. Roussel-Dupre. Lightning initiation by simultaneous effect of runaway breakdown and cosmic ray showers. *Physics Letters A*, 1999.
- [114] I. Halevy. Production, preservation, and biological processing of mass-independent sulfur isotope fractionation in the archean surface environment. *Proc. Natl. Acad. Sci. USA*, 110(44):17644–17649, 2013.
- [115] I. Halevy and A. Bachan. The geologic history of seawater pH. *Science*, 355:1069–1071, March 2017. doi: 10.1126/science.aal4151.

- [116] I. Halevy and J. W. Head, III. Episodic warming of early Mars by punctuated volcanism. *Nature Geoscience*, 7:865–868, December 2014. doi: 10.1038/ngeo2293.
- [117] I. Halevy, M. T. Zuber, and D. P. Schrag. A Sulfur Dioxide Climate Feedback on Early Mars. *Science*, 2007.
- [118] J. M. Hall-Spencer, R. Rodolfo-Metalpa, S. Martin, E. Ransome, M. Fine, S. M. Turner, S. J. Rowley, D. Tedesco, and M.-C. Buia. Volcanic carbon dioxide vents show ecosystem effects of ocean acidification. *Nature*, 2008.
- [119] M. M. Halmer, H.-U. Schmincke, and H.-F. Graf. The annual volcanic gas input into the atmosphere, in particular into the stratosphere: a global data set for the past 100 years. *Journal of Volcanology and Geothermal Research*, 2002.
- [120] R. D. Hamilton. Photochemical processes in the inorganic nitrogen cycle of the sea. *Limnology and Oceanography*, 9(1):107–111, 1964.
- [121] H. C. B. Hansen, C. B. Koch, H. Nancke-Krogh, O. K. Borggaard, and J. Sørensen. Abiotic nitrate reduction to ammonium: key role of green rust. *Environmental Science & Technology*, 30(6):2053–2056, 1996.
- [122] R. K. Hanson. Shock-tube study of carbon monoxide dissociation kinetics. *J. Chem. Phys.*, 60:4970–4976, 1974.
- [123] C. E. Harman, J. F. Kasting, and E. T. Wolf. Atmospheric production of glycolaldehyde under hazy prebiotic conditions. *Orig. Life Evol. Biosph.*, 43:77–98, 2013.
- [124] J. A. Hawkes, D. P. Connelly, M. Gledhill, and E. P. Achterberg. The stabilisation and transportation of dissolved iron from high temperature hydrothermal vent systems. *Earth and Planetary Science Letters*, 2013.
- [125] C. He, I. Gállego, B. Laughlin, M. A. Grover, and N. V. Hud. A viscous solvent enables information transfer from gene-length nucleic acids in a model prebiotic replication cycle. *Nat. Chem.*, 9(4):318–324, 2017.
- [126] J. E. Hein, E. Tse, and D. G. Blackmond. A route to enantiopure rna precursors from nearly racemic starting materials. *Nat. Chem.*, 3(9):704–706, 2011.

- [127] W. Heinen and A. M. Lauwers. Organic sulfur compounds resulting from the interaction of iron sulfide, hydrogen sulfide and carbon dioxide in an anaerobic aqueous environment. *Orig. Life Evol. Biosph.*, 26:131–150, 1996.
- [128] C. Helling, R. G. Harrison, F. Honary, D. A. Diver, K. Aplin, I. Dobbs-Dixon, U. Ebert, S.-i. Inutsuka, F. J. Gordillo-Vazquez, and S. Littlefair. Atmospheric Electrification in Dusty, Reactive Gases in the Solar System and Beyond. *Surveys in Geophysics*.
- [129] Paul G Higgs and Niles Lehman. The rna world: molecular cooperation at the origins of life. *Nature Reviews Genetics*, 16(1):7–17, 2015.
- [130] G. Hodosán, C. Helling, R. Asensio-Torres, I. Vorgul, and P. B. Rimmer. Lightning climatology of exoplanets and brown dwarfs guided by Solar system data. *Monthly Notices of the Royal Astronomical Society*.
- [131] H. D. Holland. The Geologic History of Seawater. *Treatise on Geochemistry*, 2003.
- [132] N. G. Holm and J. L. Charlou. Initial indications of abiotic formation of hydrocarbons in the Rainbow ultramafic hydrothermal system, Mid-Atlantic Ridge. *Earth and Planetary Science Letters*, 2001.
- [133] A. Horvath, S. Papp, and Z. Decsy. Formation of aquated electrons and the individual quantum yields for photoactive species in the cu(i)-kcn-h₂o system. *J. Photochem.*, 24(4):331–339, 1984.
- [134] A. Horvath, Z. Zsilak, and S. Papp. Magnetic field effects in photoredox reaction of copper(i) cyanides. *J. Photochem. Photobiol. A Chem.*, 50(1): 129–139, 1989.
- [135] C. R. Hoyle, V. Pinti, A. Welti, B. Zobrist, C. Marcolli, B. Luo, Á. Höskuldsson, H. B. Mattsson, T. Thorsteinsson, G. Larsen, and T. Peter. Ice nucleation properties of volcanic ash from Eyjafjallajökull. *Atmospheric Chemistry & Physics Discussions*, 2011.
- [136] R. Hu, S. Seager, and W. Bains. Photochemistry in Terrestrial Exoplanet Atmospheres. II. H₂S and SO₂ Photochemistry in Anoxic Atmospheres. *Astrophysical Journal*, 2013.

- [137] D. W. Hughes and I. P. Williams. The velocity distribution of periodic comets and stream meteoroids. *Mon. Not. R. Astron. Soc.*, 315:629–634, 2000.
- [138] S. Islam, D.-K. Bucar, and M. W. Powner. Prebiotic selection and assembly of proteinogenic amino acids and natural nucleotides from complex mixtures. *Nat. Chem.*, 9(6):584–589, 2017.
- [139] M. J. Janicki, S. J. Roberts, J. Sponer, M. W. Powner, R. W. Gora, and R. Szabla. Photostability of oxazoline rna-precursors in uv-rich prebiotic environments. *Chem. Commun.*, 54:13407–13410, 2018.
- [140] M. J. Janicki, R. Szabla, J. Sponer, and R. W. Gora. Electron-driven proton transfer enables nonradiative photodeactivation in microhydrated 2-aminoimidazole. *Faraday Discuss.*, 212:345–358, 2018.
- [141] H. E. Johns, J. C. LeBlanc, and K. B. Freeman. Reversal and deamination rates of the main ultraviolet photoproduct of cytidylic acid. *J. Mol. Biol.*, 13(3):849–861, 1965.
- [142] A. P. Johnson, H. J. Cleaves, J. P. Dworkin, D. P. Glavin, A. Lazcano, and J. L. Bada. The miller volcanic spark discharge experiment. *Science*, 322(5900):404, 2008.
- [143] B. W. Johnson and C. Goldblatt. A secular increase in continental crust nitrogen during the Precambrian. *ArXiv e-prints*, 2017.
- [144] Ben Johnson and Colin Goldblatt. The nitrogen budget of earth. *Earth-Science Reviews*, 148:150–173, 2015.
- [145] J. A. Johnson et al. Photochemistry of nitrous acid and nitrite ion. Master's thesis, Illinois Wesleyan University, 1992.
- [146] L. C. Jones, B. Peters, J. S. Lezama Pacheco, K. L. Casciotti, and S. Fendorf. Stable isotopes and iron oxide mineral products as markers of chemodenitrification. *Environmental science & technology*, 49(6):3444–3452, 2015.
- [147] H. Kaasalainen and A. Stefánsson. Sulfur speciation in natural hydrothermal waters, Iceland. *Geochimica Cosmochimica Acta*, 2011.

- [148] Alexey Kamyshny, Gregory Druschel, Zahra F. Mansaray, and James Farquhar. Multiple sulfur isotopes fractionations associated with abiotic sulfur transformations in yellowstone national park geothermal springs. *Geochemical Transactions*, 2014.
- [149] J. F. Kasting. Stability of ammonia in the primitive terrestrial atmosphere. *Journal of Geophysical Research*, 1982.
- [150] J. F. Kasting. Earth's early atmosphere. *Science*, 1993.
- [151] J. F. Kasting and J. C. G. Walker. Limits on oxygen concentration in the prebiological atmosphere and the rate of abiotic fixation of nitrogen. *Journal of Geophysical Research*, 1981.
- [152] J. F. Kasting, K. J. Zahnle, and J. C. G. Walker. Photochemistry of methane in the earth's early atmosphere. *Precambrian Research*, 20:121–148, 1983.
- [153] J. F. Kasting, K. J. Zahnle, J. P. Pinto, and A. T. Young. Sulfur, ultraviolet radiation, and the early evolution of life. *Origins of Life and Evolution of the Biosphere*, 1989.
- [154] James F Kasting. Theoretical constraints on oxygen and carbon dioxide concentrations in the precambrian atmosphere. *Precambrian research*, 34(3):205–229, 1987.
- [155] James F Kasting. Atmospheric composition of hadean–early archean earth: The importance of co. *Geological Society of America Special Papers*, 504:19–28, 2014.
- [156] S. Kaur and P. Sharma. Radical pathways for the formation of non-canonical nucleobases in prebiotic environments. *RSC Adv*, 9: 36530–36538, 2019.
- [157] M. C. Kavanaugh and R. R. Trussell. Design of aeration towers to strip volatile contaminants from drinking water. *Journal-American Water Works Association*, 72(12):684–692, 1980.
- [158] H.-J. Kim and S. Benner. Prebiotic stereoselective synthesis of purine and non canonical pyrimidine nucleotide from nucleobases and phosphorylated carbohydrates. *Proc. Natl. Acad. Sci. USA*, 114(43): 11315–11320, 2017.

- [159] C. Klein. Some precambrian banded iron-formations (bifs) from around the world: Their age, geologic setting, mineralogy, metamorphism, geochemistry, and origins. *American Mineralogist*, 90(10):1473–1499, 2005.
- [160] K. O. Konhauser, N. J. Planavsky, D. S. Hardisty, L. J. Robbins, T. J. Warchola, R. Haugaard, S. V. Lalonde, C. A. Partin, P. B. H. Oonk, H. Tsikos, et al. Iron formations: A global record of neoarchaeon to palaeoproterozoic environmental history. *Earth-Science Reviews*, 172: 140–177, 2017.
- [161] J. Krissansen-Totton, D. S. Bergsman, and D. C. Catling. On Detecting Biospheres from Chemical Thermodynamic Disequilibrium in Planetary Atmospheres. *Astrobiology*, 2016.
- [162] J. Krissansen-Totton, G. N. Arney, and D. C. Catling. Constraining the climate and ocean pH of the early earth with a geological carbon cycle model. *Proc. Nat. Acad. Sci.*, page 201721296, 2018.
- [163] J. Krissansen-Totton, S. Olson, and D. C. Catling. Disequilibrium biosignatures over Earth history and implications for detecting exoplanet life. *Science Advances*, 2018.
- [164] J. Kua and J. L. Bada. Primordial Ocean Chemistry and its Compatibility with the RNA World. *Origins of Life and Evolution of the Biosphere*, 2011.
- [165] K. Kvenvolden, J. Lawless, K. Pering, E. Peterson, J. Flores, C. Ponnampuruma, I. R. Kaplan, and C. Moore. Evidence for extraterrestrial amino acids and hydrocarbons in the murchison meteorite. *Nature*, 228:923–926, 1970.
- [166] M. Laneuville, M. Kameya, and H. J. Cleaves. Earth without life: A systems model of a global abiotic nitrogen cycle. *Astrobiology*, 2018.
- [167] D. E. Larowe and P. Regnier. Thermodynamic Potential for the Abiotic Synthesis of Adenine, Cytosine, Guanine, Thymine, Uracil, Ribose, and Deoxyribose in Hydrothermal Systems. *Origins of Life and Evolution of the Biosphere*, 2008.
- [168] R. Lathe. Early tides: Response to varga et al. *Icarus*, 180(1):277–280, 2006.

- [169] A. Lazcano and S. L. Miller. The origin and early evolution of life: prebiotic chemistry, the pre-rna world, and time. *Cell*, 85(6):793–798, 1996.
- [170] A. Lazcano, R. Guerrero, L. Margulis, and J. Oro. The evolutionary transition from rna to dna in early cells. *J. Mol. Evol.*, 17:283–290, 1988.
- [171] H. F. Levison, L. Dones, C. R. Chapman, S. A. Stern, M. J. Duncan, and K. Zahnle. Could the lunar "late heavy bombardment" have been triggered by the formation of uranus and neptune? *Icarus*, 151:286–306, 2001.
- [172] M. Levy and S. L. Miller. The Stability of the RNA Bases: Implications for the Origin of Life. *Proceedings of the National Academy of Science*, 1998.
- [173] L. Li, N. Prywes, C. P. Tam, D. K. O-Flaherty, V. S. Lelyveld, E. C. Izgu, A. Pal, and J. W. Szostak. Enhanced nonenzymatic rna copying with 2-aminoimidazole activated nucleotides. *J. Am. Chem. Soc.*, 139(5): 1810–1813, 2017.
- [174] W. Li, A. D. Czaja, M. J. Van Kranendonk, B. L. Beard, E. E. Roden, and C. M. Johnson. An anoxic, Fe(II)-rich, U-poor ocean 3.46 billion years ago. *Geochimica Cosmochimica Acta*, 2013.
- [175] X.-Y. Li, S. Contreras, A. Solé-Benet, Y. Cantón, F. Domingo, R. Lázaro, H. Lin, B. Van Wesemael, and J. Puigdefábregas. Controls of infiltration–runoff processes in mediterranean karst rangelands in se spain. *Catena*, 86(2):98–109, 2011.
- [176] F. T. Liu and N. C. Yang. Photochemistry of cytosine derivatives 2. photohydration of cytosine derivatives. proton magnetic resonance study on the chemical structure and property of photohydrates. *Biochemistry*, 17(23):4877–4885, 1978.
- [177] A. Löhr, T. Bogaard, A. Heikens, M. Hendriks, S. Sumarti, M. van Bergen, K. C. van Gestel, N. van Straalen, P. Vroon, and B. Widianarko. Natural pollution caused by the extremely acid crater lake kawah ijen, east java, indonesia (7 pp). *Environmental Science and Pollution Research*, 12(2): 89–95, 2005.

- [178] Michael W Lomas and Fredric Lipschultz. Forming the primary nitrite maximum: Nitrifiers or phytoplankton? *Limnology and Oceanography*, 51 (5):2453–2467, 2006.
- [179] H. S. Loring and J. M. Ploeser. The deamination of cytidine in acid solution and the preparation of uridine and cytidine by acid hydrolysis of yeast nucleic acid. *J. Biol. Chem.*, 178(1):439–449, 1948.
- [180] M. Y. Louge and R. K. Hanson. Shock tube study of cyanogen oxidation kinetics. *Int. J. Chem. Kinet.*, 16:231, 1984.
- [181] M. Y. Louge and R. K. Hanson. Shock tube study of nco kinetics. *Proceedings of the Combustion Institute*, 20:665–672, 1984.
- [182] J. Mack and J. R. Bolton. Photochemistry of nitrite and nitrate in aqueous solution: a review. *Journal of Photochemistry and Photobiology A: Chemistry*, 128(1-3):1–13, 1999.
- [183] R. L. Mancinelli and C. P. McKay. The evolution of nitrogen cycling. *Origins of Life*, 1988.
- [184] A. Mariani, D. A. Russell, T. Javelle, and J. D. Sutherland. A light-releasable potentially prebiotic nucleotide activating agent. *J. Am. Chem. Soc.*, 140(28):8657–8661, 2018.
- [185] G. M. Marion. A theoretical evaluation of mineral stability in don juan pond, wright valley, victoria land. *Antarctic Science*, 9(1):92–99, 1997.
- [186] W. Martin and M. J. Russell. On the origins of cells: a hypothesis for the evolutionary transitions from abiotic geochemistry to chemoautotrophic prokaryotes, and from prokaryotes to nucleated cells. *Phil. Trans. R. Soc. Lond. B*, 358:59–85, 2003.
- [187] W. Martin and M. J. Russell. On the origin of biochemistry at an alkaline hydrothermal vent. *Phil. Trans. R. Soc. Lond. B*, 367:1887–1925, 2007.
- [188] W. Martin, J. Baross, D. Kelley, and M. J. Russell. Hydrothermal vents and the origin of life. *Nature Reviews Microbiology*, 6(11):805–814, 2008.
- [189] B. Marty, L. Zimmermann, M. Pujol, R. Burgess, and P. Philippot. Nitrogen Isotopic Composition and Density of the Archean Atmosphere. *Science*, 2013.

- [190] B. Marty, G. Avice, Y. Sano, K. Altwegg, H. Balsiger, M. Hassig, A. Morbidelli, O. Mousis, and M. Rubin. Origins of volatile elements (h, c, n, noble gases) on earth and mars in light of recent results from the rosetta cometary mission. *Earth Planet. Sc. Lett.*, 441:91–102, 2016.
- [191] B. Marty, G. Avice, D. V. Bekaert, and M. W. Broadley. Salinity of the archaean oceans from analysis of fluid inclusions in quartz. *Comptes Rendus Geoscience*, 350(4):154–163, 2018.
- [192] T. Matsunga, K. Hieda, and O. Nikaido. Wavelength dependent formation of thymine dimers and (6-4) photoproducts in dna by monochromatic ultraviolet light ranging from 150 to 365 nm. *Photochem. Photobiol.*, 54(3):403–410, 1991.
- [193] S. E. Maurer and G. Nguyen. Prebiotic vesicle formation and the necessity of salts. *Orig. Life Evol. Biosph.*, 46(2-3):215–222, 2016.
- [194] M. Maurette, J. Duprat, C. Engrand, G. Kurat, M. Gounelle, G. Matrajt, and A. Toppani. Accretion of neon, organics, co₂, nitrogen and water from large interplanetary dust particles on the early earth. *Planet. Space Sci.*, 48:1117–1137, 2000.
- [195] T. M. McCollom. Miller-Urey and Beyond: What Have We Learned About Prebiotic Organic Synthesis Reactions in the Past 60 Years? *Annual Review of Earth and Planetary Sciences*, 2013.
- [196] T. M. McCollom and J. S. Seewald. Abiotic synthesis of organic compounds in deep-sea hydrothermal environments. *Chemical Reviews*, 107(2):382–401, 2007.
- [197] Kevin J McGuire and Jeffrey J McDonnell. A review and evaluation of catchment transit time modeling. *Journal of Hydrology*, 330(3-4): 543–563, 2006.
- [198] J. D. Mertens, A. Y. Chang, R. K. Hanson, and C. T. Bowman. Reaction kinetics of nh in the shock tube pyrolysis of hnco. *Int. J. Chem. Kinet.*, 21: 1049–1067, 1989.
- [199] J. D. Mertens, K. Kohse-Hoeinghaus, R. K. Hanson, and C. T. Bowman. A shock tube study of h+hnco=nh₂+co. *Int. J. Chem. Kinet.*, 23:655–668, 1991.

- [200] J. D. Mertens, A. Y. Chang, R. K. Hanson, and C. T. Bowman. A shock tube study of reaction of atomic oxygen with isocyanic acid. *Int. J. Chem. Kinet.*, 24:279–295, 1992.
- [201] B. Meyer, M. Rigdon, T. Burner, M. Ospina, K. Ward, and K. Koshlap. *Thermal Decomposition of Sulfite, Bisulfite, and Disulfite Solutions*, chapter 6, pages 113–125.
- [202] J. A. Miller and C. T. Bowman. Mechanism and modeling of nitrogen chemistry in combustion. *Prog. Energ. Combust.*, 15:287–338, 1989.
- [203] J. A. Miller and C. F. Melius. A theoretical analysis of the reaction between hydroxyl and hydrogen cyanide at high temperature. In *Twenty-first symposium (international) on combustion*, Twenty-first symposium (international) on combustion, pages 919–927, Pittsburgh, Pennsylvania, 1988.
- [204] N. Miller and P. Cerutti. Structure of the photohydration products of cytidine and uridine. *Proc. Natl. Acad. Sci USA*, 59(1):34–38, 1968.
- [205] S. L. Miller. A production of amino acids under possible primitive earth conditions. *Science*, 117:528–529, 1953.
- [206] C. Minero, S. Chiron, G. Falletti, V. Maurino, E. Pelizzetti, R. Ajassa, M. E. Carlotti, and D. Vione. Photochemical processes involving nitrite in surface water samples. *Aquatic Sciences*, 69(1):71–85, 2007.
- [207] N. Mirzoyan and I. Halevy. Kinetics of sulfite disproportionation and thiosulfate acid dissociation. In *Goldschmidt Conference Abstracts*, 2014.
- [208] K. C. Misra. *Introduction to Geochemistry*. Wiley-Blackwell, 2012.
- [209] S. Miyakawa, H. J. Cleaves, and S. L. Miller. The cold origins of life: A. implications based on the hydrolytic stabilities of hydrogen cyanide and formamide. *Orig. Life Evol. Biosph.*, 32:195–208, 2002.
- [210] J. Miyazaki, H. Takiyama, and M. Nakata. Isocyano compounds newly recognized in photochemical reaction of thiazole: matrix-isolation ft-ir and theoretical studies. *RSC Adv.*, 7:4960–4974, 2017.
- [211] S. J. Mojzsis, T. M. Harrison, and R. T. Pidgeon. Oxygen-isotope evidence from ancient zircons for liquid water at the Earth's surface 4,300Myr ago. *Nature*, 2001.

- [212] J. T. Moraghan and R. J. Buresh. Chemical reduction of nitrite and nitrous oxide by ferrous iron 1. *Soil Science Society of America Journal*, 41(1): 47–50, 1977.
- [213] A. Morbidelli, J. Chambers, J. I. Lunine, J. M. Petit, F. Robert, G. B. Valsecchi, and K. E. Cyr. Source regions and time scales for the delivery of water to earth. *Meteorit. Planet. Sci.*, 35:1309–1320, 2000.
- [214] A. Morbidelli, J.-M. Petit, B. Gladman, and J. Chambers. A plausible cause of the late heavy bombardment. *Meteorit. Planet. Sci.*, 36:371–380, 2010.
- [215] J. W. Morse and F. T. Mackenzie. Hadean ocean carbonate geochemistry. *Aquatic Geochemistry*, 4:301–319, 1998.
- [216] A. Y. Mulkidjanian, D. A. Cherepanov, and M. Y. Galperin. Survival of the fittest before the beginning of life: selection of the first oligonucleotide-like polymers by uv light. *BMC evolutionary biology*, 3:12, 2003.
- [217] A. Y. Mulkidjanian, A. Y. Bychkov, D. V. Dibrova, M. Y. Galperin, and E. V. Koonin. PNAS Plus: Origin of first cells at terrestrial, anoxic geothermal fields. *Proceedings of the National Academy of Science*, 2012.
- [218] M. J. Mumma and S. B. Charnley. The chemical composition of comets - emerging taxonomies and natal heritage. *Annu. Rev. Astron. Astr.*, 49: 471–524, 2011.
- [219] H. Mutschler, A. Wochner, and P. Holliger. Freeze–thaw cycles as drivers of complex ribozyme assembly. *Nat. Chem.*, 7(6):502–508, 2015.
- [220] D. N. Mvondo, R. Navarro-González, C. P. McKay, P. Coll, and F. Raulin. Production of nitrogen oxides by lightning and coroneae discharges in simulated early earth, venus and mars environments. *Advances in Space Research*, 27(2):217–223, 2001.
- [221] H. Naraoka, A. Shimoyama, and K. Harada. Molecular distribution of monocarboxylic acids in asuka carbonaceous chondrites from antarctica. *Orig. Life Evol. Biosph.*, 29:187–201, 1999.
- [222] R. Navarro-González, M. J. Molina, and L. T. Molina. Nitrogen fixation by volcanic lightning in the early earth. *Geophysical Research Letters*, 25(16): 3123–3126, 1998.

- [223] K. E. Nelson, M. Levy, and S. L. Miller. Peptide nucleic acids rather than rna may have been the first genetic molecule. *Proc. Natl. Acad. Sci. USA*, 97(8):3868–3871, 2000.
- [224] P. Neta and R. E. Huie. Free-radical chemistry of sulfite. *Environmental health perspectives*, 64:209, 1985.
- [225] M. T. Neves-Petersen, G. P. Gajula, and S. B. Petersen. *Molecular Photochemistry: Various Aspects*, chapter UV Light Effects on Proteins: From Photochemistry to Nanomedicine. 2012.
- [226] D. A. Nguyen, M. A. Iwaniw, and H. S. Fogler. Kinetics and mechanism of the reaction between ammonium and nitrite ions: experimental and theoretical studies. *Chemical engineering science*, 58(19):4351–4362, 2003.
- [227] W. Nitschke and M. J. Russell. Beating the acetyl coenzyme a-pathway to the origin of life. *Phil. Trans. R. Soc. B*, 368(1622):20120258, 2013.
- [228] A. A. Novoselov, D. Silva, J. Schneider, X. C. Abrevaya, M. S. Chaffin, P. Serrano, M. S. Navarro, M. J. Conti, and C. R. d. Souza Filho. Geochemical constraints on the Hadean environment from mineral fingerprints of prokaryotes. *Scientific Reports*, 2017.
- [229] M. A. Oehlschlaeger, D. F. Davidson, J. B. Jeffries, and R. K. Hanson. Carbon dioxide thermal decomposition: Observation of incubation. *Z. Phys. Chem.*, 219:555–567, 2005.
- [230] A. Olsen, R. M. Key, S. van Heuven, S. K. Lauvset, A. Velo, X. Lin, C. Schirnack, A. Kozyr, T. Tanhua, M. Hoppema, et al. The global ocean data analysis project version 2 (glodapv2)—an internally consistent data product for the world ocean. *Earth System Science Data (Online)*, 8(2), 2016.
- [231] L. Orgel. A simpler nucleic acid. *Science*, 290(5495):1306–1307, 2000.
- [232] L. E. Orgel. Prebiotic chemistry and the origin of the rna world. *Crit. Rev. Biochem. Mol. Biol.*, 39(2):99–123, 2004.
- [233] J. Oro. Synthesis of adenine from ammonium cyanide. *Biochem. Biophys. Res. Comm.*, 2(6):407–412, 1960.

- [234] J. Oro and A. P. Kimball. Synthesis of purines under possible primitive earth conditions. i. adenine from hydrogen cyanide. *Arch. Biochem. Biophys.*, 94(2):217–227, 1961.
- [235] C. J. Ottley, W. Davison, and W. M. Edmunds. Chemical catalysis of nitrate reduction by iron (ii). *Geochimica et Cosmochimica acta*, 61(9): 1819–1828, 1997.
- [236] J. Y. Park and Y. N. Lee. Solubility and decomposition kinetics of nitrous acid in aqueous solution. *The Journal of Physical Chemistry*, 92(22): 6294–6302, 1988.
- [237] D. L. Parkhurst and C. A. J. Appelo. Description of input and examples for phreeqc version 3: A computer program for speciation, batch-reaction, one-dimensional transport, and inverse geochemical calculations. Technical report, U. S. Geological Survey.
- [238] D. Parkos, A. Pikus, A. Alexeenko, and H. J. Melosh. Hcn production from impact ejecta on the early earth. In *AIP Conference Proceedings*, 2016.
- [239] Robert Pascal. Suitable energetic conditions for dynamic chemical complexity and the living state. *Journal of Systems Chemistry*, 3(1):1, 2012.
- [240] B. H. Patel, C. Percivalle, D. J. Ritson, C. D. Duffy, and J. D. Sutherland. Common origins of rna, protein and lipid precursors in a cyanosulfidic protometabolism. *Nat. Chem.*, 7(4):301–307, 2015.
- [241] A. A. Pavlov and J. F. Kasting. Mass-independent fractionation of sulfur isotopes in archean sediments: strong evidence for an anoxic archean atmosphere. *Astrobiology*, 2(1):27–41, 2002.
- [242] B. K. D. Pearce, R. E. Pudritz, D. A. Semenov, and T. K. Henning. Origin of the rna world: The fate of nucleobases in warm little ponds. *Proc. Natl. Acad. Sci USA*, 114(43):11327–11332, 2017.
- [243] O. Pestunova, A. Siminov, V. Snytnikov, V. Stoyanovsky, and V. Parmon. Putative mechanism of the sugar formation on prebiotic earth initiated by uv-radiation. *Adv. Space Res.*, 36(2):214–219, 2005.
- [244] H. J. S. Petersen. Reduction of nitrate by iron (ii). *Acta chemica Scandinavica. Series A: Physical and inorganic chemistry*, 1979.

- [245] P. Philippot, M. Van Zuilen, and C. Rollion-Bard. Variations in atmospheric sulphur chemistry on early earth linked to volcanic activity. *Nature Geoscience*, 5(9):668–674, 2012.
- [246] L. F. Phillips. Rate of reaction of oh radicals with cyanogen. *Combust. Flame*, 35:233–236, 1979.
- [247] F. Picardal. Abiotic and microbial interactions during anaerobic transformations of fe (ii) and nox. *Frontiers in microbiology*, 3:112, 2012.
- [248] E. Pierazzo and C. F. Chyba. Amino acid survival in large cometary impacts. *Meteorit. Planet. Sci.*, 34:909–918, 1999.
- [249] E. Pierazzo and C. F. Chyba. *Impact delivery of prebiotic organic matter to planetary surfaces.*, page 137. Springer, 2006.
- [250] E. Pierazzo and H. J. Melosh. Hydrocode modeling of oblique impacts: The fate of the projectile. *Meteorit. Planet. Sci.*, 35:117–130, 2000.
- [251] E. Pierazzo and H. J. Melosh. Understanding oblique impacts from experiments, observations, and modeling. *Annu. Rev. Earth Pl. Sc.*, 28: 141–167, 2000.
- [252] S. Pizzarello and A. L. Weber. Prebiotic amino acids as asymmetric catalysts. *Science*, 303:1151, 2004.
- [253] S. Pizzarello and A. L. Weber. Stereoselective syntheses of pentose sugars under realistic prebiotic conditions. *Orig. Life Evol. Biosph.*, 40:3–10, 2010.
- [254] Marvin Pollum, Brennan Ashwood, Steffen Jockusch, Minh Lam, and Carlos E Crespo-Hernández. Unintended consequences of expanding the genetic alphabet. *Journal of the American Chemical Society*, 138(36): 11457–11460, 2016.
- [255] Dieke Postma. Kinetics of nitrate reduction by detrital fe (ii)-silicates. *Geochimica et Cosmochimica Acta*, 54(3):903–908, 1990.
- [256] M. W. Powner, B. Gerland, and J. D. Sutherland. Synthesis of activated pyrimidine ribonucleotides in prebiotically plausible conditions. *Nature*, 459(7244):239–242, 2009.

- [257] S. Rajamani, A. Vlassov, S. Benner, A. Coombs, F. Olasagasti, and D. Deamer. Lipid-assisted synthesis of rna-like polymers from mononucleotides. *Orig. Life Evol. Biosph.*, 38(1):57–74, 2008.
- [258] Sudipta Rakshit, Christopher J Matocha, and Mark S Coyne. Nitrite reduction by siderite. *Soil Science Society of America Journal*, 72(4): 1070–1077, 2008.
- [259] S. Ranjan and D. D. Sasselov. Influence of the uv environment on the synthesis of prebiotic molecules. *Astrobiology*, 16(1):68–88, 2016.
- [260] S. Ranjan and D. D. Sasselov. Constraints on the early terrestrial surface uv environment relevant to prebiotic chemistry. *Astrobiology*, 17(3): 169–204, 2017.
- [261] S. Ranjan, R. Wordsworth, and D. D. Sasselov. Atmospheric Constraints on the Surface UV Environment of Mars at 3.9 Ga Relevant to Prebiotic Chemistry. *Astrobiology*, 2017.
- [262] S. Ranjan, R. Wordsworth, and D. D. Sasselov. The Surface UV Environment on Planets Orbiting M Dwarfs: Implications for Prebiotic Chemistry and the Need for Experimental Follow-up. *The Astrophysical Journal*, 2017.
- [263] S. Ranjan, Z. R. Todd, J. D. Sutherland, and D. D. Sasselov. Sulfidic Anion Concentrations on Early Earth for Surficial Origins-of-Life Chemistry. *Astrobiology*, 2018.
- [264] S. Ranjan, Z. R. Todd, P. B. Rimmer, D. Sasselov, and A. R. Babbín. Nitrogen oxide concentrations in natural waters on early earth. *Geochem. Geophys. Geosy.*, 20(4):2021–2039, 2019.
- [265] R. J. Rapf and V. Vaida. Sunlight as an energetic driver in the synthesis of molecules necessary for life. *Phys. Chem. Chem. Phys.*, 18:20067–20084, 2016.
- [266] P. C. Rây, M. L. Dey, and J. C. Ghosh. Xxxvi. velocity of decomposition and the dissociation constant of nitrous acid. *Journal of the Chemical Society, Transactions*, 111:413–417, 1917.
- [267] C. Reid and L. Orgel. Synthesis of sugars in potentially prebiotic conditions. *Nature*, 216:455, 1967.

- [268] S. Reiter, D. Keefer, and R. de Vivie-Riedle. Rna environment is responsible for decreased photostability of uracil. *J. Am. Chem. Soc.*, 140(28):8714–8720, 2018.
- [269] N. P. Revsbech, L. H. Larsen, J. Gundersen, T. Dalsgaard, O. Ulloa, and B. Thamdrup. Determination of ultra-low oxygen concentrations in oxygen minimum zones by the stox sensor. *Limnology and Oceanography: Methods*, 7(5):371–381, 2009.
- [270] I. Ribas, G. F. Porto de Mello, L. D. Ferriera, E. Hebrard, F. Selsis, S. Catalan, A. Garces, J. D. do Nascimento Jr., and J. R. de Medeiros. Evolution of the solar activity over time and effects on planetary atmospheres. ii. k ceti, an analog of the sun when life arose on earth. *Astrophys. J.*, 714(1):384–395, 2010.
- [271] F. M. Richter. Models for the Archean thermal regime. *Earth and Planetary Science Letters*, 1985.
- [272] P. B. Rimmer and C. Helling. A Chemical Kinetics Network for Lightning and Life in Planetary Atmospheres. *Astrophysical Journals*, 2016.
- [273] P. B. Rimmer and S. Rugheimer. Hydrogen cyanide in nitrogen-rich atmospheres of rocky exoplanets. *Icarus*, 329:124–131, 2019.
- [274] P. B. Rimmer, J. Xu, S. J. Thompson, E. Gillen, J. D. Sutherland, and D. Queloz. The origin of rna precursors on exoplanets. *Sci. Adv.*, 4(8):3302, 2018.
- [275] A. C. Rios and Y. Tor. On the origin of the canonical nucleobases: an assessment of selection pressures across chemical and early biological evolution. *Isr. J. Chem.*, 53:469–483, 2013.
- [276] D. Ritson and J. D. Sutherland. Prebiotic synthesis of simple sugars by photoredox systems chemistry. *Nat. Chem.*, 4(11):895–899, 2012.
- [277] D. Ritson and J. D. Sutherland. Synthesis of aldehydic ribonucleotide and amino acid precursors by photoredox chemistry. *Angew. Chem. Int. Ed.*, 52:5845–5847, 2013.
- [278] D. Ritson, C. Battilocchio, S. V. Ley, and J. D. Sutherland. Mimicking the surface and prebiotic chemistry of early earth using flow chemistry. *Nat. Comm.*, 9:1821, 2018.

- [279] G. M. Roberts, C. A. Williams, M. J. Paterson, S. Ullrich, and V. G. Stavros. Comparing the ultraviolet photostability of azole chromophores. *Chem. Sci.*, 3:1192–1199, 2012.
- [280] S. J. Roberts, R. Szabla, Z. R. Todd, S. Stairs, D.-K. Bucar, J. Sponer, D. D. Sasselov, and M. W. Powner. Selective prebiotic conversion of pyrimidine and purine anhydronucleosides into watson-crick base-pairing arabino-furanosyl nucleosides in water. *Nat. Commun.*, 9:4073, 2018.
- [281] A. Robock. Volcanic eruptions and climate. *Reviews of Geophysics*, 2000.
- [282] Allan Rodhe, Lars Nyberg, and Kevin Bishop. Transit times for water in a small till catchment from a step shift in the oxygen 18 content of the water input. *Water Resources Research*, 32(12):3497–3511, 1996.
- [283] D. M. Romsps, J. T. Seeley, D. Vollaro, and J. Molinari. Projected increase in lightning strikes in the United States due to global warming. *Science*, 2014.
- [284] L. Le Roy, K. Altwegg, H. Balsiger, J.-J. Berthelier, A. Bieler, C. Briois, U. Calmonte, M. R. Combi, J. De Keyser, F. Dhooghe, B. Fiethe, S. A. Fuselier, S. Gasc, T. I. Bombosi, M. Hassig, A. Jackel, M. Rubin, and C.-Y. Tzou. Inventory of the volatiles on comet 67p/churyumov-gerasimenko from rosetta/rosina. *Astron. Astrophys.*, 583:A1, 2015.
- [285] S. Rugheimer, A. Segura, L. Kaltenegger, and D. Sasselov. Uv surface environment of earth-like planets orbiting fgkm stars through geological evolution. *Astrophys. J.*, 806(1):137, 2015.
- [286] K. Ruiz-Mirazo, C. Briones, and journal=Chem. Rev volume=114 number=1 pages=285–366 year=2014 publisher=ACS Publications de la Escosura, A. Prebiotic systems chemistry: new perspectives for the origins of life.
- [287] John R. Rumble, editor. *CRC Handbook of Chemistry and Physics*. CRC Press, Boca Raton, FL, 98 edition, 2017.
- [288] M. J. Russell and A. J. Hall. The emergence of life from iron monosulfide bubbles at a submarine hydrothermal redox and ph front. *J. Geol. Soc. London*, 154(3):377–402, 1997.
- [289] G. Ryder. Lunar samples, lunar accretion and the early bombardment of the moon. *Eos*, 71:313–323, 1990.

- [290] C. Sagan. Ultraviolet selection pressure on the earliest organisms. *J. Theor. Biol.*, 39(1):195–200, 1973.
- [291] C. Sagan and B. N. Khare. Long-wavelength ultraviolet photoproduction of amino acids on the primitive earth. *Science*, 173(3995):417–420, 1971.
- [292] C. Sagan and G. Mullen. Earth and Mars: Evolution of Atmospheres and Surface Temperatures. *Science*, 1972.
- [293] R. Saladino, E. Carota, G. Botta, M. Kapralov, G. N. Timoshenko, A. Y. Rozanov, E. Krasavin, and E. Di Mauro. Meteorite-catalyzed syntheses of the nucleosides and of other prebiotic compounds from formamide under proton irradiation. *Proc. Natl. Acad. Sci. USA*, 112:E2746–55, 2015.
- [294] R. Saladino, E. Carota, G. Botta, M. Kapralov, G. N. Timoshenko, A. Rozanov, E. Krasavin, and E. Di Mauro. First evidence on the role of heavy ion irradiation of meteorites and formamide in the origin of biomolecules. *Orig. Life Evol. Biosph.*, 46:515–521, 2016.
- [295] V. A. Samarkin, M. T. Madigan, M. W. Bowles, K. L. Casciotti, J. C. Priscu, C. P. McKay, and S. B. Joye. Abiotic nitrous oxide emission from the hypersaline Don Juan Pond in Antarctica. *Nature Geoscience*, 2010.
- [296] R. Sander. Compilation of Henry’s law constants (version 4.0) for water as solvent. *Atmospheric Chemistry & Physics*, 2015.
- [297] S. G. Sander and A. Koschinsky. Metal flux from hydrothermal vents increased by organic complexation. *Nature Geoscience*, 2011.
- [298] S. P. Sander, R. R. Friedl, J. R. Barker, D. M. Golden, M. J. Kurylo, P. H. Wine, J. P. D. Abbatt, J. B. Burkholder, C. E. Kolb, G. K. Moortgat, R. E. Huie, and V. L. Orkin. Chemical Kinetics and Photochemical Data for Use in Atmospheric Studies Evaluation Number 17. Technical Report 17, NASA JPL, 2011. URL <http://jpldataeval.jpl.nasa.gov/>.
- [299] A. E. Santoro, C. M. Sakamoto, J. M. Smith, J. N. Plant, A. L. Gehman, A. Z. Worden, K. S. Johnson, C. A. Francis, and K. L. Casciotti. Measurements of nitrite production in and around the primary nitrite maximum in the central california current. *Biogeosciences*, 10(11):7395–7410, 2013.

- [300] P. K. Sarker, J.-I. Takahashi, Y. Obayashi, T. Kaneko, and K. Kobayashi. Photo-alteration of hydantoins against uv light and its relevance to prebiotic chemistry. *Advances in Space Research*, 51:2235–2240, 2013.
- [301] L. T. Schulz, E. J. Elder, K. J. Jones, A. Vijayan, B. D. Johnson, J. E. Medow, and L. Vermeulen. Stability of sodium nitroprusside and sodium thiosulfate 1: 10 intravenous admixture. *Hospital pharmacy*, 45(10): 779–784, 2010.
- [302] H. Schuster. Photochemie von ribonucleinsäuren. *Z. Naturf.*, 19(9):815, 1964.
- [303] A. W. Schwartz and R. M. De Graaf. The prebiotic synthesis of carbohydrates: A reassessment. *J. Mol. Evol.*, 36:101–106, 1993.
- [304] S. E. Schwartz and W. H. White. Solubility equilibria of the nitrogen oxides and oxyacids in dilute aqueous solution. In *Advances in environmental science and engineering*. Vol. 4. 1981.
- [305] A. Segura, K. Krelow, J. F. Kasting, D. Sommerlatt, V. Meadows, D. Crisp, M. Cohen, and E. Mlawer. Ozone Concentrations and Ultraviolet Fluxes on Earth-Like Planets Around Other Stars. *Astrobiology*, 2003.
- [306] S. Self, M. Widdowson, T. Thordarson, and A. E. Jay. Volatile fluxes during flood basalt eruptions and potential effects on the global environment: A Deccan perspective. *Earth and Planetary Science Letters*, 2006.
- [307] Luis Serrano-Andres and Manuela Merchan. Are the five natural dna/rna base monomers a good choice from natural selection?: A photochemical perspective. *Journal of Photochemistry and Photobiology C: Photochemistry Reviews*, 10(1):21–32, 2009.
- [308] R. Shapiro and S. H. Pohl. The reaction of ribonucleotides with nitrous acid. side products and kinetics. *Biochemistry*, 7(1):448–455, 1968.
- [309] C. M. Sharpless and K. G. Linden. Uv photolysis of nitrate: effects of natural organic matter and dissolved inorganic carbon and implications for uv water disinfection. *Environmental science & technology*, 35(14): 2949–2955, 2001.
- [310] Y. Shibaike, T. Sasaki, and S. Ida. Excavation and melting of the hadean continental crust by late heavy bombardment. *Icarus*, 266:189–203, 2015.

- [311] T. Shibuya, M. J. Russell, and K. Takai. Free energy distribution and hydrothermal mineral precipitation in hadean submarine alkaline vent systems: Importance of iron redox reactions under anoxic conditions. *Geochimica et Cosmochimica Acta*, 175:1–19, 2016.
- [312] A. Shimoyama, H. Naraoka, H. Yamamoto, and K. Harada. Carboxylic acids in the yamato-791198 carbonaceous chondrite from antarctica. *Chem. Lett.*, 15:1561–1564, 1986.
- [313] A. Shimoyama, H. Naraoka, M. Komiya, and K. Harada. Analyses of carboxylic acids and hydrocarbons in antarctic carbonaceous chondrites yamato-74662 and yamato-793321. *Geochem. J.*, 23:181–193, 1989.
- [314] R. L. Sinsheimer. The photochemistry of cytidylic acid. *Radiation Res.*, 6(2):121–125, 1957.
- [315] R. L. Sinsheimer and R. Hastings. A reversible photochemical alteration of uracil and uridine. *Science*, 110(2864):525–526, 1949.
- [316] T. Siu and C. Q. Jia. Kinetic and mechanistic study of reaction between sulfide and sulfite in aqueous solution. *Industrial & engineering chemistry research*, 38(10):3812–3816, 1999.
- [317] M. W. Slack. Kinetics and thermodynamics of the cn molecule. iii. shock tube measurements of cn dissociation rates. *J. Chem. Phys.*, 64:228–236, 1976.
- [318] C. Snodgrass, A. Fitzsimmons, S. C. Lowry, and P. Weissman. The size distribution of jupiter family comet nuclei. *Mon. Not. R. Astron. Soc.*, 414:458–469, 2011.
- [319] S. Sobek, G. Algesten, A.-K. Bergström, M. Jansson, and L. J. Tranvik. The catchment and climate regulation of pco₂ in boreal lakes. *Global Change Biology*, 9(4):630–641, 2003.
- [320] V. Sojo, B. Herschy, A. Whicher, E. Camprubí, and N. Lane. The Origin of Life in Alkaline Hydrothermal Vents. *Astrobiology*, 2016.
- [321] J. Sørensen and journal=Geochimica et Cosmochimica Acta volume=55 number=5 pages=1289–1294 year=1991 publisher=Elsevier Thorling, L. Stimulation by lepidocrocite (7-feooh) of fe (ii)-dependent nitrite reduction.

- [322] L. J. Spokes and P. S. Liss. Photochemically induced redox reactions in seawater, ii. nitrogen and iodine. *Marine chemistry*, 54(1-2):1-10, 1996.
- [323] J. E. Sponer, R. Szabla, R. W. Gora, A. Marco Saitta, F. Pietrucci, F. Saija, E. Di Mauro, R. Saladino, M. Ferus, S. Civis, and J. Sponer. Prebiotic synthesis of nucleic acids and their building blocks at the atomic level - merging models and mechanisms from advanced computations and experiments. *Phys. Chem. Chem. Phys.*, 18:20047-20066, 2016.
- [324] G. Springsteen. Reaching back to jump forward: Recent efforts towards a systems-level hypothesis for an early rna world. *ChemBioChem*, 16:1411-1413, 2015.
- [325] S. Stairs, A. Nikmal, D.-K. Bucar, S.-L. Zheng, J. W. Szostak, and M. W. Powner. Divergent prebiotic synthesis of pyrimidine and 8-oxo-purine ribonucleotides. *Nat. Commun.*, 8:15270, 2017.
- [326] C. L. Stanton, C. T. Reinhard, J. F. Kasting, N. E. Ostrom, J. A. Haslun, T. W. Lyons, and J. B. Glass. Nitrous oxide from chemodenitrification: A possible missing link in the proterozoic greenhouse and the evolution of aerobic respiration. *Geobiology*, 16(6):597-609, 2018.
- [327] A. M. Steer, N. Bia, D. K. Smith, and P. Clarke. Prebiotic synthesis of 2-deoxy-d-ribose from interstellar building blocks promoted by amino esters or amino nitriles. *Chem. Commun.*, 53:10362-10365, 2017.
- [328] K. L. Stevenson and J. H. Jarboe. Are excimers formed along with hydrated electrons in the uv excitation of cyanocuprate(i) ions in aqueous solution? *J. Photochem. Photobiol. A Chem.*, 150:49-57, 2002.
- [329] R. Stribling and S. L. Miller. Energy yields for hydrogen cyanide and formaldehyde synthesis: the hcn and amino acid concentrations in the primitive ocean. *Orig. Life Evol. Biosph.*, 17:261-273, 1987.
- [330] J. E. Strick. *Sparks of Life: Darwinism and the Victorian Debates over Spontaneous Generation*. Harvard University Press, 2009.
- [331] E. E. Stüeken, R. Buick, B. M. Guy, and M. C. Koehler. Isotopic evidence for biological nitrogen fixation by molybdenum-nitrogenase from 3.2 gyr. *Nature*, 520(7549):666, 2015.

- [332] S. Sugita and P. H. Schultz. Efficient cyanide formation due to impacts of carbonaceous bodies on a planet with a nitrogen-rich atmosphere. *Geophys. Res. Lett.*, 36:L20204, 2009.
- [333] D. P. Summers. Ammonia formation by the reduction of nitrite/nitrate by fes: ammonia formation under acidic conditions. *Orig. Life Evol. Biosph.*, 35(4):299–312, 2005.
- [334] D. P. Summers and S. Chang. Prebiotic ammonia from reduction of nitrite by iron (II) on the early Earth. *Nature*, 1993.
- [335] D. P. Summers and B. Khare. Nitrogen Fixation on Early Mars and Other Terrestrial Planets: Experimental Demonstration of Abiotic Fixation Reactions to Nitrite and Nitrate. *Astrobiology*, 2007.
- [336] J. D. Sutherland. The origin of life - out of the blue. *Angew. Chem. Int. Edit.*, 55:104–121, 2016.
- [337] R. Szabla, D. Tuna, R. W. Gora, J. Sponer, A. L. Sobolewski, and W. Domcke. Photochemistry of 2-aminooxazole, a hypothetical prebiotic precursor of rna nucleotides. *J. Phys. Chem. Lett.*, 4(16):2785–2788, 2013.
- [338] R. Szabla, J. Sponer, and R. W. Gora. Electron-driven proton transfer along h₂o wires enables photorelaxation of $\pi\sigma^*$ states in chromophore-water clusters. *J. Phys. Chem. Lett.*, 6(8):1467–1471, 2015.
- [339] R. Szabla, H. Kruse, P. Stradlbauer, J. Sponer, and A. L. Sobolewski. Sequential electron transfer governs the uv-induced self-repair of dna photolesions. *Chem. Sci.*, 9:3131–3140, 2018.
- [340] A. Szekely, R. K. Hanson, and C. T. Bowman. Thermal decomposition of hydrogen cyanide behind incident shock waves. *J. Phys. Chem.*, 88:666–668, 1984.
- [341] A. Szekely, R. K. Hanson, and C. T. Bowman. Shock tube study of the thermal decomposition of cyanogen. *J. Phys. Chem.*, 80:4982–4985, 1984.
- [342] Hanson R. K. Bowman C. T. Szekely, A. Shock tube study of the reaction between hydrogen cyanide and atomic oxygen. In *Twentieth Symposium (International) on Combustion/The Combustion Institute*.

- [343] J. W. Szostak. Attempts to define life do not help to understand the origin of life. *J. Biomol. Struct. Dyn.*, 29(4):599–600, 2012.
- [344] A. Tagliabue. More to hydrothermal iron input than meets the eye. *Proceedings of the National Academy of Science*, 111:16641–16642, November 2014. doi: 10.1073/pnas.1419829111.
- [345] L. L. Taylor, S. A. Banwart, P. J. Valdes, J. R. Leake, and D. J. Beerling. Evaluating the effects of terrestrial ecosystems, climate and carbon dioxide on weathering over geological time: a global-scale process-based approach. *Phil. Trans. R. Soc. B*, 367:565–582, 2012.
- [346] F. Tera, D. A. Papanastassiou, and G. J. Wasserburg. Isotopic evidence for a terminal lunar cataclysm. *Earth Planet. Sc. Lett.*, 22:1–21, 1974.
- [347] F. Tian, O. B. Toon, A. A. Pavlov, and H. De Sterck. A Hydrogen-Rich Early Earth Atmosphere. *Science*, 2005.
- [348] F. Tian, J. F. Kasting, and K. Zahnle. Revisiting hcn formation in the earth’s early atmosphere. *Earth Planet. Sci. Lett.*, 308:417–423, 2011.
- [349] K. E. Tjhung, M. N. Shokhirev, D. P. Horning, and G. F. Joyce. An rna polymerase ribozyme that synthesizes its own ancestor. *Proc. Natl. Acad. Sci. USA*, 117(6):2906–2913, 2020.
- [350] Z. R. Todd, A. C. Fahrenbach, C. J. Magnani, S. Ranjan, A. Bjorkbom, J. W. Szostak, and D. D. Sasselov. Solvated-electron production using cyanocuprates is compatible with the uv-environment on a hadean-archaeon earth. *Chem. Commun.*, 54:1121–1124, 2018.
- [351] Z. R. Todd, R. Szabla, J. W. Szostak, and D. D. Sasselov. Photostability of three 2-aminoazoles with key roles in prebiotic chemistry on the early earth. *Chem. Commun.*, 55:10388–10391, 2019.
- [352] N. J. Tosca, S. Guggenheim, and P. K. Pufahl. An authigenic origin for Precambrian greenalite: Implications for iron formation and the chemistry of ancient seawater. *Geological Society of America Bulletin*, 2016.
- [353] D. Trail, E. B. Watson, and N. D. Tailby. The oxidation state of hadean magmas and implications for early earth’s atmosphere. *Nature*, 480:79–82, 2011.

- [354] A. Treinin and E. Hayon. Absorption spectra and reaction kinetics of NO_2 , NO_3 , and NO_4 in aqueous solution. *Journal of the American Chemical Society*, 92(20):5821–5828, 1970.
- [355] J. Tröstl, W. K. Chuang, H. Gordon, M. Heinritzi, et al.
- [356] A. H. Truesdell and B. F. Jones. WATEQ, A Computer Program for Calculating Chemical Equilibria of Natural Water. *Journal Research U.S. Geological Survey*, 1974.
- [357] W. Tsang. Chemical kinetic database for propellant combustion ii. reactions involving CN , NCO , and HNCO . *J. Phys. Chem. Ref. Data*, 21:753, 1992.
- [358] F. M. Uber and F. Verbrugge. Photochemistry of the thiazole component of vitamin B_1 . *J. Biol. Chem.*, 136:81–86, 1940.
- [359] R. M. Uppu, G. L. Squadrito, and W. A. Pryor. Acceleration of peroxyxynitrite oxidations by carbon dioxide. *Archives of Biochemistry and Biophysics*, 327(2):335–343, 1996.
- [360] H. C. Urey. On the Early Chemical History of the Earth and the Origin of Life. *Proceedings of the National Academy of Science*, 1952.
- [361] O. Van Cleemput and L. Baert. Calculations of the nitrite decomposition reactions in soils. In 3. *International Symposium on Environmental Biogeochemistry. Wolfenbuettel (Germany, FR)*. 1978., 1978.
- [362] O Van Cleemput and L Baert. Nitrite stability influenced by iron compounds. *Soil Biology and Biochemistry*, 15(2):137–140, 1983.
- [363] A. C. Van Loenen and W. Hofs-Kemper. Stability and degradation of sodium nitroprusside. *Pharmaceutisch weekblad*, 1(1):424–436, 1979.
- [364] C. J. Vesey and G. A. Batistoni. The determination and stability of sodium nitroprusside in aqueous solutions (determination and stability of SNP). *Journal of Clinical Pharmacy and Therapeutics*, 2(2):105–117, 1977.
- [365] T. J. Vick, J. A. Dodsworth, K. C. Costa, E. L. Shock, and B. P. Hedlund. Microbiology and geochemistry of little hot creek, a hot spring environment in the long valley caldera. *Geobiology*, 8(2):140–154, 2010.

- [366] G. Wachtershauser. Before enzymes and templates: theory of surface metabolism. *Microbiol. Rev.*, 52(4):452–484.
- [367] M. Wainwright and F. Alshammari. The forgotten history of panspermia and theories of life from space. *Journal of Cosmology*, 7:1771–1776, 2010.
- [368] V. Wakelam, E. Herbst, and J.-C. Loison et al. A kinetic database for astrochemistry. *Astrophys. J. Suppl. S.*, 199:21, 2012.
- [369] J. C. G. Walker and P. Brimblecombe. Iron and sulfur in the pre-biogenic ocean. *Precambrian Research*, 28(3-4):205–222, 1985.
- [370] S. I. Walker, M. A. Grover, and N. V. Hud. Universal Sequence Replication, Reversible Polymerization and Early Functional Biopolymers: A Model for the Initiation of Prebiotic Sequence Evolution. *PLoS ONE*, 2012.
- [371] S. Y. Wang. Ultra-violet irradiation of 1,3-dimethylthymine. *Nature*, 184:59–61, 1959.
- [372] S. A. Watmough and J. Aherne. Estimating calcium weathering rates and future lake calcium concentrations in the muskoka-haliburton region of ontario. *Canadian Journal of Fisheries and Aquatic Science*, 65(5):821–833, 2008.
- [373] A. L. Weber and S. Pizzarello. The peptide-catalyzed stereospecific synthesis of tetroses: a possible model for prebiotic molecular evolution. *Proc. Natl. Acad. Sci.*, 103:12713–12717, 2006.
- [374] W. J. Wechter and K. C. Smith. Nucleic acids. ix. the structure and chemistry of uridine photohydrate. *Biochem.*, 7(11):4064–4069, 1968.
- [375] K. L. Wierzchowski and D. Shugar. Photochemistry of cytosine nucleosides and nucleotides ii. *Acta. Biochim. Pol.*, 8:219–234, 1961.
- [376] S. A. Wilde, J. W. Valley, W. H. Peck, and C. M. Graham. Evidence from detrital zircons for the existence of continental crust and oceans on the Earth 4.4Gyr ago. *Nature*, 2001.
- [377] T. J. Wilson and D. M. J. Lilley. Rna catalysis-is that it? *RNA*, 21(4):534–537, 2015.

- [378] S. K. Wolfe and J. H. Swinehart. Photochemistry of pentacyanonitrosylferrate (2-), nitroprusside. *Inorganic Chemistry*, 14(5): 1049–1053, 1975.
- [379] M. L. Wong, B. D. Charnay, P. Gao, Y. L. Yung, and M. J. Russell. Nitrogen Oxides in Early Earth's Atmosphere as Electron Acceptors for Life's Emergence. *Astrobiology*, 2017.
- [380] M. S. Wooldridge, R. K. Hanson, and C. T. Bowman. A shock tube study of $\text{CO} + \text{OH} = \text{CO}_2 + \text{H}$ and $\text{HNCO} + \text{OH} = \text{products}$ via simultaneous laser absorption measurements of OH and CO₂. *Int. J. Chem. Kinet.*, 28:361–372, 1996.
- [381] S. T. Wooldridge, R. K. Hanson, and C. T. Bowman. A shock tube study of reactions of CN with HCN, OH, and H₂ using CN and OH laser absorption. *Int. J. Chem. Kinet.*, 28:245–258, 1996.
- [382] S. T. Woolridge, R. K. Hanson, and C. T. Bowman. Simultaneous laser absorption measurements of CN and OH in a shock tube study of $\text{HCN} + \text{OH} = \text{products}$. *Int. J. Chem. Kinet.*, 27:1075–1087, 1995.
- [383] R. Wordsworth and R. Pierrehumbert. Hydrogen-Nitrogen Greenhouse Warming in Earth's Early Atmosphere. *Science*, 2013.
- [384] J. Xu, M. Tsanakopoulou, C. J. Magnani, R. Szabla, J. E. Sporer, R. W. Gora, and J. D. Sutherland. A prebiotically plausible synthesis of pyrimidine β -ribonucleosides and their phosphate derivatives involving photoanomerization. *Nat. Chem.*, 9:303–309, 2017.
- [385] J. Xu, D. J. Ritson, S. Ranjan, Z. R. Todd, D. D. Sasselov, and J. D. Sutherland. Photochemical reductive homologation of hydrogen cyanide using sulfite and ferrocyanide. *Chem. Commun.*, 54:5566–5569, 2018.
- [386] Y. Xu, M. A. A. Schoonen, D. K. Nordstrom, K. M. Cunningham, and J. W. Ball. Sulfur geochemistry of hydrothermal waters in Yellowstone National Park: I. the origin of thiosulfate in hot spring waters. *Geochimica Cosmochimica Acta*, 1998.
- [387] Y. Yamagata, H. Watanabe, et al. Volcanic production of polyphosphates and its relevance to prebiotic evolution. *Nature*, 352(6335):516, 1991.

- [388] K. E. Yttri, C. Dye, and G. Kiss. Ambient aerosol concentrations of sugars and sugar-alcohols at four different sites in Norway. *Atmos. Chem. Phys. Discuss.*, 7(2):5769–5803, 2007.
- [389] O. C. Zafiriou. Sources and reactions of OH and daughter radicals in seawater. *Journal of Geophysical Research*, 79(30):4491–4497, 1974.
- [390] O. C. Zafiriou and R. Bonneau. Wavelength-dependent quantum yield of OH radical formation from photolysis of nitrite ion in water. *Photochemistry and photobiology*, 45(S1):723–727, 1987.
- [391] O. C. Zafiriou and M. McFarland. Nitric oxide from nitrite photolysis in the central equatorial Pacific. *Journal of Geophysical Research: Oceans*, 86(C4):3173–3182, 1981.
- [392] O. C. Zafiriou and M. B. True. Nitrate photolysis in seawater by sunlight. *Marine Chemistry*, 8(1):33–42, 1979.
- [393] O. C. Zafiriou and M. B. True. Nitrite photolysis in seawater by sunlight. *Marine Chemistry*, 8(1):9–32, 1979.
- [394] O. C. Zafiriou, J. Joussot-Dubien, R. G. Zepp, and R. G. Zika. Photochemistry of natural waters. *Environmental Science & Technology*, 18(12):358A–371A, 1984.
- [395] K. Zahnle, M. Claire, and D. Catling. The loss of mass-independent fractionation in sulfur due to a palaeoproterozoic collapse of atmospheric methane. *Geobiology*, 4(4):271–283, 2006.
- [396] K. Zahnle, L. Schaefer, and B. Fegley. Earth's earliest atmospheres. In D. Deamer and J. W. Szostak, editors, *Cold Harbor Spring Harb. Perspect. Biol.*, page a004895. Cold Spring Harbor Laboratory Press, 2010.
- [397] K. J. Zahnle. Photochemistry of methane and the formation of hydrocyanic acid (HCN) in the Earth's early atmosphere. *J. Geophys. Res.*, 91:2819–2834, 1986.
- [398] K. J. Zahnle, M. Gacesa, and D. C. Catling. Strange messenger: A new history of hydrogen on Earth, as told by Xenon. *ArXiv e-prints*, 2018.
- [399] Richard E. Zeebe and Dieter A. Wolf-Gladrow. *Carbon Dioxide, Dissolved (Ocean)*, pages 123–127. Springer Netherlands, Dordrecht, 2009.

- [400] J. P. Zehr and B. B. Ward. Nitrogen cycling in the ocean: new perspectives on processes and paradigms. *Applied and Environmental Microbiology*, 68(3):1015–1024, 2002.
- [401] R. Zellner, M. Exner, and H. Herrmann. Absolute oh quantum yields in the laser photolysis of nitrate, nitrite and dissolved h₂o₂ at 308 and 351 nm in the temperature range 278–353 k. *Journal of Atmospheric Chemistry*, 10(4):411–425, 1990.
- [402] A. L. Zerkle and S. Mikhail. The geobiological nitrogen cycle: From microbes to the mantle. *Geobiology*, 15(3):343–352, 2017.
- [403] R. B. Zhang and L. A. Eriksson. A triplet mechanism for the formation of cyclobutane pyrimidine dimers in uv-irradiated dna. *J. Phys. Chem. B*, 110(14):7556–7562, 2006.
- [404] X.-Y. Zheng, B. L. Beard, E. E. Roden, A. D. Czaja, and C. M. Johnson. New constraints on ferrous fe concentrations in the archean ocean. In *Goldschmidt Abstracts*, page 3033, 2018.
- [405] I. Zhu and T. Getting. A review of nitrate reduction using inorganic materials. *Environmental Technology Reviews*, 1(1):46–58, 2012.
- [406] X. Zhu-Barker, A. R. Cavazos, N. E. Ostrom, W. R. Horwath, and J. B. Glass. The importance of abiotic reactions for nitrous oxide production. *Biogeochemistry*, 126(3):251–267, 2015.

Colophon

THIS THESIS WAS TYPESET using \LaTeX , originally developed by Leslie Lamport and based on Donald Knuth's \TeX . The body text is set in 11 point Arno Pro, designed by Robert Slimbach in the style of book types from the Aldine Press in Venice, and issued by Adobe in 2007. A template, which can be used to format a PhD thesis with this look and feel, has been released under the permissive MIT (X11) license, and can be found online at github.com/suchow/ or from the author at suchow@post.harvard.edu.